EXPERIMENTAL ANALYSIS OF ELECTRIC DOUBLE LAYER AND LITHIUM-ION CAPACITORS FOR ENERGY STORAGE SYSTEMS AND THEIR APPLICATION IN A SIMULATED DC METRO RAILWAY SYSTEM

EXPERIMENTAL ANALYSIS OF ELECTRIC DOUBLE LAYER AND LITHIUM-ION CAPACITORS FOR ENERGY STORAGE SYSTEMS AND THEIR APPLICATION IN A SIMULATED DC METRO RAILWAY SYSTEM

By MACKENZIE WOOTTON, B.Sc

A Thesis Submitted to the School of Graduate Studies in Partial Fulfillment of the

Requirements for the Degree of Master of Applied Science.

McMaster University

Master of Applied Science (2018) McMaster University

(Electrical & Computer Engineering) Hamilton, Ontario, Canada

Title:	Experimental Analysis of Electric Double Layer and Lithium-ion Capacitors for Energy Storage Systems and their Application in a Simulated DC Metro Railway System
Author:	Mackenzie Wootton B.Sc, Electrical Engineering Queen's University Kingston, ON Canada
Supervisor:	Dr. Ali Emadi
Number of Pages:	xxiii, 240

Abstract

This works begins by providing motivation for additional research and political interest in the use of passenger railway systems as a method of 'green' transportation. Additional motivation for the adoption of energy saving methods within new and existing railway systems is also provided. This motivation stems from the relatively small carbon dioxide emissions per passenger kilometer and large quantity of electrical energy used in association with passenger railway systems. In specific cases, both theoretical analyses and experimental implementations of energy storage in railway systems have shown a reduction in electrical energy use and/or vehicle performance gains. Current railway energy storage systems (ESS) commonly make use of battery or electric double layer capacitor (EDLC) cells. A review of select energy storage technologies and their application in railway systems is provided. For example, the developing Qatar Education City People Mover System makes use of energy dense batteries and power dense EDLCs to provide the range and power needed to operate without a conventional railway power source between stations, formally called catenary free operation.

As an alternative to combining two distinct energy storage technologies, this work looks at experimentally characterizing the performance of commercially available lithium ion capacitors (LiCs); a relatively new energy storage cell that combines characteristics of batteries and EDLCs into one cell. The custom cell testing apparatus and lab safety systems used by this work, and others, is discussed. A series of five tests were performed on two EDLC cells and five LiC cells to evaluate their characteristics under various electrical load conditions at multiple temperatures. The general conclusion is that, in comparison to the EDLC cells tested, the LiC cells tested offer a superior energy density however, their power capabilities are relatively limited, especially in cold environments, due to larger equivalent series resistance values.

The second topic explored in this work is the development of a MATLAB based DC powered passenger vehicle railway simulation tool. The simulation tool is connected to the experimental analysis of EDLC and LiC cells by comparing the volume and mass of an energy storage system needed for catenary free (no conventional DC power supply) operation between train stations using either energy storage technology. A backward facing modelling approach is used to quantify the drive cycle electrical power demands as a function of multiple vehicle parameters and driving parameters (eg. acceleration rate, travel distance and time).

Additional modelling methods are provided as a resource to further develop the simulation tool to include multiple vehicles and their interactions with the DC power supply. Completion of the multi-vehicle simulation tool with energy storage systems remains a task for future work.

Acknowledgements

I would first like to thank Dr. Emadi for his continuing drive to develop and improve opportunities for students, such as myself, to explore their interests in transportation electrification through student design teams, industry driven projects and self-motivated work. I attribute Dr. Emadi's alternative approaches to engineering education, strategic planning and passion to see students "go up" as the catalysts for success in developing an environment that fosters higher education in Ontario. Even with such a large research group, Dr. Emadi provided individual mentorship and support in my academic work, career development and personal life.

Dr. Phillip Kollmeyer has, without a doubt, provided the most genuine, helpful and passion-driven support and advice possible; something unparalleled by other post-doctorate research fellows. Phil's hands-on research approach, dedication to the success of others, self-motivation, and wealth of knowledge obtained from his extensive education and diverse work experiences has earned him the utmost respect and endless appreciation from industry professionals, academics and students. I am extremely confident that Dr. Kollmeyer has, and will continue to, play an influential role in advancing transportation electrification research while enriching educational experiences for others. I am honoured to have the opportunity to work with Phil and learn from his highly regarded continuous outpouring of technical knowledge, support and guidance. "Thank you" is simply not enough.

I owe great appreciation to several students, especially John Reimers, Alison Bayzat, Melissa He, Mike Haussmann and Mrudang Kadakia, who have enriched my educational experience through the McMaster Engineering EcoCAR 3 team, other projects at the McMaster Automotive Resource Centre (MARC) and lunch breaks. Similarly, the staff at MARC, especially Theresa Mitchell and Cam Fisher, play a large role in enabling the research activities of several students, including myself.

Finally, I must thank my family and my love. Thank you to my parents, Todd, Katherine, and Angela, for their support throughout my undergraduate and graduate school experiences. Most importantly, thank you to Kelli for the patience, encouragement, excitement, support and love she provided throughout six years of university as my friend, girlfriend and fiancée.

Mackenzie Wootton

August 26th, 2018

Contents

List of Tables

List of Figures

Abbreviations

ALSS	Aluminum Stainless Steel (normally related to 3rd rail conductor material)
AWG	American Wire Gauge
CC	Constant Current
CCCV	Constant Current Constant Voltage
CER	Community of European Railway and Infrastructure Companies
DAQ	Data Acquisition (normally related to NI hardware)
DPDT	Double Pole Double Throw
DUT	Device Under Test
EDLC	Electric Double Layer Capacitor
EIS	Electrochemical Impedance Spectroscopy
EMU	Electric Multiple Unit
EPA	Environmental Protection Agency
ESR	Equivalent Series Resistance
ESS	Energy Storage System
E-stop	Emergency stop
HESS	Hybrid Energy Storage System
HIL	Hardware in the Loop
HPPC	Hybrid Pulse Power Characterization
HWFET	Highway Fuel Economy Test
IEA	International Energy Agency
LiB	Lithium Ion Battery
LiC	Lithium Ion Capacitor
|| LiC	Parallel / Symmetrical Lithium Ion Capacitor

MARC	McMaster Automotive Resource Centre
MCT	Multi Cell Tester
MNA	Modified Node Analysis
N/C	Normally Closed
N/O	Normally Open
NI	National Instruments
OCV	Open Circuit Voltage
PLC	Programmable Logic Controller
P/N	Part Number
SEPTA	Southeastern Pennsylvania Transportation Authority
SOC	State of Charge
T.C	Thermal Chamber
THESL	Toronto Hydro-Electric Systems Limited
TTC	Toronto Transit Commission
UDDS	Urban Dynamometer Driving Schedule
UPX	Union-Pearson Express
UIC	International Railway Association
UITP	Union Internationale des Transports Publics
US06	A specific velocity drive cycle profile often used for emission standards testing

Declaration of Interest, Funding Sources and Disclaimer

This body of work was conducted as per the author's interests without influence from external non-academic sources or funding groups.

The energy storage lab used for the experimental portion of this work was funded, in part, by the Canada Excellence Research Chair (CERC) in Hybrid Powertrain program lead by Dr. Ali Emadi, the Centre for Mechatronics and Hybrid Technologies (CMHT) lead by Dr. Saeid Habibi, and the Leadership in Automotive Powertrain (LEAP) project that includes funding from Fiat Chrysler Automobiles (FCA) and NSERC Automotive Partnership Canada.

Six of the seven capacitor cells studied in this work were purchased at the author's discretion without incentives from the capacitor manufacturers nor sales offices. The remaining cell was provided by a former student design team. The cell characterization results are intended to compare the performance of EDLC and LiC cell technology rather than the performance of products offered by various manufacturers. Therefore, considerable effort was made to conceal the identity of the cell manufacturers while still providing information necessary for comparison. The experimental results are prone to systematic and measurement error and therefore the author makes no public guarantee for the accuracy of this work nor its representation of EDLC and LiC technology as a whole.

The railway simulation tool described in this work is based on a review of publicly available work and general vehicle and circuit modelling methods. The simulation results were not compared to real world measured values and therefore the simulation tool contains unquantified errors.

Considerable effort was made to properly recognize the contributions of others towards this work, including material from other resources. In the event of a reference omission or lack of acknowledgement, the author is not intentionally trying to claim credit for the respective work.

The author shall not be held responsible for the use of this work, and/or resulting outcomes, by others. Business decisions should not be made based on this work.

1. Introduction

1.1. Background and Motivation

A joint publication by the International Railway Association (UIC) and the Community of European Railway and Infrastructure Companies (CER) states that "[r]ail is the most emissions-efficient major mode of transport" [1, p. 3]. Similarily, a report from the European Rail Research Advisory Council says that "Rail transport is recognised as the most environmentally friendly form of mass transport" [2, p. 11]. For comparison, [3, p. 5] lists the carbon dioxide emissions for rail, road and air passenger transportation to be 28.39 gCO_2/pkm, 101.61 gCO_2/pkm and 244.09 gCO_2/pkm, respectively, where 'pkm' represents the distance, measure in kilometers, travelled by each passenger. The 2016 Railway Handbook published by the International Energy Agency (IEA) and IUC suggest that the total carbon dioxide emissions from passenger rail service has decreased by 60% between 1975 and 2013 [4, p. 18]. With the worldwide increase in railway electrification (163% increase between 1975 and 2013 [4, p. 18]) and increase in renewable energy powering railway systems (7.6% to 20% from 1990 to 2013 in EU28 [4, p. 28]), the author predicts that passenger rail transportation carbon dioxide emissions per passenger kilometer are likely to decrease in the future. However, the electrical power to operate electrified rail systems is considerable.

According to the International Association of Public Transport, properly called the Union Internationale des Transports Publics or UITP, the energy consumed for urban rail passenger transportation within Europe in 2013 was 0.12 kWh/pkm, which is "7x less than the average car in [an] urban context" [5, p. 2]. Even with a reduced energy demand per passenger kilometer, compared to many modes of transportation, "[t]he total urban rail energy consumption [within Europe, 2013] is ~11.000 GWh per year, which is comparable to the residential energy

consumption of the Brussels region (approximately 1 million people)" [5, p. 2]. As another example, the Toronto Transit Commission (TTC) estimates that a six car Toronto Rocket subway train replaces the necessity for approximately 980 passenger cars during a typical morning rush hour [6]. In 2016, the TTC reported an annual "passenger trip" count of approximately 538 million, with approximately 47% of transportation trips by bus and 41% by subway trains [6]. When averaging data from [7], [8] and [9], the TTC's average annual electricity consumption is approximately 441.7 million kWh, of which approximately 75-77% (~335.7 million kWh) of the energy is used for traction applications (not specified what percentage is for streetcar and subway services) [7] [8] [10]. In 2010 Toronto Hydro-Electric Systems Limited (THESL), the electricity distribution company for the City of Toronto, reported an annual distribution of "24.7 terawatt-hours of electricity representing approximately 19 percent of the electricity consumed in the province of Ontario" [11]. Using these values, it is estimated that the TTC's electrical traction energy consumption could represent approximately 1.4% of Toronto's annual electricity consumption and approximately 0.26% of Ontario's electricity consumption. Although this is a rather small percentage, with an annual electricity cost of approximately $40 million [8], it is estimated that the TTC annual traction electricity expense is approximately $30.4 million (CAD). A large ridership and electrical energy consumption can also be seen in other transportation systems. For example, the Southeastern Pennsylvania Transportation Authority (SEPTA) reported a 2016 annual combined ridership of approximately 100 million trips on the Norristown High Speed Line (NHSL), Market-Frankford Subway-Elevated Line (MFSE) and Broad Street Subway (BSS) [12, p. 3]. The total energy consumed by these three services in 2016 amounted to approximately 143 million kWh [12, p. 6].

Considering the high ridership counts and relatively low carbon dioxide emissions from passenger railway transportation, the author suggests additional research and political emphasis on the implementation of energy efficient electrified passenger railway systems powered by renewable energy. Unfortunately, the cost to develop passenger railway systems, including non-electrically powered systems, can be a barrier to adoption. For example, the 23.3 km [13] Union-Pearson Express (UPX) train in Toronto, which entered service in June 2015 [13], cost $456 million CAD to build and started with one way fares of $27.50 CAD [14]. The proposed 350 km high speed electrified passenger rail system between Windsor, ON and Toronto, ON is estimated to cost $21 billion CAD ($60 million CAD per kilometer). The recent 8.6 km [15] subway extension on the TTC subway system, which adds 6 subway stations, cost approximately $3.2 billion CAD [16]. These local examples show that the cost to implement new passenger railway systems, including surface rail (UPX), high speed rail (Windsor-Toronto) and subways is considerable. Although new passenger railway systems may be infeasible, the author believes that there may be a potential to reduce the electrical energy consumption from existing electrified rail systems and further reduce the environmental impact and electricity cost for passenger rail transportation.

The 2012 SEPTA Energy Action Plan identified eighteen initiatives aimed at reducing the entire SEPTA system CO_2 emissions by approximately 12% and subsequently save roughly $2.2 million USD annually (2011 pricing) due to energy use reductions [17, pp. 2-3]. The electricity initiatives from Table 14 of [17, pp. 23-26] include improvements in the utilization of regenerative braking energy (projects 2A-1 and 2B-1 – combined savings of approximately 15,285,889 kWh and $1.36 million USD per year, evaluated at $0.089/kWh) and using wayside energy storage (projects 2B-2, 2C-1 – combined savings of approximately 18,091,787 kWh and $1.6 million USD per year)

[17]. With approximately 40 metro networks and 180 light rail and tram networks in Europe [5, p. 2] the author believes that implementing energy saving devices or methods within existing passenger rail systems may be an alternative approach to reducing passenger rail energy consumption and carbon dioxide emissions rather than building new expensive rail systems. Additionally, if a linear relationship between energy reduction and cost savings is assumed, in the case of the TTC (see above) an electrical energy savings of even 1% may result in savings of $400,000 CAD annually (based on 1% of $40 million CAD). Aging infrastructure and rollingstock may present a considerable opportunity for energy savings, especially if there is an increase in ridership.

When evaluating energy consumption reducing measures in passenger railway systems it is important to look at the entire railway system and several variables. For example, [18] provides an excellent review of energy consumption related to vehicle motion as well as energy saving methods in railway systems. Figure 5 from [18] classifies twenty-one energy saving methods for urban rail systems based on the technology type and implementation area; being either the whole rail system, infrastructure or rollingstock (the train vehicles). Notable examples include timetable optimization (whole system), wayside energy storage (infrastructure), drive cycle modifications, and lighting improvements on rolling stock.

When looking at systems with regenerative braking capabilities, such as the TTC, which, in 2008 had 94% of subway trains and 100% of street cars with regenerative braking capabilities [7, p. 17], one future direction is to look at making that regenerated power available for other loads such as auxiliary systems, other nearby rail vehicles or station infrastructure loads. Typically, the use of regenerative braking energy by other vehicles is dependent on the power demands and

proximity of other nearby vehicles, commonly called network receptivity. The movement of electrical energy from the braking train to the DC railway power supply can result in an increase in the line voltage due to the voltage supply resistance. To prevent electrical component damage, the supply voltage, which is typically 600V, 750V, 1500V or 3000V DC, must be within the voltage limits (approximately 20% more than the nominal voltage) outlined in various standards such as EN 50163 [19, p. 33] [20] and IEC 60850 [21, p. 3]. For example, Section 9 of [22], which documents parameters for the interworking of a 750V DC 3rd rail system, says that "Regeneration voltage shall not exceed 900V at the collector shoe" [22]. Low network receptivity and rising DC transmission voltages results in the need for dissipating regenerative braking energy into braking resistors [18, p. 513]. The network receptivity can be increased by introducing grid tied inverters that regenerate energy to the high voltage three phase grid supply, commonly called reversible substations. However, the regeneration of energy to the utility supply may not be an attractive energy saving option due to losses when transmitting power to the grid tied inverters and electrical utility policies that either restrict bi-directional power flow to the grid or offer minimal monetary value for regenerated electricity [23]. The main alternative to bi-directional grid power flow is to consider energy storage systems either on the rollingstock, formally called on-board ESS, or beside the tracks, formally called way-side energy storage. The energy storage may be achieved using various methods such as mechanical flywheels [24] [25], batteries [26] [27] [28], capacitors [29] [30] [31] [32] [33], or a combination of technologies [34]. However, there are compelling arguments regarding the financial benefits of reversible substations and energy storage systems when considering system lifetime, operating costs and capital costs. For example, Gelman, author of an article titled *Energy Storage That May Be Too Good to be True*, says that "The energy savings achieved by adding ESSs to diode rectifier substations provide a payback time of well over 30 years" [35]. Although this

article raises a concern regarding cost, we can look to energy storage examples from large businesses as a source of motivation and a confirmation of the energy saving influence provided by the experimental systems.

With the potential of reducing electricity consumption, providing line voltage support, load shifting, catenary free operation (no 3rd rail or over head DC supply), increasing back up energy storage and income from frequency regulation, multiple transit authorities and research groups, such as those in [7] [17] [23] [36] and [37] are exploring the use of energy storage systems. One of the most interesting upcoming projects is the Qatar Education City People Mover System which uses a catenary free track between stations with onboard hybrid energy storage systems (batteries and capacitors) that are charged at rail stations/stops [38] [39]. We can also look to large manufacturers and the results from railway energy storage pilot projects for motivation to study this topic. When discussing a rail-based hybrid energy storage system in Portugal, Siemens suggests that "The recovery and storage of braking energy results in 20% less energy consumption" [39, p. 21]. Bombardier suggests that the energy released from its capacitor based EnerGstor wayside energy storage system can "reduce the network energy consumption/demand by up to 20 per cent" [40, p. 2]. ABB's "ENVILINE ESS is a wayside energy storage system that stores and recycles this surplus energy, helping reduce the energy consumption up to 30 percent*" [41]. Similarly, Toshiba's traction energy storage system (TESS) used in the Suesyoshi Substation field test showed that "daily traction energy consumption was reduced to 575kWh/day (-17%) during weekday and 883kWh/day (-32%) during weekend…" operation [42]. It is important to note that the energy and monetary savings from academic literature and large manufacturers often state performance gains "up to" a certain value. As

noted by the asterisk above in the quote discussing ABB's ENVILINE ESS system, "The level of savings will depend on the operating conditions of the train system" [41].

Considering the wide range of passenger railway systems, it is important to identify railway configurations that would likely benefit the most from energy storage systems. From a high-level perspective, energy storage systems may be most beneficial for rail systems with frequent acceleration and braking cycles of multiple heavy vehicles that are powered by a relatively lossy transmission line system along a track with varying altitude [43]. In an excellent review paper by González-Gil et al., the authors state that "Typical values for infra-structure energy losses [, which includes substation and distribution losses,] can be as high as 22%, 18%, 10% and 6% for 600 V, 750 V, 1500 V and 3000 V-DC networks, respectively" [18]. Therefore, the author predicts that SNCF's Atlantic high speed TGV passenger trains powered by a 2 x 25kV 50 Hz autotransformer supply [44] is less ideal for energy storage systems compared to the TTC's subway system which has a weekday headway of a few minutes [45] and is powered by 600V DC via the third rail [46]. Considering the large number of variables that impact the railway vehicle system, including drive cycle characteristics and tractive supply power flow, the author suggests that each railway system be analyzed individually to estimate the energy and monetary saving benefits of adding energy storage systems.

Although the previous discussion has focused largely on energy savings by using energy storage devices, the key ESS application studied in this work is for catenary free operation, similar to the Qatar Education City People Mover System. Catenary free operation is an attractive solution for developing city centres that want to eliminate the use of over-head wires while providing safe public rail transit in dense urban areas. On-board ESSs can be used as the only power source to

the vehicle as well as provide energy saving benefits, such as those described previously, when operated with the DC power supply system (further analysis beyond this work is necessary).

In another excellent review paper (2013) by González-Gil et al. [23], the authors show multiple tables that review the energy storage devices, study type (theoretical vs experimental) and main results for on-board and stationary ESS systems for urban rail transportation. These tables, which review publications and commercial products, show that stationary and onboard rail energy storage systems primarily make use of electric double layer capacitors as the energy storage technology. However, Figure 6 of [47] shows seventeen battery-based energy storage systems for railway applications in Japan. The authors of [47] note that the energy storage systems provide several functions such as voltage line support, emergency power backup and energy saving. Select Japanese battery-based energy storage systems are discussed in more detail in [48]. Section 10.3 of [49] discusses four German electric accumulator coaches that made use of on-board lead acid batteries stored beneath the locomotive hood (vehicle ETA 177) and under the cars (vehicles ETA 176 and ETA 150). Some of these vehicles entered service in 1908 [49]. The ETA 150 train was equipped with a 400 kWh battery that offered a 250 km range [49]. The 1928 Class E 8 locomotive commissioned by DRG featured a 417 kWh lead acid battery pack [49]. It is interesting to see how the implementation of energy storage in railway systems began with on-board lead acid battery packs and has transitioned to mainly EDLC-based systems.

When looking at large manufacturers, we can see both battery and capacitor-based energy storage systems for railway applications. For example, Kawasaki has installed multiple battery based energy storage systems each exceeding 200 kWh [50] and Bombardier developed a battery powered tram using lithium ion battery packs from AKASOL [51] that completed a 41.6

km trip without a conventional DC power supply [52]. On the other hand, Bombardier also offers their EnerGstor technology that makes uses of capacitor energy storage for wayside rail applications [40]. These examples, and many others, show that battery energy storage is primarily used for situations that need large amounts of energy, such as catenary free driving, and capacitors are primarily used for more power demanding applications such as regenerative braking energy recovery. However, as mentioned earlier, Siemen's is using the combination of energy dense batteries and power dense electric double layer capacitors to form a hybrid energy storage system (HESS) for the Qatar Education City People Mover System which features a catenary free track between stations [38] [39]. A more detailed discussion on HESS technology is provided in Section 2.4**.**

Lithium ion capacitors (LiCs) are an emerging energy storage technology that combine characteristics of electric double layer capacitors and lithium ion batteries to form an asymmetric hybrid cell. Lithium ion capacitors may be an alternative energy storage device for specific railway applications that require a longer driving range than EDLC cells can provide or more power than a battery pack of a given size can offer. The relatively limited academic research investigating the performance of LiCs for energy storage in tractive applications, specifically railway systems, is primarily documented in publications by Flavio Ciccarelli. Further investigation into understanding the performance differences between EDLC cells and LiC cells will assist in evaluating their use in railway applications.

In summary, this section provided motivation to further study the use of passenger rail transportation; primarily due to the relatively low carbon diode emissions and opportunities to further reduce electrical energy consumption for existing electrified rail systems. A brief

overview of energy saving methods in passenger rail was provided and emphasis was placed on the use of on-board energy storage systems for catenary free operation. A discussion on different energy storage technologies, such as capacitors, batteries and a hybrid combination of them, was provide with emphasis on railway energy consumption or catenary free operation. A short discussion on a relatively new energy storage technology, lithium ion capacitors, was provides to briefly highlight how their capacitor-battery hybrid characteristics may be advantageous for tractive applications. The need for additional performance comparison between EDLC and LiC cells was identified. Academic study and industry examples of energy storage technology in railway applications have shown a considerable range of performance benefits, primarily dependant on the railway system configuration and operating parameters (ie, supply voltage and drive cycle characteristics). The author suggests further investigation into the parameters that make railway energy storage systems a good solution to help reduce total energy use in rail networks.

1.2. Contributions

This thesis discusses the tools developed and results obtained in studying two main topics:

a) An experimental performance comparison of electric double layer capacitors and lithium-ion capacitors for energy storage applications, and
b) The development of a railway simulation tool used to compare the mass and volume of an EDLC and LiC based on-board ESS used for catenary free operation from one station to another

These two topics are related by introducing experimental cell characterization results from a) into the railway simulation tool of b). The author's key contributions are outlined below:

- Documentation of design considerations for developing a custom cell testing device and future improvements for other students to build upon.

- Documentation of the processes and safety systems established to enable unattended and automated capacitor cell testing in a university-based energy storage lab
- Development of a systematic experimental capacitor cell testing procedure accompanied by a MATLAB based automated data analysis tool.
- High level specification comparison of two EDLCs and five lithium ion capacitors. The capacitors studied in this work were obtained from four manufactures. This cell selection broadens experimental work from literature by testing cells from more than one manufacturer.
- Identification of endothermic charging for LiC cells (for the specified test currents used)
- Identification and comparison of how the equivalent series resistance of EDLC and LiC cells changes with state of charge, temperature and testing current.
- Identification of a current dependant equivalent series resistance for LiC cells in cold temperatures.
- Documentation of an approach to model a railway drive cycle, drive cycle power demand and DC power transmission system using a circuit simplification and modified node analysis.
- The parameters needed to model a passenger railway system were more difficult to obtain than originally expected. A collection of publicly available modelling parameters was established.
- Analysis on how the rail vehicle mass and acceleration impact the peak power demanded and maximum electrical energy required for driving between two stations
- Comparison between the mass and volume of the cells for a LiC and EDLC based on-board ESS used to power a specific catenary free drive cycle. Eight test cases are explored.

1.3. Thesis Outline

This thesis is organized into eight chapters. The first chapter provided motivation for the study of energy saving methods and catenary free operation in passenger railway systems and lithium ion capacitors as an alternative energy storage technology. Chapter 2 provides an overview and comparison of battery, EDLC and lithium ion capacitor energy storage devices with a focus on their performance differences. In Chapter 3, DC railway power distribution is discussed in more detail and a literature review of railway energy storage work is provided. Chapter 4 describes the work performed to develop the custom cell testing device and related lab safety equipment used to characterize the EDLC and lithium ion capacitors tested in Chapter 5. Chapter 5 compares the performance of two EDLCs and five lithium ion capacitors based on five different time domain characterization tests. Chapter 6 outlines the modelling methods used to represent railway vehicle drive cycles, power demands and associated DC power flow (future work). Chapter 7 provides a collection of railway modelling parameters from literature that are used as the starting point for a sensitivity analysis to evaluate on-board ESS sizing for catenary free operation. Chapter 7 relates back to the experimental work from Chapter 5 by making use of the experimental cell characterization results in the ESS sizing exercise. A conclusion is presented in Chapter 8 and references follow.

2. Capacitor and Battery Energy Storage: Overview, Current Status, and Future Trends

2.1. Overview of Conventional Capacitor Energy Storage Methods

In general, capacitors derive their energy storage capability from the electrostatic interactions between two electrodes and an insulating/dielectric medium or electrolyte that separates them. A dielectric medium is an electrically non-conductive material that polarizes when in the presence of an electric field. This results in the movement of positive and negative charges from their usual position to develop a localization of positive and negative charges. An electrolyte is a gel or liquid that can be decomposed into oppositely charged ions called cations (positively charged) and anions (negatively charged). Both dielectric and electrolyte materials/liquids are useful in capacitors due to their interactions with the presence of negative and positive charges on the electrodes. A collection of positive charges on the positive electrode results in the attraction of negative charges from the dielectric or electrolyte. The collection of positive and negative charges on the respective electrodes is developed by the presence of the electromotive force from an applied voltage source (charging). On the other hand, the repulsive nature of similar charges on a material (eg. negative charges on negative electrode) and attractive forces between opposite charges (eg. ionized electrolyte) results in an electromotive force (voltage sustained while charged) that wants to depolarize (discharge) the capacitor. Variations in electrodes, insulating/dielectric materials or electrolytes and cell geometry result in the development of various capacitor technologies and performance characteristics. Generally speaking, a capacitor's capacitance, C, can be represented by Equation 1 where A is the electrode active area, ε is the dielectric constant, and d is the distance between the parallel electrode plates.

$$C = \frac{A\varepsilon}{d}\ [Farad\ or\ coulomb/volt]$$

Equation 1: Capacitance determined by the electrode active area, dielectric constant and distance between electrode plates.

Non-polar electrostatic capacitors, such as ceramic and film capacitors, typically use two oppositely charged parallel metallic current collectors separated by a solid dielectric medium to store energy in an electric field. Ceramic and film electrostatic capacitors are typically rated in picofarads or microfarads and up to tens of kilovolts per cell. Polar electrolytic capacitors, such as aluminum and tantalum capacitors, use the formation of a metal oxide on the metallic anode as the dielectric to develop an electric field with the solid or liquid electrolyte cathode. Aluminum electrolytic capacitors are typically rated in microfarads and up to several hundred volts per cell. Although electrostatic and electrolytic capacitors are used extensively, their relatively low energy density (0.024 Wh/kg and 0.019 Wh/kg, respectively [53, p. 10]) is unfavourable for vehicle energy storage systems.

Pseudocapacitors are symmetrical electrochemical capacitors [53, p. 30] that use special electrodes, such as ruthenium dioxide or conductive polymers [53, pp. 337,341] [54, p. 1] to store energy electrostatically and electrochemically/faradaically through electrosorption, intercalation or fast surface redox reactions [55, pp. 45-46] [54, p. 642]. Despite the use of faradaic energy storage methods, which typically produce a relatively constant electrode potential (flat open circuit voltage (OCV) vs. state of charge (SOC) relationship), pseudocapacitors are characterized by a relatively constant differential capacitance (dq/dV ≈ constant) that creates a near linear OCV vs. SOC relationship [54, p. 641], similar to an EDLC. Although the use of faradaic energy storage increases energy density compared to EDLC cells, the cycle life is typically less than EDLC cells but remains greater than battery cells [53, p. 337] [55, p. 46]. The wide-spread use of pseudocapacitors has been limited by high manufacturing

costs and/or low cycle life [53, p. 340]. A more detailed discussion on pseudocapacitors and a comparison to EDLCs can be found in Table 2 of [54] and Table 1 of [56].

Electric double layer capacitors are symmetrical polar capacitors that make use of highly porous electrodes, such as activated carbon, and a liquid electrolyte to develop a high surface area Helmholtz double layer at both electrode/electrolyte interfaces. The electrolyte is polarized to develop two electrostatic energy storage interfaces within one cell without ion exchange. The electrolyte polarization and development of two capacitor interfaces within an EDLC cell is shown in Figure 2 on pg. 48. Partially due to the lack of chemical reactions, EDLC cells have a high charge-discharge cycle life, often rated at one million cycles, with minimal cell degradation. The combination of porous electrodes with a significant surface area (in the range of 1000 m^2/g) [55, p. 45] and a liquid electrolyte that fills the porous electrode structure results in a very high area/distance ratio with a magnitude of 10^{12} [53, p. 24] and capacitance values measured in Farads. However, the EDLC cell terminal voltage is limited by the decomposition voltage of the liquid electrolyte and is typically limited to a few volts, therefore requiring multiple cells in series for high voltage applications [53, p. 20].

2.2. Overview of Lithium Ion Battery Energy Storage

Batteries are electrochemical energy storage devices that make use of oxidization (losing electrons) and reduction (gain of electrons) reactions that facilitate the movement of electrons. From an electrochemistry perspective, the anode is defined as the location where oxidation occurs and the cathode is the location where reduction occurs. Therefore, depending on if a battery cell is being charged (electrolytic cell – converting electrical energy into chemical energy) or discharged (galvanic cell – converting chemical energy into electrical energy) the battery

positive and negative electrodes can both act at the cathode and anode [57, p. 245]. However, it is common practice in rechargeable battery work to use only galvanic cell notation (equivalent to discharging the battery) and therefore call the negative terminal the anode and the positive terminal the cathode.

The authors of [58] show an example of the chemical reactions that occur at the positive and negative electrode for a rechargeable $LiCoO_2$ lithium ion battery. During discharge, the positively charged lithium atoms intercalated (inserted between the layers of a crystal lattice) in the graphite layers of the negative terminal are removed (deintercalated) and move into the electrolyte as a lithium ion while leaving an electron in the graphite. At the positive electrode, the lithium ions combine with electrons delivered though the external circuit, to form lithium atoms that are deposited into the metal oxide host [58] (see Figure 2 on pg. 48). Due to the shuffling of lithium ions between the positive and negative electrodes, the electrolyte primarily acts as an ionic conductor and is therefore not consumed during charge/discharge cycles [58]. Unlike a lead-acid battery, which involves reactions between the electrodes and electrolyte, lithium ion batteries are not dependant on electrolyte reactants and therefore the quantity of electrolyte can be relatively low while still enabling ionic conductivity [58]. The limited quantity of electrolyte reduces the cell mass compared to lead-acid batteries.

The terminal voltage of a battery is dependant on the sum of reduction potentials related to the half cell reactions at each electrode. Half cell reduction tables, such as shown in [59], show that lithium has the most negative reduction potential (voltage). For comparison, [57, p. 251] shows the half cell reactions for a $LiCoO_2$ cell to have a resulting cell voltage of 3.7V while [57, p. 247] shows the half cell reactions of a lead acid battery to have a resulting voltage of 2.04V. The

increased terminal voltage and reduced mass (low electrolyte quantity) of lithium ion batteries (LiBs) make their energy density superior to many other battery types.

Although the increased negative potential related to lithium is beneficial for increasing the cell terminal voltage, lithium can be problematic when exposed to water (strong reducing agent). This concern introduces the need for a nonaqueous electrolyte that then introduces flammability concerns [58]. Additional safety concerns extend from the potential formation of dendrites/whiskers (sharp metallic growths) that may pierce through the separator and cause a short circuit within the cell. For example, over charging or quickly charging the lithium ion battery may result in lithium metal plating onto the anode rather than fully integrating into the anode though intercalation [60] [61]. On the other hand, over discharging the cell can cause the copper current collector on the anode to dissolve into electrolyte [60]. Upon recharging, the copper can reform in undesirable shapes and locations that may present a short circuit concern [60]. A more detailed explanation of battery energy storage fundamentals can be found in [57].

2.3. Performance Comparison of EDLC and LiB Cells

A very general and high-level comparison of EDLC and LiB cells is provided in Table 1. The values in Table 1 should only be considered rough guidelines as cell specifications can change drastically depending on the cell, even for cells within the same energy storage device category. The key take-away from Table 1 is that EDLC cells typically have a larger power density, larger cycle life and smaller energy density compared to lithium ion batteries. Of the energy storage devices shown in Table 1, EDLC cells would most likely be a good energy storage device for high power and low energy applications while LiB cells would most likely be best for lower power and high energy applications.

Energy Storage Device	Energy Density [Wh/kg]	Energy Density [Wh/L]	Power Density [W/kg]	Power Density [W/L]	Cycle life [cycles]
Electric Double Layer Capacitor (EDLC)	2.5-15	10-30	500-5000	100,000	10,000-100,000
Lithium-ion Battery (LiB)	100-265	250-730	250-340	100-210	400-1,200
Lead Acid-Battery	30-50	50-80	75-300	10-400	100-2,000

Table 1: Comparison of EDLC, LiB and lead acid battery technology. Adapted from Table 7.3 of [57].

As shown by Equation 2, the key components that dictate the output power capability of a cell are the cell's terminal voltage and equivalent series resistance (ESR). The equivalent series resistance is a simplified term that represents the decrease or increase in cell terminal voltage while under load compared to a no-load condition for a given state of charge. Simple battery and capacitor modelling methods use the equivalent series resistance term to represent cell characteristics such as the resistance of terminal posts/tabs, the resistance of current collectors, the ionic resistance of electrolyte and simplified electrode kinetics, if applicable.

$$P_{discharge} = V_{terminal} * I_{discharge}$$

$$P_{discharge} = (V_{OCV} - R_{ESR} * I_{discharge}) * I_{discharge}$$

$$P_{discharge} = (V_{OCV} * I_{discharge}) - (R_{ESR} * I_{discharge}^2)$$

$$P_{discharge} = Nominal\ Power - Losses$$

Equation 2: Discharge power from a battery or capacitor energy storage system

However, due to electrode kinetics, thermal concerns and other factors, the discharge current of a cell is not limitless. The cell terminal voltage (including when under load) and current must remain within the datasheet specified values. Therefore, the maximum discharge current can be defined using Equation 3, provided cell thermal limits are respected.

$$I_{discharge} = \max\left(\frac{V_{OCV} - V_{min}}{R_{ESR}}, I_{discharge,\ datasheet}\right)$$

Equation 3: Discharge power from a battery or capacitor energy storage system

Equation 2 and Equation 3 show that it is ideal to have a low equivalent series resistance to not only minimize losses but also prolong cell discharge time under high current loads (minimizes voltage drop that would result in hitting the minimum cell voltage early) and increase the maximum discharge current. A similar representation of Equation 2 and Equation 3 can be made for charging current and charging power capability.

The open circuit voltage and equivalent series resistance of a cell are not constant and may change as a function of several parameters, such as state of charge, temperature, current magnitude, current direction (charging or discharging) and cell age. Therefore, in order to fully define the power capability of a cell, assuming thermal limits are respected, it is necessary to understand how these parameters influence the open circuit voltage and equivalent series resistance. As a general trend, the equivalent series resistance of EDLC cells does not typically change with temperature, while the ESR of lithium ion batteries does.

2.4. Hybrid Energy Storage Systems

Conventional energy storage systems for tractive applications consist of one energy storage technology. However, as shown by Section 2.3, there are considerable power and energy density differences between EDLC and LiBs. Combining EDLC and LiBs to form a hybrid energy storage system (HESS) gives the opportunity to take advantage of the characteristics of both energy storage devices. A HESS may offer the following performance gains:

- Reduction of battery pack current spikes [62], resulting in decreased battery pack heat generation, battery degradation [63] and risk of battery thermal runaway

- Increase energy storage system and vehicle efficiency, therefore increasing driving range [64]
- Reduce the amplitude and frequency of battery micro cycles due to dynamic driving conditions, therefore increasing battery pack lifespan [65], and
- Increase the capability to capture regenerative braking energy due to the ultra-capacitor's favorable power capability, therefore increasing vehicle efficiency

An experimental study conducted at Xi'an Jiaotong University showed a driving range increase of 42.1% when using an ultra-capacitor and lead acid battery HESS when compared to a system utilizing exclusively lead acid batteries [64]. When using a lithium ion battery pack rather than a lead acid pack, as in [64], more modest improvements in range are expected as compared to a battery only system, in the range of 1-5% at 25°C or as high as 50% at low temperatures where the battery cannot accept regenerative braking energy [66]. The hybrid energy storage system and optimal power flow control strategy modelled in [67] show a driving range increase of approximately 25% and total energy storage system loss reduction of approximately 40% when compared to the battery only energy storage system using the US06 drive cycle.

The combination of two energy storage devices can be completed using several methods, such as the four HESS topologies shown in Figure 1. An additional eight HESS topologies are available in [68].

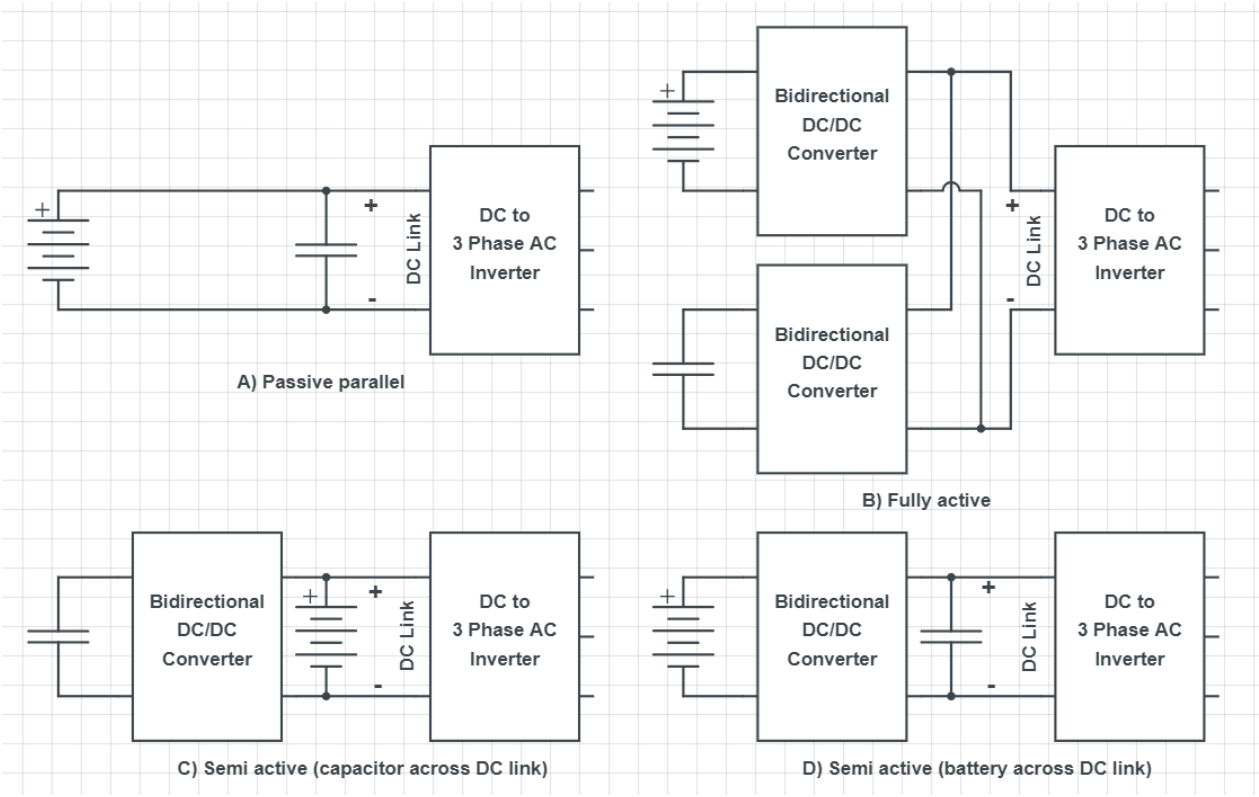

Figure 1: Select hybrid energy storage system topologies including a) passive, b) fully active, c) semi active (battery on DC link) and d) semi active (capacitor on DC link).

The relatively simple passive HESS configuration shown in Figure 1 a) does not contain any power electronic converters and therefore eliminates the need for a potentially expensive hardware component. Both the battery and capacitor pack are available to provide current to the load and therefore the current split is determined by the storage device characteristics without any influence from the user. This simplicity eliminates the need to develop a power flow control strategy and therefore simplifies the implementation. However, the direct coupling requires the battery and capacitor packs to have a similar voltage which will prevent fully discharging the energy available in the lower voltage range of the capacitor pack.

The fully active HESS topology shown in Figure 1 b) makes use of two DC/DC converters, one for each energy source, connected in parallel to the DC link. This configuration allows for a

mismatch between the voltages on the individual energy storage systems and provides the most control for selecting what energy source provides power when. However, two DC/DC converters introduces additional cost and controls complexity.

The semi active HESS topology shown in Figure 1 c) has the battery pack connected across the DC link and the capacitor pack is located 'behind' the DC/DC converter. This topology allows for the capacitor pack to operate at a different voltage range than the battery pack and be completely discharged because it no longer has to sustain the DC link voltage. The DC/DC converter must handle the full power and current rating intended for the capacitor pack.

The semi active HESS topology shown in Figure 1 d) has the capacitor pack connected across the DC link and the battery back is located 'behind' the DC/DC converter. Depending on the power split control strategy used to control the DC/DC converter, the DC link voltage may vary considerably due to the small amount of energy storage in the capacitor pack. However, the DC/DC converter is rated for the battery pack power level and therefore should be less expensive than a converter that transfers power from a capacitor pack.

Although there are performance gains from combining energy source it is important to look at the whole system, including cost, volume and weight. For example, academic literature, such as [67], often present performance gains by comparing a battery only energy storage system to a HESS that has a capacitor pack added to the original battery pack. However, the additional cost, weight and volume needed for the capacitor pack and DC/DC converter, if applicable, may outweigh the performance benefits. For example, the DC/DC converter used in [67] cost 42.4% of the total HESS budget while the battery pack was 28.6% and the lithium ion capacitor pack

was 19.7%. The capacitor pack occupied almost 1.5 times the volume of the battery pack while only holding approximately 4.1% of the HESS energy content. An argument could be made that doubling the existing battery pack would be less expensive than the HESS while providing approximately twice the driving range and a 120kW peak power rating instead of 180kW. The power rating could be increased by using less energy dense battery cells (more space available in vehicle with capacitor pack removed) that would allow for the additional output power while still eliminating the DC/DC converter expense and increasing the driving range beyond what the HESS can offer.

As shown by the vehicle in [67], there are several considerations to make in identifying situations where a hybrid energy storage system would be beneficial. Just because a vehicle has high power requirements does not mean that it needs a capacitor ESS or HESS. For example, the Tesla Model S P100D, which has two electric motors for a combined max output of approximately 500 kW, makes use of a battery only energy storage system. This is possible because the large cell count results in a reasonable power demand from each cell. However, in applications that require more power but do not have a large energy storage reservoir, such as hybrid vehicles, the need for battery cells with increased power capability becomes a priority. A similar case may be true for a railway vehicle that needs to travel a relatively short distance, maybe 1km, between stations where the 3rd rail power does not exist.

Rather than developing two separate energy storage systems and coupling then to form a HESS, there is an alternative to look at relatively new energy storage cells that combine characteristics of batteries and capacitors.

2.5. Lithium Ion Capacitors

As shown in Equation 4 the energy stored within a capacitor increases linearly with capacitance and squared with voltage. With the goal of increasing energy density and power density, it is ideal to increase the terminal voltage while maintaining a low equivalent series resistance. This can be partially achieved by combining an electrostatic electrode (similar to an EDLC) with an electrochemical electrode (similar to a battery) to develop an asymmetrical hybrid capacitor (see Figure 2). The introduction of an electrochemical anode (negative terminal) that enables lithium-ion intercalation and is pre-doped with lithium-ions lowers the anode potential [69], therefore increasing the cell terminal voltage [70, p. 282] to produce a lithium-ion capacitor. The pre-lithiation process increases the minimum cell terminal voltage [70, p. 282], in the approximate range of 2.2V-3.2V, compared to the minimum cell voltage of 0V for EDLC cells. Although the electrochemical anode limits cell discharge to a non-zero minimum voltage, it can be shown that 80% of an EDLC cell's stored energy corresponds to the upper 55.3% of the voltage range and therefore the lower voltage range contains little useful energy. The increase in cell terminal voltage is advantageous as the high currents needed to extract higher power levels from a low voltage energy storage system can be a source for considerable losses and heat generation. As shown by the charge and discharge cycle of a LiC in [70, p. 282], the Li/graphite anode potential is relatively constant (between 0.07V and 0.2V) while the activated carbon cathode potential cycled between 3.2V and 4.2V, all compared to a Li/Li^+ reference electrode. Therefore, the cell terminal voltage of the LiC under test in [70, p. 282] was shown to primarily follow the linear voltage dependency on state of charge exemplified by the active carbon cathode and perform similarly to the linear discharge curve of EDLCs. A similar result was obtained in [71, p. 2503] such that the anode potential is relatively consistent compared to the cathode potential across a -40^oC to $+60^oC$ range.

$$Energy = 0.5CV_{max}{}^2 - 0.5CV_{min}{}^2$$

Equation 4: Energy stored in a capacitor

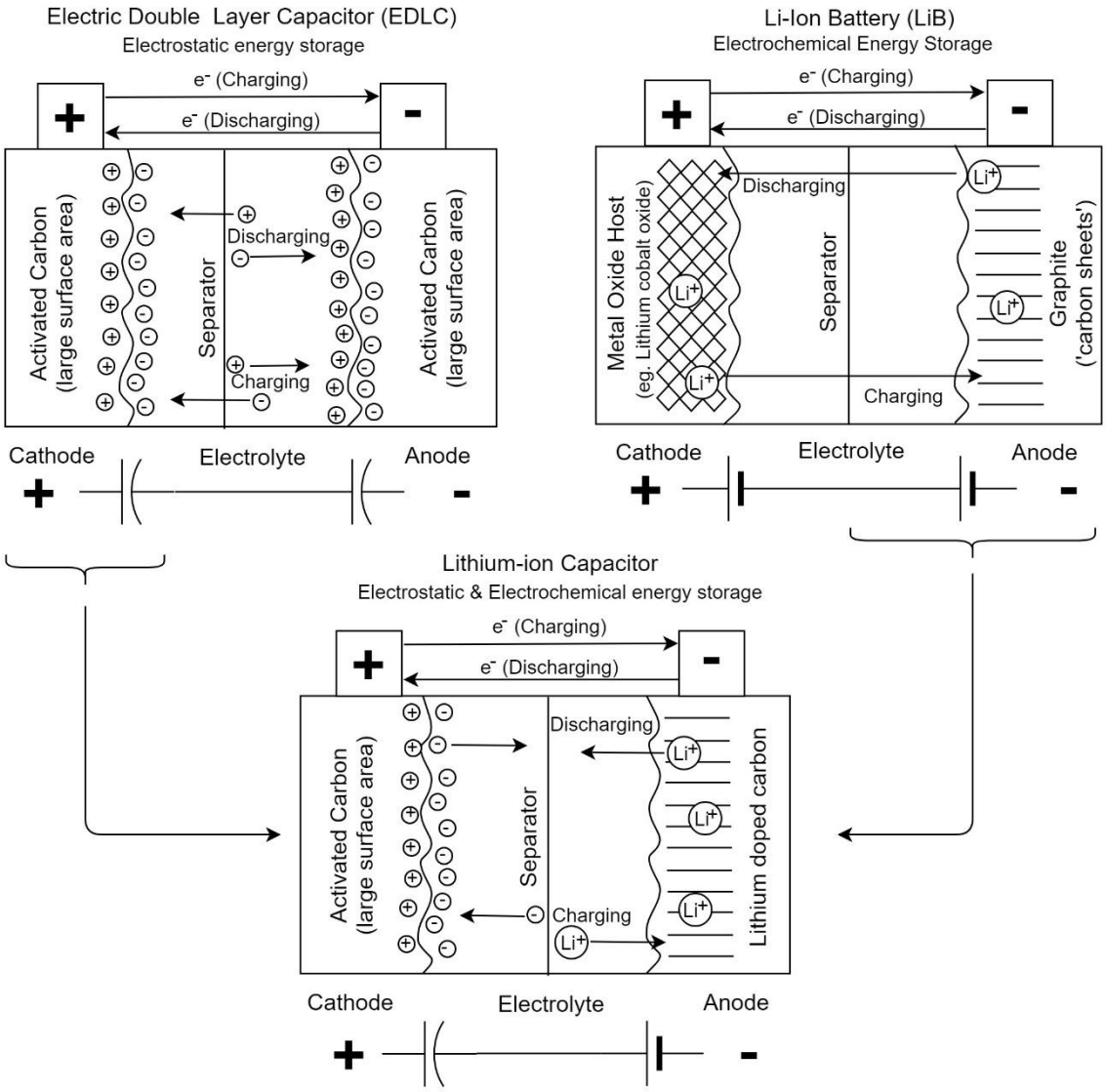

Figure 2: Simplification of a combined electrostatic positive electrode and electrochemical negative electrode to form a lithium ion capacitor. Figure based on [72].

2.6. Literature Review of Lithium Ion Capacitor Studies

Table 2 provides an overview of six research papers that discuss modelling and cell characterization of lithium-ion capacitors. Any accidental misrepresentation of the following publications is not intended.

Reference, Publication Year	Cell(s) Tested	Title, Some contributions and comment on the work
[73] 2017	2200F laminated LiC 2300F prismatic LiC Manufacturer name omitted	*A Novel Current Dependent Lithium Ion Capacitor Model: Analysis and Experimental Driving Cycle Test Validation* Development of a LiC model that makes use of four parameters – C, R and one RC branch. All four parameters are a function of current (not cell voltage) and the main capacitance is a function of voltage. Unclear what testing temperature is used. Model parameters obtained from multiple charge and discharge cycles of different current magnitudes. Very close match between simulated and experimentally determined cell voltage for both cells when exposed to NEDC and SC03 drive cycles.
[74] 2014	CLQ1100S1A laminated LiC CLQ2200S2A laminated LiC Manufactured by JSR Micro	*Modeling and Parameter Identification of Lithium-Ion Capacitor Modules* Goal to estimate the parameters, with cell voltage dependency, for a LiC model using frequency-based testing (galvanostatic electrochemical impedance spectroscopy - GEIS) in the 10 mHz to 1 kHz range. Individual cell testing performed in a 30^{o}C thermal chamber with dc polarization voltages of 2.2 to 3.8V (5 voltage breakpoints). The cell model with experimental parameters is compared to cell experimental performance using select multi current pulses. Additional experimental testing using charge and discharge cycles of 36 series connected CLQ1100S1A LiC cells at room temperature was performed. A considerable difference between the experimental pack voltage and simulated pack voltage was observed. This difference is attributed to cell balancing.
[75] 2018	CLQ1100S1A laminated LiC Manufactured by JSR Micro	*A lithium-ion capacitor model working on a wide temperature range* Extension of modelling work in [74] to include testing at multiple temperatures. Use of GEIS testing to characterize five cell modelling parameters, including their dependency on cell voltage and temperature within the range of 0^{o}C to 60 ^{o}C. Comparison of cell voltage model using GEIS obtained parameters to experimental voltages obtained form current pulse testing. Identification of current dependant cell impedance characteristics at 0^{o}C initiated additional GEIS testing at -10 ^{o}C and -20 ^{o}C.

[76] 2015	Prismatic 3300F LiC cell Manufactured by JM Energy (affiliated with JSR micro)	*Lithium-ion capacitor – Characterization and development of new electrical model* Identification of a change in cell useful capacity as a function of discharge current and ambient temperature. Identification of 8 cell model parameters expressed as a function cell voltage and testing temperature between -10 °C and 60 °C using frequency-based testing methods. Identification of model parameters as a function of SOC and current for a 2nd and 3rd order cell model using HPPC time domain testing. Classification of the Nyquist plots obtained from frequency domain testing to suggest a cell model structure that represents chemical reactions within the cell. Quantified current dependant charge transfer ohmic resistance as a function of charge and discharge current at -10 °C, 0 °C and 10 °C.
[77] 2015	1100F LiC cell Manufactured by JM Energy	*Development of an Electrical Model for Lithium-Ion Ultracapacitors* Use of AC and DC current test methods to develop a LiC model. Identification of differential capacitance as a function of the open circuit voltage. Testing performed in a controlled environment in the range of -15 °C to 65°C. Coulombic efficiency of approximately 99% for tests with 10A up to 60A currents in -15 °C to 65°C. Cell energy efficiency changes with testing current and temperature – lower efficiency at high current and low temperature. Comparison of simulated and experimental terminal voltage for a LiC pack with 120 series connected cells tested using DC current pulses.
[78] 2010	2700F EDLC Manufactured by Maxwell 2200F laminated LiC Manufacturer name omitted	*Comparison of Supercapacitor and Lithium-Ion Capacitor Technologies for Power Electronics Applications* Comparison between one ELDC and one LiC based on published specification, DC response analysis and frequency response analysis. Tests performed on three cells of each cell type and average values were used to minimize measurement differences due to manufacturing tolerances. Larger ESR for LiC cells than EDLC cells when obtained from step current change to initiate constant current discharge cycles. States that the inductive impedance of the cell cannot be obtained from the voltage drop determined using DC current pulses. Therefore, AC impedance testing is used obtain a true equivalent series resistance based on where the Nyquist plot crosses the real axis. The AC ESR was 37% and 15% lower that the DC pulse ESR for the EDLC and LiC cells, respectively – indicates that inductance of EDLC may be larger than in LiC.

Table 2: Review of select research contributions from six Li-ion capacitor focused papers

A discussion regarding how the experimental work in this thesis expands upon the work in literature is available in Section 5.1.

3. DC Railway Electrification with Energy Storage: Overview, Current Status, and Future Trends

The purpose of this chapter is to:

- Provide the reader with a very brief overview of railway system terminology and operation
- Identify different vehicle operating condition and how they influence power flow within the DC power delivery system
- Identify sources of power loss
- Identify reasons to use energy storage systems or reversible substations
- Provide reference to literature that supports the use of energy storage systems or reversible substations

3.1. High Level Railway System Architecture and Power Flow

Figure 3 a) shows a high-level interpretation of a DC powered passenger railway system.

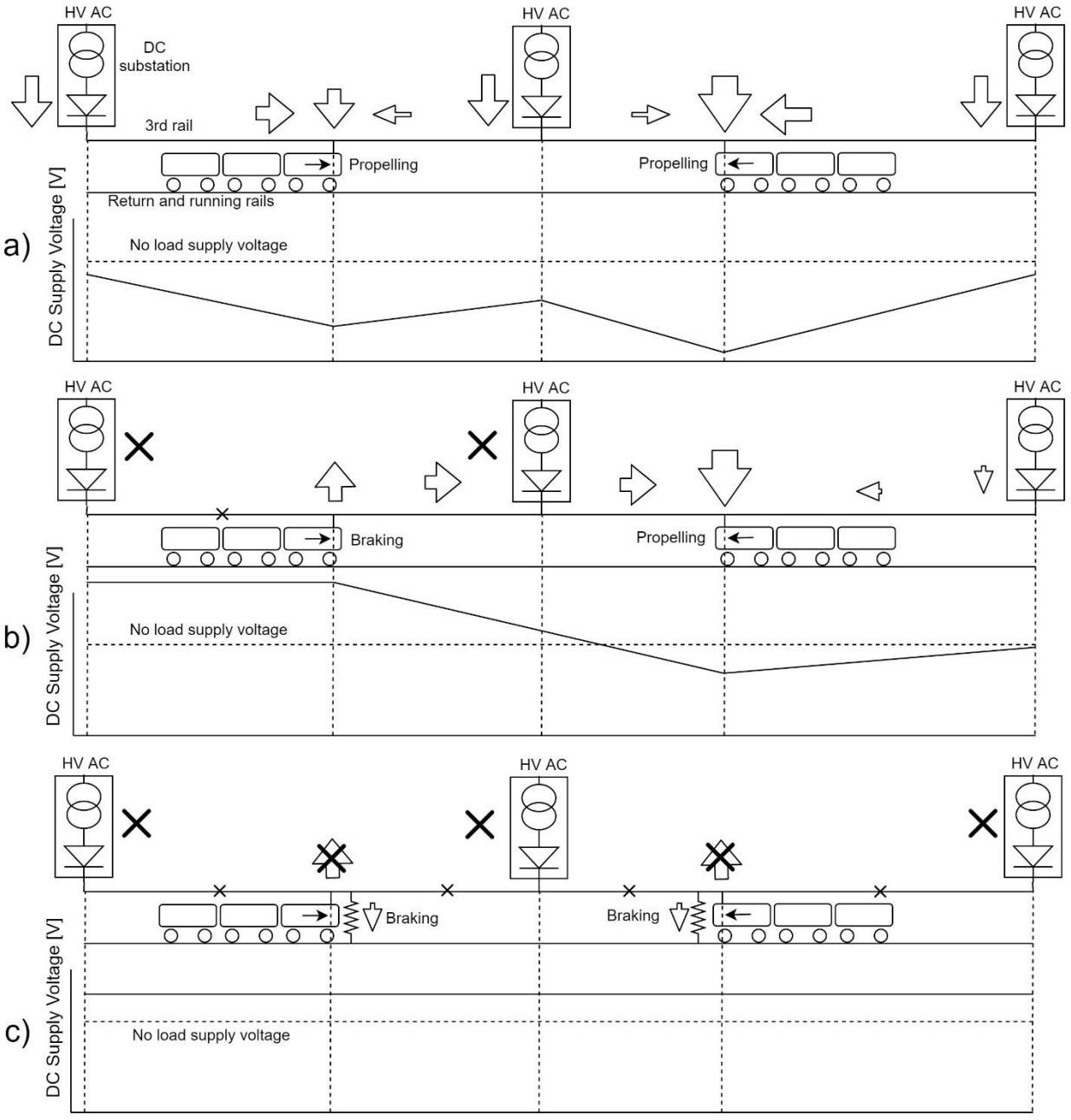

Figure 3: High level representation of a railway system with two trains. A) Both trains propelling. B) One train braking and one train propelling. C) Both trains braking. This figure is based on the work presented in a webinar from Pablo Arboleya [79].

The vehicle, or train, is typically of the electric multiple unit (EMU) type and therefore includes multiple train cars each outfitted with electric propulsion devices. Electric multiple unit type vehicles do not have one locomotive that pulls/pushes the remaining cars as done by many freight trains. The DC supply system is powered by multiple DC power supplies in parallel that

are distributed along the tracks. The DC power supplies typically use 6 pulse or 12 pulse diode rectifiers, depending on the desired voltage ripple and operation requirements for connecting to the high voltage AC three phase supply. Switched rectification systems are also in use but appear to be less common than diode-based rectifiers. The vehicle's connection to the DC voltage supply positive terminal typically makes use of either a 3rd rail system or a over head contact wire supported by the catenary. A 3rd rail system introduces a third rail, similar to the running rail, that is located beside or between the running rails. A contact or pick up shoe that extends from the vehicle makes contact with the positive terminal and provides power to the vehicle. The second approach is a catenary system in which an over head cable runs along the tracks and contact is made with the vehicle via the pantograph. The two running rails serve two functions, firstly to provide a surface for travelling and directing vehicle motion, and secondly, to act as a DC current return system to the negative terminal of the DC supplies. The running rails are not used as the positive and negative supply terminals due to the need to insulate the wheels and bearings. Additionally, the wooden sleepers used to hold the running rails are not sufficient insulators where as the 3rd rail is mechanically supported using insulating materials. The proximity of the 3rd rail and running rails introduces a considerable safety concern for passengers. You will typically see the 3rd rail covered to minimize contact surface area or missing in locations that passengers may be, such as passenger track crossings in rural train stations. The author highly suggests reading "Overview of Electric Railway Systems and the Calculation of Train Performance" by M. Chymera and C.J. Goodman [80] for additional information.

The railway system can be modelled as moving loads connected in parallel to the DC transmission system. The resistance of the running rail and 3rd rail, which are commonly expressed in the units of mΩ/km, can introduce a considerable voltage drop between the nominal no load DC supply voltage and the voltage available to the train. The position of the

train relative to the substations and other vehicles influences the resistance of the transmission system. The high power demanded by the vehicles introduces a considerable amount of current travelling through the DC transmission system, especially if the DC voltage is low (eg. 600V), and therefore introduces losses within the transmission system. To give an idea of reasonable values, details from a webinar offered by Pablo Arboleya [79] are provided. For example, Case 1 from [79], which is very similar to Figure 3 a), has two trains that consume 650 kW and 350 kW, respectively. The first train is powered by two DC substations that have an underload voltage of 622V and 590V, however, the voltage at the train is only 550 V. The positive voltage supply connection has a resistance of 51 mΩ/km and the return rails are rated at 14 mΩ/km. With 2 km from substation one, the resistance between the vehicle and substation one is 130 mΩ. With a current draw of approximately 558A (307 kW / 550 V = 558 A) and resistance of 130 mΩ, the voltage available to the train is only 550V (622 V – 558 A*130 mΩ ≈ 550 V). The transmission of power from substation one to the train results in an approximate power loss of 40 kW (558 A*(622 V-550 V) ≈ 40 kW or $(558\ A)^2$* 130 mΩ ≈ 40 kW). The power loss within the DC distribution system is highly dependant on the vehicle power demand and the resistance of the 3rd rail and running rails.

Figure 3 shows three train operation conditions for a simple two vehicle and three substation railway system. Figure 3 a) shows two trains that are in propulsion mode that are both consuming power from the DC supply system. In this case, the voltage at both trains is lower than the under load supply voltage from the substations. Figure 3 b) shows a case in which one train is braking (regenerating power back to the DC supply system) and the other train is consuming power. The voltage of the supply system at the braking train increases beyond the substation output voltage and therefore the substation no longer supplies power (unidirectional

diode bridge), as noted by the X. The regenerative braking power from the first train is transmitted to the second train and a voltage drop across the transmission system is shown. The movement of power from one train to the other train is dependant on the power required by other vehicles and their proximity. Figure 3 c) shows a case where both trains are braking and attempting to push power into the DC supply system. The supply voltage increases beyond the output voltage of the unidirectional subway stations and the vehicles cannot inject current into a system that does not have any load. Therefore, depending on the voltage of the supply system, resistor banks are used to dissipate the excess regenerative braking power. In this case, the regenerative braking power is wasted energy and the total system efficiency decreases. Additionally, the heat produced by the braking resistors may be transmitted to the open air or partially confined spaces on a subway system. The increase in temperature inside subway systems introduces additional power requirements for ventilation and air conditioning systems that moderate the station temperature.

In cases where regenerative braking cannot be used or used efficiently (far transmission that results in high transmission losses), an alternative solution is to capture the braking energy into on-board energy storage systems, way side energy storage systems or transmit power back to the AC supply using inverters to form a bidirectional substation when combined with the rectifier. On-board energy storage systems travel with the train and therefore the losses of transmitting power to another location are minimized. Wayside energy storage systems, which are commonly located in places where regenerative braking occurs, such as stations, reduce the need for retrofitting each vehicle. Bi-directional substations enable moving energy from the DC supply system to the AC supply. However, the possibility for bi-directional power flow to the AC supply may be determined by the local electrical utility supplier.

3.2. Why Use Energy Storage Systems?

The following discussion aims to outline performance gains from using energy storage in railway systems with reference to academic and industrial work.

3.2.1. Supply Voltage Support

As the need for public transportation increases there is a general trend to operate larger vehicles with existing infrastructure. Larger and/or more vehicles in operation increases the power demanded from existing infrastructure that may not be sized for future growth. As noted in [81], larger railway vehicles, such as jumbo trams, may decrease the supply voltage available to other nearby vehicles to the extent that the minimum operation voltage is hit. In this case the other vehicle(s) cannot operate due to the minimum voltage protection systems. In [48] the authors discuss the use of wayside energy storage ("battery posts") to support the electrical system in Japanese railway systems in the early 1900's. In [81] the authors use a railway system model to determine the weight, size and location of EDLC based wayside energy storage systems that act to increase the voltage of the supply system. The addition of 9.6 kWh of EDLC energy storage distributed in three locations reduced the voltage drop to be 32% of the original voltage drop at the desired location within the simulated network.

3.2.2. Capture Regenerative Braking Energy and Peak Shaving

Onboard and wayside energy storage systems can be used to capture excess regenerative braking energy that would otherwise be dissipated into resistors. The simulation tool of [82] showed the greatest energy savings in low traffic situations with a maximum energy saving of approximately 36% for both onboard and wayside energy storage systems when compared to systems without energy storage [82]. Another example comes from [83] in which the energy used by the prototype rail vehicle was reduced by up to 30% over the approximate two-year trial period. The captured regenerative braking energy can be used during the next acceleration

phase to reduce the peak power consumed by the vehicle and therefore reduce the system peak power and peak losses. Figure 2 from [83] shows that the peak power demanded from the supply line during acceleration is reduced from approximately 100kW to 60kW by using the 860 Wh EDLC based on-board energy storage system. Figure 3 from [83] shows that the supply line current and voltage drop was reduced by approximately 50% when compared to operation without the energy storage system. Besides a reduction in energy consumption, peak shaving may result in financial savings by also reducing electricity demand charges [84] [85].

3.2.3. Catenary Free Operation and Emergency Backup Power

Rather than using an energy storage system as a secondary energy source or sink, the ESS can be used as the primary power supply when the DC supply is unavailable. For example, in locations where it is unsafe or aesthetically unpleasant to have the 3rd rail or over head catenary cables, an onboard energy storage system or alternative power delivery method would be necessary. The on-board energy storage system may be sized for traversing a small track portion, from one station to another, up 41.6 km for example [52]. Chapter 7 discusses the sizing of an on-board ESS for catenary free operation in more detail. Other catenary free power delivery methods exist besides energy storage systems. For example, the innovative APS (Alimentation Par le Sol) system developed for the Bordeaux tramway makes use of an underground '3rd rail' power supply that is only activated when the tram is travelling over the segmented rails [86]. However, an energy storage system also offers a source of emergency power in the event of an infrastructure fault or power outage and can be used for energy saving applications when connected to the DC supply. In the event of a power failure the ESS may be used to further propel the vehicle to a safe location. This is important for tracks located in tunnels where an energized 3rd rail may exist [87] or for elevated tracks where there is a height safety concern.

3.3. Lithium-Ion Capacitors in Railway Energy Storage Systems

The relatively limited academic research investigating the performance of LiCs for energy storage in tractive applications, specifically railway systems, is primarily documented in publications by Flavio Ciccarelli. In [88] Ciccarelli at al. discuss a LiC based wayside ESS that uses a power flow control strategy based on the braking vehicle's kinetic energy. Additional wayside LiC ESS control strategies by Ciccarelli et al. are presented in [89] and [90].

Although several authors have contributed to the research topic of energy storage systems for railway applications, the author identifies the work of Dr. Pietro Tricoli (Birmingham, UK), Dr. Ricardo Barrero (Belgium) and Dr. Flavio Ciccarelli (Naples, Italy) to be prominent.

The work presented in Chapter 7 focuses on the use of on-board Li-ion and electric double layer capacitor-based energy storage systems for catenary free operation.

4. Development of Testing Facilities to Compare EDLC and LiC Cells for Energy Storage Systems

The energy storage lab located at the McMaster Automotive Resource Centre received considerable attention and updates over the past two years; largely motivated by the author, Dr. Kollmeyer, other students studying ESS systems, and industry projects. The key testing hardware available in the energy storage lab is listed in Table 3 and is shown in Figure 4 to Figure 8. At the start of this work the Digaton multi cell tester (MCT) device was not available and therefore the custom McMaster Automotive Resource Centre cell cycler test stand, as shown in Figure 8, was developed to enable most of this experimental work in Chapter 5. The custom MARC cell cycler was a collaborative effort between the author, Dr. Kollmeyer, and Cam Fisher to further develop the custom cell tester work originally done by Dr. Habibi's student Ali Delbari. The author was primarily responsible for hardware work while Dr. Kollmeyer was responsible for the custom LabView cell testing software. Mr. Fisher provided access to funding and helped define system safety requirements. In addition to the hardware in Table 3 , the lab was equipped with a gas sensing shut down system and CO_2 fire suppression system that were installed by an external company. The installation of these extra safety systems was necessary to enable unattended and automated cell testing. Considering the necessity to modify testing profiles, re-run test sequences, and adjust thermal chamber temperatures it is estimated that the custom MARC cell cycler was operated for over 1,100 hours for this work. Due to the large testing time, this research would be incomplete if the lab safety systems that enabled unattended and automated testing were not available. Due to the author's dependency on lab updates, the custom MARC cell cycler and other lab work that the author contributed to will be discussed in the following sections. The author's key contributions come from the hardware work associated with developing the custom cell testing device (eg. control and data acquisition box, sensor interface

box, device under test connection cables), communication with the Envirotronics SH16 thermal chamber, lab procedures (eg. equipment use, cell fixture and testing profile approval form), and designing / assembling a lab shut down system that connects the fire suppression system, gas sensing system and all testing equipment.

Device ID #	Equipment Name	Description
1	D&V Electronics BST240	Battery pack cycler 2 x 400A, 500V, 120 kW testing channels Independent, series, or parallel channel configuration
2	Digatron Multiple Cell Tester (MCT)	8 x 75A, 0-5V testing channels Independent or parallel channel configuration (up to 600A)
3	Custom MARC Cell Cycler	1 x +/- 125A, +/- 6V testing channel Custom developed – enables more advanced and user configured testing methods such as electrochemical impedance spectroscopy (EIS), multiple temperature measurement points, multiple current sensors…
4	Thermotron SE-3000 Thermal Chamber	Interior volume 2945L (104 ft^3) Temperature range: -70°C to 180°C Controlled by device #1
5	Envirotronics ET8-2-1.5 Thermal Chamber	Interior volume 227L (8 ft^3) Temperature range: -63°C to 177°C Controlled by device #2
6	Envirotronics SH16 Thermal Chamber	Interior volume 453L (16 ft^3) Temperature range: -30°C to 177°C Controlled by device #3

Table 3: Key testing hardware available in the energy storage lab at the McMaster Automotive Resource Centre

Figure 4: D&V Electronics BST240 battery pack testing equipment located in the mezzanine above the energy storage lab.

Figure 5: Inside the energy storage lab testing room – right side.

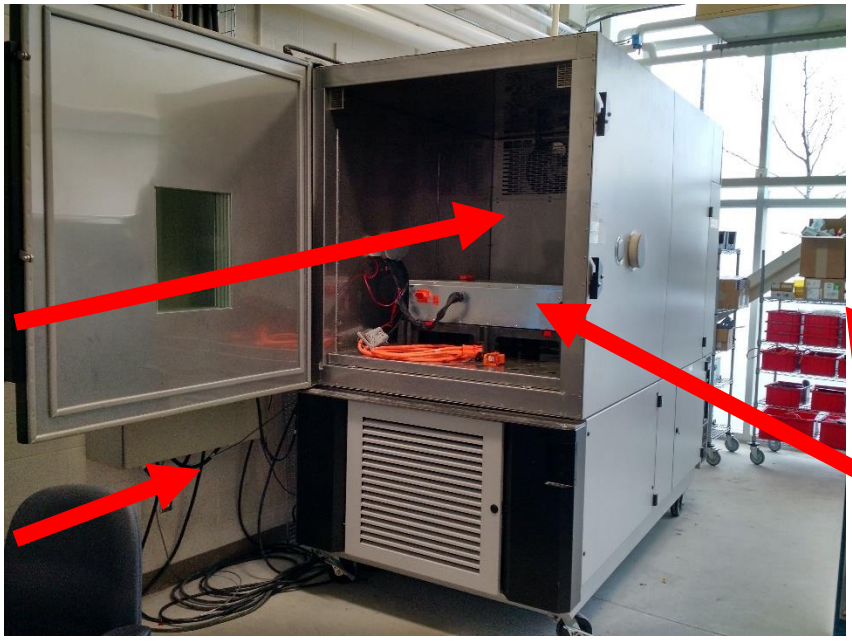

Figure 6: Inside the energy storage lab testing room – left side.

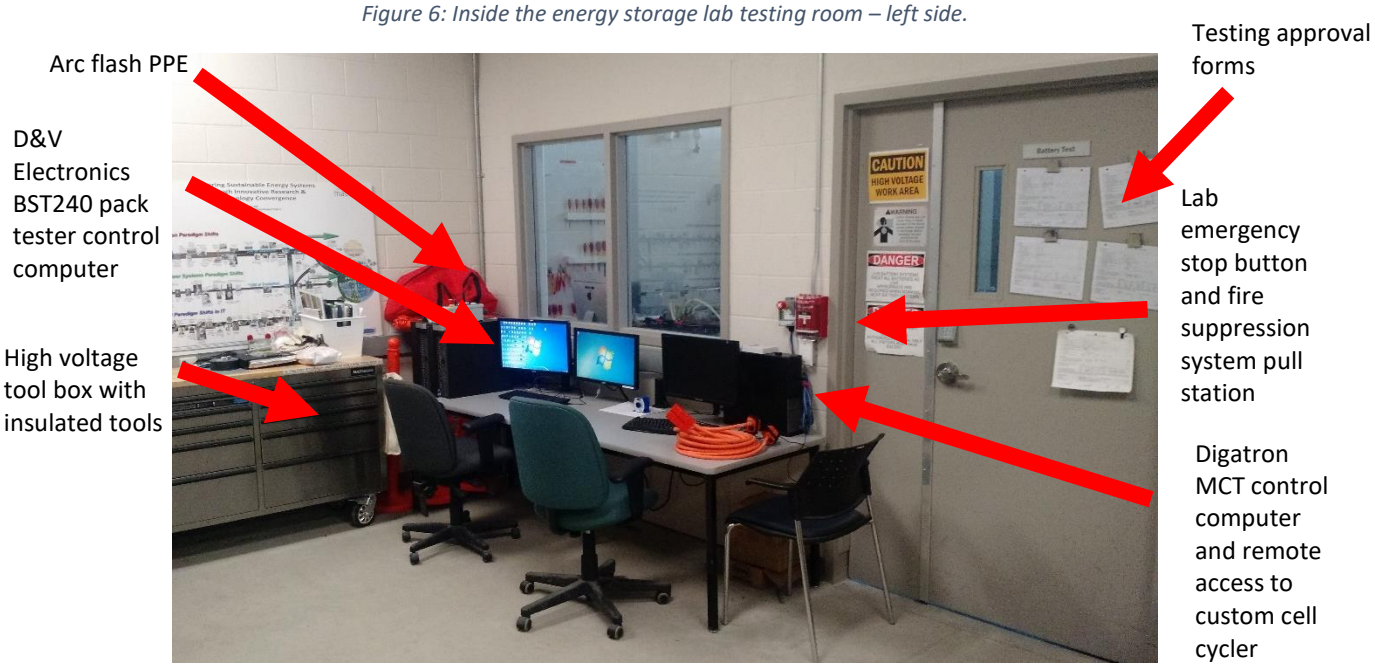

Figure 7: Control room outside the energy storage lab testing room.

4.1.1. Custom MARC Cell Cycler

The custom MARC cell cycler testing system is shown in Figure 8 and is discussed in the following subsections.

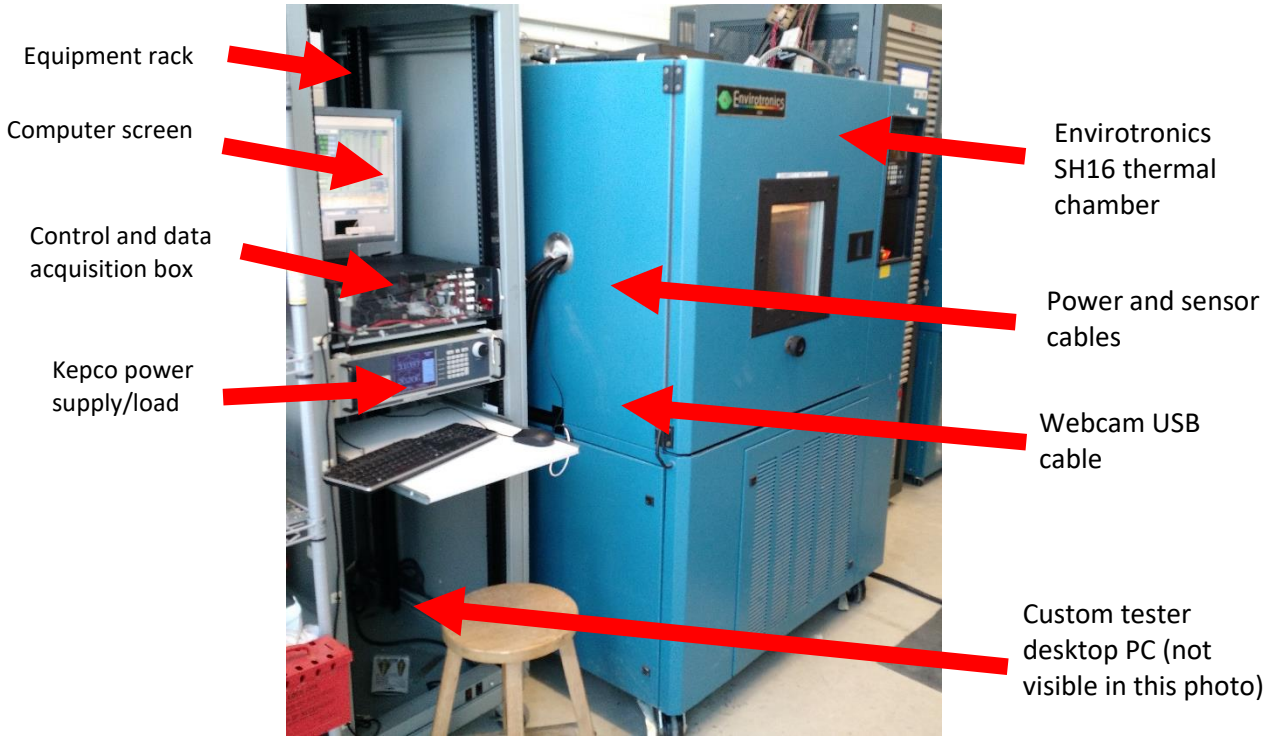

Figure 8: Custom MARC cell cycler test stand and Envirotronics SH16 thermal chamber

4.1.1.1. Cell Cycling Power Supply

The cell under test is charged and discharged using a bi-directional 1 kW Kepco BOP 6-125 MG power supply that can provide +/- 125A in the +/- 6V range. The cell testing current is limited to +/- 125A because the testing device is only a single channel. Additional Kepco BOP 6-125 MG power supplies could be added in future work to increase the current capability, however there is no need as the multichannel Digatron MCT can be used up to a maximum of 600A. Constant current constant voltage (CCCV) charging is achieved using the power supply's current supply mode of operation only, and therefore the voltage supply mode of operation is not used for cell testing. However, with software modifications, the voltage supply mode may be enabled to form a low voltage high current DC voltage supply for testing other electrical components.

National Instruments (NI) data acquisition (DAQ) modules within the control and data acquisition control box send the Kepco power supply an analog voltage signal that corresponds

to a commanded current value (+ or -). Although the cell testing software is limited to enter a protection mode of operation based on the software controller settings, the power supply has its own software limits for current and voltage that act as a second level of protection. Although it sounds ideal to limit the output voltage of the power supply to be equal with the cell maximum voltage, this created an issue. When the output voltage was limited to the maximum cell voltage, the voltage difference between the power supply output and cell under test was not great enough to charge the cells at 125A. To prevent the charging/discharging current from tapering off near the maximum and minimum cell voltage, respectively, the voltage limits on the power supply were set beyond the cell voltage limits, as shown in Figure 9.

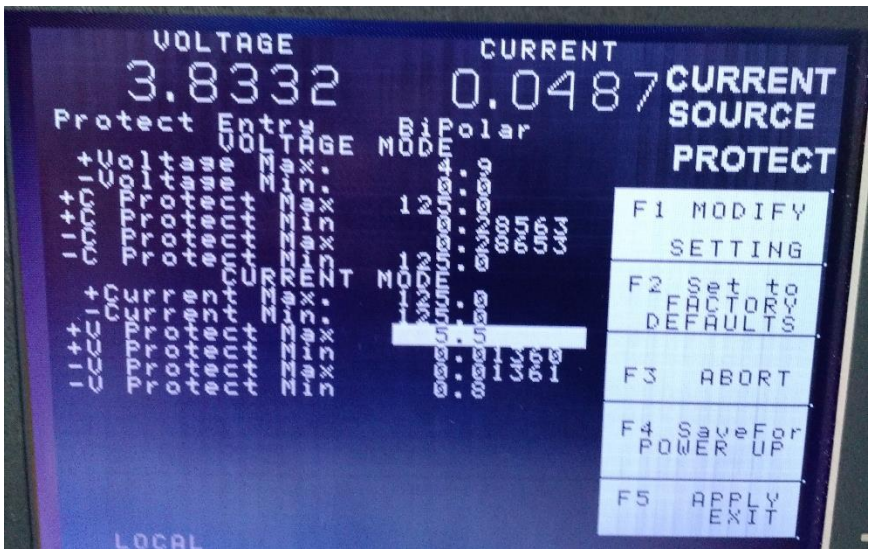

Figure 9: Kepco power supply protection limits shown on the power supply LCD screen

4.1.1.2. Power Cables and Remote Sensing

The device under test (DUT), normally a battery or capacitor cell, is connected to the output terminals of the Kepco power supply using two cable sets; one for power to charge/discharge the cells and one for remote voltage sensing. The 2 AWG power cables extend from the Kepco power supply output terminals into the control and data acquisition box where the positive cable is switched using an automotive grade contactor (see Figure 14). The power cables then extend into the Envirotronics SH16 thermal chamber and are terminated with an SB 120

Anderson connector, as shown in Figure 10, that mates with another SB 120 connector on the DUT.

The power supply remote voltage sense cable extends from the DUT to the control and data acquisition box where the positive cable is switched using a small automotive grade contactor. The switched remote sense voltage cables terminate at the remote voltage sense leads on the back of the Kepco power supply. The power cable and remote sense cable contactors are switched together based on software commands. However, when the remote voltage sense lead contactor is open the power supply is unable to self regulate the output voltage due to the lack of a feedback reference. This issue was solved by bridging a resistor between the local voltage output terminal to the remote voltage sense input terminal.

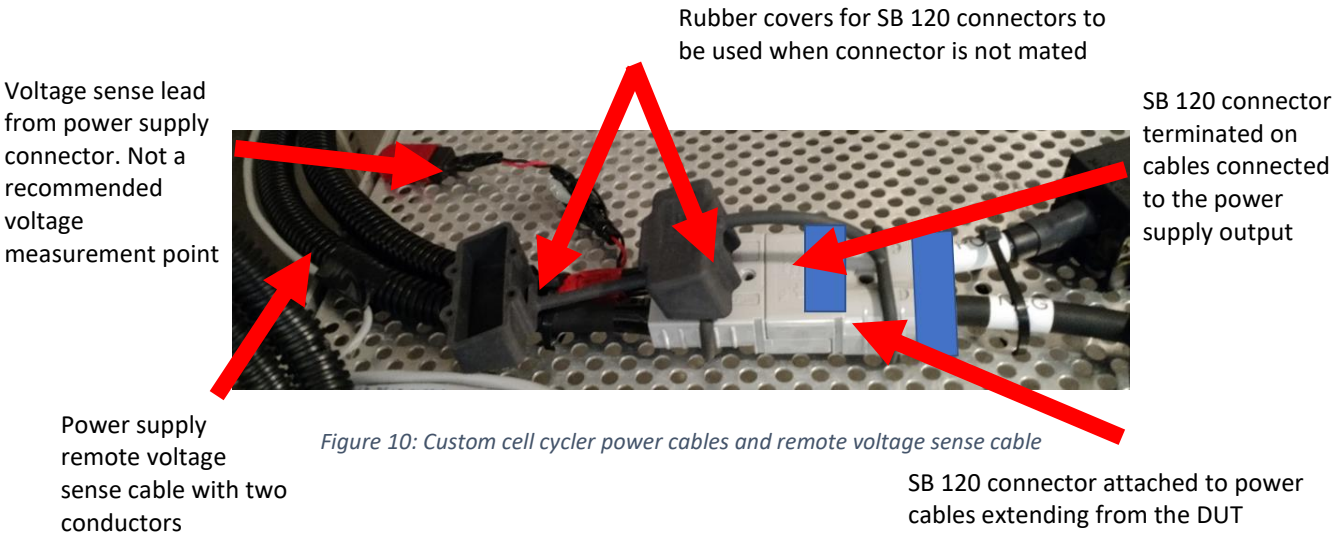

Figure 10: Custom cell cycler power cables and remote voltage sense cable

4.1.1.3. Control and Data Acquisition Box

The control and data acquisition box, shown in Figure 11 to Figure 15, provides six key functions:

1. Send commands from the NI DAQ system, specifically NI module 9264, to control the Kepco power supply
2. House the NI DAQ modules that are used for data acquisition and provide a means of connecting re-usable sensor cables to the measurement modules, specifically NI

modules 9205 (temperature measurement) and 9239 (voltage and current measurement). See Figure 14.

3. House switching devices such as the DUT power cable contactor, voltage sense contactor, watchdog relay and 8-channel relay module. See Figure 14.
4. House the LEM current sensor, current sensor load resistor and voltage divider perforated circuit board used for temperature measurements.
5. Power distribution for the NI DAQ, switching devices and measurement devices. See Figure 14.
6. Provide feedback to the user regarding the status of switching devices and power supply functionality using status LEDs. See Figure 12.

Figure 11 to Figure 15 include several notes that assist in explaining the control and data acquisition box functionality and internal components. Table 4 describes the hardware, and associated measurement error, used to measure/calculate the cell surface temperature, thermal chamber ambient temperature, testing current and cell terminal voltage.

Measurement Type (Measurement Range)	Measurement Device and Associated Error
Cell Terminal Voltage (0V to 4.1V)	NI 9239 module Gain error of +/- 0.3% (Max exposure 4.1V) Offset error of +/- 0.11% (range of 10.52V) Voltage measurement error +/- 0.024V
Cycling Current (-125A to 125A)	LEM IT 200-S Ultrastab current sensor Output error of 83.1 ppm (200mA output range) Secondary current output error +/- 0.017 mA 61.55 Ω bleed resistor Error associated with measuring 61.55 Ω resistor: +/- 0.034 Ω TCR +/- 300ppm/^{o}C (62 Ω rating, assume +/- 10 ^{o}C) Resistance error +/- 0.22 Ω Bleed resistor voltage measurement with Ni 9239 Gain error of +/- 0.3% (Max exposure 7.72V) Offset error of +/- 0.11% Voltage measurement error +/-0.035V

Temperature (-15°C to 45°C)	Murata 10K NTC thermistor (P/N NXFT15XH103FA2B100) Connected to GND Resistance tolerance +/- 1% B value tolerance +/- 1% 10KΩ 1% resistor for voltage divider Connected to 5V supply with reference voltage measurement AC/DC power supply, 5V output (P/N PMT-D1V100W1AA) Output voltage tolerance 1% 5V reference measured with Ni 9239 Voltage measurement with NI 9205 module Residual gain error of 135 ppm Residual offset error of 20 ppm (range of +/- 5V)

Table 4: Voltage, current and temperature measurement hardware for custom MARC cell cycler

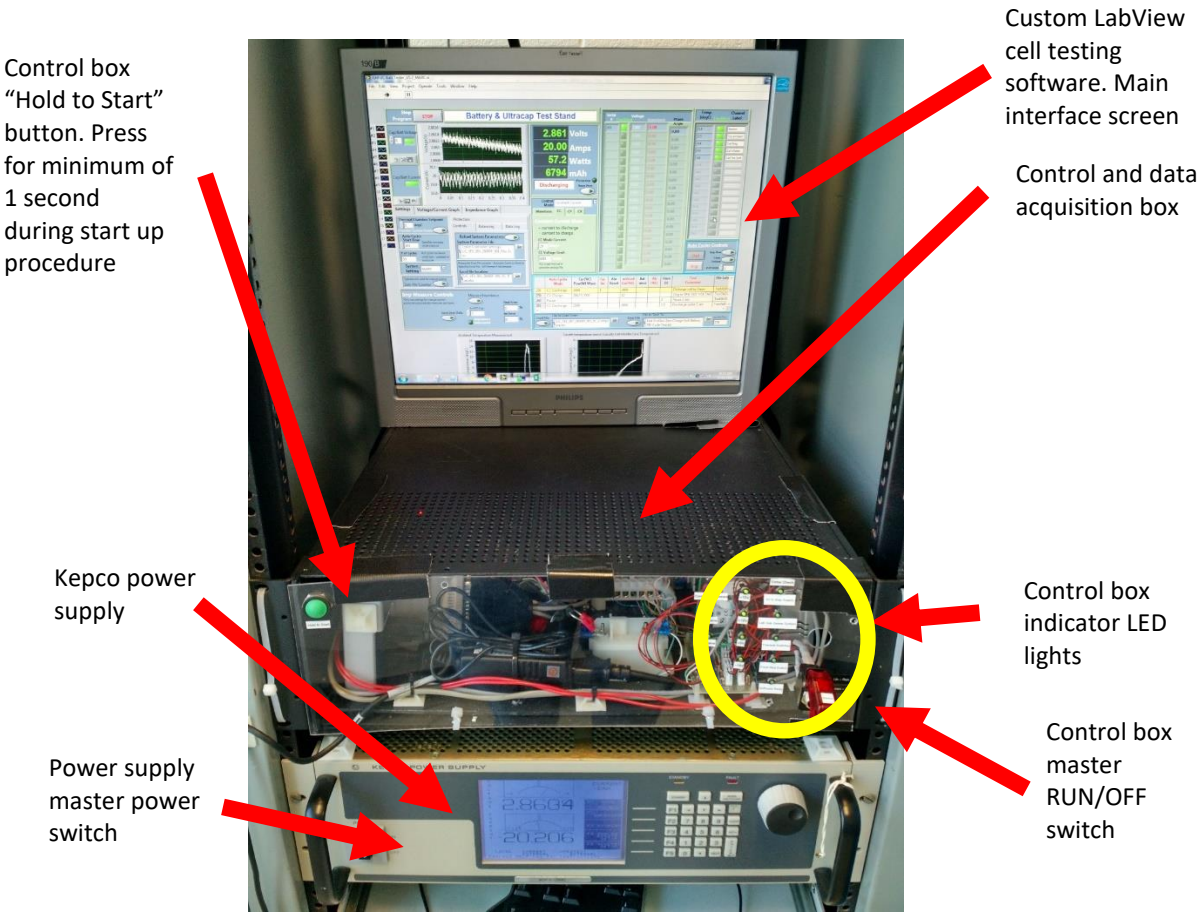

Figure 11: Custom MARC cell cycler power supply, computer monitor and control/data acquisition box

LED status indicators to show if testing power cable contactor coil is powered and if the DUT is being charged or discharged

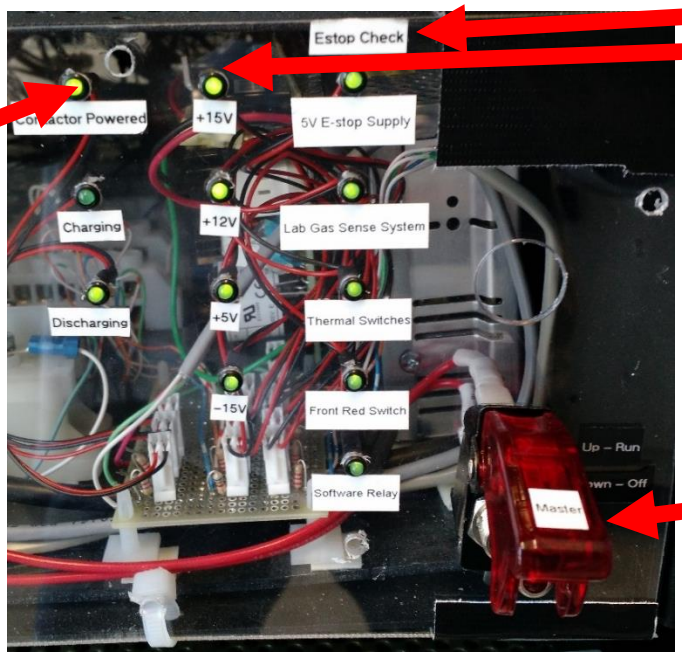

Must have all four power supply LEDs and all 5 Estop check LEDs on for the system to work

Control box master RUN/OFF switch

Figure 12: Control and data acquisition box indicator LEDs.

Figure 13: Back of the control and data acquisition box (top). Back of the Kepco power supply (bottom)

Power supply remote voltage sense leads. The positive cable is switched via the small control box contactor. The positive sense lead on the power supply has a resistor added to the local sense lead so that the output voltage can be regulated when the contactor is open.

8 channel relay module that uses a 5V supply and switches:
-main contactor coil
-Kepco remote shut down
-discharging LED
-charging LED
-software E-stop

Energy wasting resistors used to meet minimum load requirement for +/- 15V power supply

Perforated circuit board with voltage divider resistors for temperature measurement using thermistors

Power resistor used to create voltage drop from current sensor's output current. Mounted on fan in attempt to minimize temperature rise

Box 120V AC input power cable and main power switch

Current sensor – outputs a current proportional to the measured current.

Positive power cable that connects to the cell

Contactor used to break positive connection between the cell and power supply

5 and 12V power supply

Power supply terminal blocks and GND

+15V and -15V power supply

Perforated circuit board with connections for LED indicators and current limiting resistors

Mini contactor used to break the positive voltage sense lead between the cell under test and the voltage sense

Variable time watch dog relay (120V AC coil). The relay contacts are in series with the 12V main contactor coil. If the LabVIEW software is closed during operation, the digital control pins to the relay board will not change and the contactor will remain powered until the time delay watchdog relay opens after approx. 5 seconds (time depends on setting on relay knob). Provides hardware protection in case the software crashes.

Solid state relay with coil control performed by multiple DAQ digital outputs. Switches 120V AC to watch dog relay coil

NI DAQ device with 4 modules:
-NI 9205 analog input
-NI 9239 analog input (24 bit isolated)
- NI 9264 Analog out
-Ni 9403 Dig. I/O

USB cable that connects DAQ to desktop PC

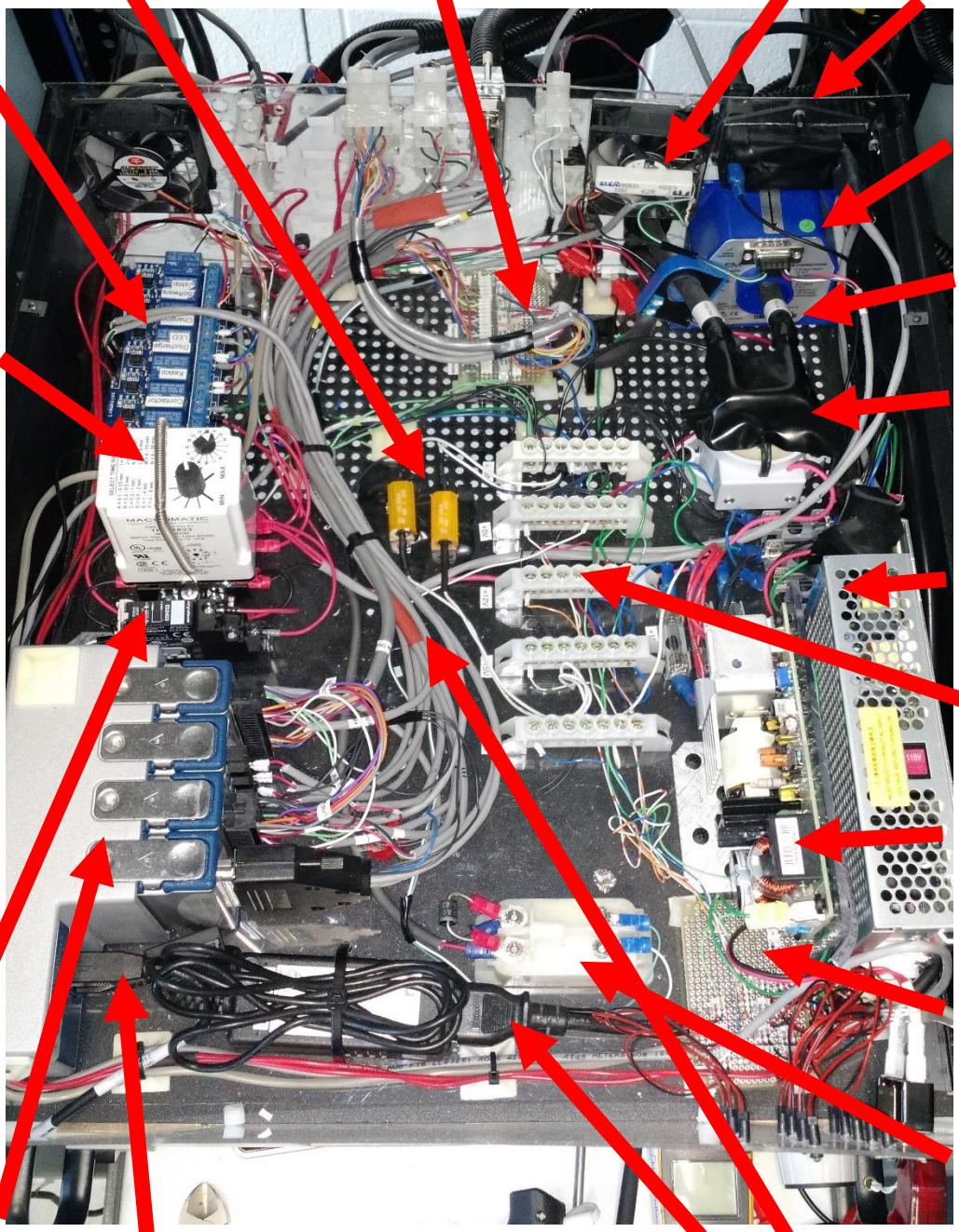

Figure 14: Inside the control and data acquisition box

Power supply cable for the National Instruments DAQ device

I/O cables for sensors and control from the DAQ

The control box has an E-stop system made up of switches in series, as shown by Figure 15. The indicator LEDs on the front of the control box are connected to voltage tap points along the series set of switches to show where the circuit has opened. The first switch is a relay contact located in the lab's gas sense/e-stop shut down system box that is mounted on the lab wall. The second switch is a set of two normally closed thermal switches that are mounted on the device under test and open at a temperature of 75 degrees C. The third switch is the red master switch located on the front of the control box (see Figure 12). The last switch is one of the relay contacts on the 8-channel relay board (see Figure 14). The relay board needs a 5V supply and then uses digital inputs (GND = energize a relay, 5V = do not energize a relay) to control opto-isolators that switch the coil of individual relays using the 5V board input supply for the coils. This 5V board supply is taken from the "software e-stop" relay contacts. Before testing begins, the relay board is not powered because the "software e-stop" relay is not energized and therefore none of the other relays, including the power supply enable and main contactor relays, are energized either. Even if a digital input from the DAQ is commanding the software e-stop relay to be energized, it won't be because the relay board is lacking a 5V supply for driving relay coils. To overcome this, the green momentary "Hold to Start" button is connected across the "software e-stop" relay contacts. Pushing the momentary N/O switch will provide 5V to the relay board 5V input and then the DAQ's control pin will command the "software e-stop" relay to close via the opto-isolator. The "software e-stop" relay is wired to be a latching relay and will remain energized until the coil 5V power supply is removed. This latching wiring method was used so that the tester cannot be started remotely without the need to push the momentary start button. This encourages the user to check over the testing hardware while in the energy storage testing room before starting tests remotely. Provided the software e-stop relay control pin stays low (GND) then the user can pause and restart the testing remotely. There is no need

to press the momentary start button when the software goes into protection mode because the "software e-stop relay" control pin is not controlled by the software protection state – it is only controlled by the user clicking a software button. This allows the user to shut down the power supply output and open the main contactor from home if he/she feels the need. In this event, if anyone else tried to remote login to the computer and start a test, it will not work because the momentary "Hold to Start" button must be pressed, therefore forcing someone to visit the lab and presumably check for any issues. The lab gas sense system shutdown relay shown in Figure 15 is non-latching and therefore the latching nature of the custom MARC cell cycler e-stop system ensures that the cell cycler will not restart without momentary input from someone in the lab space.

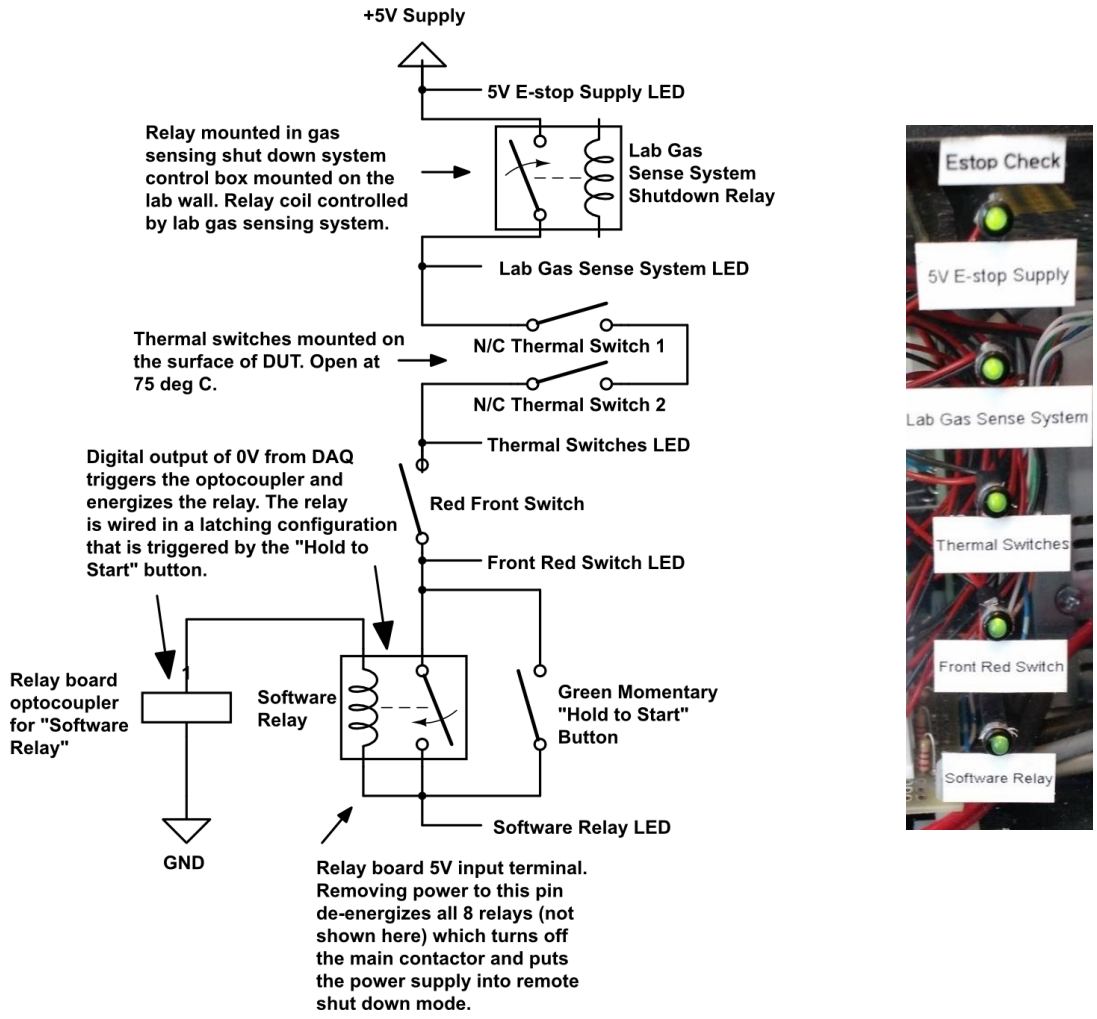

Figure 15: Simplified e-stop schematic for the control and data acquisition box

4.1.1.4. Sensor Interface Box

The sensor interface box, shown in Figure 16, acts as a sensor cable breakout box and extension to the back end of the control and data acquisition box. The sensor interface box provides a convenient location for shorter sensor cables to connect to the cell testing device rather than running multiple long cables through the thermal chamber and to the back of the control and data acquisition box. The sensor interface box provides connectors for ten thermistors, three voltage measurement points, and two E-stop thermal switches (see Figure 15).

4.1.1.5. Desktop Computer and LabView Software

As noted in Figure 8, the custom MARC cell cycler computer is located at the bottom of the mobile equipment rack. Custom LabView based cell testing software that was developed by Dr.

Kollmeyer runs on the desktop computer and communicates to the NI DAQ hardware located in the control and data acquisition box using a USB cable. An example of the software interface is shown in Figure 11 and the NI hardware is shown in Figure 14. The feature rich software offers a variety of functions such as:

- Constant current (CC) charge and CC discharge commands
- Constant voltage charge command
- Current waveform command - used for making drive cycle current profiles
- Impedance spectroscopy commands
- Autocycler - automatically executes a sequence of testing commands and counts cell cycles
- Data logging to specified Excel worksheets at specified data logging rates (up to 10 Hz).
- Cell voltage, testing current and multiple temperature measurements

4.1.1.6. Thermal Chamber

The Envirotronics SH16 thermal chamber was used for all testing performed with the custom cell cycler. Figure 16 shows inside the thermal chamber prepared with the DUT connected to the power cables and sensor interface box. Figure 16 also shows part of the lab gas sensing system and CO_2 fire suppression system which are discussed in Section 4.1.2. Figure 17 shows the thermal chamber foam insert modifications performed by other ESS students. In the event of a cell explosion, it is intended that the foam inserts will be blown out the top of the chamber, rather than breaking the thermal chamber door latch and blowing the door open. The rubber flaps that cover holes in the foam (approximately 4-inch diameter) are intended to act as a pressure release when the CO_2 fire suppression system discharges into the thermal chamber. The rubber flap is intended to close, as shown in Figure 17, when the pressure wave equalizes. The rubber flap is the preferred CO_2 pressure release method rather than blowing out the foam inserts because it is desirable to contain the cold carbon diode in the thermal chamber to assist

in cooling the DUT and prolong the release of CO_2 into the lab testing room. Due to the rather small opening available to pass cables through the thermal chamber side wall, the author modified the thermal chamber to add a second, and much larger, cable passage port as shown in Figure 18.

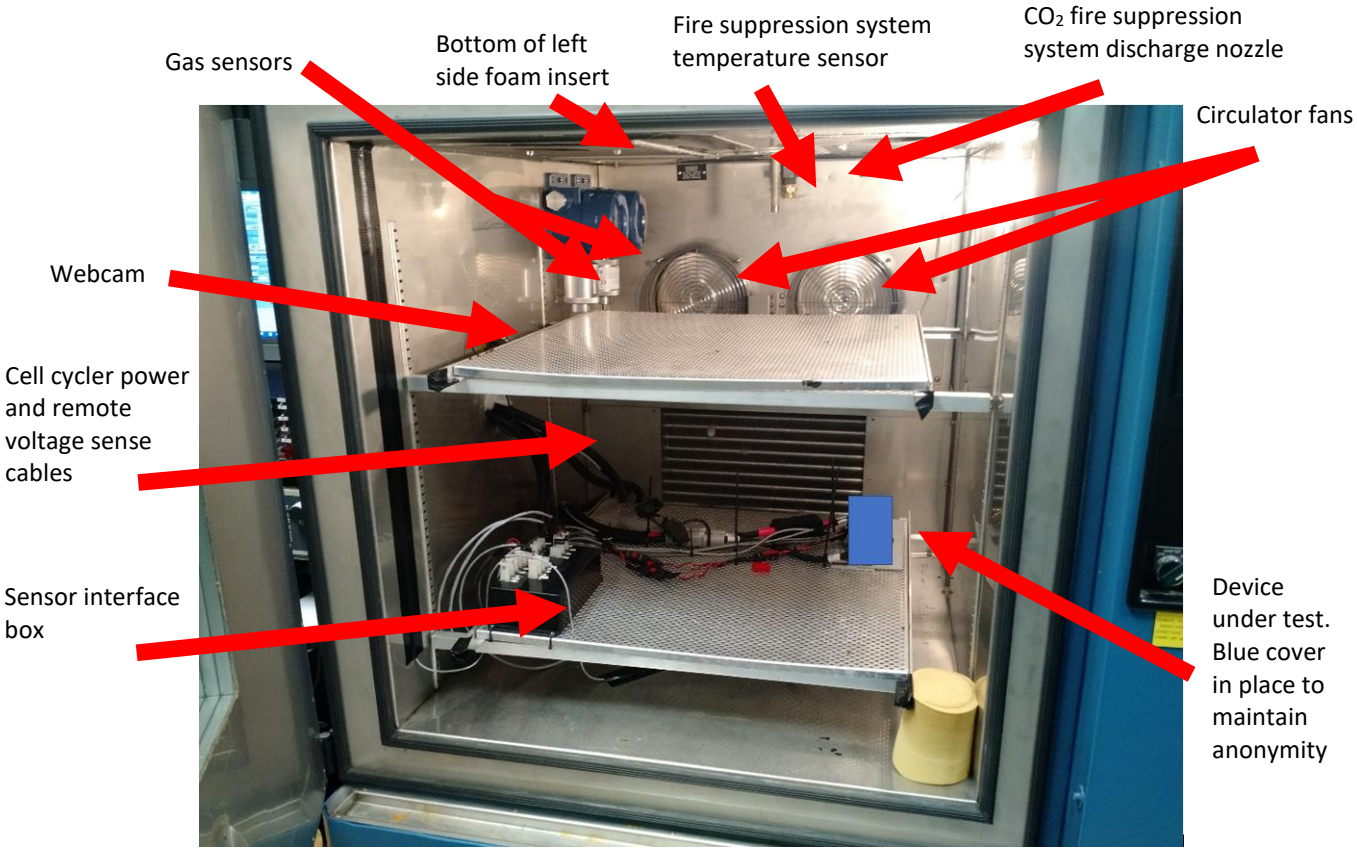

Figure 16: Inside the Envirotronics SH16 thermal chamber

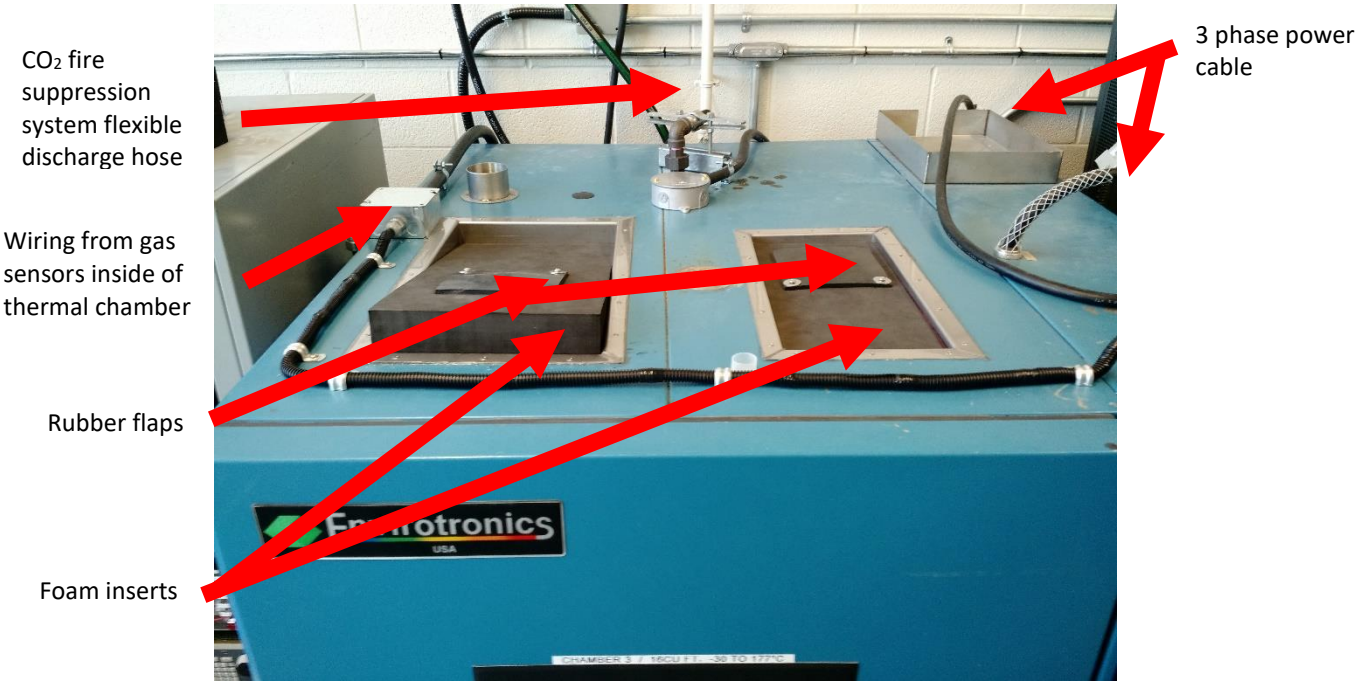

Figure 17: Top of the Envirotronics SH16 thermal chamber

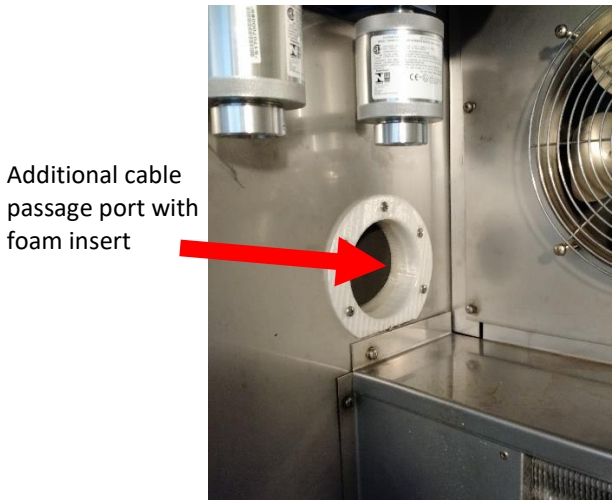

Figure 18: Additional cable passage port added at the back-left corner of the Envirotronics SH16 thermal chamber

Due to very limited LCD screen functionality, the Envirotronics SH16 thermal chamber was originally hard to control using keypad inputs. An update was made so that the custom cell cycler desktop computer communicates with the thermal chamber via ASCII commands using a USB to serial converter and *RealTerm* software (see Figure 19). Due to the limited frequency that the thermal chamber temperature setpoint and circulator fan settings were changed, the ASCII

commands are not linked to the LabView cell testing software. Although the *RealTerm* remote commands provided most functionality needed to operate the thermal chamber, the remote key pad and was used to access programmable logic controller (PLC) memory bits for diagnostic purposes. The memory bits helped identify pressure switch issues that prevented the thermal chamber from operating a couple times.

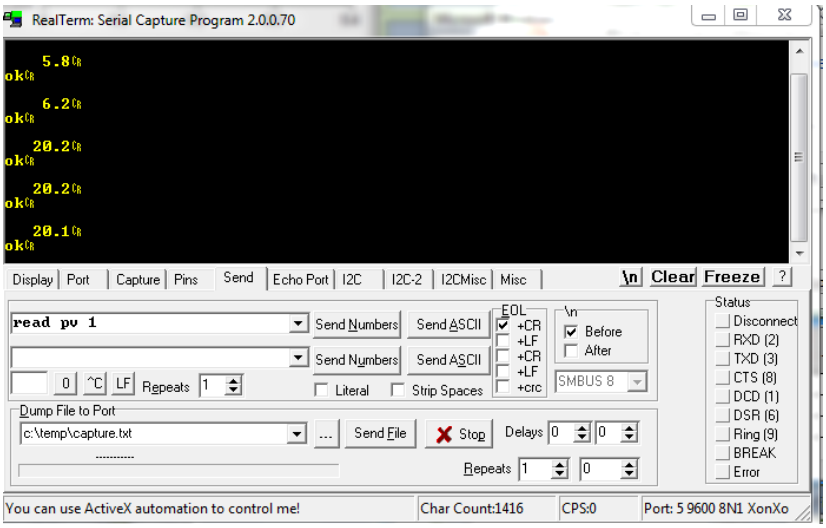

Figure 19: Example interface from RealTerm software showing a command to read the Envirotronics SH16 thermal chamber present temperature value.

The desktop computer interfaces with a computer webcam mounted inside the thermal chamber using a USB connection. The image quality was reduced to enable high data rate communication with the NI DAQ hardware. Although one would not expect any movement inside the thermal chamber, the webcam was useful to remotely detect the presence of ice that would accumulate on the internal heat exchanger (see Figure 20). The presence of ice would restrict the thermal chamber from maintaining temperatures below 0°C and would therefore require a manual thermal cycle to melt the ice.

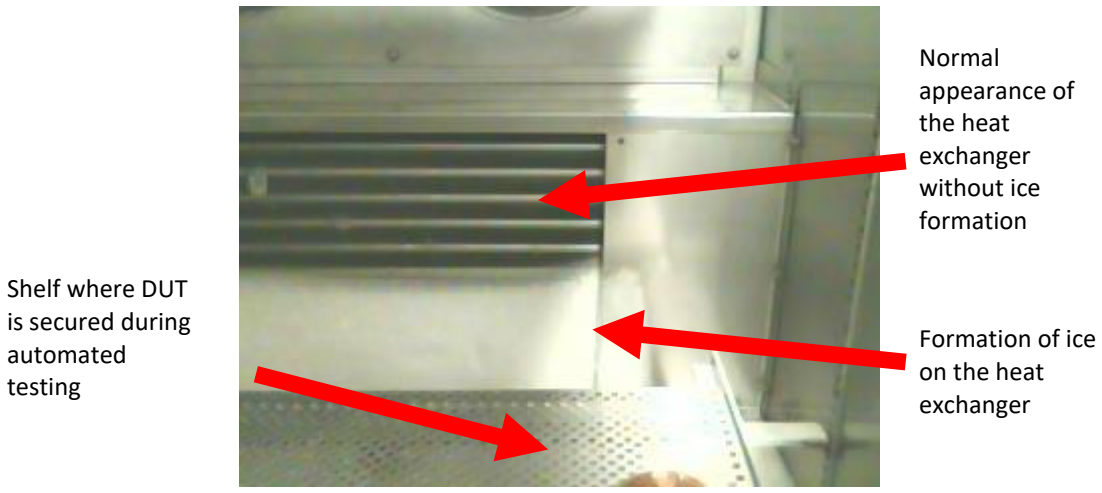

Figure 20: Photo taken using the interior thermal chamber webcam that shows ice forming on the heat exchanger.

4.1.2. Lab Safety Systems

The development of the custom MARC cell cycler enabled cell testing a few months before the Digatron cell testing equipment was commissioned. However, additional safety measures were necessary before unattended testing could begin. The following list outlines the multitude of safety systems developed and their operation sequence as a line of defence to minimize damage from a device under test catching fire:

1. Testing approval form and fixture review
2. Cell / pack cycler software and hardware limits on voltage, temperature and current
3. All testing performed in thermal chambers equipped with gas sensing hardware and pressure release ports
4. Activation of lab shut down system that turns off all cell/pack testing equipment and thermal chambers
5. Automated CO_2 fire suppression system plumbed into all three thermal chambers

The author integrated a master lab emergency stop (e-stop) button and select hardware from items 3 and 5 to develop an automated lab shut down system. The following subsections documents some of the work completed to enable unattended testing and therefore enable the experimental work of this study.

4.1.2.1. Testing Approval Form and Fixture Review

Along with Dr. Kollmeyer and other ESS students, the author initiated the development of a testing approval and cell fixture review process. This process requires students to review the safe operating area limits for the DUT, such as voltage and current limits, and document the software safety limits used on the testing hardware. This paperwork outlines the anticipated testing duration, equipment in use, device under test, and emergency contact information for the equipment user. The lab manager signs off on the paperwork once satisfied with the cell/pack testing methods, safety settings and cell testing fixture design. By affixing the testing approval form to the lab testing room door (see Figure 7), the lab manger and other students are made aware of any testing underway.

4.1.2.2. Gas Sensing System and Automated CO_2 Fire Suppression System

Tyco Integrated Fire and Security installed a thermal chamber gas sensing system and automated CO_2 fire suppression system. Each thermal chamber was fit with two Oldham iTrans2 gas sensors to detect CO_2 (sensor with P/N 7703-6321) and combustible gasses such as CH_4 and H_2 (sensor with P/N 7702-2606). Figure 16 shows two gas sensors installed in the Envirotronics SH16 thermal chamber. The gas sensing system is intended to detect battery cell/pack off gassing before the DUT catches fire. In combination with the lab shut down system, the gas sensors may prevent further cell testing that provokes a cell/pack fire. If the gas sensors and equipment shut down are unsuccessful in eliminating the fire hazard, the fire suppression system can be triggered automatically using temperature sensors in the thermal chambers (see Figure 16), manually using the manual pull station shown in Figure 23 or manually by pulling the firing plunger in Figure 21. The fire suppression system control panel is integrated with the building fire alarm system.

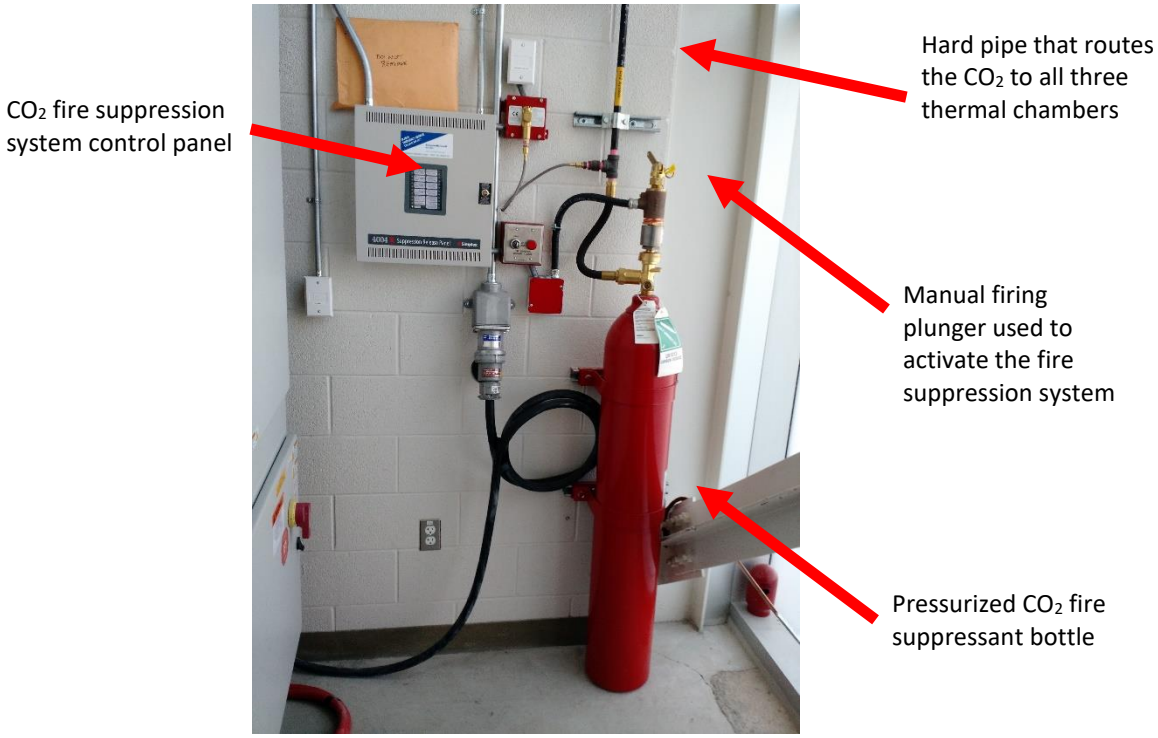

Figure 21: CO_2 pressurized fire suppression system located in the energy storage lab testing room

4.1.2.3. Lab Shut Down System

The author was responsible for designing and implementing a system that shuts down the equipment listed in Table 3 under any of the following three conditions:

1) The lab CO_2 fire suppression system is activated (activates the building fire alarm)
    - Latching condition until fire alarm panel is reset
2) The gas sensing system is activated due to the presence of an undesirable gas
    - Non-latching system
3) A master lab wide emergency stop button is pushed.
    - E-stop button reset by twisting the button plunger

This requirement was achieved by developing the shutdown relay control box shown in Figure 22 and the lab master e-stop button shown in Figure 23.

The energy storage lab shutdown relay control box primarily consists of four double pole double throw (DPDT) relays with normally open contacts wired in series. These contacts control the power delivered to the 24V switched power terminal strip (yellow terminal blocks in Figure 22) that provides coil power to a shut down relay installed in each testing device listed in Table 3. Due to space constraints, the custom cell cycler shut down relay is installed inside the shutdown relay control box. The coils of the four series connected relays are independently controlled by the lab master E-stop button (see Figure 23), CO_2 fire suppression system alarm panel, relays within the gas sensors that signify a sensor fault and finally, relay contacts within the gas sensors to signify that a concerning gas was detected.

The non-latching relays from the gas sensors were initially of concern as the lab equipment could re-start after the concerning gas dissipated and the gas sensors retuned to a normal operating state. This issue was corrected by implementing a latching system that uses the relays from the gas sensors to add a parallel load of resistors that increases the load on the 24V supply and therefore blows fuse Z (see Figure 22). Fuse Z is in series with the gas sensor alarm relay, therefore causing the switched 24V bus to de-energize and remain de-energized until fuse Z is replaced by someone in the lab space that would presumably investigate the concern.

The lab master emergency stop button shown in Figure 23 is installed next to the lab's CO_2 fire suppression system trigger point located in the lab control room shown in Figure 7. The second set of contacts on the four series connected main lab shut down system relays are used to indicate the status of each relay via the LED lights on the E-stop button box (Figure 23). A red LED indicates the relay is not energized and therefore the corresponding safety system, such as the gas sensor fault relays, indicates a condition to shut down the lab equipment. A sequence of

five green LEDs indicates that the lab safety systems do not detect an unsafe condition and the lab equipment should be in a “ready” state. If neither light per row on the e-stop button box is illuminated, this indicates either a wiring concern, a loss of power or a faulty LED light. These status LEDs are located on the e-stop box relay so that students can see what issue is present before entering the lab testing room.

E-stop relay

CO_2 fire suppression system alarm panel relay

Gas sensor fault relay

Gas sensor alarm relay

Terminal block for connecting blue cables that run to the e-stop box and power the e-stop box LEDs

Fuse Z – this fuse should blow if any of the three gas sensor systems trigger a low gas alarm

Current limiting resistors for E-stop box LEDs

E-stop button connection – continues the e-stop relay coil power through the e-stop button

Panel mount LEDs to show if 24V power supply is present and if fuse Z is not blown (LED = green)

Mechanical switch to shut off 24V input (after fuse 0) to the rest of the panel.

24V supply ground bus bar – all black terminal blocks connected via red jumper.

Custom cycler shut down relay that switches the custom cycler's 5V E-stop line.

Terminal block for all cables coming from the three gas sensing systems.

Yellow terminal block for the switched 24V supply that powers the coils of shutdown relays installed in each piece of testing equipment.

Thee separate resistor banks used to intentionally blow fuse Z when any of the size gas sensors in the lab are triggered. Blowing fuse Z should de-energising the gas sensor low alarm relay coil and therefore de-energize the 24V supply that powers the coil for the equipment shut down relays

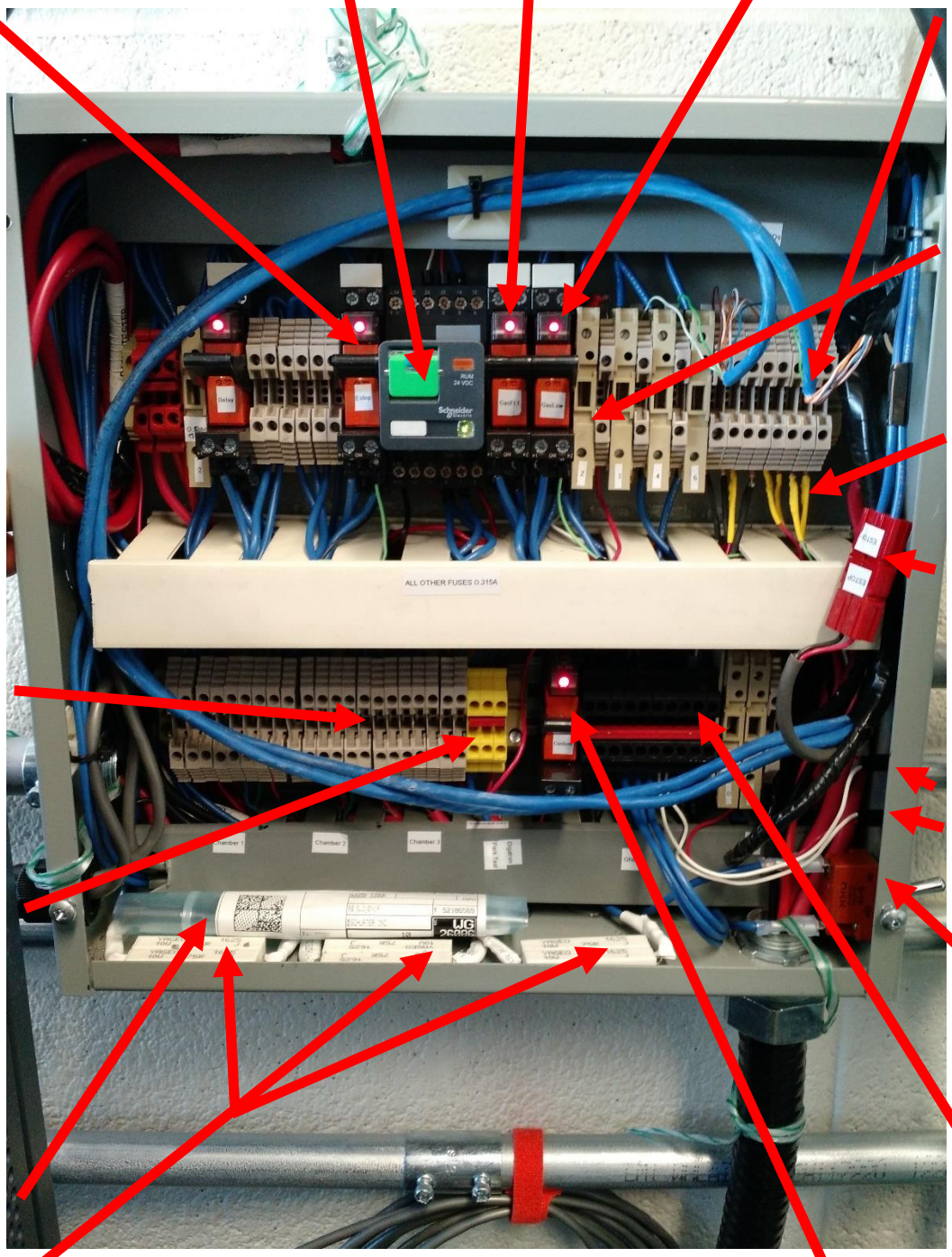

Figure 22: Energy storage lab shutdown relay control box

Figure 23: Energy storage lab emergency stop button and CO_2 fire suppression system pull station

5. Experimental Performance Comparison of EDLC and LiC Cells for Energy Storage Applications

5.1. Chapter Overview and Research Contributions

This chapter presents the experimental methods, select raw data, and analysis of over 881 hours of experimental testing used to characterize and compare the performance of two electric double layer capacitors, four asymmetric Li-ion capacitors and one unique symmetric/parallel Li-ion capacitor (||LiC) for energy storage applications. The study of seven cells, including five lithium-ion capacitors from four different manufacturers, extends the work of [74], [75], [76] and [91] which study lithium-ion capacitor(s) from one well known manufacturer. Section 5.2 extends the high-level supercapacitor performance comparison in [92] by showing datasheet and experimentally determined cell specifications that are used to develop a volumetric and gravimetric Ragone plot. Unfortunately, the information available from publicly available EDLC, LiC and LiB cell data sheets is rather limited. For example, most manufacturers will provide only one equivalent series resistance value. Often, it is unknown if the published value is an average of the experimental results from multiple testing conditions or one selected condition. As shown by this work, the equivalent series resistance of a LiC cell changes with state of charge (minor change), current direction and testing temperature. Therefore, additional experimental work is necessary to extend one's knowledge of the cell behaviour under testing conditions that are not discussed on the datasheet. Additionally, some of the datasheets acquired for the LiC cells in this work did not show a charge and discharge terminal voltage vs capacitor or state of charge relationship. Although limited datasheet values and several assumptions can be used to model a cell, the author's experimental work extensively builds upon datasheet values to show how cell behaviour changes under multiple conditions.

The custom cell testing fixtures and related hardware are discussed in Section 5.3. Section 5.4 outlines the five time-domain experimental methods used to electrically and partially thermally characterize the capacitor cells. Section 5.5 examines the cell charge/discharge cycling energy loss and temperature rise to estimate the cell internal resistance and case-to-ambient thermal resistance. Section 5.6 discusses the cell charge/discharge voltage vs. SOC profiles and associated hysteresis at various temperatures. To build upon the work in [76] and [91], Section 5.6.3 documents the impact of temperature and current on both discharge and charge capacity (measured in Ah) as well as useful energy stored/discharged (measured in Wh) in both EDLC and lithium-ion capacitors. Section 5.7 extends the work in [91] by showing how the cells' charge and discharge equivalent series resistance changes across 5% SOC breakpoints. This information is also presented as an average cell ESR and normalized average cell ESR. Section 5.7.5 addresses the need for a multi-temperature current dependant ESR model, as described in [75], by evaluating the internal resistance with time domain based HPPC testing using three different current rates for both charging and discharging pulses at 5% SOC increments. Cell performance during the US06 and UDDS drive cycles at 25°C and 0°C are compared in Section 5.8. Additionally, Section 5.8 presents a simple cell model and select cell characterization data validation using the drive cycle data at 25°C. Section 5.9 shows the change in cell terminal voltage and approximate self discharge current over a nearly eight-day self discharge test. Research results and discussion are documented within each section while Section 5.10 provides a chapter conclusion.

The author's contributions to the experimental work in this chapter include, but are not limited to, the following:

- Selecting and acquiring the cells to test

- Development of seven cell testing fixtures
- Selecting the five experimental tests performed and all conditions / parameters associated with the testing (eg. thermal chamber temperatures, current amplitudes…)
- Developing the cell testing profiles loaded onto the custom cell cycler
- Development of a drive cycle power profile for test #4 using a vehicle modeling and power profile tool develop by Dr. Kollmeyer
- Operating the testing equipment and running the tests both locally and remotely
- Correcting most issues experienced with the testing equipment
- Developing a MATLAB based data analysis and plotting tool

5.2. Device Under Test – Cell Selection, Specifications and Sources of Experimental Error

The majority of commercially available EDLC cells with capacitance ≥2000 F are limited to an upper voltage of 2.7V to 2.85V. EDLC Cell A was chosen because of it's relatively high maximum voltage of 3V. EDLC Cell B was chosen as a "standard" 2.7V EDLC benchmark and has the same cylindrical form factor as Cell A. LiC Cell C was selected because of the unique prismatic form that offers a better packing factor compared to cylindrical cells. LiC Cell D was chosen because it has the same cylindrical form factor as cell A and B but greater than six times the energy density when measured in Wh/kg. LiC Cell E was chosen due to it's high energy density while LiC Cell F was selected for it's relatively high cycle life compared to the other LiC cells. Finally, ||LiC Cell G was selected due to it's relatively high gravimetric power density and unique symmetric/parallel capacitor design. The author focused on testing a larger quantity of LiC cells than EDLC cells due to the considerable amount of EDLC testing work publicly available in sources such as [92], [93], and [94]. The capacitors were selected and purchased at the authors discretion without an incentive from the manufacturers / suppliers.

The author did not test any battery cells for a few reasons. The author originally though that the LiC cells would behave more closely to EDLC cells and therefore a comparison to EDLC cells was of more interest. This assumption was based on the linear LiC cell discharge curve (terminal voltage vs capacity), the cell naming method and small datasheet capacity values. Additionally, the time required to experimentally characterize LiB cells can be considerably longer than EDLC and LiC cells. This increase in time comes from the increased capacity that requires additional time to fully charge and discharge. For example, compare the testing time row in Table 5 for Cell D and Cell F. As discussed in Section 5.7.1, the use of coulomb counting to change the cell state of charge, which would be necessary for LiB testing, can extend the testing time considerably if testing protection limits are hit. The ability to test LiC and EDLC cells faster than LiB cells allowed the author to test more cells than normally studied in academic literature. The experimental study of seven cells is a large quantity of work considering that a majority of experimental cell comparison literature tests one or two cells. The time invested into establishing the lab facilities, acquiring the cells and running tests was considerable. The time between acquiring the first cell and the end of cell testing was approximately 9 months (Sept. 2017 to May 2018). Although it would be ideal to also test LiB cells, the time necessary was beyond the scope of this work. An alternative would be to test less LiC cells and introduce a LiB cells, however, the author preferred to publish more data on various LiC cells to provide a larger representation of LiC technology than what is publicly available to date.

Table 5 contains a combination of cell specifications obtained from datasheets and experimental testing. The cell volumetric and gravimetric energy density are determined by dividing the average measured energy by the measured volume or mass, respectively. The power density values are calculated using Equation 5 and Equation 6. Although the experimental ESR results

obtained in Section 5.7 are considerably larger than the datasheet values for select cells, the author does not think a single power density number can accurately represent the power capability of the cell. For example, although EDLC Cells A and B have the smallest ESR values, the cell output power capability is relatively low near the 0V minimum cell voltage. This output power is considerably different from values determined using the maximum cell voltage. To accurately represent the power density of the cell for a given temperature, a plot of maximum output power as a function of cell temperature, ESR and SOC would be necessary. This level of detail is not helpful in comparing cells via a Ragone plot and is therefore beyond the scope of this work. Figure 24 compares the cells' energy and power density using two Ragone plots, one for volumetric densities and one for gravimetric densities, using a combination of datasheet and measured values. Figure 24 also includes one data point on each Ragone plot that corresponds to A123's AMP20M1HD-A lithium ion pouch cell, noted as Cell H. The data for Cell H was obtained from the manufacturer datasheet [95].

$$Power\ Density\ [Wh/L] = \frac{0.12 * V_{Max}^2}{ESR_{Datasheet} * Volume}$$

Equation 5: Cell volumetric power density calculated using the datasheet ESR

$$Power\ Density\ [Wh/kg] = \frac{0.12 * V_{Max}^2}{ESR_{Datasheet} * Mass}$$

Equation 6: Cell gravimetric power density calculated using the datasheet ESR

Cell ID	A	B	C	D	E	F	G
Cell Type	EDLC	EDLC	LiC	LiC	LiC	LiC	||LiC
Format	Cyl.	Cyl.	Prismatic	Cyl.	Pouch	Pouch	Pouch
Test Fixture Compression	No	No	No	No	No	Yes	Yes
Capacitance [F]	3,000[1]	3,000[1]	3,300[1]	28,000[1]	14,000[1]	1,100[1]	3,467[5]
Max Cell Voltage [V]	3[1]	2.7[1]	3.8[1]	4.05[1]	4.05[1]	3.8[1]	2.7[1]
Min Cell Voltage [V]	0[2]	0[2]	2.2[1]	2.8[1]	2.8[1]	2.2[1]	1.35[1]
Capacity [Ah]	2.5[4]	2.25[4]	1.47[4]	9.72[4]	4.86[4]	0.49[4]	1.3[1]
Measured Capacity [Ah][7] (Charge / Discharge)	2.321[3,8] 2.291[3,8]	2.180[3,8] 2.129[3,8]	1.465[3] 1.461[3]	10.774[3] 10.725[3]	5.607[3] 5.625[3]	0.488[3] 0.483[3]	1.668 1.528
Energy [Wh]	3.75[4]	3.04[4]	4.40[4]	33.30[4]	16.65[4]	1.47[4]	3.15[4]
Measured Energy [Wh] [7] (Charge / Discharge)	3.79 [3,8] 3.64 [3,8]	3.21[3,8] 3.03[3,8]	4.44[3] 4.40[3]	37.59[3] 37.12[3]	19.58[3] 19.45[3]	1.48[3] 1.45[3]	3.73[3] 3.27[3]
Datasheet ESR [mΩ]	0.27[1]	0.23[1]	1[1]	0.35[1]	0.8[1]	≤5[1]	1[1]
Experimental DC ESR [mΩ]*	0.33	0.20	1.19	1.04	2.42	4.66	6.00
Mass [kg]	0.52[1]	0.503[3]	0.348[3]	0.830[1]	0.321[3]	0.102[3]	0.087[3]
Volume [L] [10]	0.391[5]	0.392[5]	0.217[5]	0.394[5]	0.142[5]	0.055[5]	0.046[5]
Max Operation Temp. [°C]	65[1]	65[1]	70[1]	55[1]	55[1]	65[1]	55[1]
Min Operation Temp. [°C] [11]	-40[1]	-40[1]	-30[1]	-25[1]	-25[1]	-30[1]	-40[1]
Cycle Life [cycles]	1 M[1]	1 M[1]	Unknown	50 k[1] (1 M[1] for 2.8V – 3.8V)	>50 k[1]	>100 k[1]	10 k[1]
Testing Time [h]	60.07	49.40	52.53	362.72	177.74	41.57	137.25
Energy density [Wh/kg]	7.14[6,9]	6.20[5,9]	12.70[5,9]	45.00[6,9]	60.79[5,9]	14.36[5,9]	40.23[5,9]
Energy density [Wh/L]	9.50[5,9]	7.96[5,9]	20.37[5,9]	94.81[5,9]	137.43[5,9]	26.64[5,9]	76.09[5,9]
Power density [kW/kg]	7.69[6]	7.56[6]	4.98[6]	6.78[6]	7.66[6]	3.40[6]	10.06[6]
Power density [kW/L]	10.23[6]	9.70[6]	7.99[6]	14.27[6]	17.33[6]	6.30[6]	19.02[6]

Table 5: Select datasheet values and experimental results used to compare cell specifications.

[1] Datasheet or manufacturer provided
[2] Assumed value
[3] Measured value
[4] Calculated from datasheet/assumed values
[5] Calculated from measured values
[6] Calculated from datasheet/assumed and measured values
[7] Top value - 2A constant current (CC) charge, bottom value - 2A CC discharge, 25°C
[8] Use minimum voltage of 0.05V, not 0V
[*] Data replicated from Figure 8 a) – average discharge ESR determined at 25 °C using 25A discharge current pulses with 3 second relaxation time
[9] Calculated using average of measured energy values
[10] Volume measured for active cell area only, excludes terminals
[11] Some manufacturers advise against charging the cells below 0°C

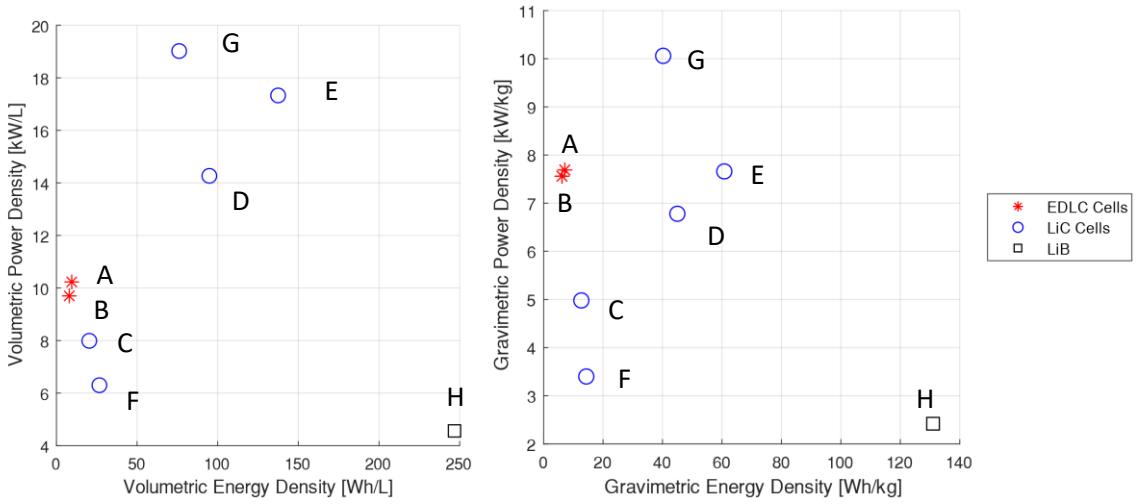

Figure 24: Volumetric (left) and gravimetric (right) Ragone plots using data from Table 5. Power density values are from cell datasheets while energy density values are calculated from the measured cell mass/volume and measured energy content. The Cell IDs are located next to the corresponding data point. The data for Cell H, which is a lithium ion battery, was obtained from [95].

Although the purpose of this chapter is to compare the performance trends between EDLC and LiC cells, the results shown only apply to the specific cells tested and may not be representative of all EDLC nor LiC cells. Due to the extensive amount of time necessary for testing, only one sample of each cell was tested and therefore the results may not represent average specifications. This chapter is not intended to reflect upon the work of the cell manufacturers / suppliers and therefore the cells are described using unique identifiers “A” though “G”, as shown in Table 5. As shown in Table 5 there are some discrepancies between datasheet listed values and those obtained from the experimental work explained in this chapter. These discrepancies may be the result of:

- Inconsistent cell testing methods between the manufacturer and the experimental work presented. For example, the manufacturer may determine the cell equivalent series resistance using an AC current sine wave rather than DC current pulses; which can significantly change the ESR value. Using [96] as an example, Cell SCA0500 has a rated DC ESR of 0.40mΩ while the rated 100 Hz AC 10ms ESR is 0.29mΩ. The author attempted to mitigate the concern regarding different testing methods as a source

of data comparison by testing all the cells using the same, or very similar, testing profiles.

- The electrical connection between the bus bars and cells with tab terminals may introduce a source of resistance that is measured as a cell resistance. The author attempted to mitigate this issue by using the manufacturer provided cell testing fixture for Cell G and by securing two bus bars to each cell tab using bolted connections for Cells E and F. Due to packaging and short circuit issues when compressing a cell, the author made multiple bolted tab connections on Cell E and Cell F using plastic bolts and metal hardware. The experimental and datasheet ESR values for Cell E in Table 5 are very different, however, the experimental and datasheet ESR values for Cell F are close. The datasheet and experimental ESR values are close for Cells A, B and C which all have threaded connections. However, Cell D, which also has a threaded connection, shows a large discrepancy between the datasheet and experimental ESR value in Table 5. These cell connection methods and related comparisons to datasheet values show that the author's cell testing fixtures may have an influence on the results. However, these results may also show that the manufacturer datasheets are claiming performance values under ideal conditions. One of the LiC cell manufacturers provided the author with incorrect datasheet specifications and therefore there is a concern regarding the validity of certain datasheet values.
- Tolerances in cell specifications, such as the capacitance, may result in a difference between nominal datasheet values and experimental values. For example, the measured capacity for Cell A is less than the value calculated from the nominal datasheet capacitance and voltage limits. On the other hand, the measured capacity

for Cell D was larger than the value calculated from the nominal datasheet capacitance and voltage limits.

The following conclusions are made using data available in Table 5 and Figure 24.

- The measured charge and discharge capacity (Ah) of all cells aligns well with the theoretical values, falling within -7.2% (Cell A) and +28% (Cell G).
- For all cells, the measured discharge capacity (Ah) is a fraction of the measured charge capacity (Ah) within a range of 87.7% (Cell G) to 99.3% (Cell E). With the exception of Cell G, the other cells have an energy (Wh) cycle efficiency greater than 94% under the 2A constant current charge/discharge testing performed.
- Both EDLC cells are rated for 1 million cycles while the largest LiC cycle life is >100k cycles. However, the datasheet for Cell D lists 1 million cycles when operated at a limited maximum cell voltage of 3.8V. Generally speaking, the LiC cells have a significantly lower rated cycle life.
- Figure 24 shows that the LiC cells all have a volumetric and gravimetric energy density larger than the EDLCs. However, neither cell type is strictly more power dense when calculated using manufacturer provided ESR values.
- Li-ion capacitor Cell E and Cell G appear to have the best combination of power density and energy density (points E and G are furthest from the origins in Figure 24) when calculated with datasheet ESR values. This result would change if the power densities were calculated using measured ESR values as the measured ESR values for Cell E and G (see Table 5) are multiple times larger than the datasheet values.

5.3. Cell Testing Fixture Design

The author assembled a custom testing fixture for each cell that provides a power connection for cycling, a terminal voltage measurement connection and multiple thermistor extension cable connections. All cells and cell testing equipment in the energy storage lab use Anderson SB 120 connectors for the power cable and mini Anderson connectors for voltage sensing. This standard lab practice allows for cells to quickly and easily be transferred between the custom cell cycler and Digatron MCT. Considering that the cells are always energized, with the exception of EDLC cells discharged to zero volts, all of the testing fixtures feature two fuses; one on the positive power cable and one on the positive terminal voltage sensing cable. A variety of Littelfuse MEGA fuses and fuse holders were used for the power cable fuse due to the variety of current ratings available and ease of use. The cell voltage measurement cables are connected to the cell terminals directly or using a Kelvin connection where possible. This voltage measurement method is used to reduce any voltage change that results from the voltage drop across the power cable and power cable fuse during high current testing. The voltage sensing fuse may introduce a considerable resistance to the voltage measurement cable, however, the voltage drop across the fuse is negligible due to the NI 9293 module input impedance of 1 MΩ. The terminal voltage measurement fuse is primarily used to protect the voltage sense wires from an external short circuit within the control and data acquisition box or during storage. Note that rubber covers are to be used on the SB 120 power connector and mini Anderson voltage sense connector when not in use.

As noted in Table 5, Cell F and Cell G require a compression force applied to the larger pouch surfaces. The author made a custom compression fixture for Cell F and made modifications to a manufacturer developed cell compression text fixture for Cell G. The manufacturer developed

testing fixture required modifications to decrease the risk of unintentionally short circuiting the cell and to develop better electrical contact with the cell tabs.

To ensure the cell surface temperature sensors would not move during thermal cycles, the thermistors were attached to the cells using Kapton tape. The compression text fixture on Cell F was designed so that the temperature sensors remain in contact with the cell surface without being compressed and pushed into the cell surface. However, the manufacturer developed compression fixture for Cell G was difficult to modify in an equivalent way and therefore the thermistors were mounted closer to the cell tabs and not on the cell surface. For this reason, the thermal cycling data in Section 5.5.3. does not include Cell G. Thermal cycling data for Cell F is included in Section 5.5.3, however the author encourages the reader to consider the inconsistent thermal packaging from the compression fixture that may influence the cell's temperature rise.

For illustrative purposes, Figure 25 shows the seven cell testing fixtures with any cell identification covered with blue boxes.

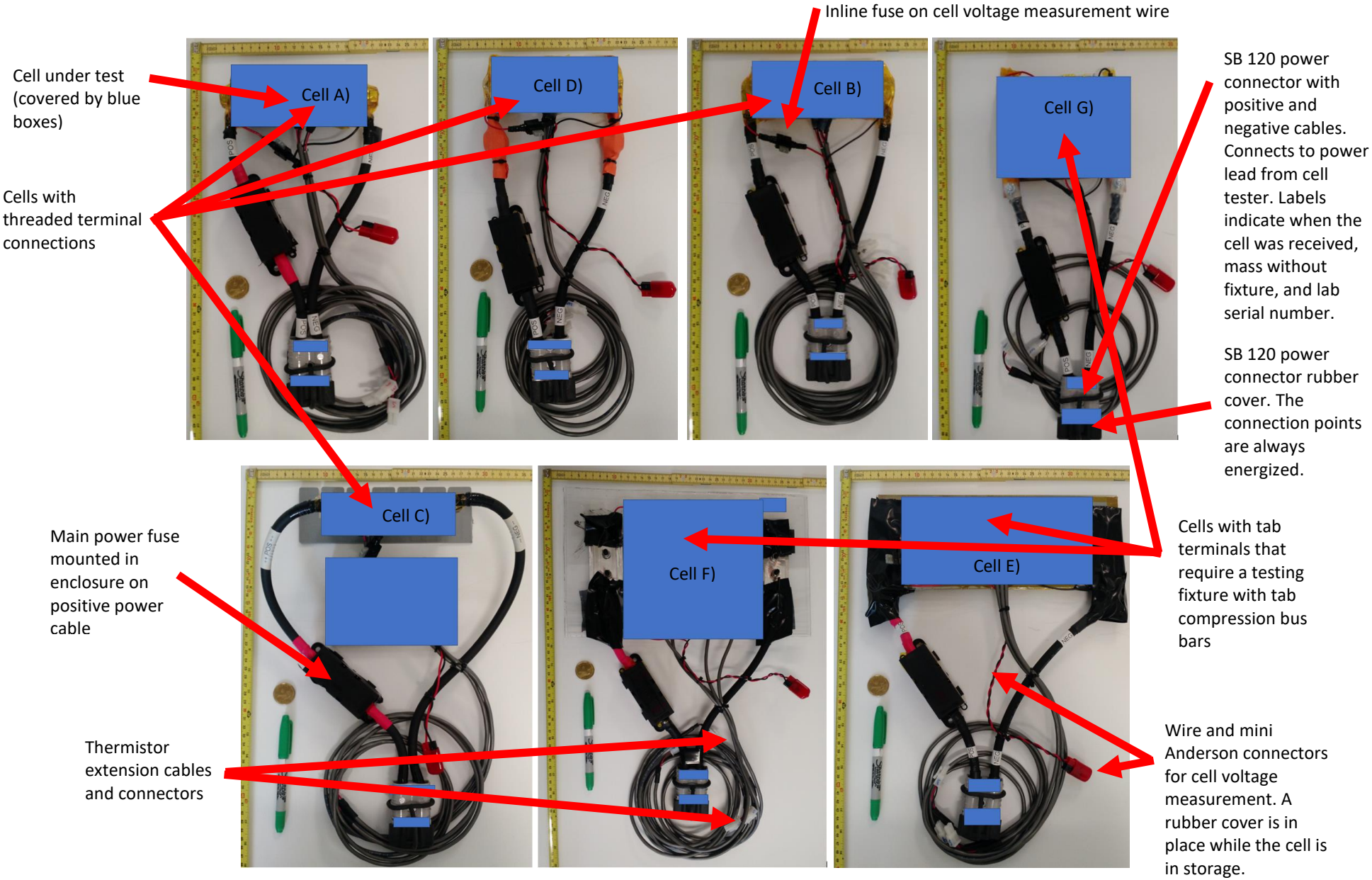

Figure 25: Cell testing fixtures with cell identification covered by blue boxes.

5.4. Overview of Testing Profile Creation, Data Logging and Analysis Workflow

The custom cell cycler offers an autocycler function that automatically executes a series of battery/capacitor testing commands from a text file and logs user selected data to Excel worksheets. To ensure the use of consistent testing and data logging methods, the author developed a universal Excel file that automatically updates the autocycler profile based on cell specifications, naming conventions and the desired thermal chamber temperature. The autocycler profile includes operations to sequentially complete tests 1) thru 3) from Table 6. With the exception of very few noted cases, all seven cells were exposed to very similar testing conditions as defined by the autocycler commands. In examining the capacitor cell datasheets from multiple manufacturers, it became very evident that the method used to characterize the cells varied. The author's testing was based on commonly-used time domain testing methods such as continuous charge/discharge cycling, constant current capacity tests [97], hybrid pulse power characterization [97], self discharge tests [97] and drive cycle model validations, but made use of custom testing durations, configurations and current amplitudes to fit the cell limitations and testing time constraints. For example, rather than charging and discharging cells based on C-rates, the author used fixed current values. Due to the large range in cell capacity, from approximately 0.5Ah to 10Ah, and testing equipment limit of 125A, there would be a limited amount of higher current testing performed on small capacity cells if consistent C-rates were used. For example, with a capacity of 10Ah, the maximum C-rate would be 12.5C, which is rather small for high power capacitor applications. The equivalent 12.5 C-rate for a 0.5Ah cell would correspond to 6.25A max. With a range of 0-6.25A, the cell is not exposed to a large enough current range to compare how current impacts the cell characteristics. Additionally, by only testing the cell to 6.25A, the maximum testing capabilities would not be used, and the data would be rather unhelpful. On the other hand, the 0.5Ah cell could be the base value for a

maximum C-rate of 250C using 125A testing equipment. Assuming the cells are tested at five C-rates at equal intervals (50C, 100C, 150C, 200C, 250C), the 10Ah cell would have a minimum test current of 500A which is beyond the equipment and cell performance limitations.

Test ID & Name	Test Description / Process		
	Testing Temperature(s)	Testing Current(s) [12]	Data log frequency
1) Constant loss thermal cycling	Charge the cell using a constant current until the maximum voltage minus 50 mV is hit. After a one second pause, discharge the cell to the minimum voltage plus 50 mV using a constant current. Repeat for approximately 3.5 hours. The charging and discharging current are chosen to give approximately 2.15W of I^2R losses for the EDLC cells and approximately 1W of I^2R losses for the LiC cells based on the datasheet listed internal resistance (R).		
	25 [°C]	Unique to each cell	0.5 [Hz]
2) Constant current capacity	Starting with a fully discharged cell, use a constant current to charge the cell until the maximum voltage is hit. Then do a CCCV charge to bring the cell to 100% state of charge (SOC). Use constant current to discharge the cell until the minimum voltage is hit. Discharge the cell to 0% SOC and then repeat this cycle for each test current.		
	-10, 0, 10, 25, 35 [°C]	+/- (2, 25, 50, 75, 100, 120) [A]	5 [Hz]
3) Hybrid pulse power characterization (HPPC)	Charge the cell to a SOC breakpoint (eg. 5%), perform a 2.5 or 1.5 second discharge/charge current pulse and allow the cell to relax. Continue this process, charging the cell in increments of 5% SOC. Fully discharge the cell and repeat with a charging pulse of the same magnitude. Repeat the charging and discharging HPPC sweep for all three current magnitudes.		
	-10, 0, 10, 25, 35 [°C]	+/- (10, 25, 50) [A]	10 [Hz]
4) Self discharge	Connect the cell to a single ended voltage measurement port on a NI 9205 module (input resistance of >10 GΩ || 100 pF) and log the cell voltage for approximately 8 days.		
	Room temperature	No supply/load current	1/60 [Hz]
5) Drive cycle validation	Connect each cell to a unique cell testing channel on the Digatron MCT. Fully charge the cells using a CCCV profile and then start a power demand based US06 drive cycle profile. Upon completion fully charge the cell and perform a power demand based UDDS drive cycle profile. When the cell is incapable of meeting the power demand, the cycling current is minimized.		
	0, 25 [°C]	US06, UDDS drive cycle	10 [Hz]

Table 6: Overview of the five time-domain tests performed on each capacitor cell

12 Positive current values correspond to discharging and negative current values correspond to charging

The Excel based autocycler commands were designed to save select testing data to specific worksheets within the same Excel file. For example, the testing data to obtain the cell capacity using a constant current 2A charge and 10A charge are saved on separate Excel worksheets. This method was used to ensure the cell specifications, autocycler commands and data were all contained within one file. Additionally, separating specific test data into consistent worksheets eliminated the need to filter through hours of useless data and made the comparison of data from different tests much easier. A new Excel file is created for every testing temperature for

each cell, therefore resulting in a total of 35 Excel files (seven cells tested at five temperatures) with 141 worksheets each.

Rather than analyzing the 35 Excel files (1.4 Gb of data) manually, the data was imported into Matlab and assigned variable names based on the structured and consistent data saving method discussed earlier. The majority of the cell testing involved repeating very similar multi-day long testing profiles at multiple temperatures for each cell. This repetitive nature lends itself nicely to scripted data analysis that can simply be expanded to include new data as it becomes available. Scripted data analysis allowed for easy detection of missing or inconsistent data. Additionally, the scripted analysis provided a much faster method to compare data from different cells that was originally stored in different Excel files.

5.5. Test 1 – Constant Loss Thermal Cycling

The purpose of Test 1 is to evaluate the energy loss and temperature rise from repeated constant current charge and discharge cycles that persist for approximately 3.5 hours. An approximate power loss is determined from the average energy loss over the cycling time. An approximate equivalent series resistance is estimated from the approximate power loss and known testing current. The cell's equivalent series resistance will also be evaluated in Section 5.7 using a hybrid pulse power characterization method. The same cell cycling data used to estimate the energy loss can be used to evaluate the cell temperature rise and an approximate case-to-ambient thermal resistance. The following subsections will describe the testing method, provide analysis of the test results and end with a conclusion to compare the EDLC, LiC and ||LiC cell technologies based on Test 1.

5.5.1. Test 1 Method

The cell is connected to the custom cycler and left inside the thermal chamber for several hours. This thermal saturation period is intended to make the capacitor cell reach the same

temperature as the testing environment. Unlike Tests 2 thru 4, this test is only performed at a desired temperature of 25°C. However, Cell B is also tested under supervision at room temperature with the thermal chamber foam inserts removed. This additional testing condition is used to show how the thermal chamber temperature-controlled environment with turbulent airflow impacts the cell temperature rise.

The testing begins by fully discharging the cell and performing an amp hour counter reset to 0Ah. The cell is charged at a constant current that would result in an I^2R loss equivalent to 2.15W for EDLC cells and approximately 1W for LiC based cells based on the datasheet listed internal resistance (R). The constant current is terminated to 0A when the cell voltage reaches the maximum cell voltage minus 50mV. After a commanded 1 or 2 second pause the cell is then discharged using a constant current selected to match the charging current I^2R losses until the cell voltage reaches the minimum cell voltage plus 50mV. The 50mV buffer was introduced to prevent the cells from violating cell voltage limits set in the cell testing software.

The charge and discharge cycles, which are separated by one second testing pauses, are repeated for approximately 3.5 hours. The number of charge/discharge cycles that occur within 3.5 hours is dependant on the testing current and cell capacity. Therefore, the number for charge/discharge cycles was determined beforehand and the Excel based autocycler profile was manually changed. The cell was left to rest with zero testing current for 2.5 hours after the approximate 3.5 hours of cycling is complete.

5.5.2. Test 1 Analysis – Energy Loss

Figure 26 and Figure 27 show the energy cycled through the capacitors during the repeated charge and discharge cycles. Note that Test 1 is repeated twice for Cell B to evaluate the thermal

chamber's impact on the cell energy loss and temperature rise in comparison to testing in a room without active thermal control active. Therefore, Figure 26 contains two plots for Cell B.

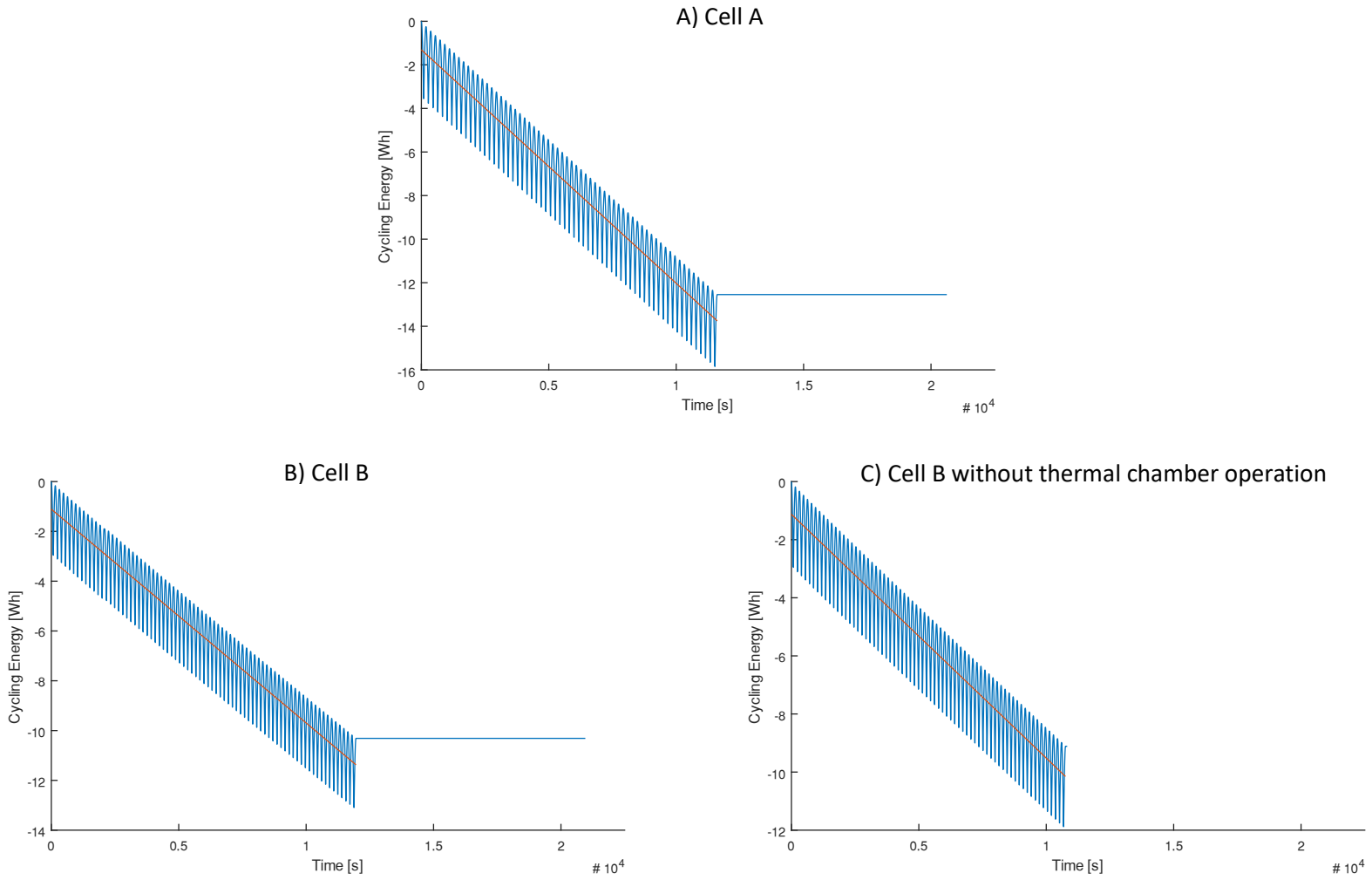

Figure 26: Energy loss from repeated charge and discharge cycles – Cells A and B

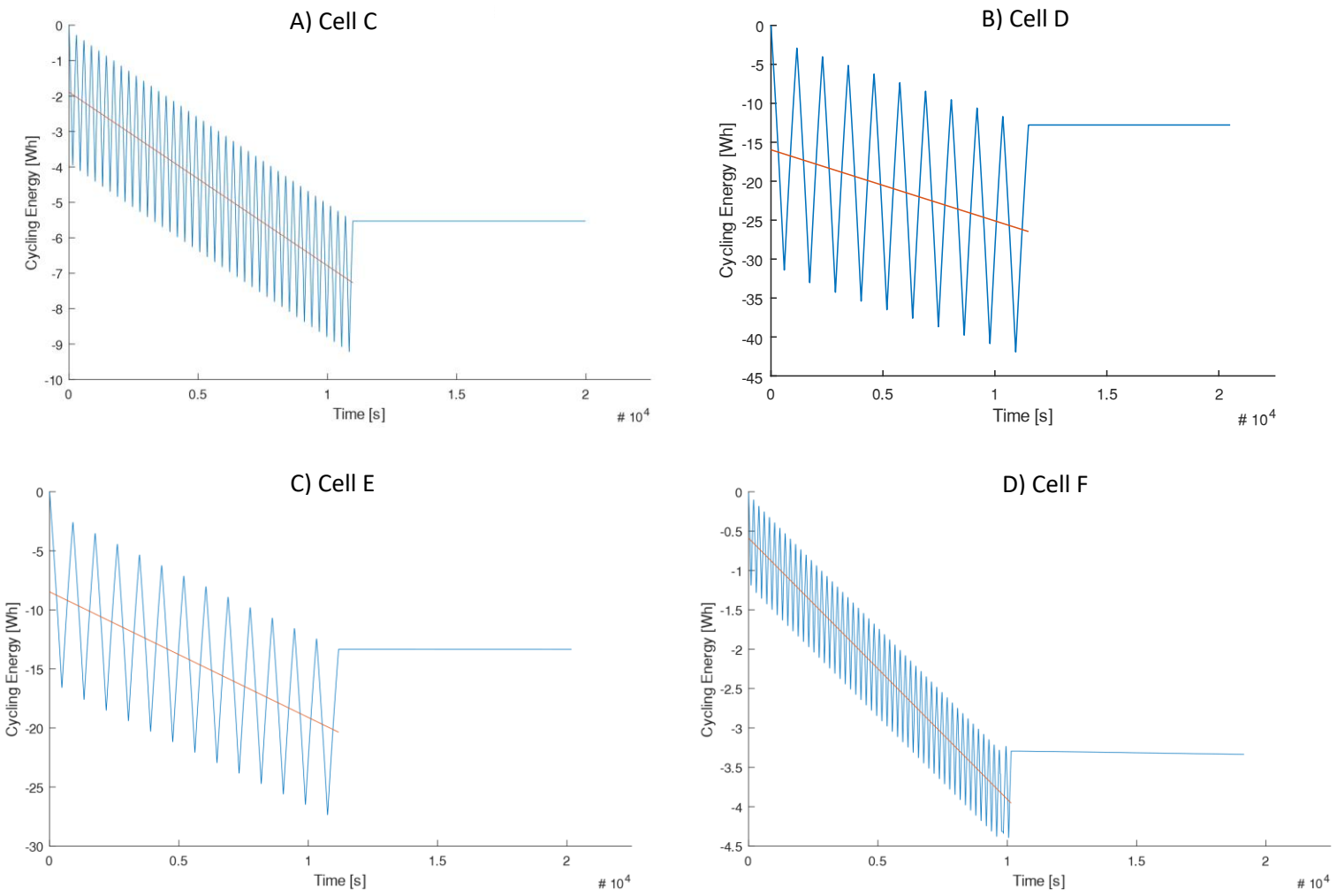

Figure 27: Energy loss from repeated charge and discharge cycles – Cells C thru F

Recall that the cell starts fully discharged and therefore, the first energy change corresponds to a charge cycle which is noted by the negative energy value. As listed in the footnotes of Table 6, a positive current corresponds to discharging the DUT and a negative current corresponds to charging the DUT. Using Subplot C from Figure 27 as an example, we can see that Cell E experienced thirteen charge and discharge cycles that started and ended in the discharged state. As shown by the orange trend lines on all subplots in Figure 26 and Figure 27, the amount of energy discharged is less than the energy charged and therefore we see a general trend of energy loss (negative slope) over repeated charge/discharge cycles. This trend indicates a cyclic energy efficiency of less than 100% and therefore an opportunity to identify the power loss as a variable for comparison. The power loss associated with this test, $P_{cycling}$, is represented by the rate of energy loss and is determined from the slope of the orange line. Using Equation 7, an equivalent series resistance associated with Test 1 is determined and recorded in Table 7.

$$R_{ESR,\ Test1}[\Omega] = \frac{P_{cycling}[W]}{I^2_{cycling,\ RMS}[A]}$$

Equation 7: Test 1 ESR calculated from cell cycling energy loss

Cell ID	A EDLC	B EDLC	B No T.C[13] EDLC	C LiC	D LiC	E LiC	F LiC	G ||LiC
Number of cycles	63	75	75	38	10	13	50	N/A
Cycling Energy Slope [Wh/s]	-1.07E-3	-8.58E-4	-8.39E-4	-4.90E-4	-9.97E-4	-1.06E-3	-3.32E-4	N/A
Cycling Energy Slope [W]	-3.87	-3.09	-3.02	-1.76	-3.59	-3.83	-1.19	N/A
Intercept [Wh]	-1.30	-1.11	-1.13	-1.89	-15.64	-8.48	-0.59	N/A
$I_{RMS\ Cycling}$ [A][14]	87.24	94.06	94.11	31.49	53.80	35.30	13.65	N/A
Commanded Cycling Current	90	97	97	32	54	35.5	14	N/A
Datasheet ESR [mOhm]	0.27	0.23	0.23	1	0.35	0.8	5	1
$R_{ESR,\ Test1}$ [mOhm][15]	0.51	0.35	0.34	1.78	1.24	3.07	6.41	N/A
Theoretical Loss[16] [W]	2.05	2.03	2.04	0.99	1.01	1.00	0.93	N/A

Table 7: Calculated energy loss and equivalent series resistance from Test 1.

[13] Test on Cell B repeated without the thermal chamber (T.C) operating to maintain the ambient temperature. Starting ambient temperature ~ 23.5^{0}C, ending ambient temperature ~ 28^{0}C

[14] RMS cycling current from time zero until end of cycling (approx. 3.5 hours), does not include zero current from the 2.5-hour cell cool down phase

[15] ESR calculated using the change in energy over time during continuous cycling. Uses Equation 7.

[16] Theoretical loss = $I_{RMS\ Cycling}$ * $I_{RMS\ Cycling}$ * Datasheet ESR

Recall from Section 5.4 that the cells were cycled using a current value that would result in approximately 2.15W of I^2R losses for EDLC cells and approximately 1W of I^2R losses for LiC cells. Table 7 show that the theoretical loss values calculated using the RMS cycling current and datasheet listed ESR closely match the desired 1W for LiC cells but are approximately 0.1W less than desired for the EDLC cells. The discrepancy for EDLC cells extends from the difference between the commanded cycling current and RMS cycling current. The cycling profile for EDLC Cell A used a commanded 2 second pause between the transition from charging to discharging and vice versa while all other cells used a commanded 1 second pause. It should be noted that although the data for Test 1 was logged at 0.5 Hz (one sample every two seconds), Cell A has a near zero current value for three sample points (6 seconds) and the other cells have a near zero current value for two sample points (4 seconds). The additional near zero current sample point is a result of the power supply transitioning from the desired testing current to zero amps while in a "Constant Current" command. This result is shown in Table 8 and Table 9 as an example.

Time [s]	Command	Cell Voltage [V]	Testing Current [A]
174	Constant Current	0.245209	90.00004
176	Constant Current	0.169335	90.00119
178	Constant Current	0.09343	89.99842
180	Constant Current	0.068855	-0.8652
182	Standby	0.072267	0
184	Standby	0.074342	0
186	Constant Current	0.145592	-93.3157
188	Constant Current	0.22628	-89.7248
190	Constant Current	0.306062	-89.6011
192	Constant Current	0.385065	-89.6712

Table 8: Select data from Test 1 for Cell A

Time [s]	Command	Cell Voltage [V]	Testing Current [A]
310	Constant Current	0.214418	96.999118
312	Constant Current	0.136686	96.999108
314	Constant Current	0.059022	96.998888
316	Constant Current	0.06024	-0.292485
318	Standby	0.062642	0
320	Constant Current	0.118551	-96.446569
322	Constant Current	0.201176	-97.030718
324	Constant Current	0.282879	-97.039925
326	Constant Current	0.363739	-97.032034

Table 9: Select data from Test 1 for Cell B

The RMS cycling current is determined by taking the RMS value of all current values during the approximate 3.5 hour cycling period and not the relaxation period. Considering that the number of cycles were xecuted in integer values the actual cycling time for each cell varies slightly. Therefore, the time used to calculate the RMS current and energy loss slope is modified for each cell. However, the author believes that the discrepancy between the RMS cycling current and commanded current is largest for cells with high cycle counts due to the introduction of additional near zero amp data log points. For example, the cycling period for Cell A occupied 5805 samples (11610 seconds) with approximately 327 samples (654 seconds) within the range of -2A to +2A. In the case of Cell A, the near non zero amp samples represent approximately 5.6% of sample points and therefore the RMS current value is shown to be considerably less, approximately 3%, than the commanded current value. In the case of Cell C, the near non-zero amp samples within the range of -2A to +2A represent approximately 2.9% of all samples and the RMS current value is shown to be similar, within 1.6%, of the commanded value. Although the discrepancy between the desired current command and RMS testing current exists, the author continued to use this method to analyze the energy loss and $R_{ESR,\ Test1}$ for the following reasons:

- The theoretical loss values from Table 7 are within a maximum error of approximately 7% compared to the respective desired loss values of 2.15W and 1 W.
- The energy loss slope and RMS current are calculated over the entire cycling period and therefore the energy loss slope and RMS current both consider the near zero current data entries.
- Test 1 is an atypical method to determine a cell's DC ESR and therefore a considerable difference between the datasheet and experimentally determined values may exist.
- The purpose of this chapter is to provide a high-level comparison between the EDLC and LiC based cell performance. Considering that all of the cells are compared using a very similar testing profile in Test 1, the author believes a comparison between the cells using this data is reasonable. Therefore, the $R_{ESR,\ Test1}$ values in Table 7 should be compared between cells but not to the datasheet values.

5.5.3. Test 1 Analysis – Temperature Rise

Figure 28 and Figure 29 show the cycling current in orange, the thermal chamber temperature in solid blue and multiple cell surface temperature measurements in blue patterns. These plots show the cell temperature rises to a near steady state range via a repeating temperature rise and fall profile that aligns with the changes in current direction (charge vs. discharge) and resembles plots in [98]. Subplots A and B of Figure 28 show the cell surface cooling during a relaxation period when the cycling current is 0A. However, Subplot C, which displays data for testing Cell B without the thermal chamber maintaining the ambient temperature, hits the programmed maximum cell temperature limit and therefore data recording is stopped during the relaxation period. The temperature change from the start of charge/discharge cycling and the average cell surface temperature when the relaxation begins is recorded in Table 10 as ΔT [^{o}C]. This temperature change is used in Table 10 to determine a case to ambient thermal

resistance, $R_{CA}[℃/W]$, based on the datasheet ESR and $R_{ESR,\ Test1}[\Omega]$. The results are recorded in Table 10.

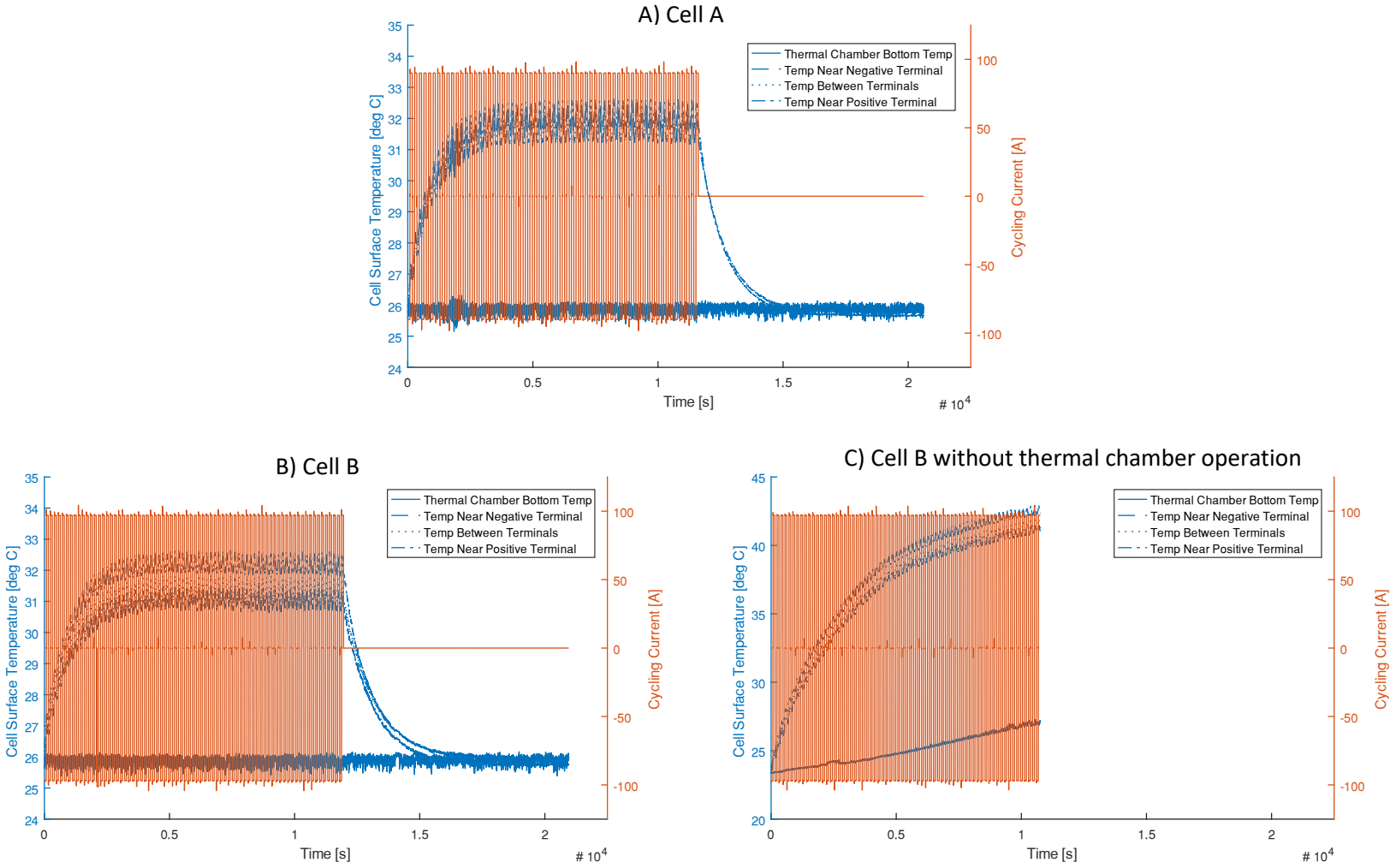

Figure 28: Cell temperature rise from repeated charge / discharge cycles – Cells A and B

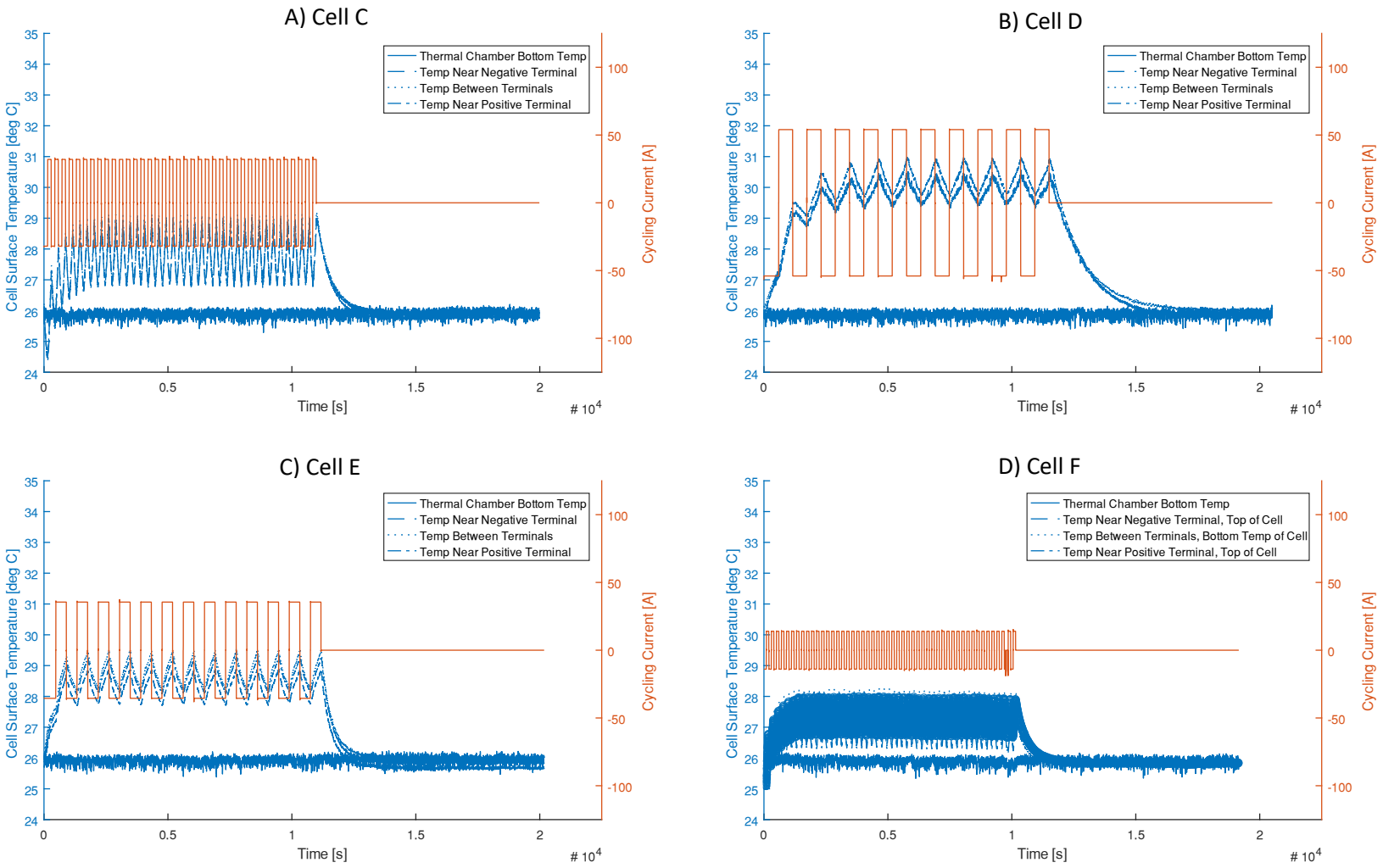

Figure 29: Cell temperature rise from repeated charge / discharge cycles – Cells C thru F

$$R_{CA}[℃/W] = \frac{\Delta T\ [℃]}{I^2_{cycling,\,RMS}[A] * ESR[\Omega]}$$

Equation 8: Cell case to ambient thermal resistance determined using the change in temperature, ESR and cycling current

Cell ID	A EDLC	B EDLC	B No T.C[13] EDLC	C LiC	D LiC	E LiC	F LiC	G ||LiC
$I_{RMS\ Cycling}$ [A][14]	87.24	94.06	94.11	31.49	53.80	35.30	13.65	N/A
$R_{ESR,\ Test1}$ [mOhm][15]	0.51	0.35	0.34	1.78	1.24	3.07	6.41	N/A
Datasheet ESR [mOhm]	0.27	0.23	0.23	1	0.35	0.8	5	1
ΔT [°C][17]	6.57	5.99	18.9[21]	1.9	4.1	2.8	1.5	N/A
$R_{CA,\ RESR,Test1}$ [°C/W][18]	1.69	1.93	6.28	1.08	1.14	0.73	1.26	N/A
$R_{CA,\ Datasheet\ ESR}$ [°C/W][19]	3.20	2.94	9.28	1.92	4.05	2.81	1.61	N/A
ΔTemp During Discharge[20]	Decrease	Decrease	Decrease	Increase	Increase	Increase	Increase	N/A
ΔTemp During Charge[20]	Increase	Increase	Increase	Decrease	Decrease	Decrease	Decrease	N/A

Table 10: Temperature rise, ESR and calculated case to ambient thermal resistance results

[15] ESR calculated using the change in energy over time during continuous cycling. Uses Equation 7.
[17] Temperature change from start of cycling test to the average temperature of the highest reading thermistor at the end of cycling.
[18] Thermal resistance from case to ambient calculated using calculated ESR from cycling energy loss (row with note 15)
[19] Thermal resistance from case to ambient calculated using ESR from datasheet
[20] During a positive cycling current (discharging) the cell temperature will increase or decrease until the current becomes negative (charging)
[21] Due to programmed temperature limits, this test was stopped and the cell does not reach a steady state temperature.

5.5.4. Test 1 Conclusions

The following conclusions are made using data available in Table 7, Table 10 and Figure 26 thru Figure 29.

- As shown by Cell B in Figure 28 Subplots B and C, the temperature change from cycling is highly dependant on the thermal chamber turbulent air acting as a forced air-cooling system. The cell temperature increased approximately 5.99°C with the thermal chamber in operation at a setpoint of 25 °C. However, without the thermal chamber in operation, the cell temperature increased by 18.9°C at which point the testing ended due to hitting the cell maximum testing temperature programmed in the custom tester. Figure 28 Subplot C shows an increase in the thermal chamber temperature while Subplot B does not. This shows that the thermal chamber is removing heat from the cell while in

operation because the thermal chamber temperature does not rise while the cell expels heat losses.

- However, the cycling energy slope for Cell B in Figure 26 Subplot C (thermal chamber circulation fans off) is 97.7% the result in Subplot A (thermal chamber circulation fans on). This result suggests that the energy loss in cell cycling has very little dependency on the cooling system, assuming the ESR is not highly temperature dependant, and therefore $R_{ESR,\ Test1}$ calculations are less affected by active cooling than R_{CA} calculations.
- $R_{ESR,\ Test1}$ values are consistently larger than the datasheet ESR, in the range of 128.2% to 383.8%, therefore suggesting further investigation into quantifying the ESR using other testing methods.
- Cell E has the lowest $R_{CA,\ RESR,Test1}$ which may be the result of a large pouch cell surface area without a compression fixture. Otherwise, there is no clear trend to compare the thermal case to ambient resistance for the cells.
- The LiC cells experienced a surface temperature decrease while charging and a surface temperature increase while discharging. This result aligns with the endothermic charging results obtained in [99].
- The EDLC cells experienced a surface temperature increase while charging and a surface temperature decrease while discharging, which aligns with the exothermic charging and endothermic discharging results obtained in [98].
- The difference between the LiC cells charging endothermically and the EDLC cells charging exothermically may be the result of the different desired I^2R losses. Both cells may exhibit endothermic (temp. decrease) charging at low currents but the EDLC losses (2.15W) may exceed the endothermic effects. Additional analysis with different cycling

currents is needed to determine if the EDLC cells charge exothermically and LiC cells charge endothermically at all charging currents.

5.6. Test 2 – Constant Current Capacity and Energy

The purpose of test 2 is to evaluate how the useful charge and discharge capacity of each cell changes with the testing current and temperature. In Test 2 each capacitor cell was charged and discharged using a variety of constant current tests, in the range of 2A to 120A, while subjected to multiple operating temperatures in the range of -10°C to 35°C. A 2A charge and discharge profile were used to identify the cell's low current terminal voltage vs state of charge characteristics. The results below discuss how the useful capacity and energy that can be stored or discharged from the cells changes with temperature.

5.6.1. Test 2 Method

Test 2 was performed after the completion of the 2.5 hour resting period from Test 1. However, if the testing temperature was not set at 25°C then the testing procedure began at Test 2 with a several hour-long thermal saturation period to change the capacitor temperature. The cell was discharged to the minimum testing voltage using several low current discharge phases until the cell reaches a discharged state using a 0.25 A discharge current. The capacity counter was reset to 0Ah and the cell was considered to be at 0% SOC. The cell was then charged using a constant current that is dependent on the testing conditions. This charging process continued until the cell terminal voltage reaches the maximum cell voltage as listed in Table 5. The capacity, measured in Ah, and energy, measured in Wh, used to charge the cell is noted as the useful charging capacity/energy for the given test current and testing temperature. Considering the voltage increase above the cell's open circuit voltage during charging, the cell may have not reached a complete charge during the constant current charging phase. For this reason, the cell was charged using a CCCV charging profile until the maximum cell voltage is achieved and the charging current reduced below a cut-off condition of 100mA or less. Upon completion of the

full charge and an additional 15 second pause, the capacity counter was reset to 0Ah and a constant current discharge is initiated. The constant current discharge terminated when the cell hit the minimum testing voltage from Table 5. Considering that the cell was nearly fully discharged, the next charge and discharge cycle began with a cell discharge process to reset the cell at 0% SOC. This process was repeated using constant current charge and discharge currents of 2A, 25A, 50A, 75A, 100A and 120A, where allowed by the cell testing limits. Upon the completion of all constant current charge and discharge cycles, the autocycler proceeded to perform Test 3.

5.6.2. Test 2 Analysis – 2A Charge and Discharge Voltage Profile

The open circuit voltage (OCV) vs state of charge (SOC) profile for battery cells is typically derived using a relatively small constant current in the approximate range of 1/20 C to 1/25 C. This corresponds to a full charge and discharge cycle that requires approximately 40 to 50 hours to complete. Considering the large quantity of cells characterized in this work the time required to complete five 50-hour charge and discharge cycles per cell was unrealistic. As an alternative, the author used a 2A charge and discharge current to examine the cell voltage vs state of charge characteristics. While this method is not representative of a typical open circuit voltage vs SOC that use 1/25 C rates, the 2A test provided insight into the cell voltage characteristics regarding linearity and hysteresis.

The 25^{o}C 2A charge and discharge voltage profiles vs capacity for all seven cells are shown in Figure 30. The legend in Figure 30 show the charging/discharging C-rate using the capacity measured from each charge/discharge test that is equivalent to a test current of 2A. As shown in Figure 30 and Table 5, Cell G has a charging capacity (1.668 Ah) that is considerably larger than the discharging capacity (1.528 Ah). Therefore, the charging C-rate is smaller (1.2C) than the discharging C-rate (1.31C).

As an extension to Figure 30, the data in Figure 31 and Figure 32 shows the 25°C 2A charge and discharge terminal voltage vs state of charge relationships, respectively. The capacity data from Figure 30 is normalized by the respective measured charged and discharged capacity to present the data as a function of state of charge instead of capacity. It should be noted that the normalizing capacities used for each cell in Figure 31 and Figure 32 are not necessarily equal. Therefore, Cell G shows a voltage profile to 100% SOC in both plots even though the normalizing capacities are unequal.

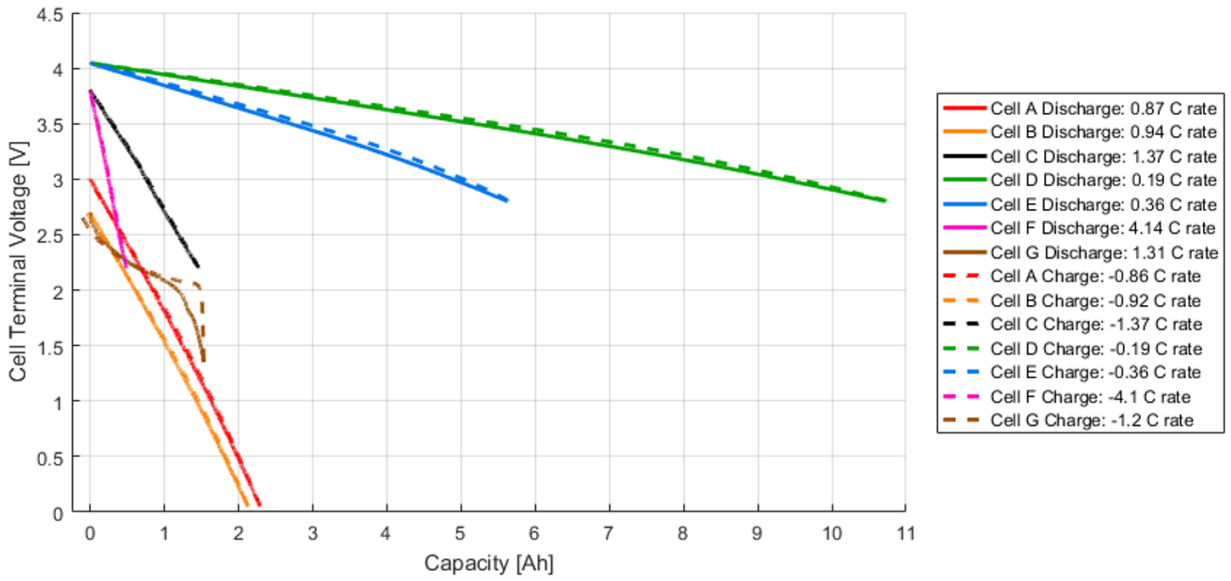

Figure 30: Cell terminal voltage vs capacity measured using a 2A constant current charge and discharge profile at 25°C

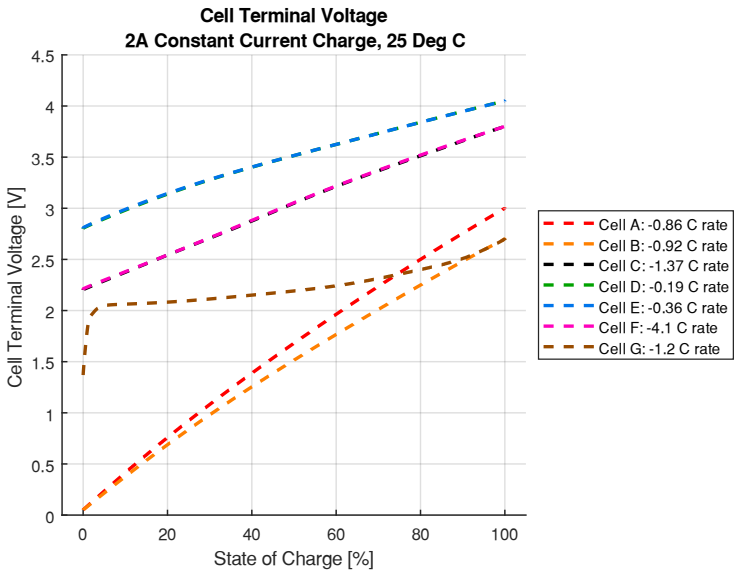

Figure 31: Cell terminal voltage vs state of charge measured using a 2A constant current charge profile and normalized by the measured charging capacity at 25°C

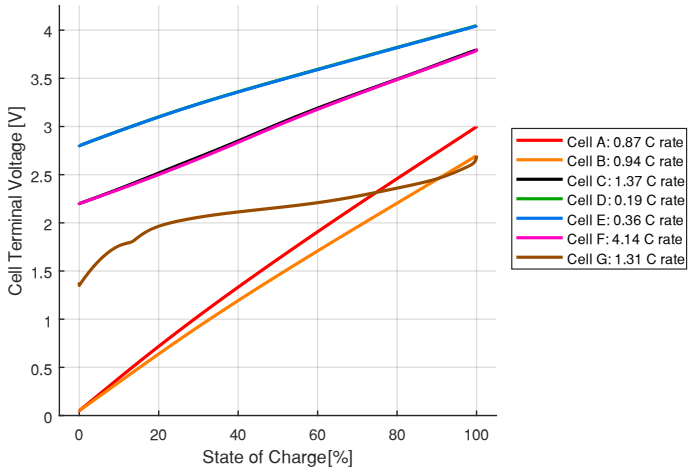

Figure 32: Cell terminal voltage vs state of charge measured using a 2A constant current discharge profile and normalized by the measured discharging capacity at 25°C

Figure 30 to Figure 32 show the 2A charge and/or discharge profile for all seven cells when tested at 25°C. Figure 33 shows the 2A charge and discharge terminal voltage vs capacity profile for each cell when tested at -10°C, 0°C, 10°C, 25°C, and 35°C. The charging profiles are noted by dashed lines on the left-side plots while the discharging profiles are noted by solid lines on the right-side plots. Although unconventional, the subplots in Figure 33 include titles that contain

the equivalent C-rate used for charging / discharging. Table 11 compares the 2A measured charge and discharge capacity of each cell at 10°C and 35°C.

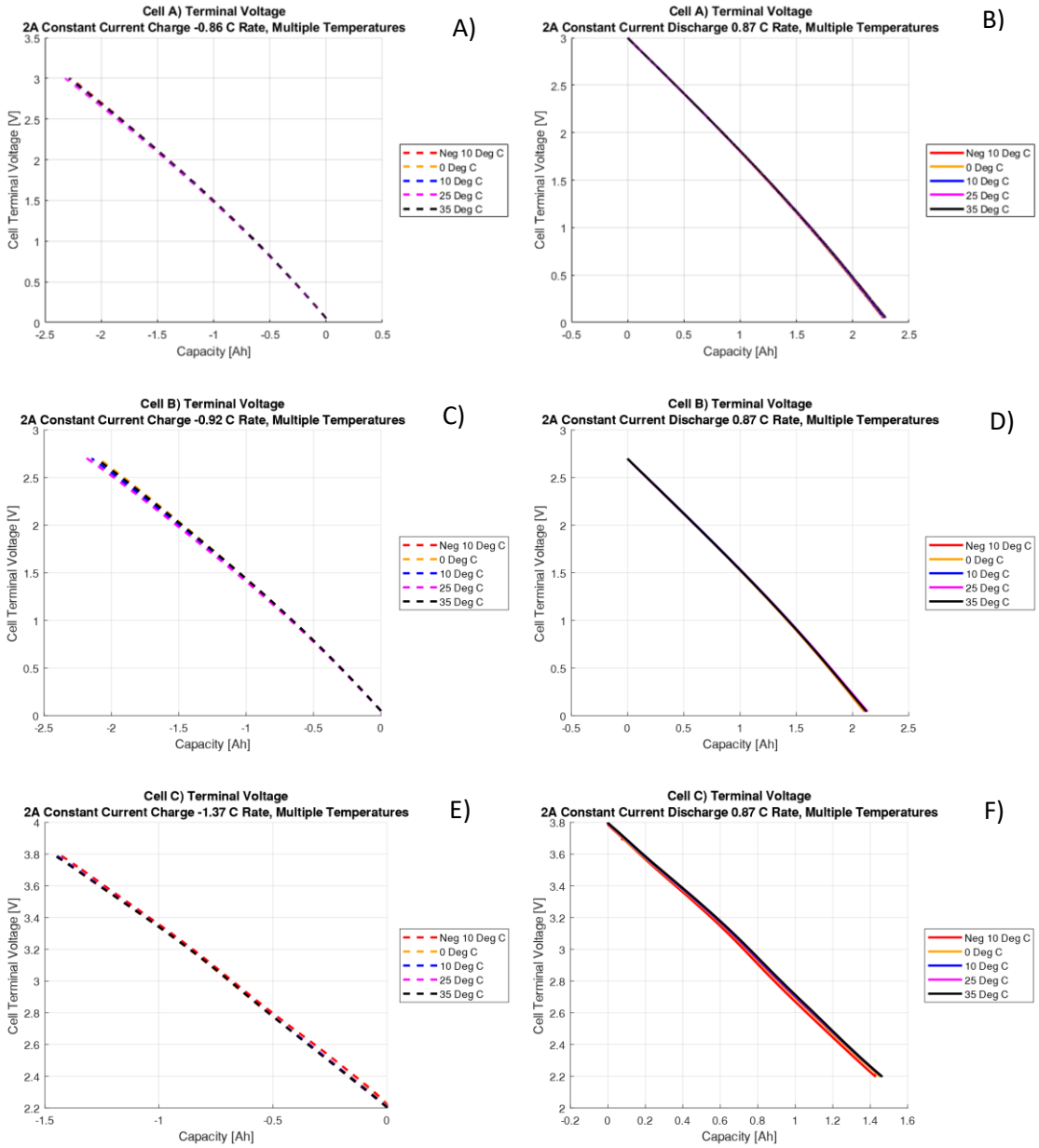

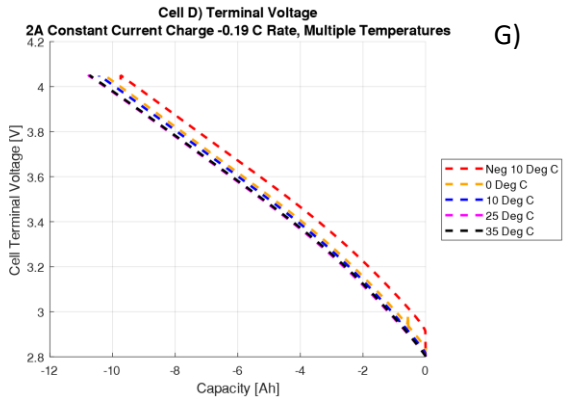
Cell D) Terminal Voltage
2A Constant Current Charge -0.19 C Rate, Multiple Temperatures
Cell Terminal Voltage [V]
Capacity [Ah]
Neg 10 Deg C
0 Deg C
10 Deg C
25 Deg C
35 Deg C

G)

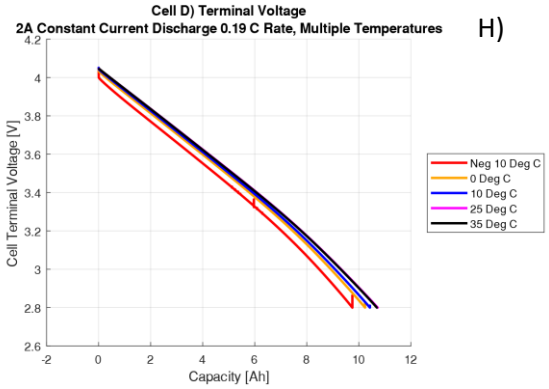
Cell D) Terminal Voltage
2A Constant Current Discharge 0.19 C Rate, Multiple Temperatures
Cell Terminal Voltage [V]
Capacity [Ah]
Neg 10 Deg C
0 Deg C
10 Deg C
25 Deg C
35 Deg C

H)

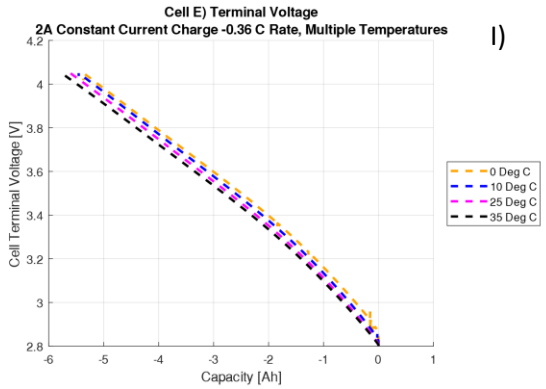
Cell E) Terminal Voltage
2A Constant Current Charge -0.36 C Rate, Multiple Temperatures
Cell Terminal Voltage [V]
Capacity [Ah]
0 Deg C
10 Deg C
25 Deg C
35 Deg C

I)

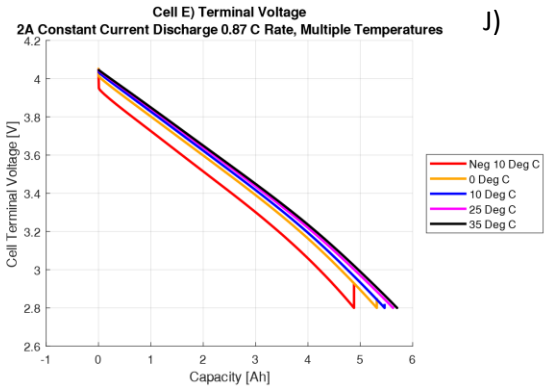
Cell E) Terminal Voltage
2A Constant Current Discharge 0.87 C Rate, Multiple Temperatures
Cell Terminal Voltage [V]
Capacity [Ah]
Neg 10 Deg C
0 Deg C
10 Deg C
25 Deg C
35 Deg C

J)

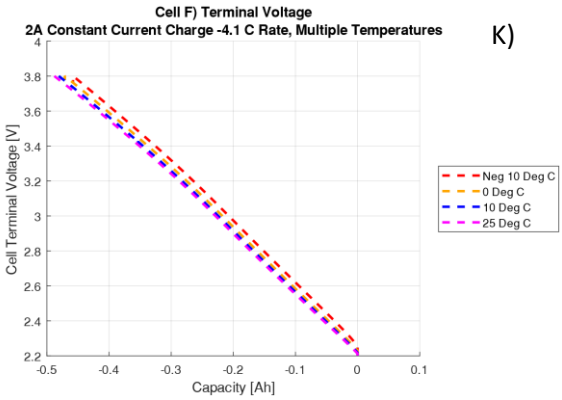
Cell F) Terminal Voltage
2A Constant Current Charge -4.1 C Rate, Multiple Temperatures
Cell Terminal Voltage [V]
Capacity [Ah]
Neg 10 Deg C
0 Deg C
10 Deg C
25 Deg C

K)

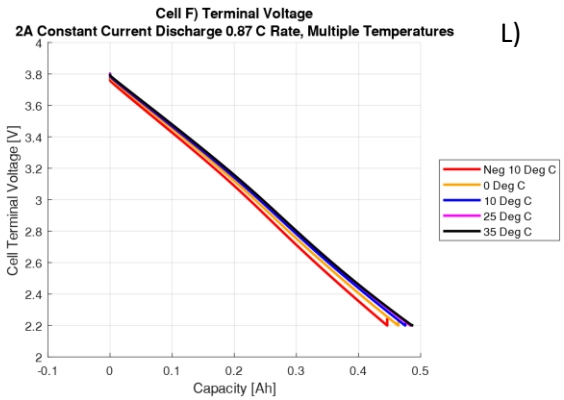
Cell F) Terminal Voltage
2A Constant Current Discharge 0.87 C Rate, Multiple Temperatures
Cell Terminal Voltage [V]
Capacity [Ah]
Neg 10 Deg C
0 Deg C
10 Deg C
25 Deg C
35 Deg C

L)

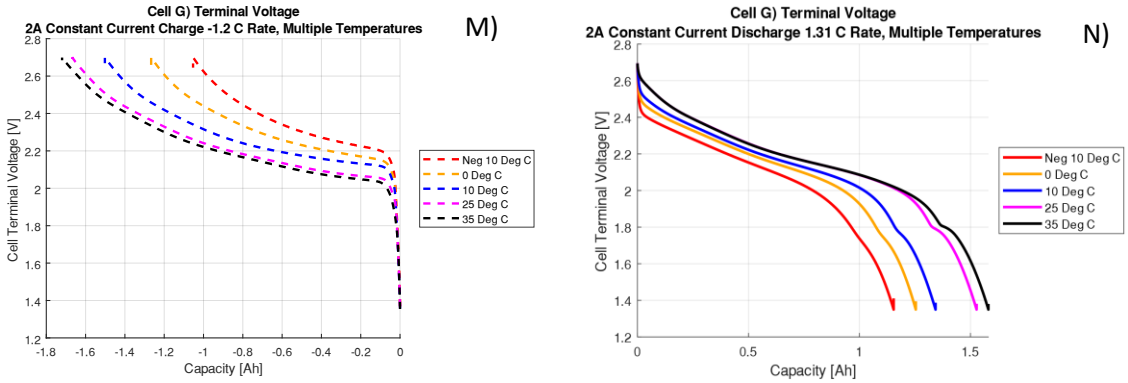

Figure 33: Charge and discharge terminal voltage vs capacity characteristics for each cell tested at -10°C, 0°C, 10°C, 25°C, and 35°C.

Discharge / Charge capacity [Ah]	A EDLC	B EDLC	C LiC	D LiC	E LiC	F LiC	G ||LiC
@ Neg 10°C [Ah]	2.269 / -2.268	2.102 / -2.100	1.425 / -1.440	9.753 / -9.741	4.880 / -4.783	0.446 / -0.458	1.154 / -1.053
@ 35°C [Ah]	2.292 / -2.284	2.119 / -2.113	1.461 / -1.467	10.696 / -10.731	5.702 / -5.767	0.486 / -0.302[22]	1.581 / -1.720
$\frac{Ah\ @\ Neg\ 10^oC}{Ah\ @\ 35^oC} * 100\%$ [%]	99.0 / 99.3	99.2 / 99.4	97.5 / 98.2	91.2 / 90.8	85.6 / 82.9	91.6 / 152.7[22]	73.0 / 61.2

Table 11: Comparison of the 2A discharge (left number) and charge (right number) measured capacity at -10°C and 35°C.

[22]The charge capacity of 0.302 Ah at @ 35°C is inconsistent with other results and therefore should not be used for comparison

5.6.3. Test 2 Analysis – Multi-Temperature and Multi-Constant Current Useful Capacity and Energy Measurement

Section 5.6.2 focused on displaying the 2A charge/discharge voltage profile and their dependency, or lack of, on temperature. This section further analyzes the multi-current and variable temperature capacity and energy measurements from Test 2 by displaying the total useful capacity and energy measured vs. the cycling current. The test results are displayed in Figure 34. Left-side plots show the cell's normalized charge/discharge capacity [%, base unit of Ah] while the right-side plots show the normalized charge/discharge energy [%, base unit of Wh]. Similar to Figure 33, the subplots in Figure 34 contain titles that identify the cell and normalizing capacity/energy. Due to current and charging temperature limits some plots contain less testing data. Table 12 provides a comparison of the normalized usable capacity and energy for each cell under two specific testing cases.

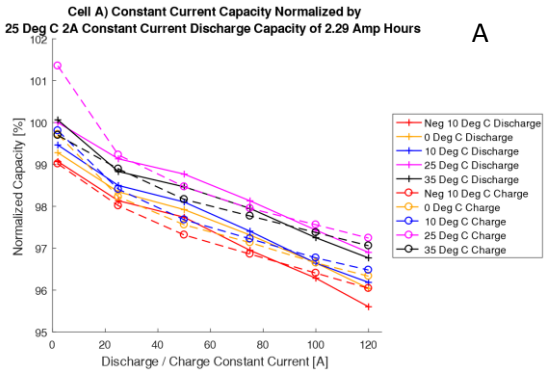
Cell A) Constant Current Capacity Normalized by
25 Deg C 2A Constant Current Discharge Capacity of 2.29 Amp Hours
Normalized Capacity [%]
Discharge / Charge Constant Current [A]
Neg 10 Deg C Discharge
0 Deg C Discharge
10 Deg C Discharge
25 Deg C Discharge
35 Deg C Discharge
Neg 10 Deg C Charge
0 Deg C Charge
10 Deg C Charge
25 Deg C Charge
35 Deg C Charge

A

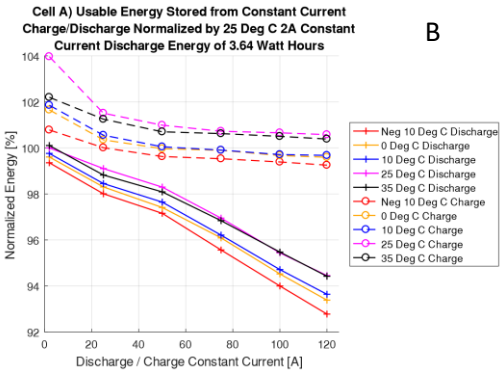
Cell A) Usable Energy Stored from Constant Current
Charge/Discharge Normalized by 25 Deg C 2A Constant
Current Discharge Energy of 3.64 Watt Hours
Normalized Energy [%]
Discharge / Charge Constant Current [A]
Neg 10 Deg C Discharge
0 Deg C Discharge
10 Deg C Discharge
25 Deg C Discharge
35 Deg C Discharge
Neg 10 Deg C Charge
0 Deg C Charge
10 Deg C Charge
25 Deg C Charge
35 Deg C Charge

B

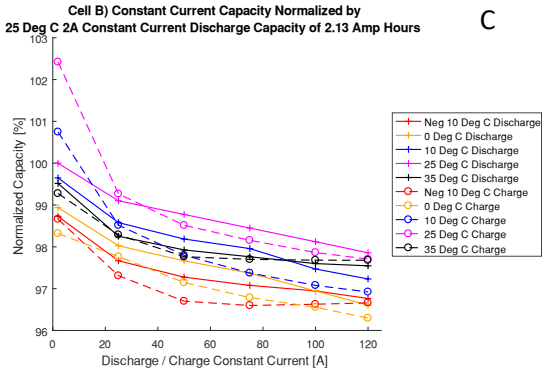
Cell B) Constant Current Capacity Normalized by
25 Deg C 2A Constant Current Discharge Capacity of 2.13 Amp Hours
Normalized Capacity [%]
Discharge / Charge Constant Current [A]
Neg 10 Deg C Discharge
0 Deg C Discharge
10 Deg C Discharge
25 Deg C Discharge
35 Deg C Discharge
Neg 10 Deg C Charge
0 Deg C Charge
10 Deg C Charge
25 Deg C Charge
35 Deg C Charge

C

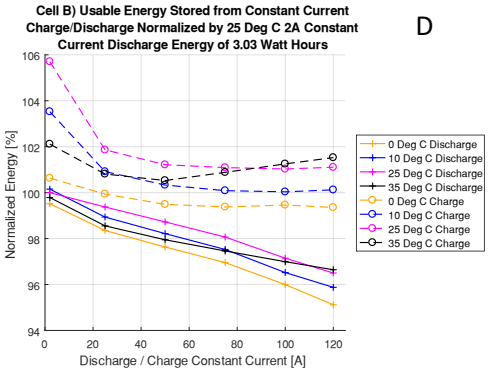
Cell B) Usable Energy Stored from Constant Current
Charge/Discharge Normalized by 25 Deg C 2A Constant
Current Discharge Energy of 3.03 Watt Hours
Normalized Energy [%]
Discharge / Charge Constant Current [A]
0 Deg C Discharge
10 Deg C Discharge
25 Deg C Discharge
35 Deg C Discharge
0 Deg C Charge
10 Deg C Charge
25 Deg C Charge
35 Deg C Charge

D

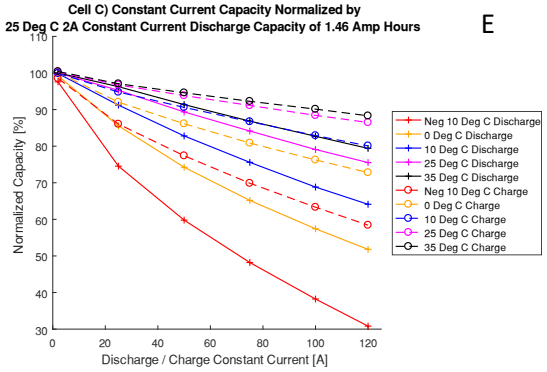
Cell C) Constant Current Capacity Normalized by
25 Deg C 2A Constant Current Discharge Capacity of 1.46 Amp Hours
Normalized Capacity [%]
Discharge / Charge Constant Current [A]
Neg 10 Deg C Discharge
0 Deg C Discharge
10 Deg C Discharge
25 Deg C Discharge
35 Deg C Discharge
Neg 10 Deg C Charge
0 Deg C Charge
10 Deg C Charge
25 Deg C Charge
35 Deg C Charge

E

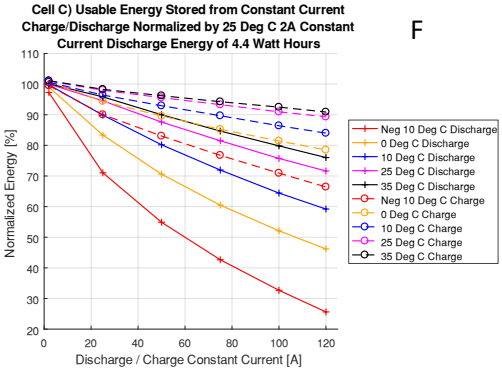
Cell C) Usable Energy Stored from Constant Current
Charge/Discharge Normalized by 25 Deg C 2A Constant
Current Discharge Energy of 4.4 Watt Hours
Normalized Energy [%]
Discharge / Charge Constant Current [A]
Neg 10 Deg C Discharge
0 Deg C Discharge
10 Deg C Discharge
25 Deg C Discharge
35 Deg C Discharge
Neg 10 Deg C Charge
0 Deg C Charge
10 Deg C Charge
25 Deg C Charge
35 Deg C Charge

F

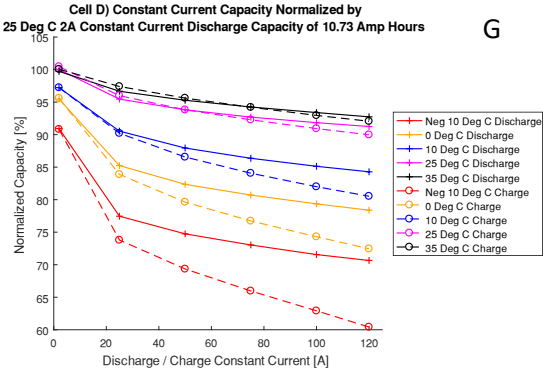
Cell D) Constant Current Capacity Normalized by
25 Deg C 2A Constant Current Discharge Capacity of 10.73 Amp Hours
Normalized Capacity [%]
Discharge / Charge Constant Current [A]
Neg 10 Deg C Discharge
0 Deg C Discharge
10 Deg C Discharge
25 Deg C Discharge
35 Deg C Discharge
Neg 10 Deg C Charge
0 Deg C Charge
10 Deg C Charge
25 Deg C Charge
35 Deg C Charge

G

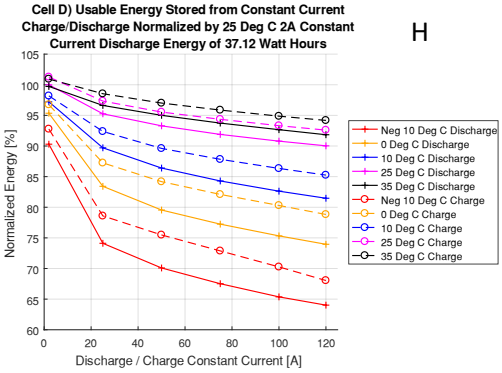
Cell D) Usable Energy Stored from Constant Current
Charge/Discharge Normalized by 25 Deg C 2A Constant
Current Discharge Energy of 37.12 Watt Hours
Normalized Energy [%]
Discharge / Charge Constant Current [A]
Neg 10 Deg C Discharge
0 Deg C Discharge
10 Deg C Discharge
25 Deg C Discharge
35 Deg C Discharge
Neg 10 Deg C Charge
0 Deg C Charge
10 Deg C Charge
25 Deg C Charge
35 Deg C Charge

H

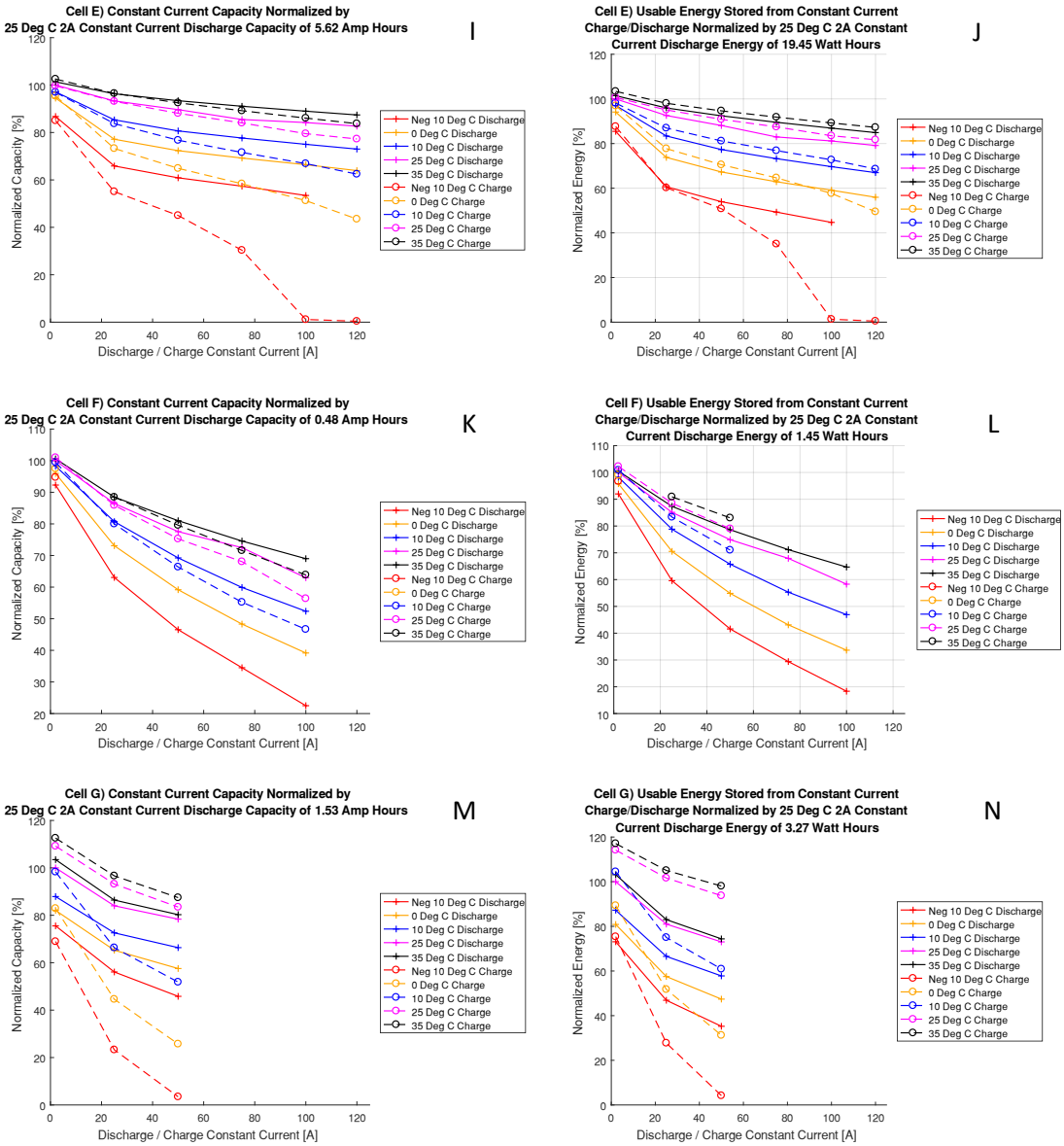

Figure 34: Measured useful capacity and energy from constant current charge and discharge profiles as a function of testing current and temperature

Test Condition	Normalized Measurement	A EDLC	B EDLC	C LiC	D LiC	E LiC	F LiC	G ||LiC
100A, 0°C, Discharge	Capacity [%]	96.7	97.0	57.4	79.4	66.4	39.2	N/A
	Energy [%]	94.5	96.0	52.1	75.3	59.1	33.7	N/A
50A, 10°C Charge	Capacity [%]	97.7	97.8	90.6	86.6	76.7	66.4	51.8
	Energy [%]	100	100	93.0	89.6	81.2	71.0	60.9

Table 12: Two specific test conditions with the measured capacity and energy normalized by the cell's 25°C 2A constant current discharge capacity/energy. The normalized values are obtained from data in Figure 34.

5.6.4. Test 2 Conclusions

The following conclusions are made using information from Section 5.6.2.

- Figure 30 shows that EDLC Cells A and B have a linear 2A charge and discharge profile with little to no hysteresis. LiC Cells C, D, E and F have a near linear 2A charge and discharge profile with a small amount of hysteresis. However, ||LiC Cell G has a very non-linear 2A charge and discharge voltage profile with a unique "knee" in the discharge profile near 85% depth of discharge and considerable hysteresis near the minimum cell voltage.
- Table 11 shows that the 2A charge/discharge capacity (Ah) for EDLC Cells A and B barely changed with temperature (minimum 99%) while LiC Cells C, D, E and F experienced minor capacity change (between 82.9% and 98.2% retained). However, ||LiC Cell G experienced a large capacity change from -10°C to 35 °C (between 62.2% and 73% retained). Figure 33 Subplots M and N shows a considerable change in Cell G's terminal voltage curve as a function of temperature for both the charge and discharge cycles. Figure 33 Subplots M and N further highlight the unique discharge "knee" and considerable hysteresis near the minimum cell voltage. The discharge voltage "knee" appears to decrease in size as the temperature is reduced. Cell G's charge/discharge profile temperature dependency may require additional testing to evaluate if the cell voltage changes while submitted to thermal cycles during storage (no intentional capacity change). Additionally, this temperature dependency may introduce the need for an advanced temperature dependent open circuit vs. SOC model for Cell G.

The following conclusions are made from information in Section 5.6.3.

- For all seven cells the charging energy is typically larger in magnitude than the discharge energy at a given temperature and cycling current. This indicates a cyclic energy efficiency of less than 100% for all cells.
- In Figure 34 EDLC Cells A and B, show a worst-case normalized capacity and energy all greater than 92% (Subplot B). In general, the worst-case normalized capacity and energy for Subplots E thru N, which correspond to LiC Cells C thru F and ||LiC Cell G, show a significantly lower normalized capacity and energy; in the approximate range of 5% to 65%.
- The two specific test cases in Table 12 show that the EDLC cells have the largest normalized capacity and energy (least affected by high current testing at low temperatures), followed by the LiC cells and then the ||LiC cell which is the lowest. Comparatively speaking, the useful energy stored for the EDLC cells is minimally affected by temperature, while the LiC cells and ||LiC are considerably affected by temperature. This trend will be further explored in Section 5.7.4 by analysing the cell's internal resistance as a function of temperature.

5.7. Test 3 – Hybrid Pulse Power Characterization (HPPC)

This section makes use of a modified version of the hybrid pulse power characterization testing method described in [97] to identify the cell's equivalent series resistance as a function of state of charge, temperature and pulse current magnitude. Rather than identifying a single equivalent series resistance value using an energy loss model, as done in Section 5.5, Test 3 aims to expose each cell to a large variety of feasible operating conditions to explore how the ESR changes with state of charge, temperature and testing current. The large quantity of ESR data points are averaged to produce a representative ESR for specific conditions.

5.7.1. Test 3 Method

The custom cycler testing commands are programmed as part of the Excel based autocycler profile discussed in Section 5.4 and were executed upon the completion of Test 2. If applicable, Tests 1, 2, and 3 were executed sequentially all at one testing temperature. Upon completion of Test 3 the thermal chamber temperature was changed to the next testing temperature and the set of tests performed on the custom MARC cell cycler were repeated.

Hybrid power pulse characterization, commonly called HPPC, consists of a series of short charge and discharge current pulses performed under different operating conditions to create an opportunity for a change in the cell behaviour. For example, the short pulses may be executed at increments of 10% SOC to see how the cell behaves in response to charging and discharging pulses depending on the state of charge. The main purpose of HPPC testing is to use the change in cell voltage during the current pulse, which should cause a negligible change in SOC, to determine the cell's equivalent series resistance (ESR) under the operating conditions studied. The ESR is typically calculated using an equation similar to Equation 9, however the way in which ΔV and ΔI are defined can vary by the study.

$$ESR_{HPPC}[\Omega] = abs\left(\frac{\Delta V}{\Delta I}\right)$$

Equation 9: Simple formulation to calculate the HPPC ESR

Figure 35 shows the change in cell terminal voltage for Cells A thru F from a 50A discharge pulse when charged to 45% and operating in a controlled 25°C environment. The data from Cell F (pink lines) in Figure 35 will be used to explain a variety of methods to determine the ESR based on how ΔV and ΔI are defined. Note that the left side vertical axis shows the change in cell voltage rather than the actual cell voltage. Considering the variety in terminal voltages among the cells that represent 45% SOC, the left side vertical axis was modified to better show how the cell voltage changes from a common SOC reference. The cell terminal voltage is noted with "+"

marks while the discharging current is identified by "x" marks and corresponds to the right side vertical axis. In this work, the time before the current pulse starts is referred to as the pre-pulse relaxation time. The pre-pulse relaxation time is necessary to ensure that the cell voltage has stabilized and is representative of the desired SOC operating condition. During the current pulse, from approximately -1.5 to 0 seconds, the cell voltage decreases. This decrease is noted by the combination of ΔV_1 and ΔV_2. ΔV_1 typically represents the initial voltage change due to current collector resistance, electrolyte conductivity and separator resistance. Considering the very small time step during the ΔV_1 phase, the current discharging the cell has a negligible impact on the SOC and therefore the open circuit voltage. It is therefore assumed that the change in cell voltage noted by ΔV_1 may represent the cell's equivalent series resistance for that operating point. However, depending on the energy storage device, especially batteries with additional chemical reactions, the time duration used to define ΔV_1 becomes more difficult to select as the cell voltage changes in a more continuous and curved manner rather than the sharp change shown in Figure 35. For this reason, the ΔV_1 value is not used to represent ΔV from Equation 9 in this work. The next logical approach would be to look at the combined voltage change from $\Delta V_1 + \Delta V_2$. Recall that the HPPC pulse currents should stimulate the cell to cause a voltage change while minimizing the change in SOC during the charging/discharging pulse. For example, a 50A discharge pulse with a duration of 2.5 seconds would discharge the cell by approximately 0.0347 Ah. While this capacity change is relatively small, it represents approximately 7% the capacity of Cell F, which has the smallest capacity (approximately 0.5Ah) of all the cells tested. This can be shown in Figure 35 such that the largest change in cell voltage during the ΔV_2 phase occurs on the pink line that represents Cell F. It should be noted that the voltage change profile during the ΔV_2 phase is rather non-linear. This non-linearity may be the result of electrode kinetics within the lithium doped anode. As a contrast, the voltage profile for the equivalent ΔV_2

phase on EDLC Cell A and B, which are represented by the red and orange lines, respectively, are very linear. The author expected the linear profile for both EDLC cells due to the lack of electrochemical reactions within the cell that would eliminate the development of cell over potentials from electrode kinetics. When examining batteries, the non-linear behaviour that may result from electrode kinetics is commonly modelled as a parallel resistor and capacitor to form an RC pair in a second order equivalent circuit battery model. However, due to the desire for a simple equivalent series capacitor model that allows for easy cell comparison, this work does not explore second order equivalent circuit modelling. For this reason, the voltage change in ΔV_2 is not of interest for modelling purposes. The remaining option, and the option used in this work, is to represent ΔV using ΔV_3. The starting voltage for the ΔV_3 voltage range is easily defined as the cell voltage when the pulse current is commanded to 0A. The ending voltage that defines ΔV_3 is more difficult to identify. During the post-pulse relaxation period the cell voltage may change, and in the case of a discharge pulse, increase over time. When testing battery cells with complex chemical reactions it may be desirable to define the ending voltage at a post relaxation period of several minutes to an hour. However, the capacitors studied in this work showed very little voltage change beyond three seconds into the post-relaxation period. Additionally, a shorter post-pulse relaxation period is advantageous for HPPC testing on multiple cells at several operating conditions due to the time saved in not waiting for a very minimal no-load cell voltage change. The ESR calculation method used in this work was further refined to Equation 10. Both voltage and current values in Equation 10 are extracted from a total of two data log times; first from time 0, the last sample point where the commanded pulse current is at the desired value, and than again three seconds later. See Figure 35 for clarification.

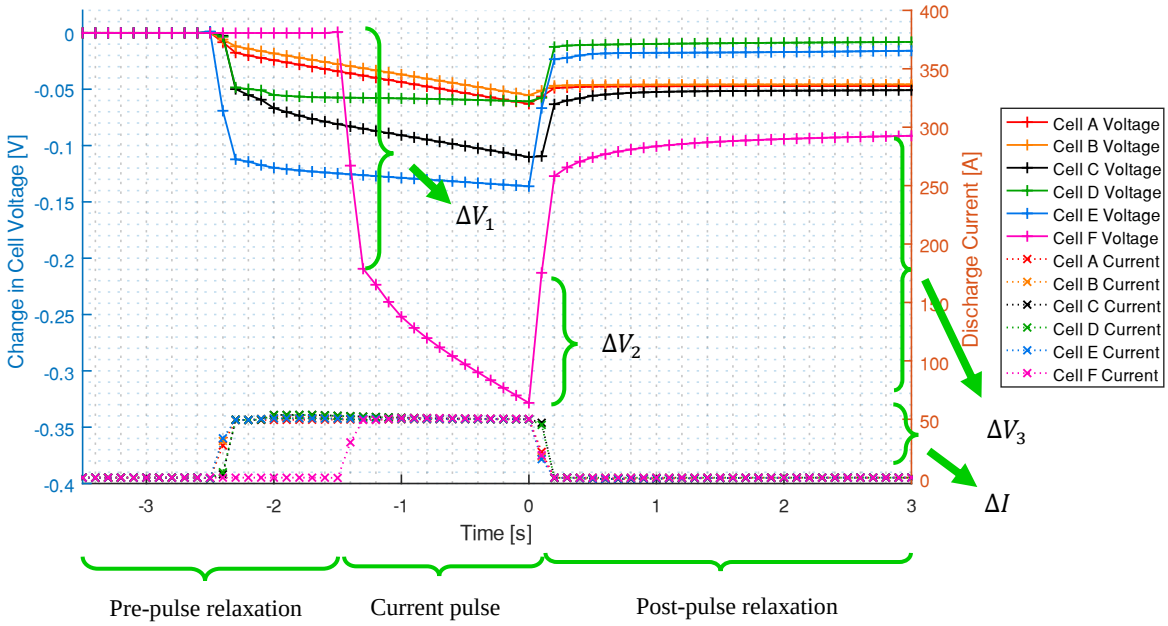

Figure 35: Example HPPC pulse response for Cells A thru F using a 50A discharge pulse at 45% SOC at 25°C.

$$ESR_{HPPC}[\Omega] = abs\left(\frac{\Delta V}{\Delta I}\right) = abs\left(\frac{V_{End\ of\ Current\ Pulse} - V_{End\ of\ Post\ Pulse\ Relaxation}}{I_{End\ of\ Current\ Pulse} - I_{End\ of\ Post\ Pulse\ Relaxation}}\right)$$

Equation 10: Refined formulation to calculate the HPPC ESR

The author selected to perform HPPC charge and discharge pulses at increments of 5% SOC rather than 10% increments as commonly seen in literature. However, recall that a 50A pulse with duration of 2.5 seconds would charge Cell G by approximately 7%, which is larger than the 5% SOC increments. Therefore, as shown in Figure 35, the current pulse duration for all HPPC testing on Cell F was limited to 1.5 second current pulses rather than the 2.5 second pulses that are used on Cells A thru E. It should be noted that voltage and current values used in Equation 10 are not collected at exact 5% SOC increments due to charging/discharging that occurs during the current pulse. Therefore, the 5% SOC breakpoints are used as approximate values and a minor degree of modelling uncertainty is introduced. Equation 11 provides an example of Equation 10 using data available from Cell F in Figure 35.

$$ESR_{HPPC}[\Omega] = abs\left(\frac{\Delta V}{\Delta I}\right) = abs\left(\frac{(-0.3284) - (-0.09136)}{50.34 - 0}\right) = \frac{0.23704}{50.34} = 4.7\ [m\Omega]$$

Equation 11: Refined formulation to calculate the HPPC ESR

The typical method used to change the cell state of charge in preparation for HPPC current pulses involves performing a CC charge or discharge until a specified capacity is charged/discharged based on coulomb counting. This approach aims to create HPPC testing points at equal SOC breakpoints. However, the capacity charged or discharged from a HPPC pulse can introduce an offset and therefore make the SOC breakpoint spacing uneven. One approach to over come this issue is to perform a charge pulse followed by a reasonable post-pulse relaxation period and then perform a very similar discharge current pulse and relaxation period. By performing an equal charge and discharge pulse near the same SOC breakpoint, it is intended that the net SOC change is nearly zero and therefore moving between SOC breakpoints based on coulomb counting is rather successful. However, the coulomb counting approach to establishing SOC breakpoints can present additional concerns, specifically when using the custom cell cycler. For example, performing a 50A discharge pulse at 10% SOC in a cold environment often results in an ESR voltage drop that extends below the minimum cell voltage. In this case the custom cycler enters protection mode and must be reset. The main concern is that the coulomb or amp hour counter is reset to zero when entering protection mode. Therefore, performing a manual reset to test at the next SOC breakpoint requires the cell to be fully discharged from the previous SOC breakpoint, reset the Ah counter and then proceed to charge the cell to the desired SOC breakpoint. Depending on the cell and testing conditions, this time consuming full discharge and partial recharge process may need to be repeated several times before reasonable ESR data can be obtained without hitting voltage protection limits. To mitigate this issue, the author defined the SOC breakpoints by performing CCCV charging to selected cell terminal voltages. Recall from Section 5.6.2 that the 2A charge and discharge

terminal voltage vs capacity relationship was very linear, unlike the open circuit voltage vs capacity relationship for batteries. The author divided the voltage range of Cells A thru F into voltage breakpoints that represent 5% SOC breakpoints. Even through the cells would still hit protection limits, the need to fully discharge and recharge the cells was eliminated as the testing profile could be continued using the next testing command to perform a CCCV charge to the next voltage breakpoint. Due to the non-linearity of the 2A terminal voltage vs capacity profile of Cell G, as shown in Figure 33 Sublot M and N, Cell G was tested using capacity breakpoints based on coulomb counting rather than cell voltage. This modification resulted in the development of a new autocycle testing profile specifically for Cell G.

In general, the HPPC testing profile consisted of multiple “passes”. During one pass the cell would be fully discharged and then charged using a CCCV profile to the lowest desired voltage breakpoint. Due to the inability to perform discharge HPPC pulses at 0% SOC, the discharge pulses started at the voltage corresponding to 5% SOC. Once the desired voltage was achieved the custom tester would perform a 10A discharge pulse for 2.5 seconds (1.5 seconds for Cell F). The tester would enter a paused state with zero output current and the cell would be allowed to rest for 120 seconds. This formed the post-pulse relaxation phase. The cell would then be charged to the next desired cell voltage and a similar discharge pulse was performed. This process would repeat until the cell reached the maximum cell voltage and the final discharge pulse and post-pulse relaxation were complete. This concludes the completion of one HPPC “pass”. The HPPC pass would be repeated by discharging to the minimum cell voltage and starting over. However, the next pass would use charging pulses of equal magnitude from voltage breakpoints that correspond to 0% SOC up to 95% SOC. These two HPPC “passes”, one

charging and one discharging, were repeated three times using pulse currents of 10A, 25A and 50A for a total of 120 HPPC current pulses for each cell at all five testing temperatures.

5.7.2. Test 3 Analysis – 25°C and Negative 10°C Charge and Discharge ESR vs SOC

Figure 36 presents the ESR data collected from 25A charge and discharge HPPC current pulses in a controlled 25°C and negative 10°C environment. Note that due to the custom cell tester's inability to perform CCCV profiles below 0.6V, Figure 36 excludes ESR data for Cells A and B below approximately 20% SOC.

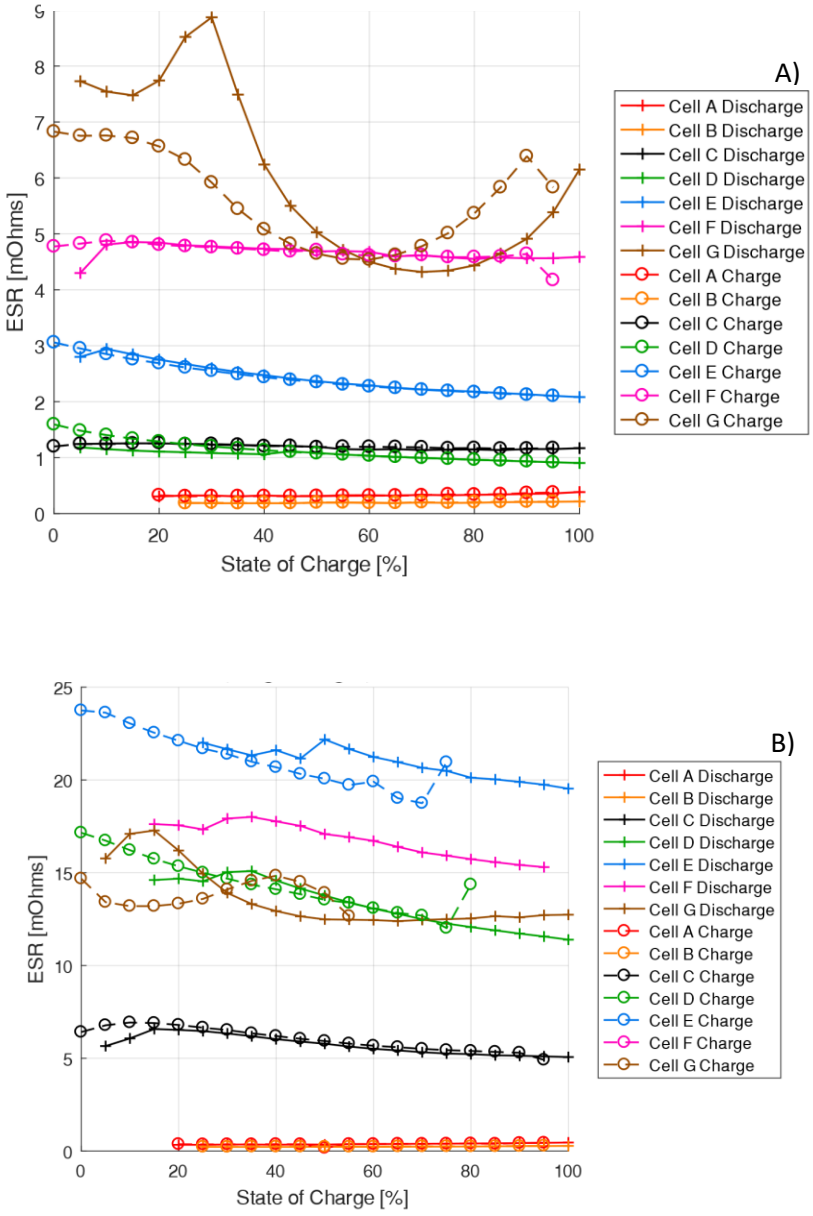

Figure 36: Charging and discharging ESR vs SOC for all seven cells tested at 25°C (Subplot A) and negative 10°C (Subplot B) determined using 25A charge and discharge pulses with a 3 second post-pulse relaxation period and 5% SOC breakpoints.

5.7.3. Test 3 Analysis – Multi-Temperature Charge and Discharge ESR vs SOC

In Figure 37, each subplot presents the charge and discharge ESR values (25A HPPC current pulses, 3 second post-pulse relaxation period) at five testing temperatures for one cell. It is important to note that the vertical axis is not consistent among the subplots. For example,

Subplot A shows a relatively small range from 0.3 mΩ to 0.48 mΩ while Subplot F shows a relatively large range from 0 mΩ to 18 mΩ. Note that due the custom cell testers inability to perform CCCV profiles below 0.6V, Figure 37 excludes ESR data for Cells A and B below approximately 20% SOC.

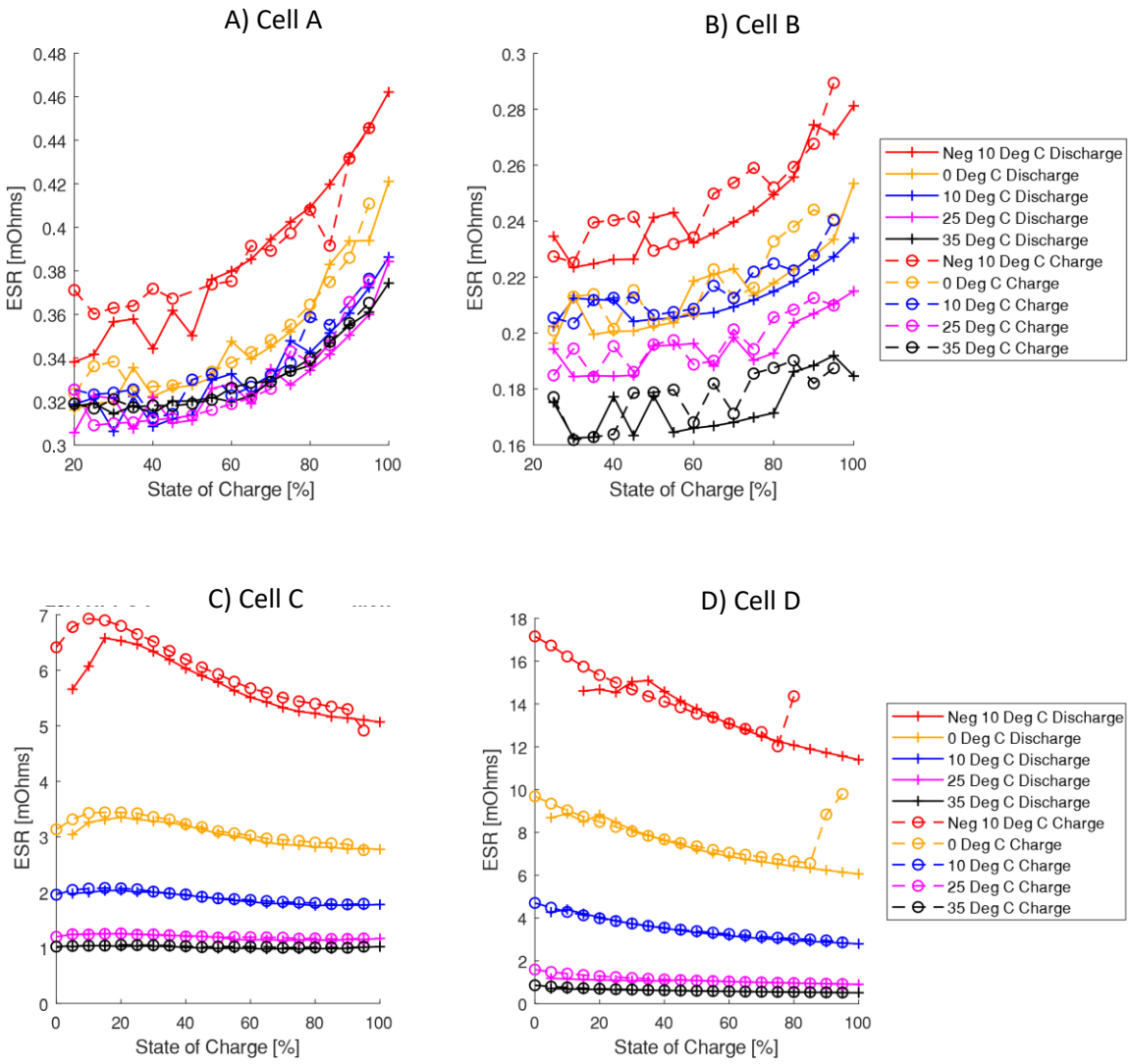

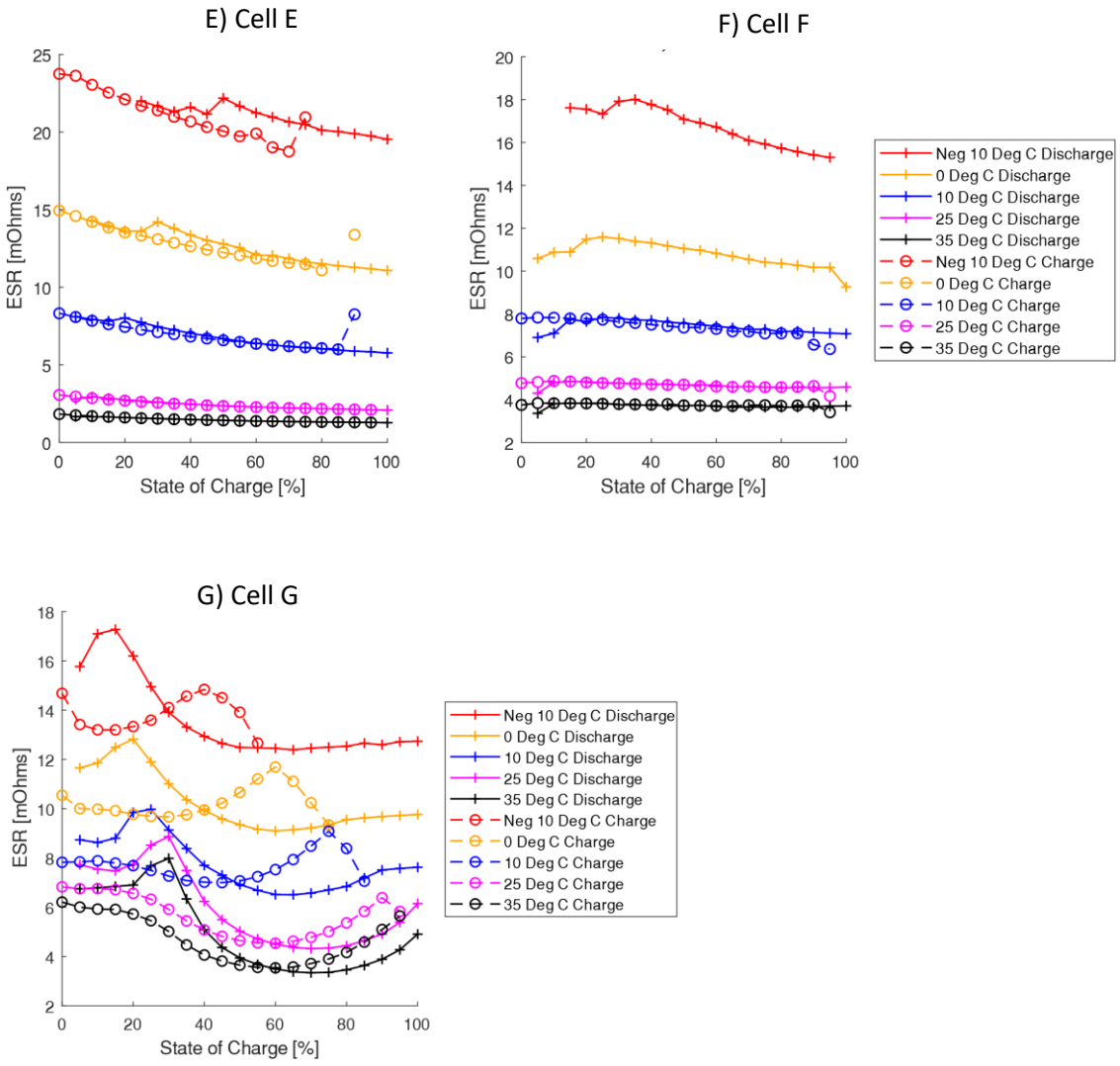

Figure 37: Charge and discharge ESR of each cell determined at five testing temperatures with 25A current pulses and a 3 second post-pulse relaxation period.

5.7.4. Test 3 Analysis – Average and Normalized ESR Change vs Testing Temperature

Figure 38 Subplot A presents the average charge and discharge ESR at each testing temperature for all cells. The average charge and discharge resistance are calculated using all of the ESR data points available using a 25A pulse current where the cell has not hit protection limits. For example, the average ESR value for a cell that hit protection limits with charging pulses near the upper SOC range will have less data points to form the average value than a cell that did not hit protection limits. Figure 38 Subplot B shows the average ESR values from Subplot A normalized by the average ESR from testing at 25^{O}C. In comparison to Subplot A, Subplot B provides a

normalized comparison metric to evaluate how the average ESR changes with temperature. Note that Subplot B shows a normalized ESR of 100% for all cells when tested at 25^{O}C.

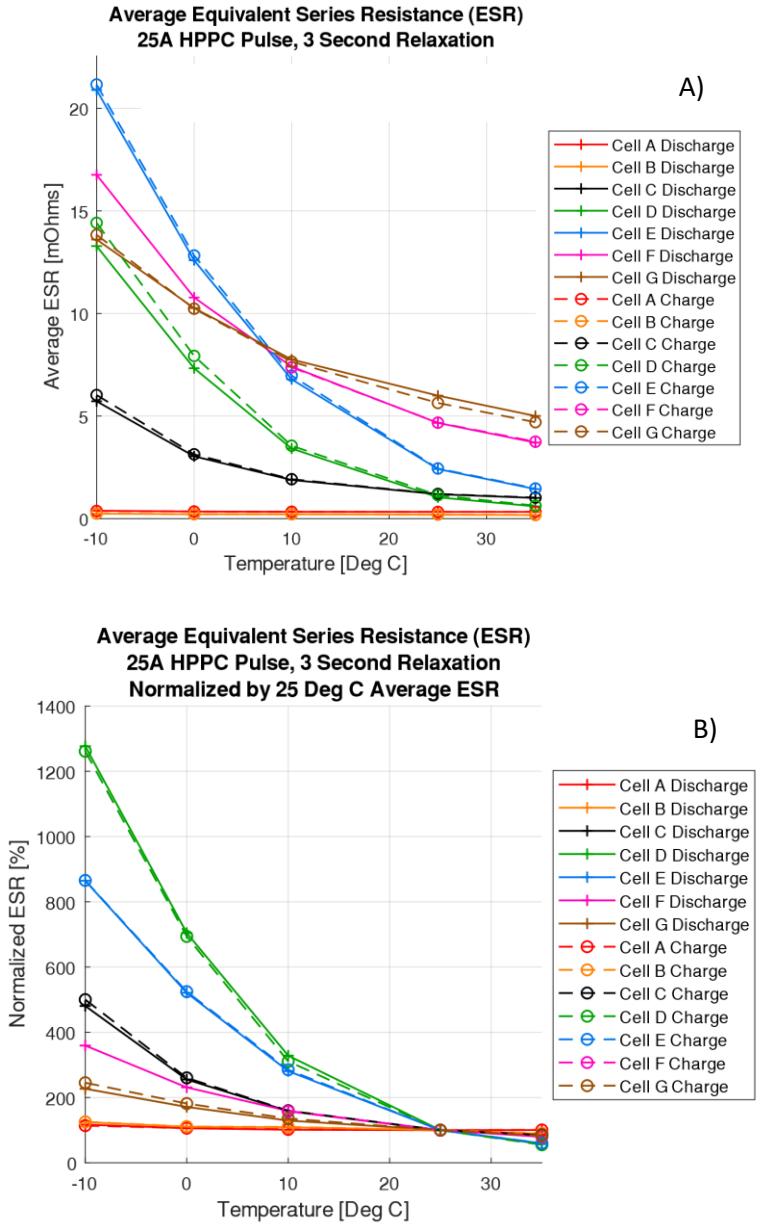

Figure 38: Average (Subplot A) and normalized (Subplot B) ESR as a function of the testing temperature. Data collected using 25A charge and discharge HPPC current pulses with a 3 second post-pulse relaxation time.

5.7.5. Test 3 Analysis – Current Dependent ESR

As discussed in [100] and [101], the use of a temperature insensitive energy storage device in combination with lithium-based batteries can increase the energy storage system power capabilities in cold temperatures as a whole. Compared to EDLC cells, the increased energy

density of LiCs is attractive for hybrid energy storage applications and pure capacitor-based energy storage systems. However, the performance of each energy storage device in cold temperatures must be analysed. Although Sections 5.7.3 and 5.7.4 have addressed EDLC, LiC and ||LiC cell performance changes from -10°C to 35°C, the ESR data presented was collected using 25A charge and discharge HPPC current pulses. However, as discussed in [100], [102], and [103], the cell's internal resistance, and/or over potential of lithium based batteries may be a function of the current, especially in cold temperatures. This characteristic is similar to the electrochemical Butler-Volmer effect. Considering the presence of lithium in LiC and ||LiC cells, the ESR's dependency on current will be addressed and compared to EDLC cell performance.

Figure 39, shows HPPC ESR data for all cells determined from 10A, 25A and 50A charge and discharge pulses at 25°C and -10°C.

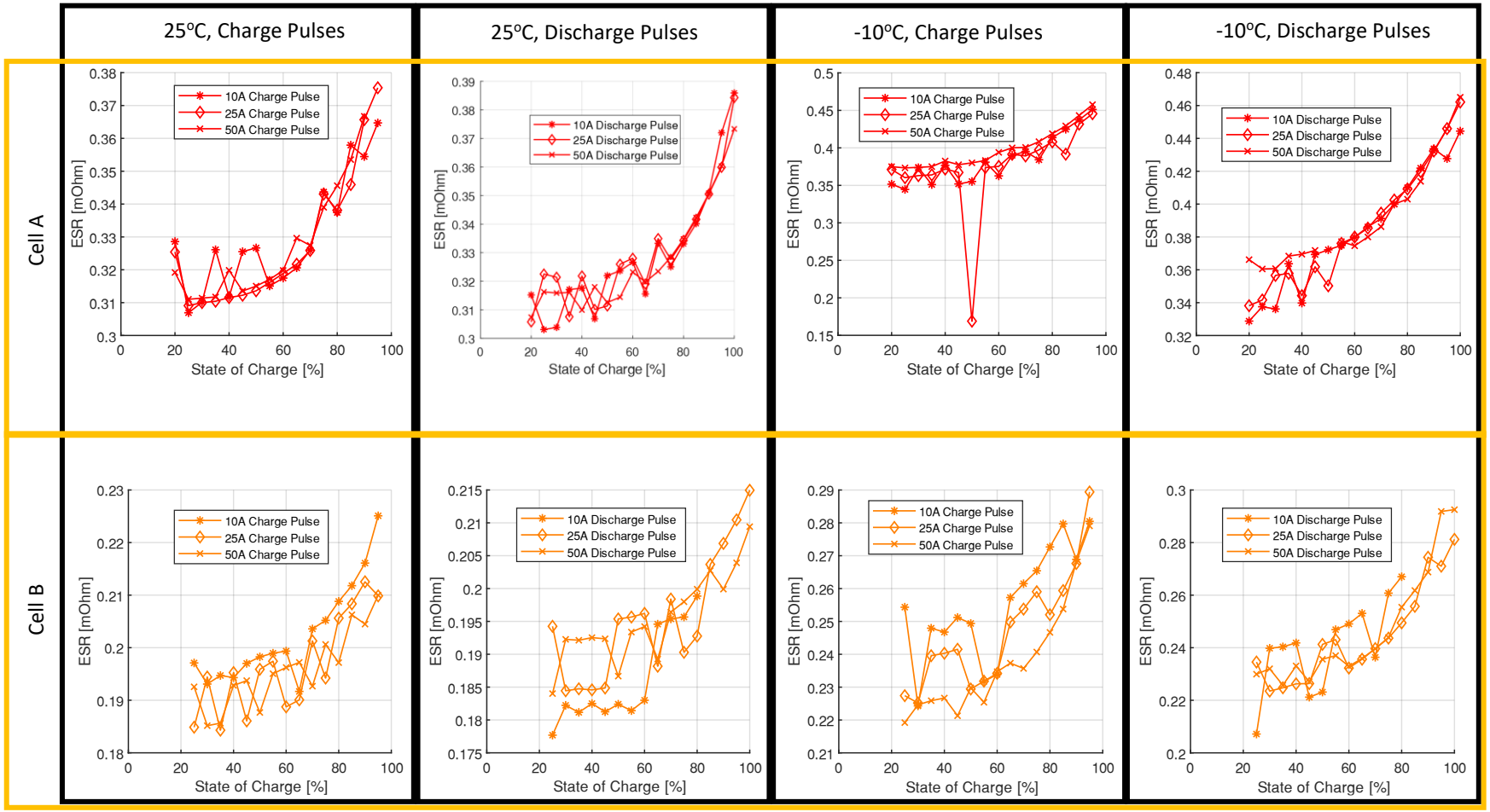
25°C, Charge Pulses
25°C, Discharge Pulses
-10°C, Charge Pulses
-10°C, Discharge Pulses
Cell A
Cell B
ESR [mOhm]
State of Charge [%]
10A Charge Pulse
25A Charge Pulse
50A Charge Pulse
10A Discharge Pulse
25A Discharge Pulse
50A Discharge Pulse

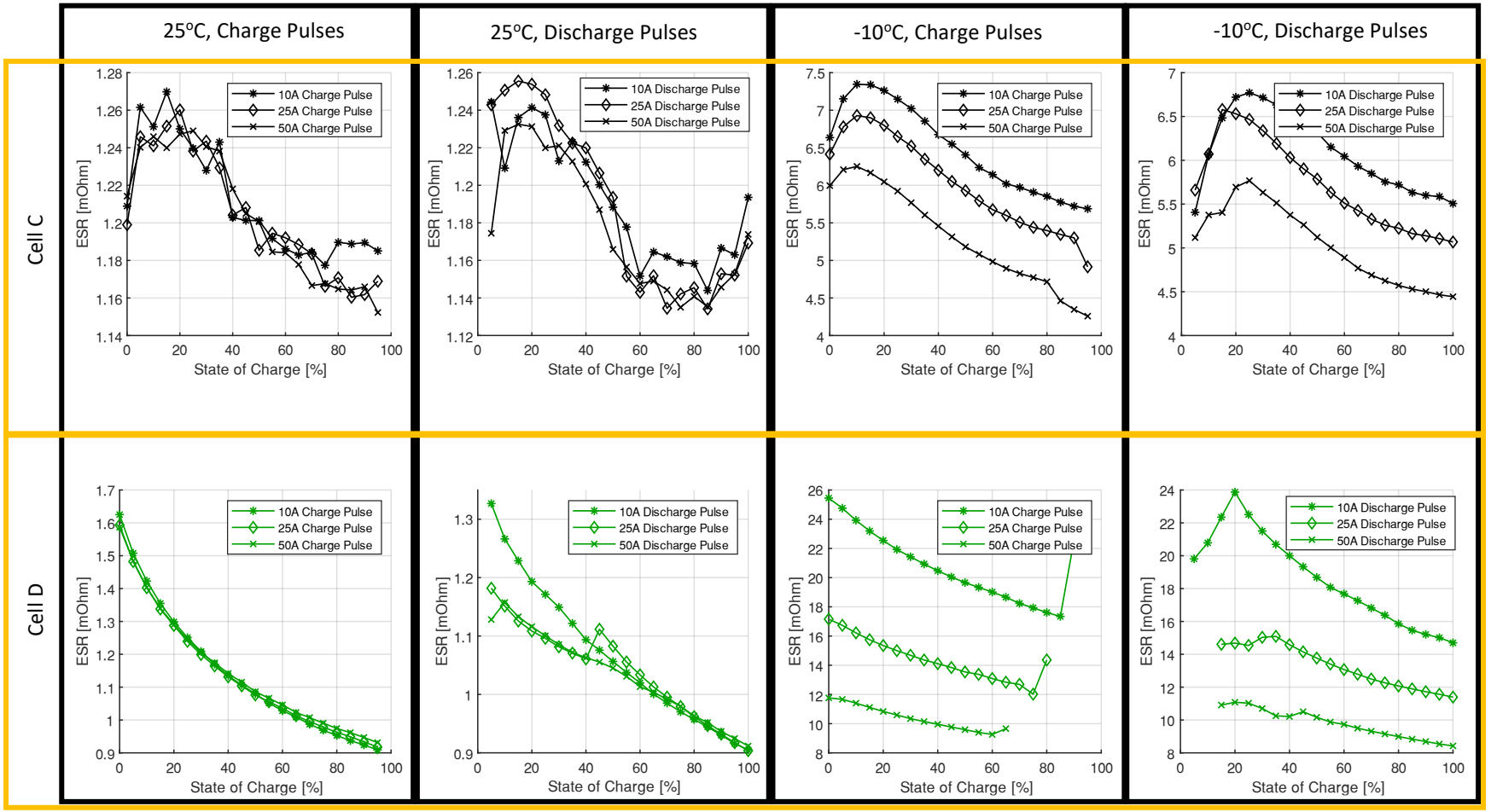
25°C, Charge Pulses
25°C, Discharge Pulses
-10°C, Charge Pulses
-10°C, Discharge Pulses
Cell C
Cell D
ESR [mOhm]
State of Charge [%]
10A Charge Pulse
25A Charge Pulse
50A Charge Pulse
10A Discharge Pulse
25A Discharge Pulse
50A Discharge Pulse

	25°C, Charge Pulses	25°C, Discharge Pulses	-10°C, Charge Pulses	-10°C, Discharge Pulses
Cell E	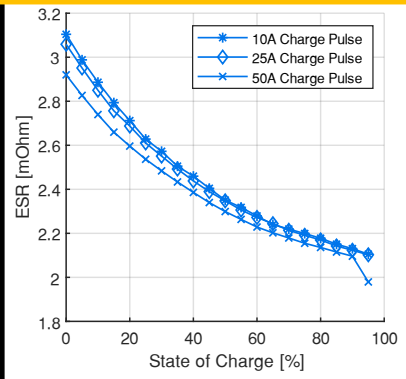	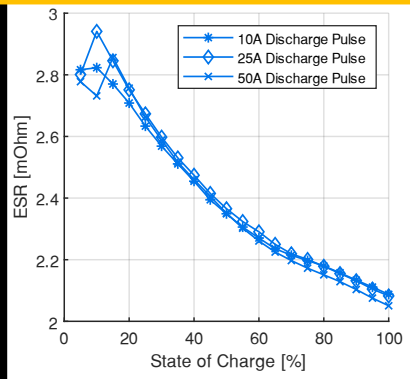	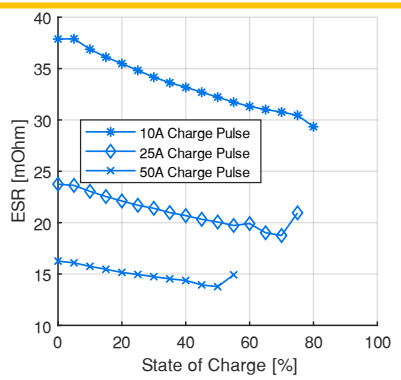	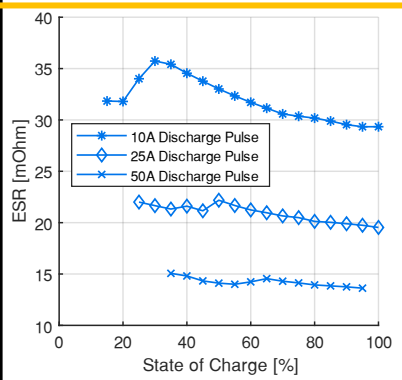
Cell F	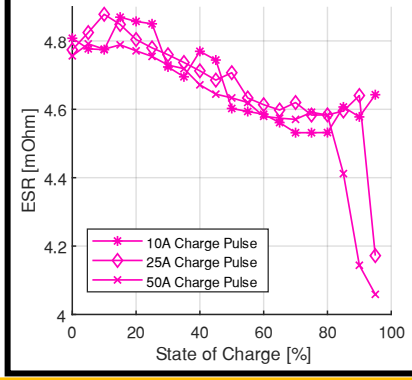	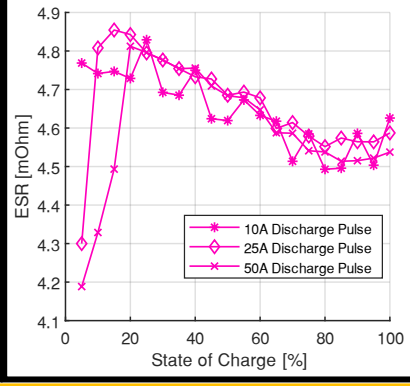	Data not available due to charging temperature limitations	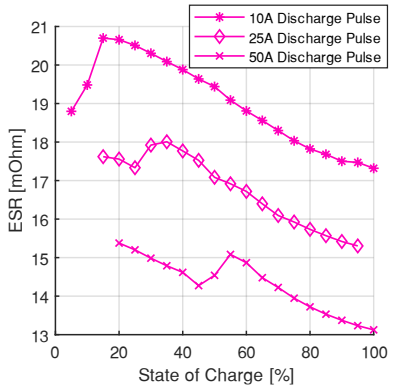

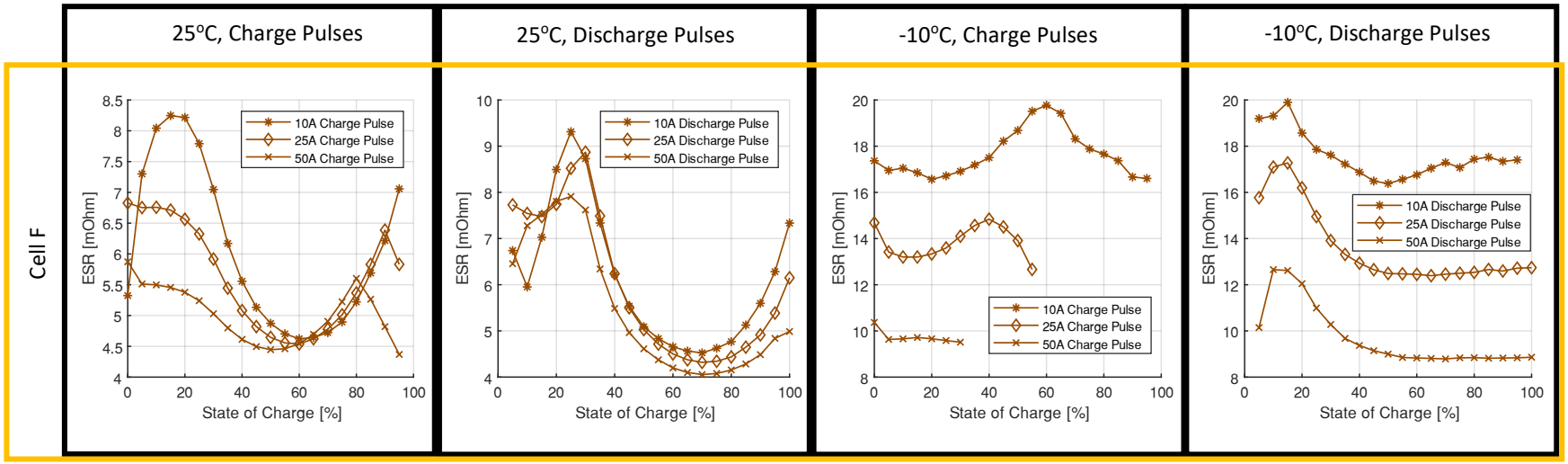

Figure 39: ESR vs SOC determined using 10A, 25A and 50A charge and discharge pulses at 25°C and -10°C.

5.7.6. Test 3 Conclusions

The following conclusions are made using data available in Section 5.7.2 and Figure 36.

- Both subplots in Figure 36 show that EDLC Cells A and B have the lowest ESR. The EDLC and LiC cells have a near linear ESR vs. SOC relationship, while Cell G (||LiC) has a unique ESR vs. SOC relationship. Additionally, Figure 36 shows that Cells C-G (LiCs and ||LiC) all have a considerably larger ESR when tested at -10°C compared to 25°C.

The following conclusions were made using data available in Section 5.7.3 and Figure 37.

- Figure 37 further shows that the ESR of EDLC Cells A and B are barely affected by temperature (e.g. Cell A plot vertical axis between 0.3 to 0.48 mOhms) while the LiC cells are significantly impacted by temperature (e.g. Cell E plot vertical axis between 0 mOhms and 25 mOhms).
- The EDLC and LiC cells have ESR charging and discharging characteristics that are relatively similar for a given cell. The ESR vs. SOC trends for Cells A-F are relatively consistent with a near vertical shift in response to temperature change. However, ||LiC Cell G features a vertical, horizontal and minor curve shape change in the ESR plot in response to temperature change. For example, the plot for Cell G in Figure 37 has a maximum charge ESR (~14.84 mOhms) at 40% SOC when at -10°C and maximum charge ESR (~9.08 mOhms) at 75% SOC when at 10°C.

The following conclusions were made using data available in Section 5.7.4 and Figure 38.

- Figure 38 shows that the average ESR for EDLC Cells A and B does not increase significantly at -10°C. Of all the lithium-ion capacitors, ||LiC Cell G featured the lowest increase in average ESR at -10°C of ~227%.

The following conclusions were made using data available in Section 5.7.5 and Figure 39.

- The EDLC and LiC cells show a charging and discharging ESR with very little dependency on current when tested at 25°C. The ||LiC Cell G ESR shows a small current dependency at low SOC at 25°C with charging pulses, but the current dependency is reduced for discharging pulses.
- EDLC Cells A and B show a relatively insignificant ESR current dependency for charging and discharging pulses at -10°C. Note that the y-axis for each subplot in Figure 39 is unique.
- LiC Cells C, D, E and F show a considerable ESR current dependency for charging and discharging pulses at -10°C. The ESR is largest for the 10A pulses and smallest for the 50A pulses. Using Cell C as an example, at -10°C the 10A charging 10% SOC ESR is ~7.35 mOhms and the 50A charging 10% SOC ESR is ~6.25 mOhms.
- ||LiC Cell G shows a large ESR current dependency for charging and discharging pulses at -10°C. The ESR is largest for the 10A pulses and smallest for the 50A pulses. For example, at -10°C the 10A discharging 60% SOC ESR is ~16.76 mOhms and the 50A discharging 60% SOC ESR is ~8.83 mOhms (nearly half the 10A ESR).
- The author advises against modelling current dependant ESR or overpotentials for EDLC cells due to the increase in modelling complexity. The author encourages the use of a current dependant ESR for LiC cells when operating in cold temperatures. Considerations should be made for a current dependant ESR for ||LiC cells, especially in cold temperatures. However, the ||LiC sample size was very small and the need for a detailed current dependant model may not be necessary for other cells.

5.8. Test 4 – Drive Cycle Model Validation

The purpose of Test 4 was twofold: to compare cell performance from drive cycle testing in 0°C and 25°C environments as well as validate select cell characterization data obtained from Test 2

and 3. Rather than performing rather simple constant current charge/discharge cycles or current pulses, the cells were exposed to a scaled version of the power profile that corresponds to a Fiat 500e driving the US06 and UDDS drive cycles in both 0°C and 25°C environments. The cells were modelled using the characterization data from Tests 2/3 and the error between the models is discussed as a source of model validation.

5.8.1. Test 4 Method

As shown in Figure 40, Cells A thru F were mounted on a rack inside the Thermotron SE-3000 thermal chamber and connected to individual testing channels from the Digatron multiple cell tester. The cells and identifying labels are covered with blue boxes to maintain anonymity. The original SB 120 power connectors and mini Anderson voltage sense connectors were compatible with the Digatron tester and therefore they were re-used for this test. However, the Digatron tester does not interface with the thermistors used on the custom cycler and therefore the author assembled multiple compatible temperature sensors.

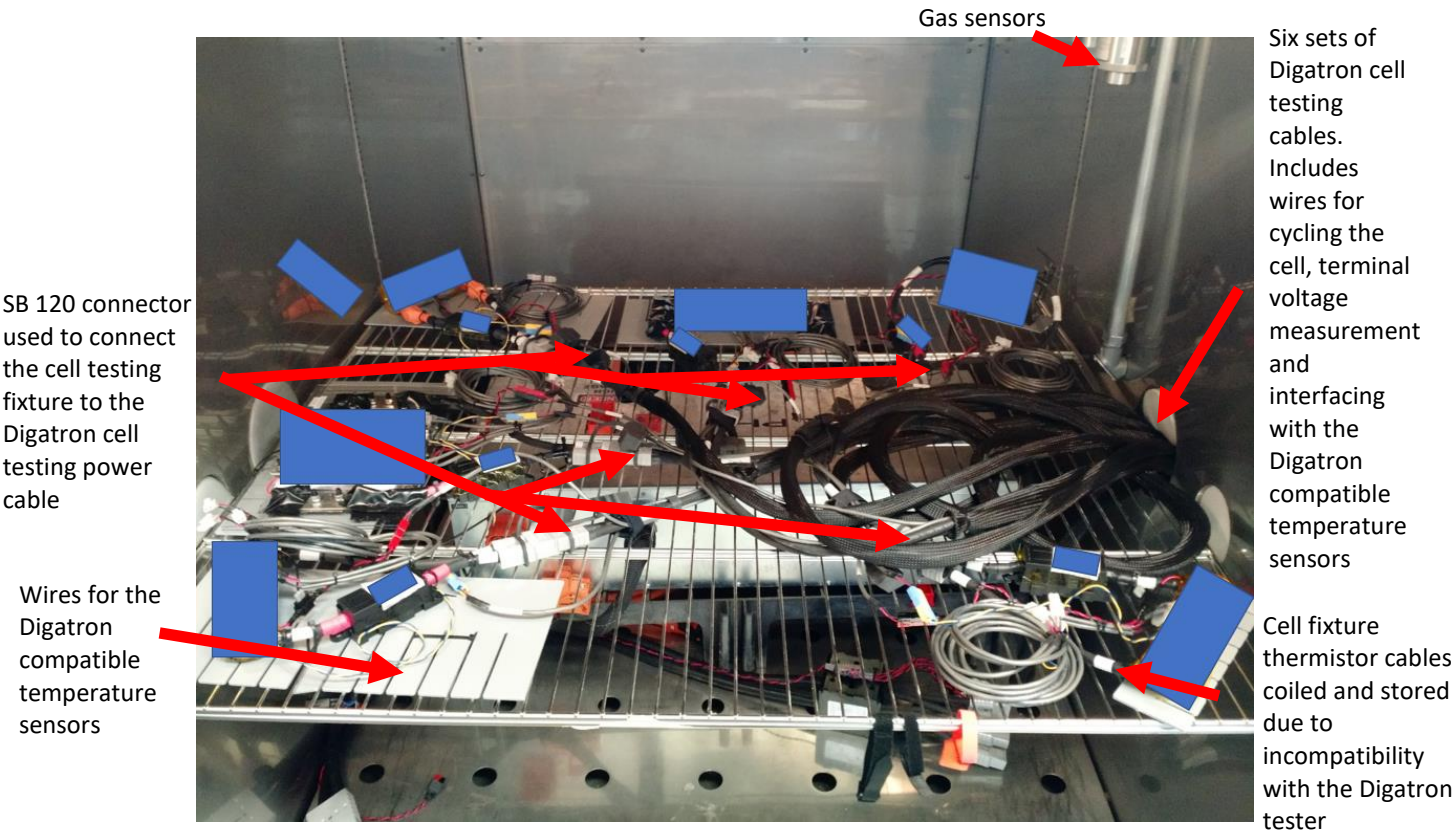

Figure 40: Cells A thru F mounted inside the Thermotron SE-3000 thermal chamber for simultaneous testing with the Digatron multiple cell tester.

Using a tool developed by Dr. Kollmeyer, the power profile used to test each cell was determined by scaling the power required for a Fiat 500e vehicle to drive both the US06 and UDDS drive cycles. The Fiat 500e vehicle was modelled using Davis equation coefficients (see Section 6.4 for more detail) available from the American Environmental Protection Agency [104]. The vehicle power profile was scaled to ensure that the maximum cell testing current would not exceed the Digatron's 75A per channel limit. The scaled UDDS and US06 drive cycles consume more energy than the cells can hold and therefore the desired drive cycle power requirements are not met. The Digatron testing equipment adheres to the cell voltage limits and reduces the actual charging / discharging current during infeasible conditions. For this reason, the cells with small energy content often show relatively uneventful drive cycle data because the cells are discharged for most of the test duration.

5.8.2. Test 4 Results – 25°C and 0°C Drive Cycles

Figure 41 to Figure 45 show the measured drive cycle testing power (upper subplots), current (lower subplots) and cell terminal voltage (middle subplots) for Cells A to D and F at 25°C and 0°C. Drive cycle data is not available for Cells E and G. Figure 41 and Figure 42, which correspond to EDLC Cells A and B, appear to only show data collected at 0°C (blue lines). However, as shown in Section 5.7.2 and 5.8.2, temperature has little to no impact on the EDLC cell performance and therefore the data for 0°C and 25°C testing are very similar and overlap in the plots. A discrepancy between the cell terminal voltage in 0°C and 25°C is first evident in the terminal voltage subplot for LiC Cell C in Figure 43. Note that the y-axis ranges are not equal in Figure 41 to Figure 45.

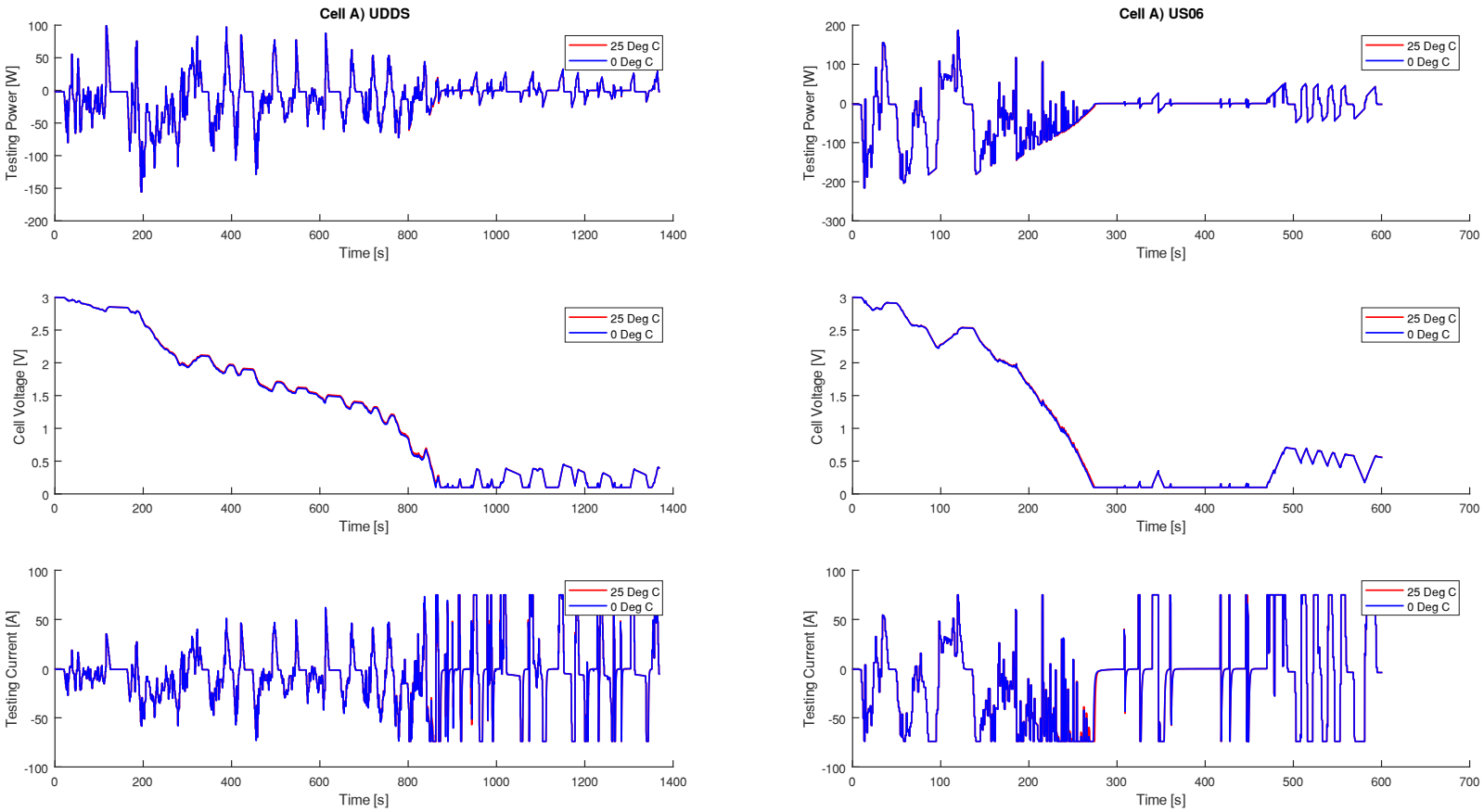

Figure 41: Cell A - UDDS and US06 measured drive cycle power, current and cell voltage at 25°C and 0°C

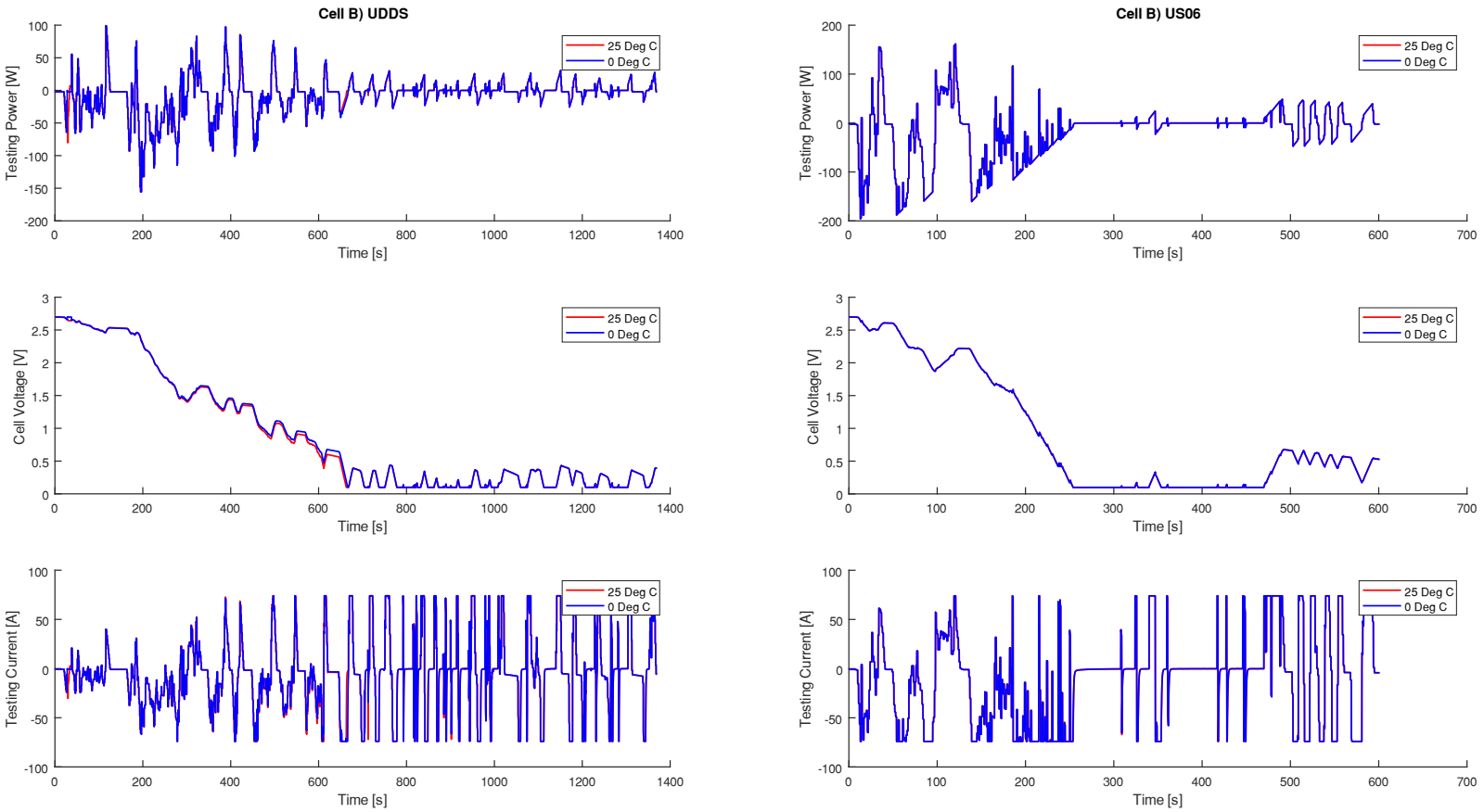

Figure 42: Cell B - UDDS and US06 measured drive cycle power, current and cell voltage at 25°C and 0°C

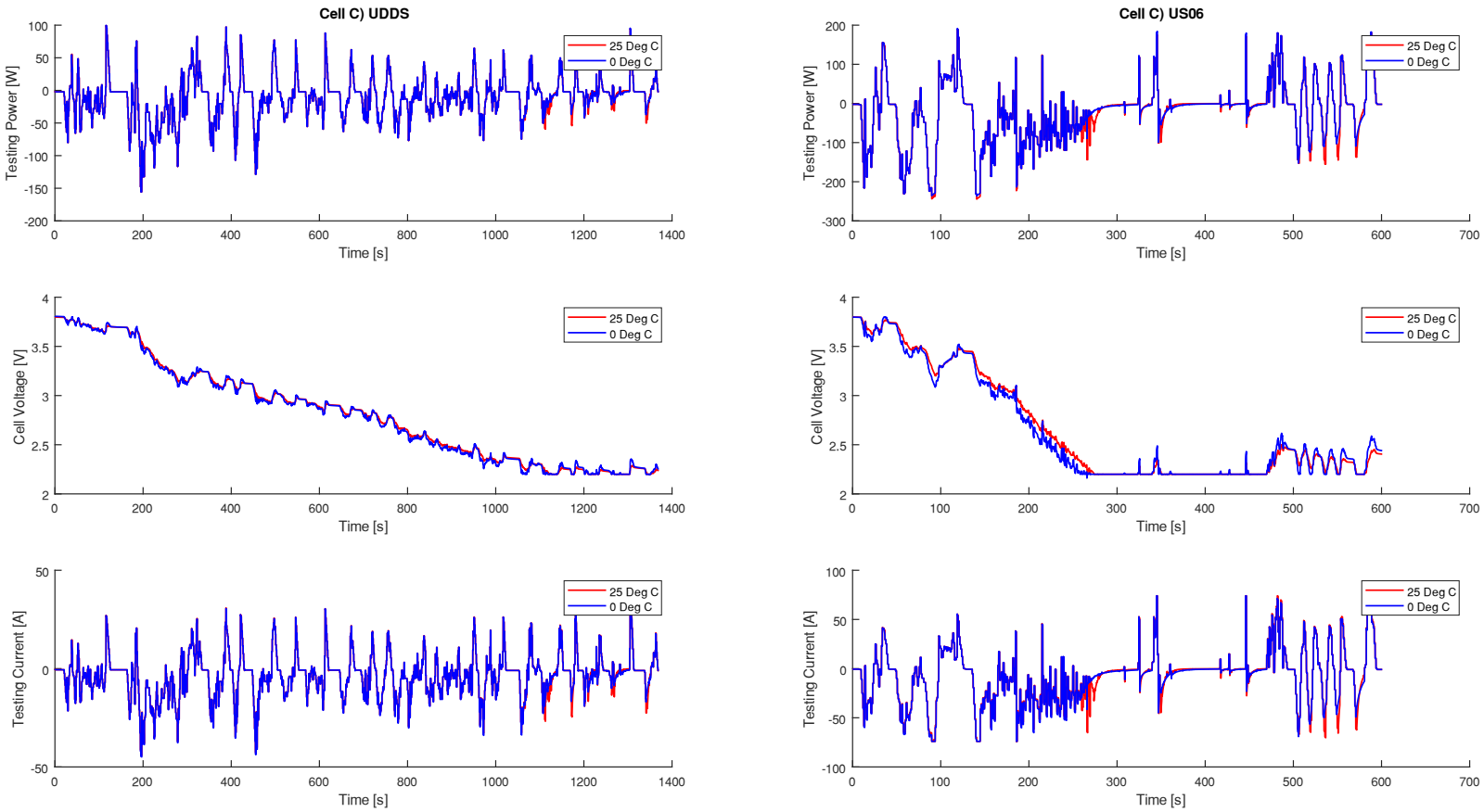

Figure 43: Cell C - UDDS and US06 measured drive cycle power, current and cell voltage at 25°C and 0°C

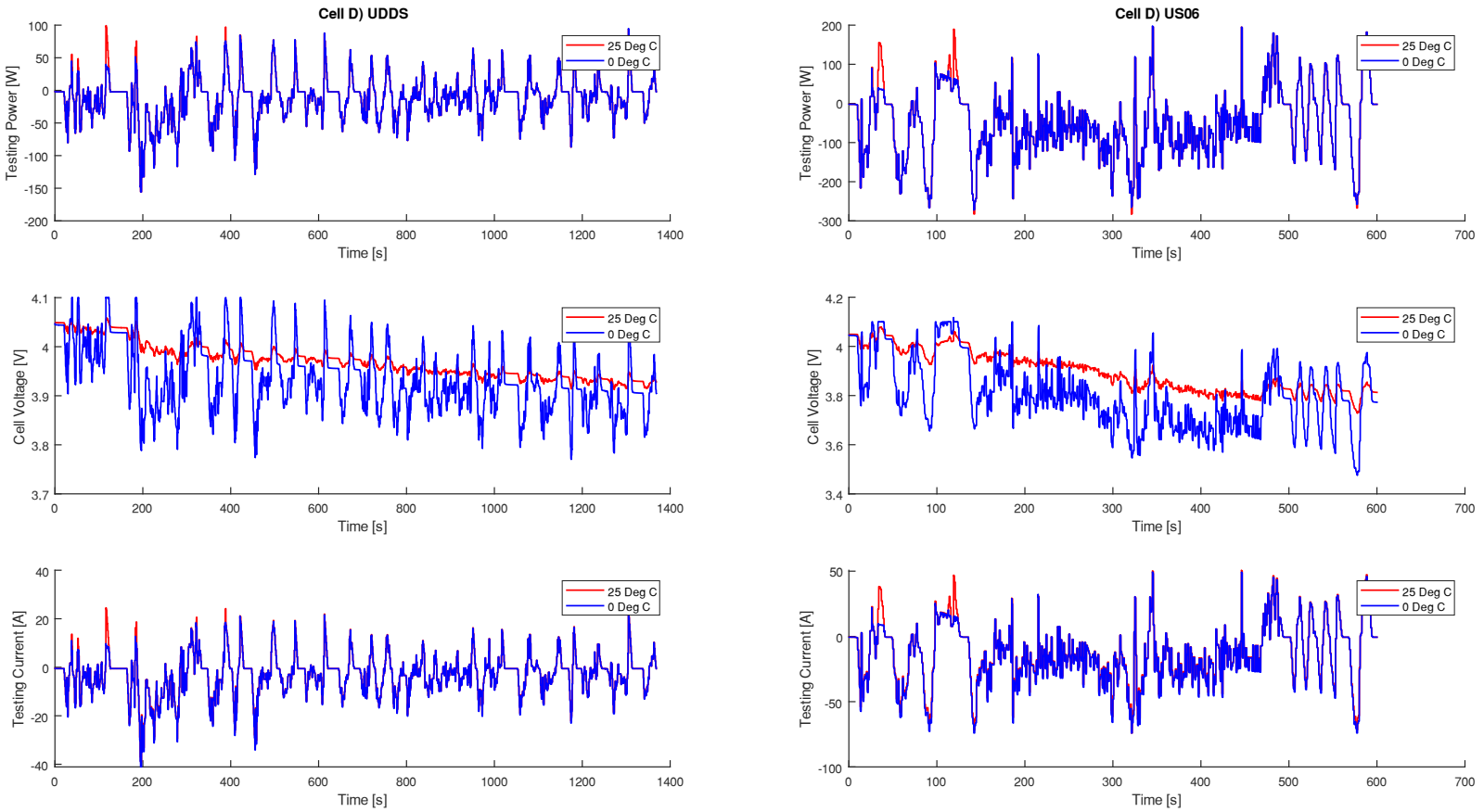

Figure 44: Cell D - UDDS and US06 measured drive cycle power, current and cell voltage at 25°C and 0°C

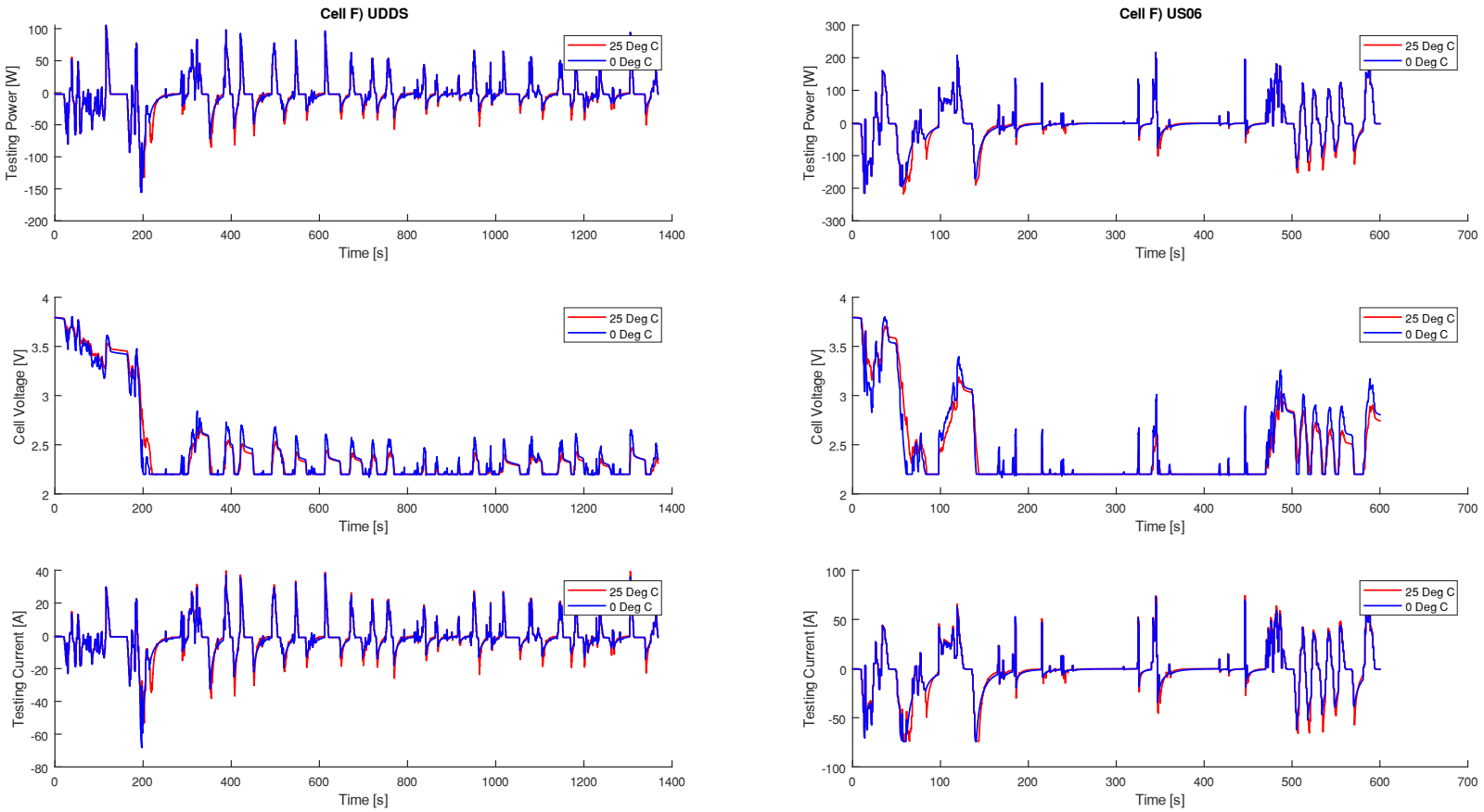

Figure 45: Cell F - UDDS and US06 measured drive cycle power, current and cell voltage at 25°C and 0°C

5.8.3. Cell Modelling Method

The capacitor cells were modelled using the circuit model shown in Figure 46. The circuit model makes use of a capacity / state of charge dependant ideal voltage source based on the 25°C 2A constant current charge voltage profile from Section 5.6.2. The cell impedance is modelled by a current direction and state of charge dependant resistor. The cell model examines the current direction (charging or discharging) and extracts the equivalent series resistance from either a charging or discharging ESR look up table filled with data from Test 3 using 25A current pulses at 25°C (see Figure 37). Where ESR data is unavailable due to cell voltage limits or hardware limitations, typically near the minimum and maximum state of charge, the ESR from the next available SOC breakpoint was used. For example, due to limitations of the custom cell testing device the EDLC cells did not undergo HPPC testing below 0.6V, which represents approximately 0% to 20% SOC. Therefore, the ESR values that correspond to this SOC range were approximated by the ESR value obtained at the next available breakpoint; commonly 25% SOC. In the range where ESR data is available, interpolation was used between the 5% SOC breakpoints. This modelling effect is expressed in Figure 46 as the charge and discharge resistances connected to ideal diodes. The ideal diodes represent the selection of resistance based on current direction without any additional voltage increase/decrease.

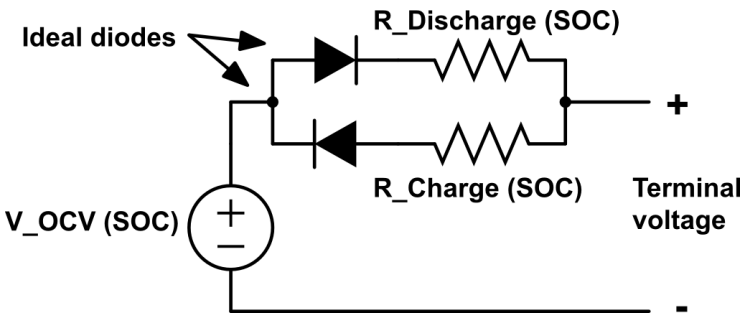

Figure 46: Equivalent circuit model used to simulate capacitor cell behaviour

The model accepts an array of current values and cell parameters. The cell model can be modified to accept a power input; however, this additional work is not necessary to validate select experimentally determined cell characteristics and is therefore beyond the scope of work for this chapter. Similarly, the model parameters could be updated to be a function of testing temperature, including a current dependent ESR, but is beyond the scope of this work.

5.8.4. Test 4 and Modelling Analysis – Drive Cycle Comparison

Figure 47 to Figure 51 show the measured cell terminal voltage, measured testing current and simulated cell terminal voltage for Cells A thru D and F at 25°C for the UDDS and US06 drive cycles. The simulated terminal voltage is determined using the measured testing current as the input. Note that the vertical axis range is not consistent on Figure 47 to Figure 51. Table 13 quantifies the RMS error between the measured and modelled cell terminal voltage for Figure 47 to Figure 51 using Equation 12.

$$RMS\ Error = RMS(V_{terminal,\ measured} - V_{terminal,\ simulated})$$

Equation 12: Determining the RMC error between the measured drive cycle terminal voltage and modelled/simulated voltage

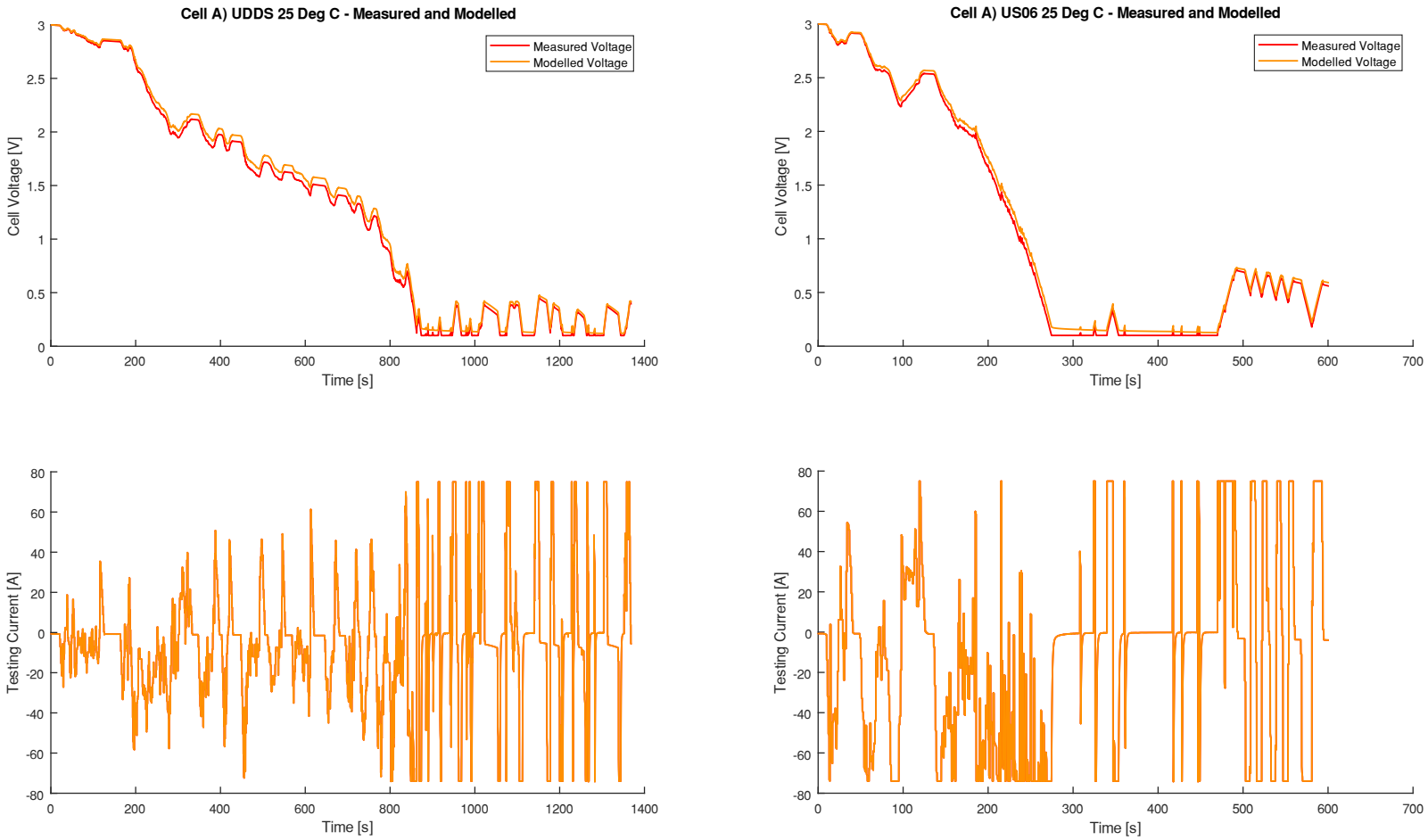

Figure 47: Cell A – measured and modelled terminal voltage for the UDDS and US06 drive cycles at 25°C

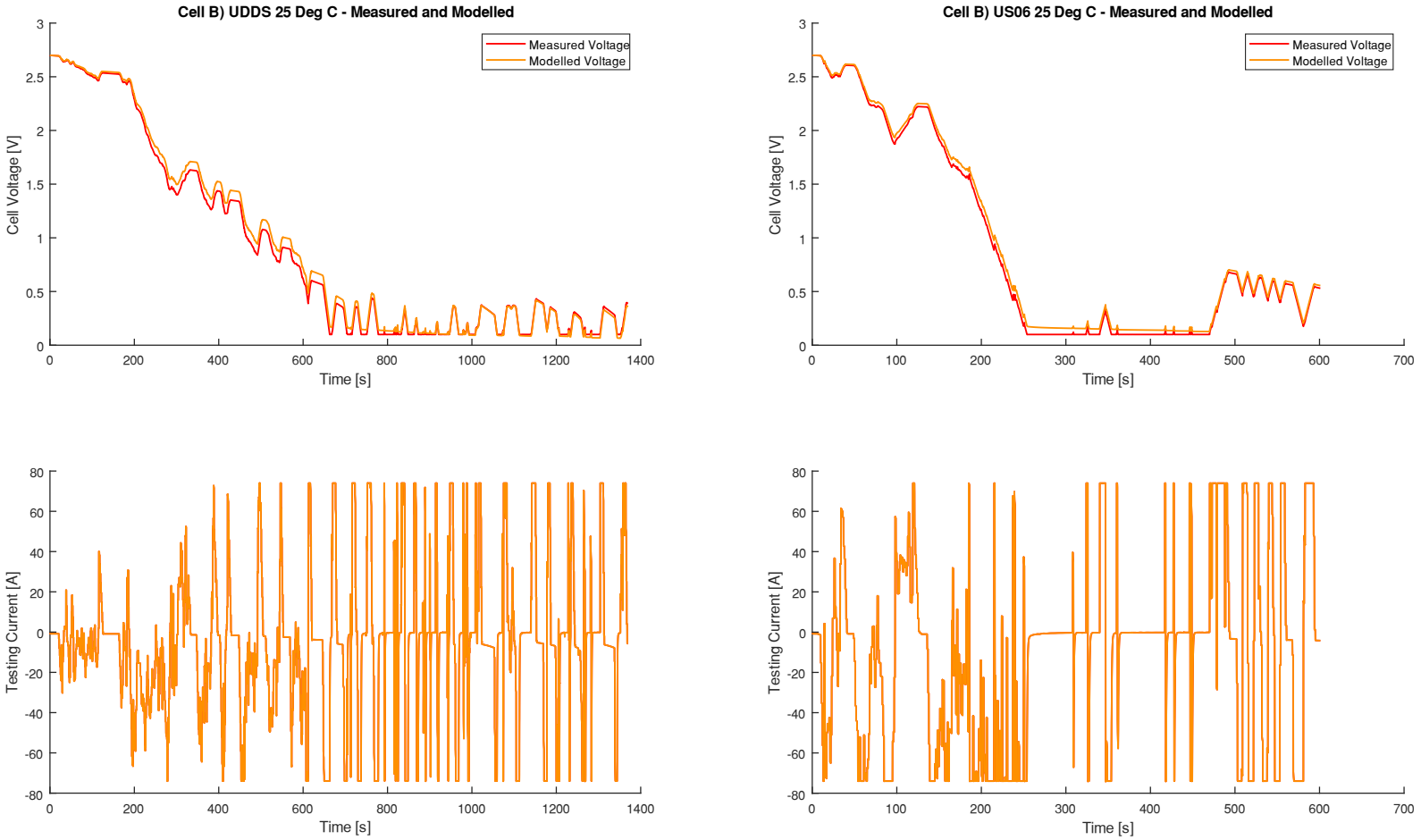

Figure 48: Cell B – measured and modelled terminal voltage for the UDDS and US06 drive cycles at 25°C

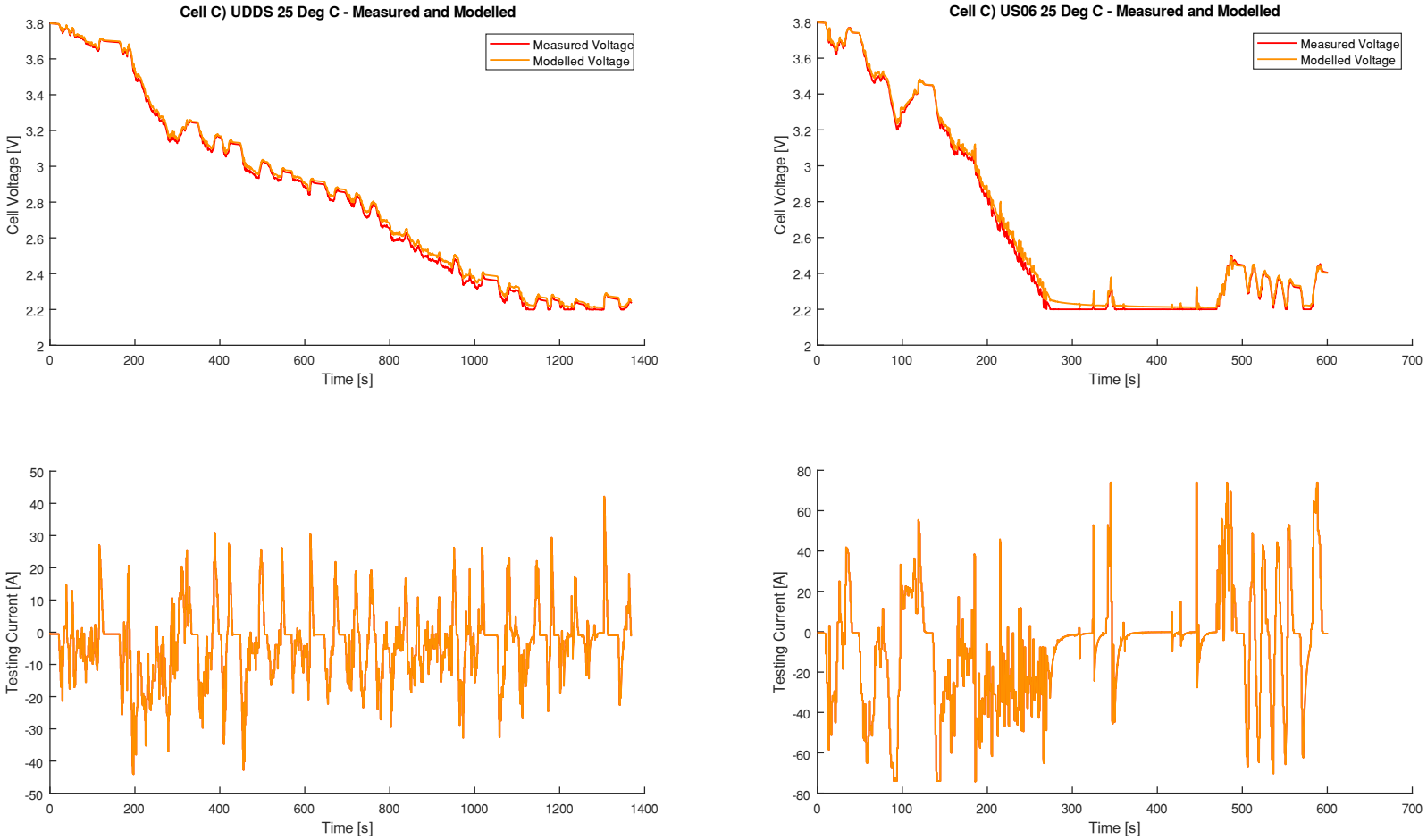

Figure 49: Cell C – measured and modelled terminal voltage for the UDDS and US06 drive cycles at 25°C

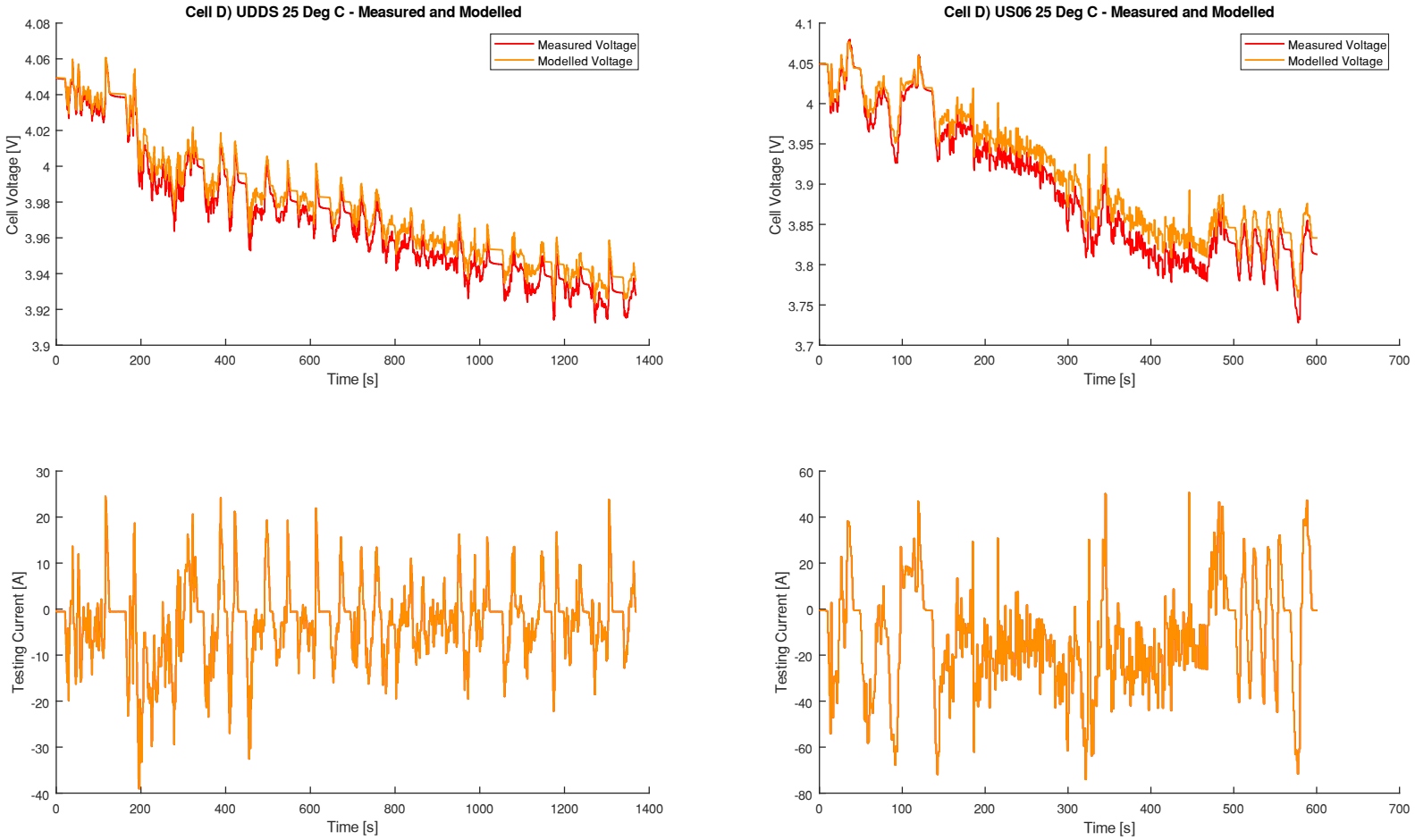

Figure 50: Cell D – measured and modelled terminal voltage for the UDDS and US06 drive cycles at 25°C

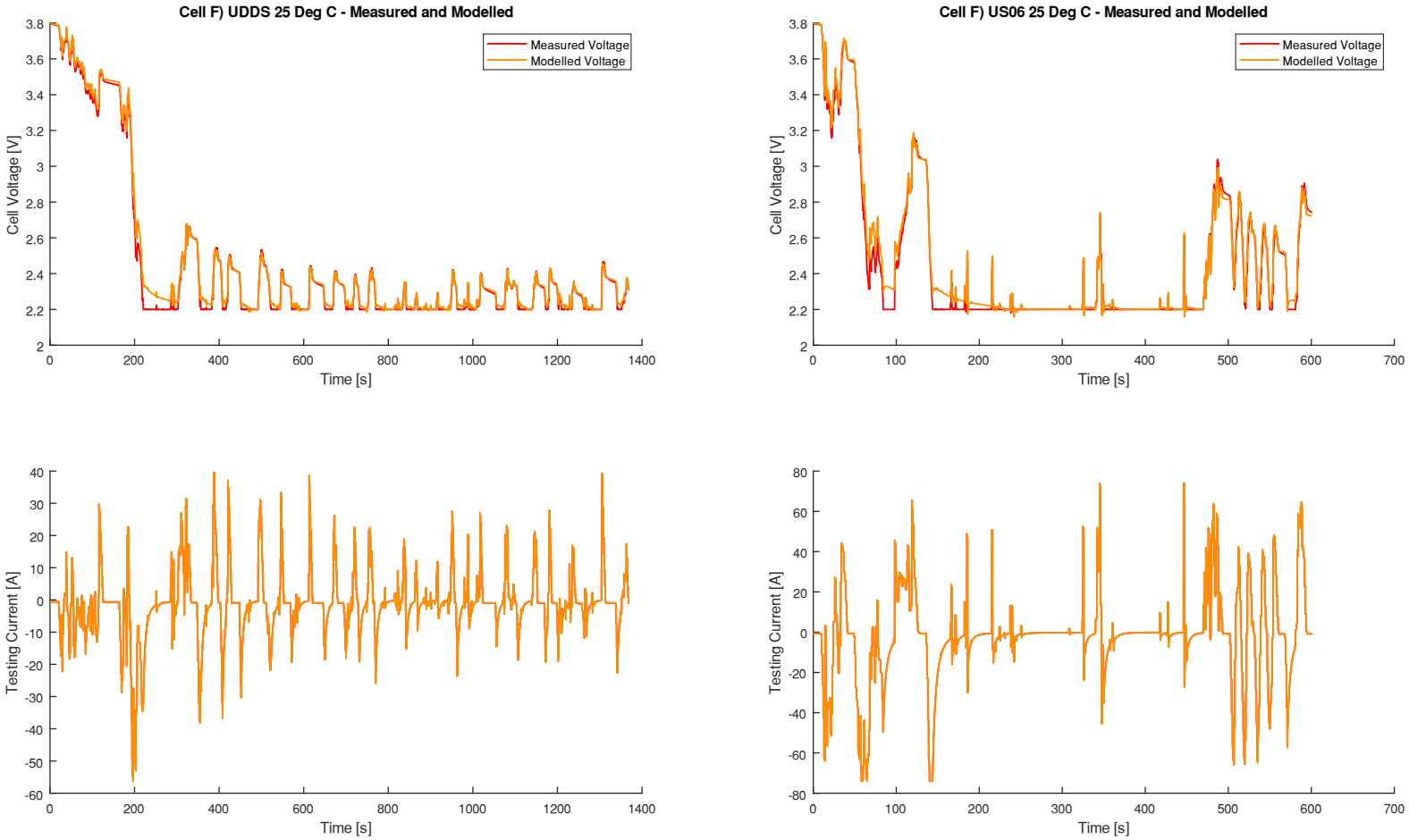

Figure 51: Cell F – measured and modelled terminal voltage for the UDDS and US06 drive cycles at 25°C

Drive Cycle	Temp [°C]	A EDLC	B EDLC	C LiC	D LiC	E LiC	F LiC	G ||LiC
UDDS	25	0.0515	0.0564[23]	0.0204	0.0079	N/A	0.0293	N/A
US06	25	0.0494	0.0488[23]	0.0258	0.0227	N/A	0.0473	N/A

Table 13: RMS of cell terminal voltage modelling error for UDDS and US06 drive cycle at 25°C

[23]Open circuit voltage modelled using 2A charge cycle from 35°C testing, not 25°C testing

5.8.5. Test 4 Conclusions

The following conclusions are made using data available from Figure 41 to Figure 51 and Table 13.

- The RMS value of the difference between the cell terminal voltage measured from drive cycle tests at 25°C and 0°C should not be used as a comparison metric to measure how much the cell performance is limited by cold temperature. This conclusion is made because the testing power levels, and therefore the testing current, are not necessarily equal for both temperatures due to cell voltage limitations that are hit sooner into the drive cycle in the 0°C environment.
- An alternative method to compare the cell drive cycle performance at 25°C and 0°C would be to look at the power cycle for both tests and visually evaluate any performance limiting that exists in cold temperatures. It is very important to recall that the testing current is limited to 75A and therefore the voltage increase/decrease due to the cell ESR can be considerably small. Larger testing currents would make the power difference between both testing temperatures more evident as the increase in ESR at cold temperatures would result in a larger terminal voltage change and therefore increase the need for additional testing current to achieve the desired power level.
- The 25°C and 0°C measured drive cycle data in Figure 41 to Figure 45 show very little cell performance difference for EDLC Cells A and B. However, LiC Cell C (Figure 43) and especially LiC Cell D (Figure 44) show considerable power limiting at 0°C compared to the

25°C data. Recall from Figure 38 that LiC Cell D showed the average 0°C ESR to be approximately 700% the average ESR at 25°C. This ESR increase is shown in Figure 44 by the additional terminal voltage variations presented by the 0°C test results.

- The results in Table 13 show that the capacitor cell model and experimentally determined cell characterization data from 25°C tests match the US06 and UDDS drive cycle data rather well with a maximum RMS terminal voltage error of 0.0564 V. The author considers this RMS error to be small and therefore justifies that the 25°C cell characterization data is useful for future cell modelling projects.

5.9. Test 5 – Self Discharge

The purpose of Test 5 was to quantify an approximate cell self discharge for each cell. This information is useful as it provides the energy storage system designer with a starting point to estimate how the ESS cells discharge without any load over an extended period. For example, it may be useful to know that an ESS discharges 20% of it's energy over one month without any load connected so that someone relying on an ESS in storage can estimate the useful energy content in the future. A self discharge test was performed my measuring the terminal voltage of each cell stored at room temperature over approximately 8 days. While this period is relatively short, the results reveal a considerable self discharge performance difference between the cells.

5.9.1. Test 4 Method

Cells A thru F were mounted inside the Thermotron SE-3000 thermal chamber and connected to individual channels on the Digatron cell tester, as shown in Figure 40. The cells were fully charged simultaneously in a 25°C environment. The original intention was to perform the self discharge testing from all cells at 100% SOC. However, due to the necessity to redo select drive cycle testing, the lack of availability for six Digatron testing channels simultaneously, and the author's absence, the self discharge was completed with the cells starting at different states of charge. The cells remained connected to the storage rack shown in Figure 40 and the Digatron

power cables were removed. Instead, cell terminal voltage extension cables were connected and routed to a NI 9205 module with input resistance of >10 GΩ || 100 pF. The cells were left at room temperature for approximately eight days while cell terminal voltage data was collected.

5.9.2. Test 4 Analysis

Figure 52 shows the change in cell terminal voltage for Cell A thru D and Cell F during the approximate 8 day self discharge test. Cell E is not included in this test due to issues experienced during the self discharge test. Cell G is not included in the test because the cell was unavailable due to additional time needed to complete Test 3 with a modified autocycler testing profile. Note that the vertical axis in Figure 52 shows the change in cell voltage relative to the voltage at the start of the self discharge test. The self discharge trends shown in Figure 52 are represented by five linear fit relationships and the key linear trend information is listed in Table 14. The approximate capacity change values in Table 14 were obtained by matching the starting and ending voltage from the self discharge tests to the 25°C 2A discharge profiles in Figure 30.

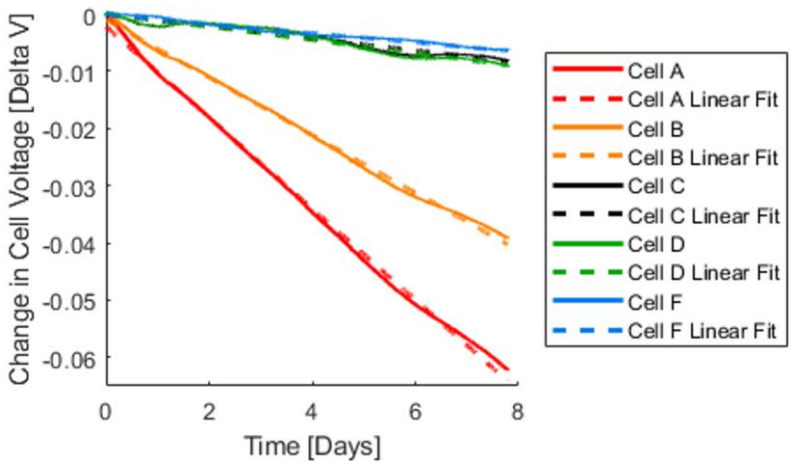

Figure 52: Change in cell voltage during an approximate 8-day self discharge test performed at room temperature

	A EDLC	B EDLC	C LiC	D LiC	E LiC	F LiC	G ||LiC
Starting Voltage [V]	1.780069	1.59764	2.797601	3.05397	N/A	3.223916	N/A
Ending Voltage [V]	1.717774	1.558425	2.789436	3.044893	N/A	3.222360	N/A
Voltage Change [ΔV]	0.062295	0.039215	8.165e-3	9.077e-3	N/A	1.556e-3	N/A
Linear Fit - Slope [V / Days]	-0.00795	-0.00503	-0.00105	-0.00117	N/A	-0.00019	N/A
Slope R^2	0.997	0.998	0.938	0.941	N/A	0.641	N/A
Y Intercept [ΔV]	-0.0022	-0.0010	-7.152e-05	0.0002	N/A	5.655e-06	N/A
Approx. Capacity Change [ΔmAh] [24]	50.22	32.89	7.00	67.11	N/A	0.44	N/A
Approx. Capacity Change [% SOC][24]	2.19	1.54	0.48	0.63	N/A	0.09	N/A
Approx. Self Discharge [mAh/day]	6.442	4.219	0.898	8.609	N/A	0.057	N/A
Approx. Self Discharge Current [mA]	0.268	0.176	0.037	0.359	N/A	0.002	N/A

Table 14: Self discharge test results obtained over approximately 7.8 days of voltage measurements.

[24] Compared to measured discharge capacity from Table 5

5.9.3. Test 4 Conclusions

The following conclusions are made using data available in Figure 52 and Table 14.

- EDLC Cells A and B experienced the largest cell voltage decrease and approximate change in SOC.
- LiC Cells C and F have the smallest approximate self discharge current. However, LiC Cell D showed the largest approximate self discharge current (mA) while having a relatively small voltage change. Recall that Cell D has the largest capacity and therefore a small voltage change corresponds to a large capacity change (2nd largest capacity change was from EDLC Cell A).

5.10. Conclusion to Compare EDLC and LiC Cell Performance

This chapter presented select analysis of over 881 hours of performance testing for two EDLC cells, four LiC cells and one ||LiC cell. Section 5.2 provided a cell specification comparison and Ragone plots, both containing datasheet and experimentally derived data. This section concluded that the ||LiC and LiC cells exceeded the volumetric and gravimetric energy density of the EDLC cells, however, there was no superior power density trend between the LiC and EDLC

cells. Section 5.3 explained the custom cell testing fixtures developed for the capacitor cells. Section 5.4 provided an overview of the cell testing methods and data analysis workflow. Section 5.5 discussed Test 1 which examined constant loss thermal cycling and the impact on cell energy loss and temperature rise. This section concluded that the ambient temperature considerably impacts the calculated thermal case to ambient resistant (R_{CA}). However, estimating the ESR using energy loss values for constant cycling showed very little dependence on the ambient temperature. During charging the LiC cells decreased in temperature while the EDLC cells increased for the given testing conditions. Section 5.6 discussed Test 2 which analysed the 2A constant current charge and discharge voltage vs. SOC profile for all cells. The EDLC and LiC cells had a near linear charge and discharge profile with very little hysteresis. However, ||LiC Cell G demonstrated a very non-linear 2A constant current voltage profile with considerable hysteresis. The 2A constant current voltage profile for the EDLC and LiC cells showed very little dependency on cell temperature while the ||LiC cell's unique 2A constant current voltage profile changed considerably with temperature. Section 5.6.3 evaluated the usable constant current charge/discharge capacity and energy of each cell for a variety of currents and temperatures. It was concluded that all cells had a larger charging energy than discharging energy which indicates a cyclic energy efficiency of <100%. In comparison to test results at 25°C, the EDLC cells experienced the smallest performance change in usable charge/discharge energy and capacity when used in cold temperatures; followed by the LiC cells and then the ||LiC cell, which showed the largest performance change. This result was explored further in Section 5.7.2 which analyzed the cells' ESR dependency on SOC and temperature. These results concluded that the EDLC cells had the lowest average ESR which was relatively consistent across the SOC range with very little dependency on temperature. The ||LiC and LiC cells showed a considerable ESR increase when tested in cold temperatures. The ||LiC ESR vs. SOC profile was uniquely non-linear and changed

shape based on the cell temperature. Section 5.7.5 analyzed the ESR dependency on current to evaluate if a Butler-Volmer type of relationship existed. The ESR for EDLC cells showed very little dependency on the charge/discharge current magnitude. However, LiC Cells C thru F showed considerable ESR dependency on the testing current, especially at cold temperatures and ||LiC Cell G demonstrated the largest ESR current dependency. In general, the lithium based capacitor cells demonstrated a larger ESR at low test current pulses. Section 5.8 presented modified US06 and UDDS drive cycle testing results at 0°C and 25°C as well as cell modelling results compared to drive cycle tests at only 25°C. Similar to Section 5.6.3 and 5.7, the experimental drive cycle work in Section 5.8 confirmed that the EDLC cells have little performance degradation in cold temperatures while the lithium based capacitors do show a performance difference. The minimal RMS error between the 25°C measured and modelled cell terminal voltage confirmed that select cell characterization data can be used to model certain cells with reasonable accuracy. Section 5.9 evaluated the cell self discharge of six cells over approximately 8 days. This section concluded that although the EDLC cells experienced the largest cell voltage change and approximate change in SOC, LiC Cell D showed the largest approximate self discharge current.

In general, the ||LiC and LiC cells showed a considerable increase in energy density compared to the EDLC cells. However, the lithium-based capacitors exhibit a relatively large ESR (lower power output capability) that shows considerable dependency on temperature. Depending on the application, lithium-based capacitors may be an alternative to EDLC cells in volume and mass restricted applications that operate at room temperature or slightly warmer. Considering these temperature dependencies and the limited cycle life compared to EDLC cells, additional consideration should be made to explore the use of high power battery chemistries, such as lithium titanite, for higher power applications.

6. Towards the Development of a DC Metro Railway System Modelling Tool

6.1. Modelling Approach

The railway vehicle model presented in this chapter makes use of a backward-facing modelling approach such that the power flow is calculated "backwards" from the drive cycle velocity profile through to the energy supply. In a backward-facing modeling approach the velocity profile is used as an input to a vehicle model that then determines the power required to meet the desired velocity profile. The power demand is used as the input to the torque producing device; whether it be the internal combustion engine, electric motor or any combination. Efficiency maps are typically used to determine the power required from the energy source (gasoline fuel system, electrical energy storage and/or the electrical supply system) to power the torque producing device. Backward-facing models generally assume that the vehicle can provide the power required for the drive cycle and therefore act as a useful resource for component sizing. However, if the vehicle components are undersized in terms of power performance then a backwards-facing model will typically not limit the vehicle performance and may provide a false sense of performance. The inability to meet a drive cycle based on backward-facing models is evident when the supplied components are not specified to produce the required power levels as determined from the backward-facing model. A general layout for a backward-facing model is shown in Figure 53**.**

The main alternative to backward-facing modelling methods is to use forward-facing modelling. This modeling method is generally based on the vehicle trying to achieve the desired drive cycle using a driver model and performance limitations of powertrain components. The drive model typically uses one or more controllers to request propulsion or braking torque to the wheels in

attempt to meet the desired drive cycle. If the powertrain components are undersized then the vehicle will provide insufficient power levels and the actual drive cycle will not closely match the desired drive cycle. The forward-facing modelling approach is typically more useful to determine vehicle performance once powertrain components are selected. Additionally, it is typically less difficult to develop vehicle control strategies and perform hardware in the loop (HIL) testing using the forward-facing modelling method. However, considering the limited availability of powertrain component modelling resources for DC powered metro systems, the forward-facing method would be rather difficult to implement. Similarly, considering that the focus of this work is to look at the net vehicle power and energy consumption, the need for vehicle controls development and HIL testing is non-existent. A general model layout for a forward-facing model is shown in Figure 53**.** Additional comparison between forward-facing, backward-facing, and backward/forward combined modelling methods can be found in [105] [106] and [107].

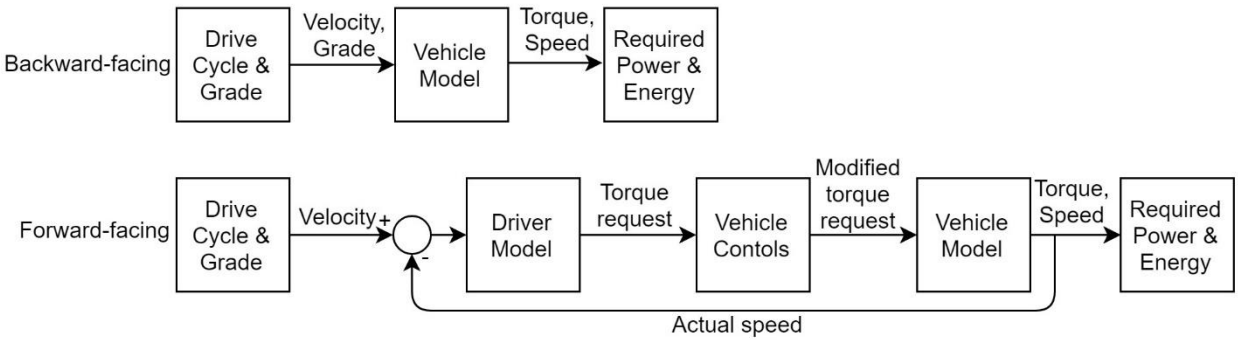

Figure 53: Simplified vehicle model workflow using the backward-facing (top) and forward-facing (bottom) methods

The backward-facing modelling workflow used to develop the railway simulation tool is broken down into the blocks shown in Figure 54. The red blocks represent a collection of data that could be used as input parameters to the vehicle simulation tool. The green blocks primarily represent kinematic and mechanical power calculations while the yellow blocks primarily represent electrical calculations.

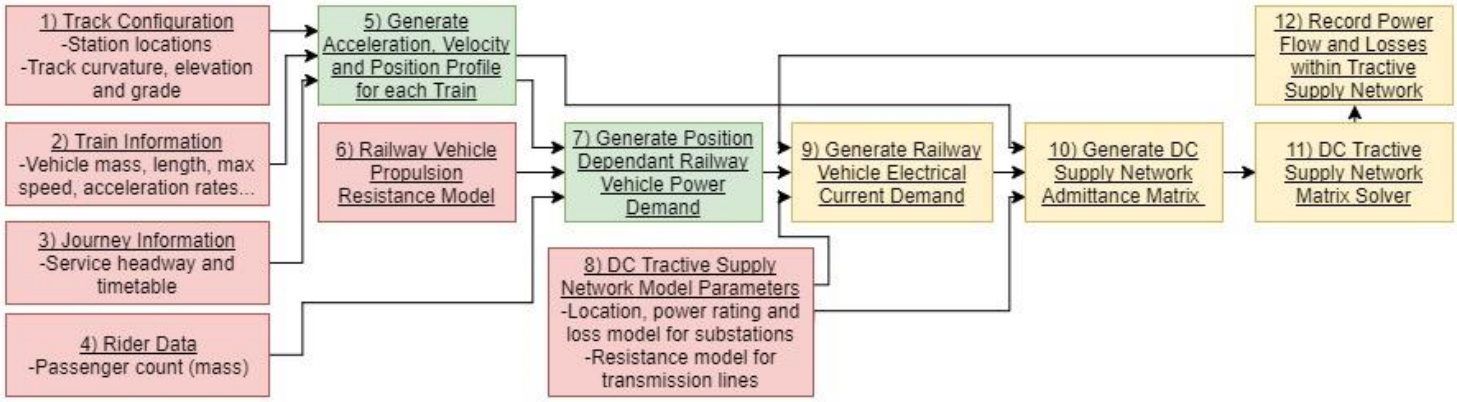

Figure 54: Modelling workflow used to develop the railway simulation tool

The following subsections will explore the relationships used to model the inner workings of most blocks within Figure 54. Select input data from blocks 1) thru 4), 6) and 8) will be discussed as a collection of parameters in Chapter 7. Chapter 7 makes use of blocks 1 thru 9 to compare the mass and volume of cells for a LiC and EDLC based ESS for a catenary free station to station drive cycle for one vehicle. As a guide for future work, additional discussion on proposed modelling methods for a multi vehicle railway simulation tool, including blocks 10) and 11) is included in this chapter.

6.2. Block 5 - Drive Cycle Development

A shown in Figure 53, the first input to the backward-facing modelling method is the velocity vs time drive cycle. Standardized velocity drive cycles, such as US06, UDDS, and HWFET, are commonly used for automotive modelling. However, these standardized drive cycles are not representative of railway velocity vs time profiles and therefore a modular metro drive cycle

creation function was developed in this work. This section describes the modelling methods used to generate the output from block 5) in Figure 54.

6.2.1. Station-To-Station Drive Cycle Generation

The drive cycle for one subway train consists of several smaller drive cycles between the subway stations. Therefore, the first step in developing the subway train drive cycle is to develop the miniature drive cycle between each subway station. The development of mini station-to-station drive cycles must consider the following:

- Not all stations have an equal travel distance between them
- The subway train must drive the exact distance between the subway stations without overshooting or undershooting the station platforms
- The subway train has a maximum acceleration and braking rate
- The subway train has a maximum travelling speed that may be limited by the rollingstock or track configuration

As shown by Figure 5 in [33, p. 670], which displays the DC supply line power and speed for an MVV Verkehr AG prototype light rail vehicle, the velocity profile for passenger rail can have a trapezoidal shape consisting of an acceleration phase, constant speed phase and braking phase. The velocity profile for passenger trains, including metro/subway trains, may be more complicated than shown in [33, p. 670] by introducing coasting phases and/or or speed limited regions used to navigate specific track sections. However, due to simplicity, the velocity profile between stations will be defined using the simplified trapezoidal velocity vs time relationship shown in Figure 55.

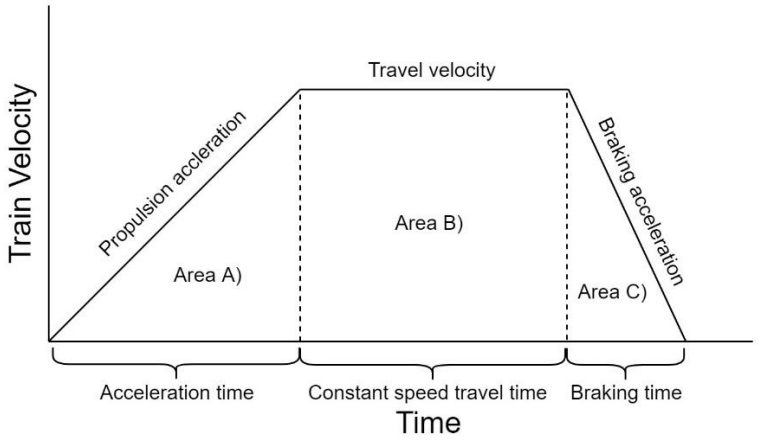

Figure 55: Simplified metro train station-to-station velocity profile

In knowing the desired train acceleration, braking acceleration, travel distance and travel time, the station-to-station velocity profile can be defined using the following relationships in Equation 14 to Equation 22.

$$x_{travel} = v * t$$

Equation 13: Distance travelled when moving at a constant velocity (v) for duration of (t)

$$x_{travel} = v_o t + \frac{1}{2} a t^2$$

Equation 14: Distance travelled, (x_{travel}), when accelerating at a constant rate (a) from a starting velocity (v_o) for a duration of (t)

With reference to Figure 55, Equation 13 and Equation 14, the train's total distance travelled can be represented as the sum of the distances travelled during the acceleration, constant speed and braking times. The distances travelled can be represented by the sum of the areas A thru C under the velocity profile.

$$x_{station-to-station} = A_A + A_B + A_C$$

Equation 15: Distance travelled between stations, ($x_{station\text{-}to\text{-}station}$), represented as the sum of areas A, B and C

$$x_{station-to-station} = \left(\frac{1}{2} v_{travel} t_{acceleration}\right) + \left(v_{travel} t_{constant\ speed}\right) + \left(\frac{1}{2} v_{travel} t_{braking}\right)$$

Equation 16: Distance travelled between stations, ($x_{station-to-station}$), represented as the sum of areas A, B and C using kinematic representations

The acceleration and braking times can be represented by the related acceleration rates and the train travel speed.

$$v_{travel} = v_o + at \qquad v_{travel} = a_{propulsion} t_{acceleration} \qquad v_{travel} = a_{braking} t_{braking}$$

$$t_{acceleration} = \frac{v_{travel}}{a_{propulsion}} \qquad t_{braking} = \frac{v_{travel}}{a_{braking}}$$

Equation 17: Relate the acceleration time ($t_{acceleration}$) and braking time ($t_{braking}$) to the respective acceleration values and train travel speed (v_{travel})

Equation 16 can be updated using the relationships in Equation 17 to form Equation 18.

$$x_{station-to-station} = \left(\frac{1}{2} v_{travel} \frac{v_{travel}}{a_{propulsion}}\right) + \left(v_{travel} t_{constant\ speed}\right) + \left(\frac{1}{2} v_{travel} \frac{v_{travel}}{a_{braking}}\right)$$

$$x_{station-to-station} = \left(\frac{{v_{travel}}^2}{2 * a_{propulsion}}\right) + \left(v_{travel} t_{constant\ speed}\right) + \left(\frac{{v_{travel}}^2}{2 * a_{braking}}\right)$$

Equation 18: Relate the acceleration time ($t_{acceleration}$) and braking time ($t_{braking}$) to the respective acceleration values and train travel speed (v_{travel})

The total travel time between stations can be represented as the sum of the acceleration, constant speed travel and braking times.

$$t_{constant\ speed} = t_{total} - t_{acceleration} - t_{braking}$$

$$t_{constant\ speed} = t_{total} - \frac{v_{travel}}{a_{propulsion}} - \frac{v_{travel}}{a_{braking}}$$

Equation 19: Relate the acceleration time ($t_{acceleration}$) and braking time ($t_{braking}$) to the respective acceleration values and train travel speed (v_{travel})

Equation 18 can now be updated with Equation 19 to eliminate the constant speed travel time variable.

$$x_{station-to-station} = \left(\frac{{v_{travel}}^2}{2 * a_{propulsion}}\right) + \left(v_{travel}(t_{total} - \frac{v_{travel}}{a_{propulsion}} - \frac{v_{travel}}{a_{braking}})\right) + \left(\frac{{v_{travel}}^2}{2 * a_{braking}}\right)$$

$$x_{station-to-station} = \left(\frac{{v_{travel}}^2}{2 * a_{propulsion}}\right) + t_{total}v_{travel} - \frac{{v_{travel}}^2}{a_{propulsion}} - \frac{{v_{travel}}^2}{a_{braking}} + \left(\frac{{v_{travel}}^2}{2 * a_{braking}}\right)$$

$$x_{station-to-station} = \left(-\frac{{v_{travel}}^2}{2 * a_{propulsion}}\right) + t_{total}v_{travel} + \left(-\frac{{v_{travel}}^2}{2 * a_{braking}}\right)$$

Equation 20: Distance between stations ($x_{station-to-station}$) represented in terms of the constant travel speed (v_{travel}), total travel time (t_{total}), acceleration rate ($a_{propulsion}$) and braking rate ($a_{braking}$).

Equation 20 is a quadratic equation that can be modified to find the quadratic roots.

$$0 = \left(-\frac{{v_{travel}}^2}{2 * a_{propulsion}}\right) + t_{total}v_{travel} + \left(-\frac{{v_{travel}}^2}{2 * a_{braking}}\right) - x_{station-to-station}$$

$$0 = {v_{travel}}^2\left(-\frac{1}{2} * \left(\frac{1}{a_{propulsion}} + \frac{1}{a_{braking}}\right)\right) + v_{travel}t_{total} - x_{station-to-station}$$

$$0 = {v_{travel}}^2\left(-\frac{1}{2} * \left(\frac{1}{a_{propulsion}} + \frac{1}{a_{braking}}\right)\right) + v_{travel}t_{total} - x_{station-to-station}$$

$$0 = (x^2 * a) + (x * b) - c$$

$$x = v_{travel} \qquad a = -\frac{1}{2} * \left(\frac{1}{a_{propulsion}} + \frac{1}{a_{braking}}\right) \qquad b = t_{total} \qquad c = -x_{station-to-station}$$

$$v_{travel} = x = \frac{-b \pm \sqrt{b^2 - 4ac}}{2a}$$

Equation 21: Formulation of the quadratic equation coefficients (a, b, and c) used to determine the travel velocity (v_{travel})

The quadratic roots that come of Equation 21 provide significant insight into the viability of the drive cycle for the given propulsion and braking acceleration rates, travel time and distance between the stations. One or more complex roots indicate that the drive cycle is not possible with the given drive cycle parameters. Two real roots indicate that the drive cycle is possible. However, the larger constant speed travel time root typically corresponds to a negative constant speed driving time, which is not practical, and therefore the minimum driving speed should be used.

$$if\ roots[a\ b\ c] == real$$

$$v_{travel} = \min(roots[a\ b\ c])$$

$$else$$

$$v_{travel} = impractical$$

Equation 22: Constant speed travel time determined from the maximum real

The mini station-to-station drive cycle can now be fully defined using the given total travel time (t_{total}), travel distance ($x_{station-to-station}$), propulsion acceleration ($a_{propulsion}$) and braking acceleration ($a_{braking}$). The travel velocity (v_{travel}), which is determined using Equation 21 and Equation 22, can be used to determine the accelerating time ($t_{acceleration}$) and braking time ($t_{braking}$) using Equation 17. The final drive cycle parameter, the constant speed travel time ($t_{constant\ speed}$), can be determined using Equation 19. Figure 56 shows an example mini station-to-station drive cycle that was produced using the `MakeMiniDriveCycle` MATLAB function (shown below) that makes use of Equation 13 to Equation 22.

```
function [DriveProfile, DCKeySpecs, FailFlag] =
MakeMiniDriveCycle(Distance, Time, TimeStep, MaxAllowedVelocity,
PosAccel, NegAccel)
```

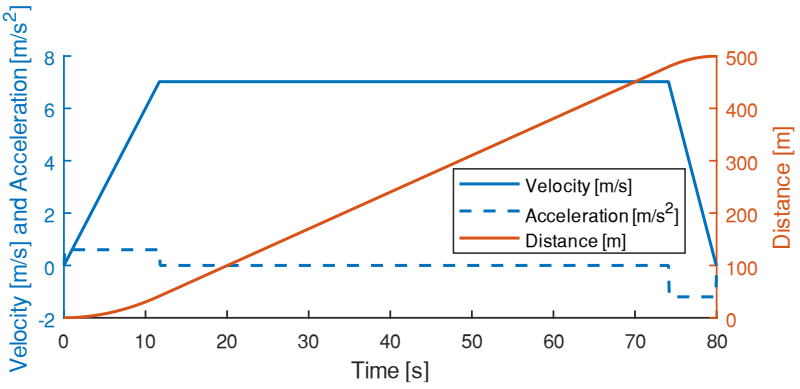

Figure 56: Example mini station-to-station drive cycle for a subway train with station spacing of 500m, travel time of 80s, acceleration of 0.6m/s^2 and braking acceleration of 1.2 m/s^2

6.2.2. One Way and Round-Trip Drive Cycle Generation – Proposed

The catenary free ESS sizing exercise in Chapter 7 relies on a station-to-station drive cycle for one vehicle. The details within this subsection are provided as an aid for future work.

It is proposed that the railway simulation tool record the location of each train relative to the first station at a location of 0m. The trip travelling from the starting station to the end station is referred to as the forward trip. Similarly, travelling from the end station to the starting station is called the return trip. The combination of an initial rest at the starting station followed by the forward trip, a turn around delay, and the return trip form one "round-trip" (see Figure 57).

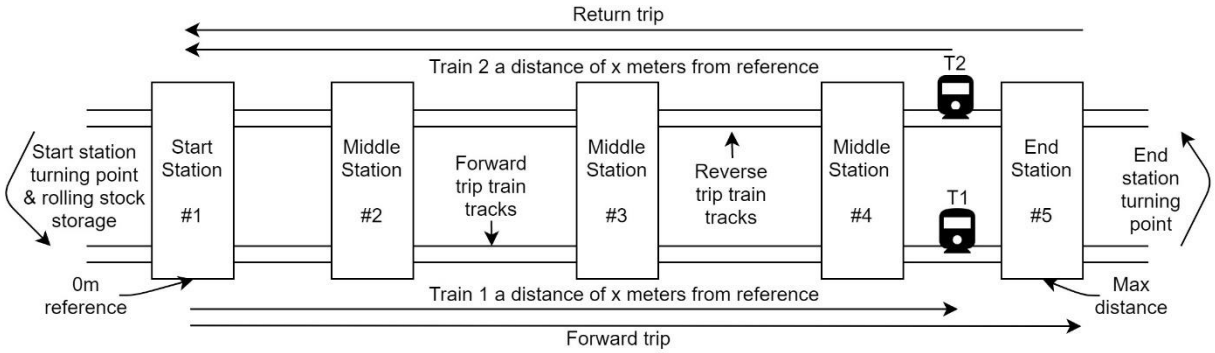

Figure 57: Simulated railway system track configuration, naming conventions and train locations relative to starting station

The forward trip drive cycle is developed by concatenating a series of mini station-to-station drive cycles separated by station stop times. Considering that the subway stations are not equally spaced apart, and the time required to travel between them may vary, the MATLAB function `MakeLargeDriveCycle`, shown below, calls the `MakeMiniDriveCycle` several times with unique inputs. The time delay between mini station-to-station drive cycles is determined according to the `StopTimes` input variable that represents the time needed to unload and reload passengers at the start of the trip between stations. Figure 58 shows an example of a forward trip drive cycle developed using the `MakeLargeDriveCycle` function with three subway stations.

```
function [LargeDriveProfile, LargeDCKeySpecs, LargeDCFailFlag] =
MakeLargeDriveCycle(StationLocations, TravelTimes, StopTimes, TimeStep,
MaxAllowedVelocity, PosAccel, NegAccel)
```

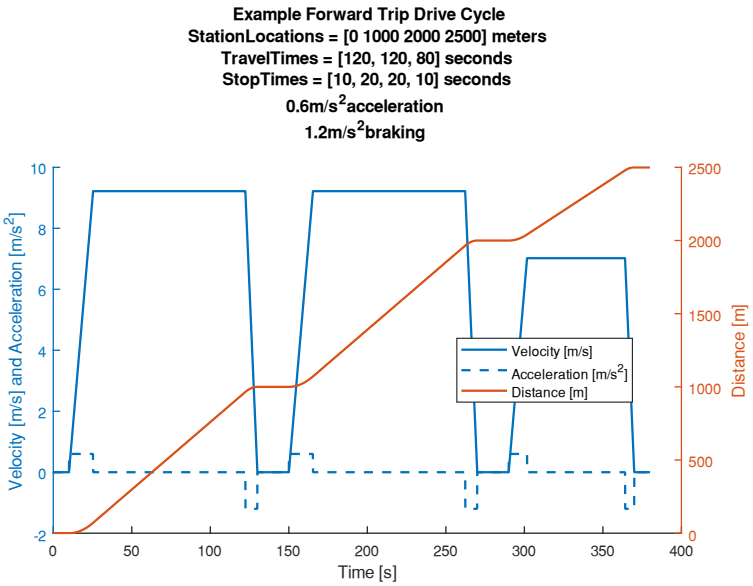

Figure 58: Example forward trip drive cycle. The trip parameters are listed in the plot title.

The round-trip drive cycle is developed using the `MakeFullDC` function shown below. The `MakeFullDC` function calls the `MakeLargeDriveCycle` function twice; once for the forward trip and once for the return trip. The return trip is determined separately from the forward trip using the original station locations, travel times and stop times but rearranged in a different order. The return trip cannot simply be represented as the forward trip driven in reverse as the propulsion and braking accelerations would be incorrectly switched and not represent the vehicle's driving behaviour. The time required to turn the train around between the forward and return trips, noted by `UTurnTime`, is inserted between the two trips. It is assumed that the train is travelling at a very slow speed during the track change and therefore the power required during this time will not be modelled. Figure 59 shows an example return trip developed using the `MakeFullDC` function. Note that the positive acceleration values are smaller in magnitude compared to the braking, regardless of the travelling direction.

```
function [MetroDC, MetroDCFwd, MetroDCRev] =
MakeFullDC(StationLocations, TravelTimes, StopTimes, TimeStep,
UTurnTime, DelayTime, MaxAllowedVelocity, PosAccel, NegAccel)
```

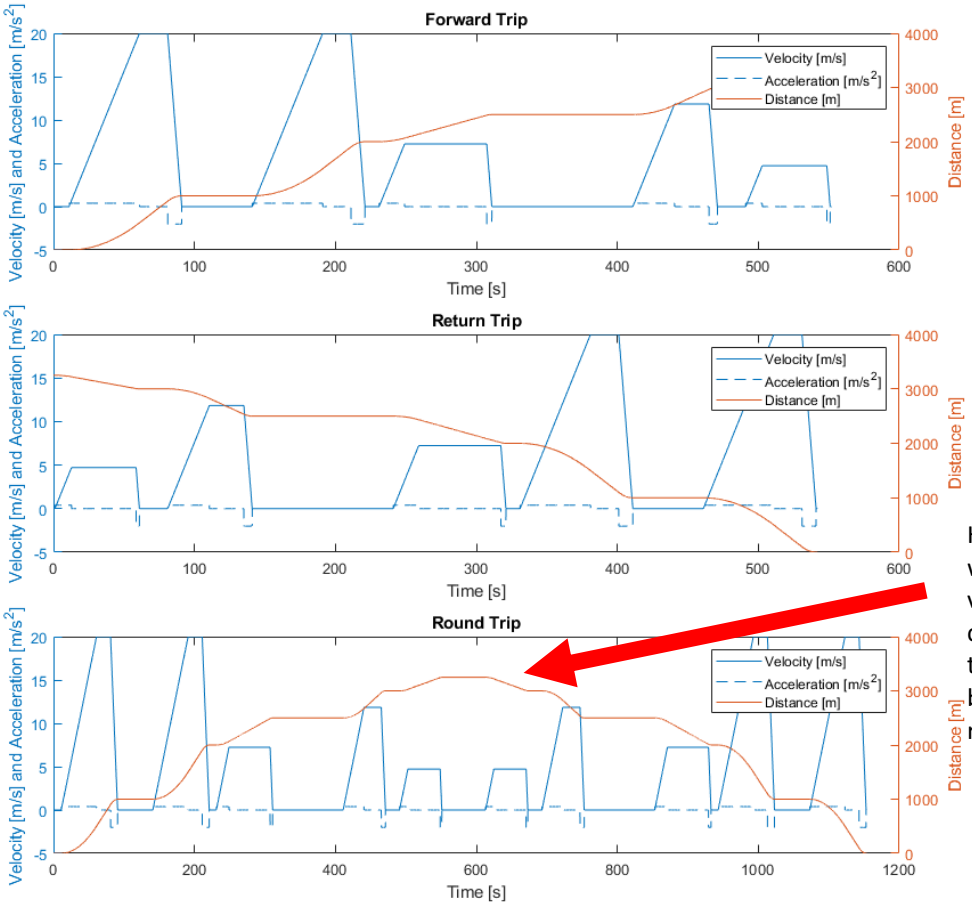

Figure 59: Example forward, return and round-trip drive cycle for a railway system with ten stations.

6.2.3. Multi Vehicle Drive Cycle - Proposed

The catenary free ESS sizing exercise in Chapter 7 only relies on a station-to-station drive cycle for one vehicle. The details within this subsection are provided as an aid for future work.

Considering that the DC supply micro-grid provides power to multiple rail vehicles simultaneously, it is necessary to model the power, and therefore the drive cycle, required by all vehicles in operation. A multi vehicle drive cycle is developed using the `MakeMultiTrainFullDC` function (shown below) that calls the `MakeFullDC` function for each vehicle. The number of trains required to provide transit service for the duration

`ApproxRunningTime` is determined based on the return trip time and headway. The headway defines the time between trains arriving at a desired station. The vehicles are delayed at the starting station in integer intervals of the headway time. In repeating the same round-trip drive cycle for each vehicle, a new vehicle will arrive at the stops within the headway period after the previous vehicle departed. The effect of placing vehicles into service with delays that are integer multiples of the headway results in a very repetitive trip schedule, as shown in Figure 60 and Figure 61.

```
function [MetroDC, NumTrips, NumTrains, ActualRunningTime,
CollissionData] = MakeMultiTrainFullDC(ApproxRunningTime, Headway,
StationLocations, TravelTimes, StopTimes, TimeStep, UTurnTime,
MaxAllowedVelocity, PosAccel, NegAccel, TrainLength)
```

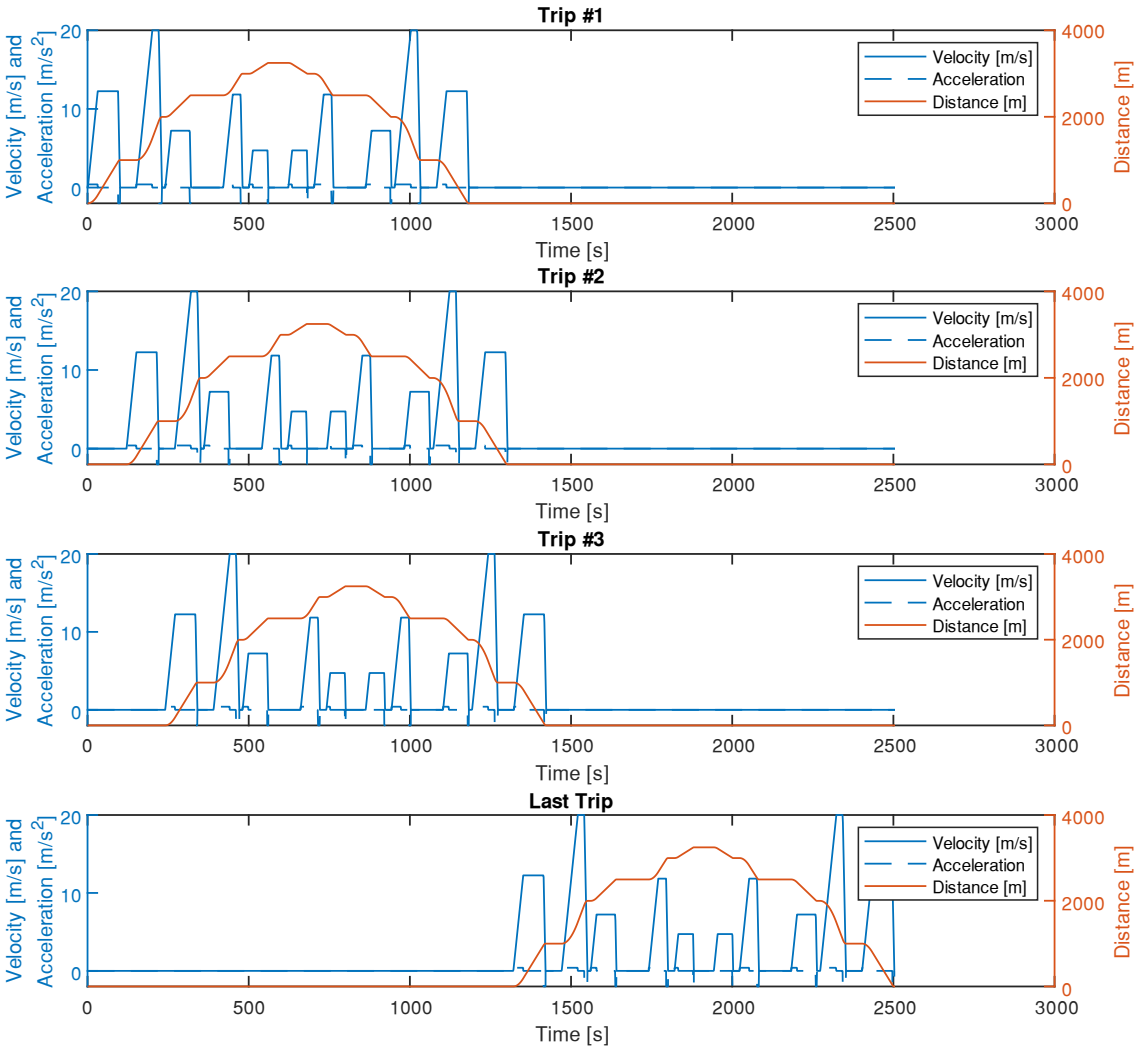

Figure 60: Return trip drive cycle for a multi vehicle railway system. The first three and final vehicle trip are shown in succession with the same drive profile repeated but with a start delay equal to an integer multiple of the headway time.

Figure 61 provides an alternative representation of the drive cycle data in Figure 60 by showing the vehicle locations for all trips during the service time.

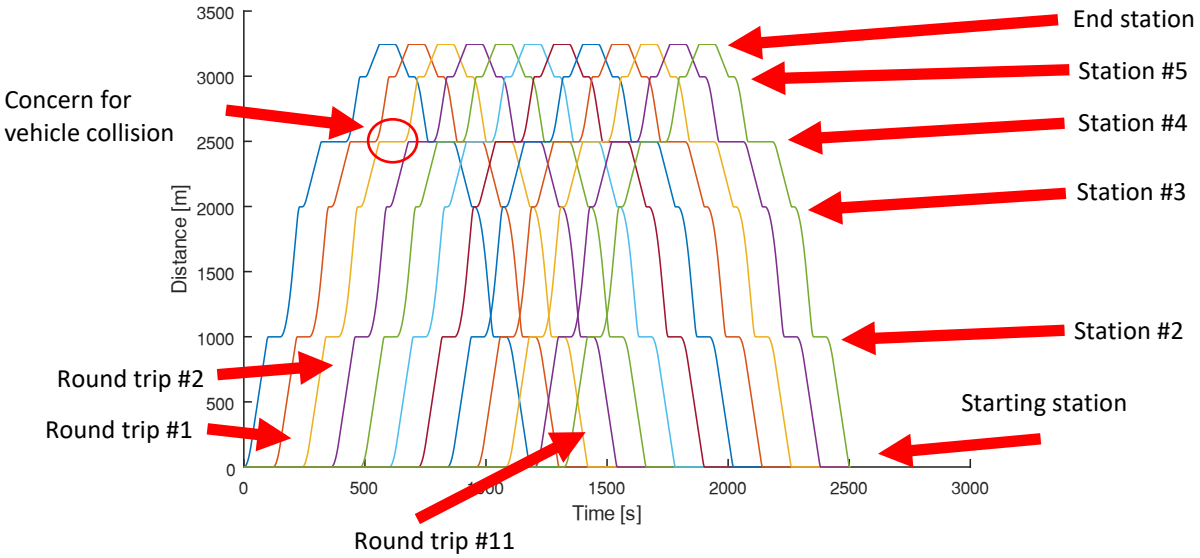

Figure 61: Example of a multi train schedule showing the location of all trains in service. This schedule corresponds to the drive cycles shown in Figure 60.

Each line in Figure 61 represents a different round trip required to provide transit service for the specified duration. The horizontal lines in each trip represent the vehicles stopping to change passengers or change travel directions. Although there may be 'X' number of trips necessary to meet the transit requirements, the number of trains may be less than or equal to 'X'. For example, in Figure 61 round trip #1 returns to the starting station (distance of 0 meters) at approximately 1182 seconds. Round trip #11 starts at approximately 1203 seconds. The 21 second difference between these trips may be sufficient to move the vehicle from the return tracks to the forward tracks.

The circled area on Figure 61 highlights a concern regarding a collision between vehicles. The `MakeMultiTrainFullDC` function makes use of the input variable `TrainLength` to determine if the vehicles travelling round-trip #1 and #2 remain a minimum distance apart equal to the train length. If not, then the simulation tool will identify when and where the collision would occur, with respect to the reference starting station. If the proposed multi vehicle drive

cycle is infeasible due to a collision, then the `MakeMultiTrainFullDC` function inputs should be modified. For the case shown in Figure 61, the collision concern could be reduced by minimizing the stop time at station #4 or by increasing the headway time which introduces a larger time delay between the trips.

In summary, the `MakeMultiTrainFullDC` function provides the multi vehicle drive cycle information needed as the output of block 5) and input to block 7) from Figure 54. Section 6.3 explores how the power profile for each trip is developed using the drive cycle data as an input.

6.3. Block 7 - Power Profile Development

This section primarily describes the kinematic and mechanical power equations used to determine the power required by a vehicle to achieve the desired trip velocity profile. With reference to Figure 54, this section explains the inner workings of block 7) which provides the position dependant power levels needed by block 9). The major forces acting on a simplified railway vehicle are summarized by Figure 62, Equation 23 and Equation 24.

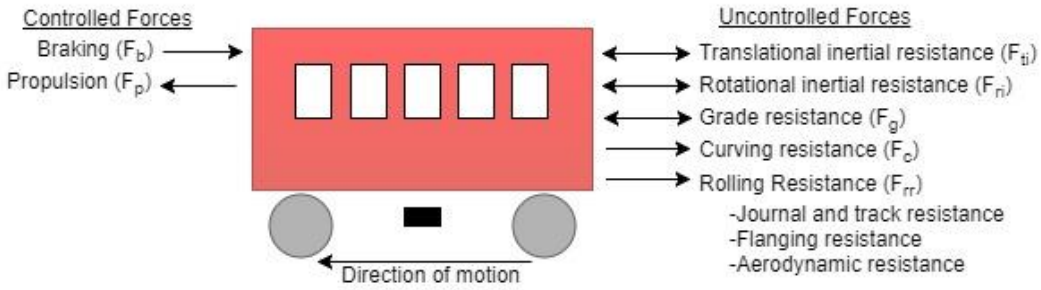

Figure 62: Simplification of the forces acting on a railway vehicle.

$$P_{train,mech} = F_p * v_{train}$$

Equation 23: Mechanical power required to move the railway vehicle

$$F_p = F_b + F_{ti} + F_{ri} + F_g + F_{rr}$$

Equation 24: Sum of forces acting on the railway vehicle as shown in Figure 62.

6.3.1. Propulsion Resistance / Drag Power

The difficulty to decouple, quantify and model the individual rolling resistance forces (F_{rr}) acting on a railway vehicle (shown in Figure 62) introduces the need for experimentally derived relationships. In Rochard and Schmid's review of train resistance measurement and calculation methods [108], the authors state that "all railway undertakings base their calculations of train resistance to motion on run-down tests for given types of rolling stock" [108, p. 191]. Run-down testing, or commonly called coast-down testing, typically involves driving a vehicle to a desired speed and then allowing it to naturally slow down on a level straight surface without the drive system enabled. The vehicle velocity vs time profile is differentiated to obtain an acceleration vs time profile. The vehicle's equivalent mass, velocity profile and acceleration profile are multiplied to obtain a coast down drag power vs velocity relationship. The cost down drag power vs velocity relationship typically follows a 3rd order polynomial relationship. The third order nature of the drag power vs velocity function aligns well with the cubic representation for the air drag power shown in Equation 25.

$$P_{air\ resistance} = F_{air\ resistance} * v_{vehicle}$$

$$P_{air\ resistance} = \frac{1}{2} p A v_{vehicle}^2 C_d * v_{vehicle} = \frac{1}{2} p A C_d v_{vehicle}^3 C_d$$

Equation 25: General representation of the power required to overcome air resistance

In automotive and railway applications the coast down power vs velocity profile represents several drag forces that are not necessarily related to velocity squared. Therefore, the drag power vs velocity profile is fit using a 3rd order polynomial with three unique cost down coefficients A, B and C as shown in Equation 26. The coast down force representation in Equation 26 is commonly referred to as the Davis equation. The power required to over come the forces from the Davis equation, and therefore drive at a constant speed on a level surface, can be represented by Equation 27. A detailed explanation and example of experimentally

determined coast down coefficients for an electric passenger truck are described by Dr. Kollmeyer in Section 3.2 of [109].

$$F_{drag} = A + Bv_{vehicle} + Cv_{vehicle}^2 \text{ (Davis equation)}$$

Equation 26: General 3rd order polynomial representation of a vehicle's coast down drag forces as a function of velocity

$$P_{drag} = Av_{vehicle} + Bv_{vehicle}^2 + Cv_{vehicle}^3$$

Equation 27: General 3rd order polynomial representation of a vehicle's coast down power as a function of velocity

The Davis equation approach to modelling the mechanical power required to propel a railway vehicle is used in the railway simulation tool. Due to several difficulties in obtaining experimental coast down results, including instrumentation costs, lack of readily available railway vehicles, and considerable time, the coast down coefficients A, B and C were obtained from literature.

For railway applications, the A coefficient, which can be measured in Newtons [N], is typically used to collectively represent mass dependent resistive forces such as bearing/journal resistance and track resistance. As the weight of the train cars pushes the wheels against the track, the rail may experience deflection and create a small "uphill" resistive force of up to 1.5 lb/ton [110, p. 71].

The B coefficient, which can be measured in [N/(m/s)], is typically used to represent speed dependent forces such as flanging resistance. Railway wheels have a unique conical shape with a larger inner diameter that is complemented by an inner flange. Depending on the slack between the track gauge and wheel flange separation, the train's trajectory follows a lateral path, almost "bouncing" from rail to rail in a motion commonly called hunting [110, p. 73]. The flanging resistance that results from hunting typically increases with speed [110, p. 73]. In addition to the B coefficient, the flange contributes to a separate term; the flanging curve resistance (F_c) which can be modeled in many ways [49, p. 39]. Two simple formulations for the flanging curve

resistance are shown in Equation 28 where F_{c1} is in [N/tonne of wagon mass], F_{c2} is in [kN/t], R is the curve radius in [m] and k is dimensionless and varies from 500 to 1200 (800 average) depending on the vehicle [108, p. 188]. The railway simulation tool developed in this work assumes the rail vehicles are travelling straight and therefore the flanging curve resistance is omitted.

$$F_{c1} = \frac{6116}{R} \text{ [111, p. 143]}$$

$$F_{c2} = 0.01\ \frac{k}{R} \text{ [108, p. 188]}$$

Equation 28: Two representations for the force resulting from the curve resistance.

The C coefficient, which can be measured in $[N/(m/s)^2]$, represents resistance forces that vary with the velocity squared; such as air resistance. In subway applications the air pressure wave from travelling in tunnels should be considered [49, p. 38] [80, p. 9] [112, pp. 11-15]. As shown in [113, p. 6] and [114, p. 35] the C variable used to represent travelling in a tunnel is approximately two to three times the C value used for surface (not in a tunnel) trips. The railway simulation tool presented in this work makes use of the input variable C which can be modified to represent surface or tunnel driving conditions. However, a more advanced simulation tool could make use of a varying C coefficient that is determined based on the proportion of the rail vehicle that is travelling above ground and in tunnels.

6.3.2. Grade Power - Proposed

Considering the extended vehicle length, the gradient resistance (F_g) and gravitational potential energy of each independent car should be modelled each time step as the train moves over geographic features [111, p. 144]. Figure 63 demonstrates how the independent inertial masses of each train car can contribute to or reduce the power required to drive over an elevation change. The author suggests using a quasi-dynamic longitudinal vehicle model that represents the train cars as multiple independent inertial loads/cars connected by longitudinally rigid

couplers [115, p. 344]. This modelling methods simplifies car-to-car coupler interactions and therefore assumes that all train cars move at the same velocity. Therefore, the power required to travel on a grade can be represented by the sum of power required to traverse a grade for each train car, as shown in Equation 29. Equation 29 requires the car mass, passenger mass and location dependant track grade (θ) for each train car. The gravitational constant g and vehicle speed remain constant for all train cars.

$$P_{g,\ vehicle} = \sum_{1}^{NumCars} m_{car} * g * \sin(\theta) * v_{vehicle}$$

Equation 29: Power required for a train to travel over a grade represented by the sum of power required by individual train cars

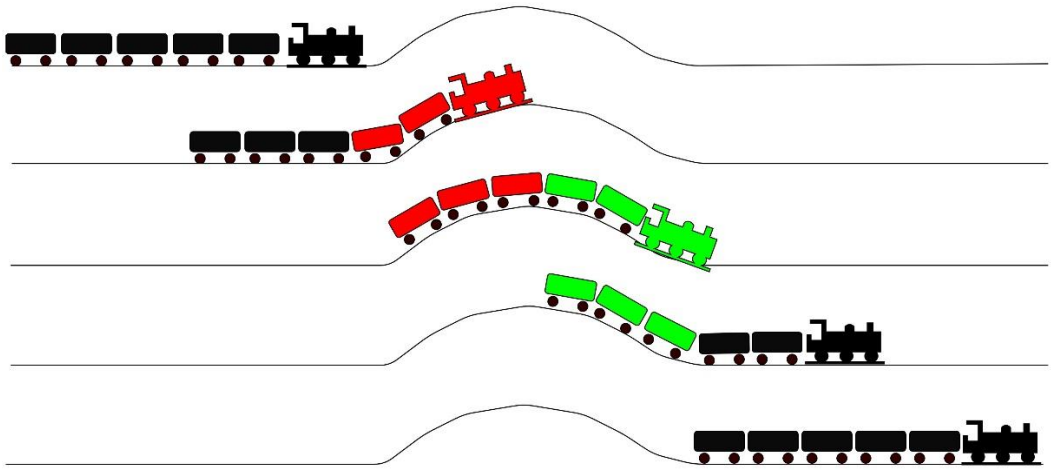

Figure 63: Multi car rail vehicle travelling over a change in elevation. Cars that require additional power for an elevation gain are notes in red while cars that assist in moving the train forward are in green.

The railway simulation tool developed in this work simplifies the proposed grade power simulation method discussed above by lumping the train and passenger mass into one location independent mass. The previous discussion was provided as a guide for future improvements to the simulation tool.

6.3.3. Acceleration Power in the Translational Frame

The power required to accelerate the rollingstock and passenger mass in the linear fame can be represented by Equation 30. Although the rollingstock mass is nearly constant over the vehicle

lifetime, the passenger mass can change between stations. The simplified railway simulation tool in this work assumes the passenger mass remains constant in attempt to simplify the modelling.

$$P_{accel} = F_{ti} * v_{vehicle}$$

$$P_{accel} = (m_{rolling\ stock} + m_{passengers}) * a_{vehicle} * v_{vehicle}$$

Equation 30: Power to accelerate rollingstock and passenger mass in the translational frame

The power required to accelerate a vehicle should also consider the force and power associated with accelerating the wheels, axles and other rotating parts – noted as F_{ri} and P_{ri}, respectively. Rather than modelling the power needed to accelerate rotational components independently, a simpler modelling approach can be used by transferring an equivalent mass to the translational frame.

As derived in [66], the equivalent translational mass for a rotating component can be determined using Equation 31. The rotational inertia of the component studied is noted by $J_{component}$. The gear ratio may be determined using the product of a transmission gear ratio and the differential ratio.

$$m_{rot,equiv} = J_{component}\left(\frac{Gear\ ratio}{r_{wheel}}\right)^2$$

Equation 31: Equivalent mass of a rotating component transferred to the translational frame

Subway trains often have six cars with approximately eight heavy wheels each. Therefore, the rotational inertia of each wheel when transferred to the translational frame may add a considerable effective mass. For example, Table 1 from [116, p. 378] lists specifications for a full-size bogie wheelset from a BR Mk4 passenger coach (not a subway vehicle). The wheelset is listed to have a diameter of 0.914m and rotational inertia of 174 kg m^2, which represents an equivalent translational mass of approximately 833 kg as noted in Equation 32. With a total of four wheelsets per coach the total additional translational equivalent mass is approximately

3332 kg or about 3.3 metric tonnes. The equivalent translational mass for the four wheelsets contributes approximately an additional mass 8.25% of the coach mass (approximately 40 metric tonnes [117]).

$$m_{rot,equiv} = 174\ kg\ m^2 \left(\frac{1}{0.457\ m}\right)^2 = 833kg$$

Equation 32: Equivalent translational mass for a BR Mk4 passenger coach wheelset

The rail simulation tool developed in this work models the additional translational mass that represents rotating components by modifying Equation 30 to include an equivalent mass term as shown in Equation 33.

$$P_{accel} = (m_{rolling\ stock} + m_{passengers} + m_{rot,equiv}) * a_{vehicle} * v_{vehicle}$$

Equation 33: Power required to accelerate a train including considerations for the equivalent mass from rotating components

6.3.4. Auxiliary Load and Total Train Power Requirements

The last power consuming aspect of the train model comes from auxiliary loads such as power outlets for passengers, climate control systems and lighting. The total power required to operate the train is modelled using Equation 34 where u_{DT} is the net drivetrain efficiency that considers losses within the motor drives, electric motors, and mechanical systems such as gear boxes. P_{train} represents the total power required from the electrical supply to operate the train.

$$P_{train} = \mu_{DT}(P_{drag} + P_{grade} + P_{accel}) + P_{aux}$$

$$P_{train} = u_{DT}\Big(\left(Av_{vehicle} + Bv_{vehicle}^2 + Cv_{vehicle}^3\right) + (m_{car}g * \sin(\theta) * v_{vehicle}) + (m_{rolling\ stock} + m_{passengers} + m_{rot,equiv}) * a_{vehicle} * v_{vehicle})\Big) + P_{aux}$$

Equation 34: Model to represent the power required to operate a vehicle including considerations for drag, the grade, acceleration of translational and rotational parts and finally, auxiliary loads.

6.4. Block 10 - Modelling the DC Network with Modified Node Analysis – Proposed

The catenary free ESS sizing exercise in Chapter 7 does not depend on the vehicle's interaction with the DC power supply. However, the following discussion is provided as an aid for future work.

The next step in developing a multi vehicle train simulation tool is to explore how the individual trains consume power from the DC network and how this power flow influences the supply voltage along the 3rd rail. Figure 64 shows an example of a simple railway system with three DC substations and three trains.

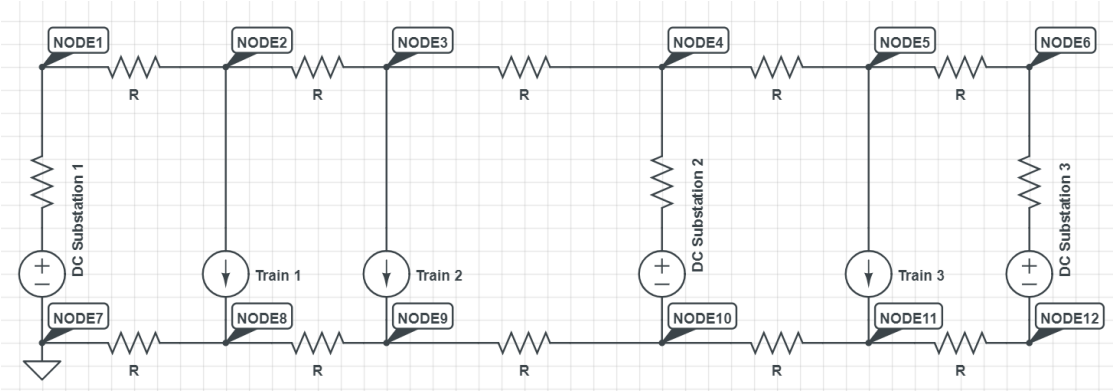

Figure 64: Circuit representation of a DC powered railway system

6.4.1. DC Substation Modelling

The DC electrical distribution system is powered by multiple DC power sources, formally called substations, that are spaced along the tracks. Common DC supply voltages include 750V, 1500V and 3000V [118]. The DC supply voltages can be produced using a three-phase step-down transformer followed by a multi-pulse rectifier. Although the simplest, the use of a three-phase diode bridge to create a six pulse rectifier results in considerable DC voltage ripple and significant 5th and 7th harmonics of AC line current that may interfere with railway signalling components [118]. However, a more complex diode rectifier system that uses a phase shifting

transformer and multiple series connected three phase diode bridges can reduce the DC ripple while eliminating select AC supply harmonics and improve the overall power factor [119]. As discussed in [120], "[t]he most common rectifier configuration […] is the parallel 12-pulse, which features low harmonic distor[t]ion of AC line current and DC voltage, together with acceptable structure complexity and cost. The rectifiers are normally equipped with diodes and voltage regulation is not performed". Considering the trend to minimize DC voltage ripple, the DC substations are modelled, in part, by an ideal voltage source without any voltage ripple. Due to the lack of voltage regulation, the output voltage of the rectifier can vary based on the DC current. Figure 1 of [120] shows an example of the output DC voltage vs DC current for a 5400 kW, 3600V, 1500A rated 12-pulse diode rectifier from the Italian State Railways. The slope of the near linear voltage vs current relationship is dependant on the substation transformer's commutation reactance [120]. This near linear relationship may be expressed as an equivalent series resistance for DC circuit modelling simplification. Therefore, similar to the work in [121] [122] and [123], the substations are modelled as ideal voltage sources with an equivalent resistance. However, due to the reactive impedance of the transformer the voltage drop across the transformer's modelled equivalent series resistance does not result entirely in real power loss. In attempt to determine the real power losses in the substation, the substation could be modelled using a more complex model, such as Equation 38 in [122]. However, it is rather difficult to differentiate between the voltage drop from reactive components and real power loss when looking at experimental results. Therefore, this work proposes to model the substations as lossless voltage sources as shown in Figure 65. The substation's unidirectional current flow is modelled using an ideal diode. However, when using nodal analysis to solve for the DC network power flow, the non-linearity of an ideal diode is not trivial to model. Therefore, it is suggested to change the series resistance to be nearly infinite when nodal analysis

determines the DC substation to be a load (ie. not providing power). This method of changing the resistance requires the nodal analysis calculation to be repeated as the power originally injected into the DC substation must be diverted elsewhere. Although the current through the nearly infinite resistor is non-zero, this modelling method error is considered negligible.

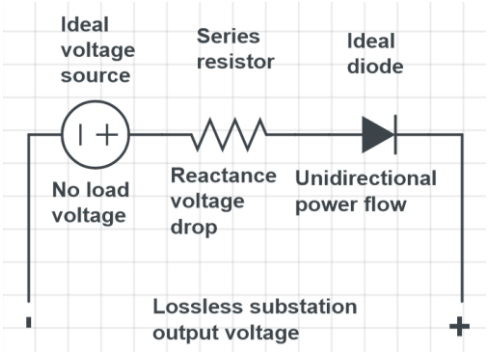

Figure 65: Lossless substation model with an ideal voltage source and equivalent series resistance

6.4.2. 3rd Rail Power Supply Modelling and Circuit Simplifications - Proposed

Subway systems generally use a 3rd rail power delivery system. The use of a 3rd rail is advantageous for subway systems that have restricted space allowance for over head cables. The positive DC voltage supply from the traction substations are typically connected to a 3rd rail, commonly called the conductor rail, that runs beside or between the two train tracks/rails that the wheels roll on, formally called running rails. The 3rd rail does not need to support the weight of the rollingstock and therefore can be made of a less strong but more conductive material compared to the running rails. For example, a stainless-steel rail/track may be covered in an aluminum cap to decrease the rail resistance [124] . For example, [125] lists the resistance of 150 lbs steel conductor rail to be 0.0117 mΩ/km while 6000A ALSS (aluminium/stainless steel) conductor rail is 0.00463 mΩ/km.

The running rail(s) complete the tractive power supply circuit by acting as the return path connecting to the substation negative terminal. As noted in Section A.10 of [22], the return

circuit may consist of only one running rail and therefore have a higher resistance than systems with two conducting running rails. The segmented running rails are electrically connected together using bonding wires to ensure a continuous current return path.

Due to the proximity, within a reasonable walking step, between the running rails (negative terminal) and 3rd rail (positive terminal), 3rd rail systems often cover the positive conductor and provide power to the rolling stock on the bottom of the rail. The rollingstock typically make sliding contact with the 3rd rail using a contact or pick-up shoe. Where the rails may pose a safety hazard, such as at a road crossing or passenger crossing, the 3rd rail is discontinued. The rolling stock may obtain electrical power from contact shoes on other cars that are still connected to the 3rd rail at a different location. However, for 3rd rail gaps that exceed the length of the rollingstock the vehicle must propel itself across the gap or risk getting stuck. Similarly, a loss of power can occur when travelling at higher speeds as the contact shoe(s) may loose physical contact with the 3rd rail due to rollingstock movement.

The railway simulation tool proposed in this work assumes that the 3rd rail and running rails are continuous. Therefore, the electrical model of the DC transmission system will not have any discontinuities. Additionally, it is assumed that the vehicle will contact the 3rd rail and running rail(s) at only at the leading car. This simplifies modelling as each train can be presented by only one connection to the DC supply.

The transmission system in Figure 64 can be simplified by combining the resistance of the 3rd rail and return rails into one resistor value. It is assumed that the length of 3rd rail and return rails are equivalent and therefore a net transmission line resistance per unit length can be assigned.

Rather than evaluating the voltage change across the 3rd rail and return rails independently, the return rail is modelled to be at 0V and the combined voltage drop occurs on the positive lead. The net supply voltage supplied to the vehicle remains the same in both modelling methods. However, the simplification of a single transmission line resistance per unit length value drastically reduces the number of nodes within the circuit. Figure 66 shows an example of a simple railway DC transmission system with two substations and two trains (modelled as resistors). The top circuit represents both the 3rd rail (positive) and return rails (negative) using an equivalent resistance. The lower circuit represents the 3rd rail and return rails as one common resistor. The key objective of Figure 66 is to show that the voltage across the train loads, which are resistors in this case, are equal for both transmission line modelling methods. For example, the voltage across R8 and R16 is the same at approximately 4.23V.

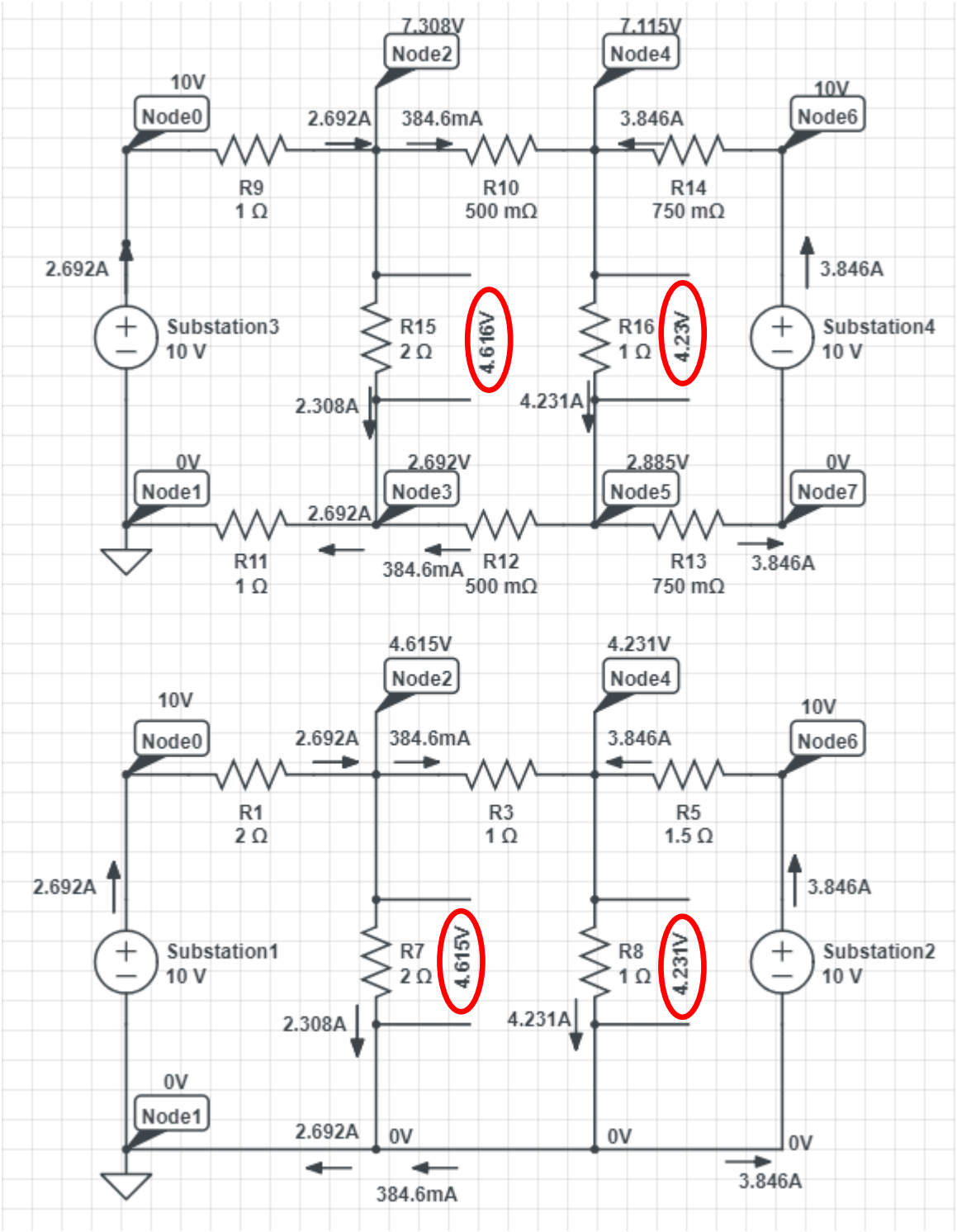

Figure 66: Example DC circuit showing the similarity in vehicle supply voltage using two transmission line modelling methods

6.4.3. Block 9 -Train Electrical Power Consumption Modelling – Proposed

The catenary free ESS sizing exercise in Chapter 7 does not depend on the vehicle's interaction with the DC power supply. However, the following discussion is provided as an aid for future work.

The power required by each vehicle can be calculated each time step using Equation 34 from Section 6.3. Ideally, each vehicle would be modelled as a power source/load. However, the recursive nature required to determine the current required from the variable voltage power supply is beyond the scope of this work. The author explored modelling each vehicle as a voltage controlled current source where the current source/load could be determined by a gain ratio relating the desired power and the 3rd rail supply voltage at the vehicles' current location. The voltage reference and current values are related using the conductance term G_m in Equation 35. However, as shown in Equation 35, the conductance term G_m and power are not equivalently nor inversely related through voltage and current. Therefore, as shown in Figure 64, each vehicle is modelled using an independent current source/load rather than a voltage controlled current source. The current value at each timestep is determined using the present time desired power value and the supply voltage from the previous time step.

$$I = G_m V$$

$$G_m = I/V$$

$$P = IV$$

Equation 35: Relating current and voltage through conductance for a voltage controlled current source

6.4.4. Admittance Matrix Stamps – Proposed

The catenary free ESS sizing exercise in Chapter 7 does not depend on the vehicle's interaction with the DC power supply. However, the following discussion is provided as an aid for future work.

The DC rail network power flow can be determined using modified node analysis (MNA). As discussed in [126] and [127], MNA involves the construction of two matrices that contain the linear equations used to describe a circuit using Kirchhoff's current and voltage laws. The general matrix formulation for MNA can be shown as Ax = z. When working with linear loads and independent sources, the matrix A generally contains known conductance values (inverse of resistance) and binary values that represent the node numbers for voltage and current sources. Generally speaking, matrix x is a column vector that contains unknown values such as node voltage (top values in column) and the current through voltage sources (lower values) [126]. The z matrix is a column vector that contains known values related to the current through current sources and the supply voltage from voltage sources [126].

Rather than developing and solving linear circuit equations manually, an algorithm can be used to form matrices A, x and z and also solve for the unknown quantities in the matrix x [126]. Matrices A and z are formed using what are called element 'stamps' where the contributions to A and/or z are dependant on the nodes surrounding the circuit element, the element type and it's value. The first step in developing the matrices using matrix stamps is to define the node numbers in the circuit. When working with linear components and independent sources, Matrix A is of size (n+m)*(n+m) where n is the number of nodes and m is the number of independent voltage sources [126]. It is beneficial to reduce the number of nodes to make the matrix smaller and therefore reduce memory demands and computation time. Recall from Figure 66 that simplifying the railway DC power delivery system to use one equivalent per unit resistance for the 3rd rail and return rail(s) combined reduced the number of nodes in the relatively small circuit. The first node, Node 0, is generally used to mark the ground point of 0V and the

remaining nodes are numbered in any increasing order. The element stamp method is applied to all circuit elements; resistors, current sources, and voltage sources. The stamps from all elements are combined to form the complete A, x and z matrices. Table 3 of [128] provides an excellent overview of circuit element stamps for various components and their respective equations. The element stamps for resistors, current sources and voltage sources used in this work are shown in Figure 68. Matrix element stamps exist for other components such as switching components [129], capacitors [130], diodes [131], op amps [132] and dependant sources such as voltage controlled current sources and current controlled voltage sources.

The author's `MNA` function, shown below, is used to identify the unknown node voltages and voltage supply currents based on the `NetList` input variable. The `NetList` matrix contains a row for each component and identifies the component type, connection node numbers and component value. The netlist provided below represents the example circuit shown in Figure 67. The netlist is annotated to identify the data within each column as well as the circuit element that each row represents. The node voltages and voltage source current values shown on Figure 67 were determined using the author's MNA function and the results align with values from another circuit simulation tool.

```
function [NodeVoltages,VoltageSupplyCurrents]  = MNA(NetList)

% Component Types:
%       1 = Voltage supply
%       2 = Current supply
%       3 = Resistor

Row structure = [Component Type, From(-) Node, To(+) Node,
ComponentValue]
NetList = [ 1 0 1 600;... -> V1
            1 0 2 600;... -> V2
            1 0 3 600;... -> V3
            2 4 0 300;... -> I4
            2 5 0 300;... -> I1
            2 6 0 250;... -> I2
            2 7 0 500;... -> I3
            3 1 8 0.1;... -> R1
            3 2 9 0.1;... -> R2
            3 3 10 0.1;... -> R3
```

```
3  4  8  0.1;... -> R4
3  8  5  0.1;... -> R5
3  5  6  0.1;... -> R6
3  6  9  0.1;... -> R7
3  9  7  0.1;... -> R8
3  7  10  0.1]; -> R9
```

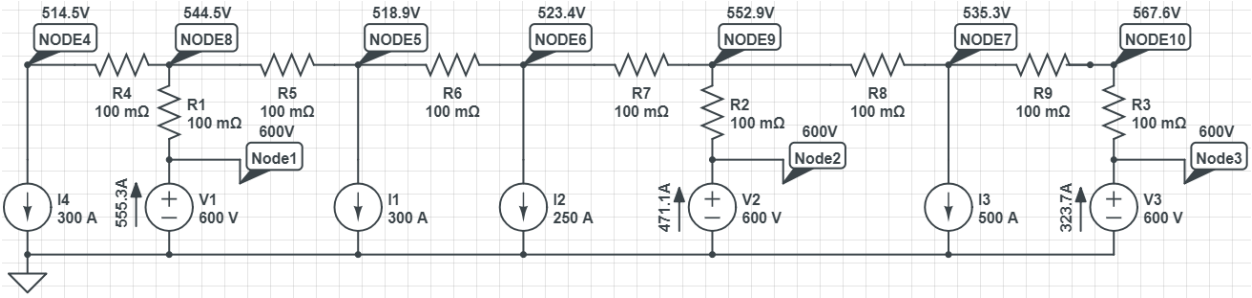

Figure 67: Example DC railway circuit with node voltages and voltage source current values determined using MNA

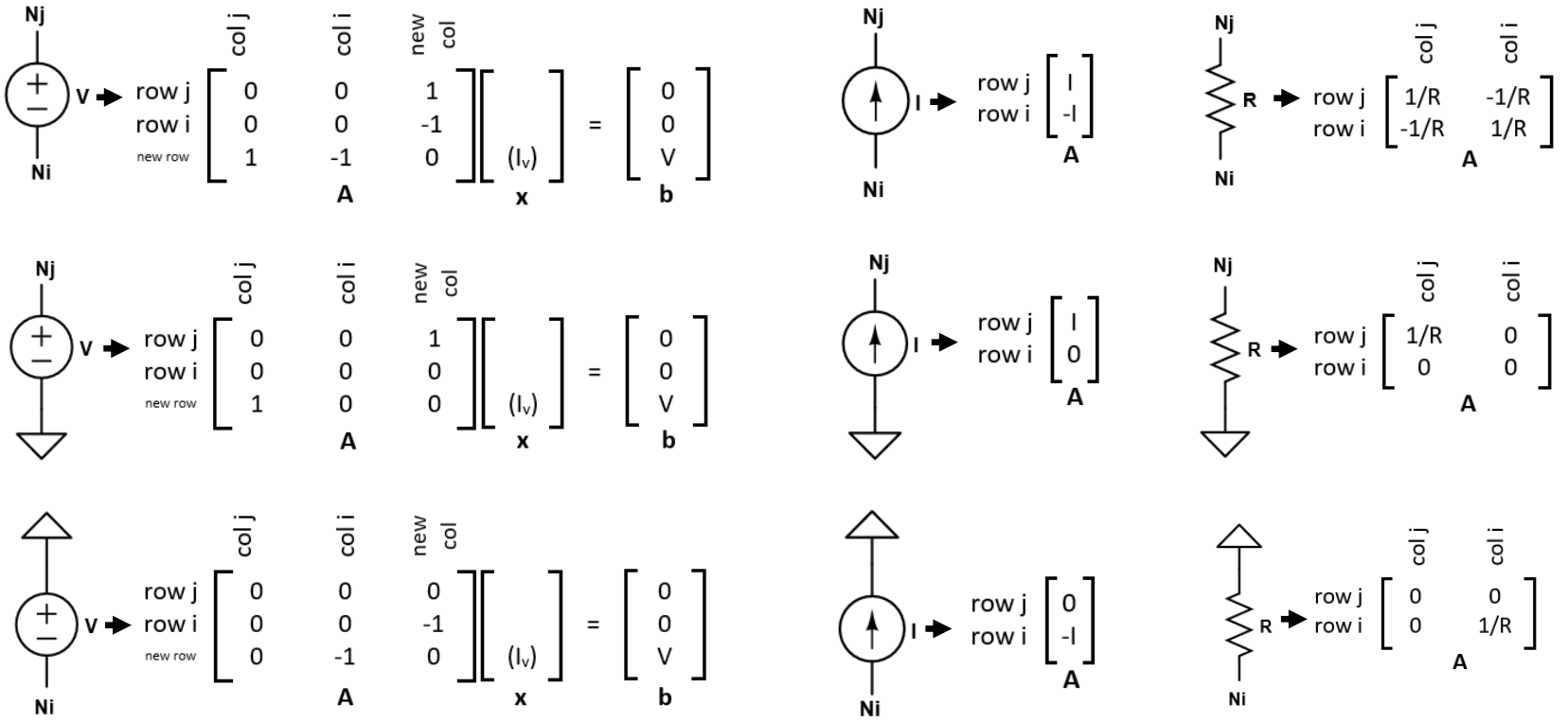

Figure 68: Element stamps and associated notation for voltage sources, current sources and resistors in three configurations relative to ground (node 0). Unknown values are recorded in parentheses

6.4.5. Development of NETLIST Input - Proposed

The final part required to fulfill block 10 from Figure 54 is to develop the NETLIST input variable based on the location of each railway vehicle and the associated power requirements. It is proposed that a standardized node numbering method be applied to simplify the process of saving and manipulating MNA function output variables. The position of each railway vehicle should be used to determine the resistance between adjacent nodes, which may be other vehicles or substations. The current required by each substation may be modelled based on the present power demanded by each vehicle and the supply voltage at the vehicle from the previous time step. The current value can be determined using the power-based modelling method described in Section 7.4. The completion of a function that develops the NETLIST variable at each time step and connects the vehicles to the DC supply remains a task for future work. However, the completion of drive cycle modeling and vehicle power modelling is sufficient for ESS sizing exercises for catenary free operation, as discussed in Chapter 7.

7. Evaluation of Vehicle Power Requirements and On-board Energy Storage for Catenary Free Operation

7.1. Chapter Overview

The purpose of this chapter is to perform a sizing exercise for an on-board energy storage system used to propel a rail vehicle from one station to another without the 3rd rail or catenary supply. The experimental data and cell model from Chapter 5 are used to model the rail vehicle energy storage system. Due to the lack of information available from capacitor datasheets (ie. only one ESR value at one temperature and one current), the experimental work of Chapter 5 provides additional information to model the cell outside of the specific test case presented by the datasheet. The comparison of the railway vehicle onboard energy storage system cell mass and cell volume for a LiC and EDLC based system will be presented. This comparison is achieved by:

- Creating a collection of railway vehicle and system modelling parameters based on literature. These values serve as a guideline to define typical model parameters
- Using one set of modelling parameters to evaluate the power required for a train to travel from one station to another. The drive cycle parameters and vehicle efficiency parameters will be modified to perform a parameter sensitivity analysis. For example, depending on efficiency values, the vehicle may consume less power by accelerating quickly and then travelling at a low speed rather than accelerating slowly and travelling at a higher speed to achieve the same travel distance and time.
- Expanding the cell modelling method from Section 5.8.3 to use a power command as the input variable rather than a current value. A cell model is scaled to represent a capacitor pack of series and parallel connected cells that will meet the power and energy demands

for the drive cycle. Pack current and voltage limitations will be respected. It is assumed that the ESS system remains within the operating thermal limits.

- A comparison of the LiC ESS system operation at 35^{o}C and -10^{o}C will be presented

7.2. Collection of Modelling Parameters

Table 15 shows a collection of railway system simulation parameters collected from over ten publications. The values are categorized into vehicle related and DC network related parameters. Table 16 provides a collection of Davis equation parameters that are used to represent the vehicle's resistance to motion (see Equation 26 and Equation 27). Although a complete set of model parameters is not available, the purpose of Table 15 and Table 16 is to provide insight into reasonable values that may be used to develop a full set of modelling parameters. In addition to these tables, Table 2.4 from [49, p. 41] indicates an approximate equivalent translational mass for rotation components of various rail vehicle types as a ratio to the vehicle weight. For example, 8-12% of the vehicle mass for electric coaches and 15-30% for electric locomotives [49, p. 41]. Although considerable attention was made to replicate the published parameters, the author encourages readers to confirm values with the original publications before using this information for other work.

Paper and Author	Reference	[133] [134]	[135]	[82]	[136]	[137]	[138]	[81]	[113]	[139]	[140]	[141]	[122]	[120]
	Select author[25]	Barrero	Tricoli	Barrero	Ciccarelli	Ciccarelli & Tricoli		Tricoli			Barrero	Tricoli	Barrero	
Vehicle Parameters	Type	Bombardier Flexity tram T3000	Ansaldo Breda Sirio tram	Metro		Metro					Metro			
	Weight (unloaded) [Tons]	38.6		4 x 30.4 = 121.6	60			114.8	154	186				
	Weight (loaded) [Tons]	56.1	58	4 * 45.1 = 180.4		46	500					277.8		
	Motor power [kW]	4*105 = 420 kW	2*106 212 kW	8* Nom. 264 = 2112 8* peak. 420 = 3,360	800 prop. 400 braking	4*250 = 1,000	Max 9800	4* 275 = 1,100	Max 1700			12*250 = 3,000		
	Auxiliary power [kW]						300		120					
	Max speed [km/h]	70	80	72		80	85		115			80		
	Acceleration (propulsion) [m/s^2]		1	1.33	0.7	1.2	0.7	1	1			1.2		
	Acceleration (braking) [m/s^2]		1	1.7	0.8	1.1		1	1.1			1.1		
	Rolling resistance coefficient	0.006									0.005			
	Aerodynamic drag coefficient	0.6									0.6			
	A [N]						1.2 N/ kN [26]		2541					
	B [N/(m/s)]						$1.6x10^{-3}$ N/(kN*km/h) [26]		77.616					
	C [$N/(m/s)^2$]						$15*10^{-4}$ $N/(kN*km/h)^2$ [26]		14.5696					
	Gearbox or mechanical efficiency [%]	93				98	98	93			93	98		
	Motor efficiency [%]	90				86 [27]		91			90	86 [27]		
	Motor drive efficiency [%]	91					90	95			91			
	ESS DC/DC converter efficiency [%]	91						95			91			
Network Parameters	Overhead line or 3rd rail resistance [mΩ/km]	170	125 (contact wire)	24.6	156 (contact wire)	27.6	62	≈27.7	21		24.6 3rd rail	27.6		
	Return rail(s) resistance [mΩ/km]	17.2		17.2	16			≈4.4	15 (parallel rails)		17.2			
	Substation internal resistance [mΩ]	30	100	13	20	10	13		20	22.5	13	10	24 [28]	12.7 to 15.8 [28]
	Substation power [kVA or kW]		1150 kVA			3500 kVA	5400 kW					3500 kVA		
	Distance between substations [km]	1.5	1								1			
	Substation no load voltage [V]	700	750	876	750	1500	3000		1500	1590	876	1500		

Table 15: Railway system simulation parameters gathered from literature. Some values are an alternative representation (change of units) of the original values published

[25] Title as Dr. removed to occupy less cell area
[26] Force per kN of vehicle weight
[27] Combined motor and inverter efficiency
[28] Approximate values determined from slope of experimental rectifier voltage vs current plot

Vehicle Type	A	B	C	Translational Mass	Additional details
London Underground subway above ground [114]	2900 [N]	1.9 [kg/h] 6.84 [N/(m/s)] [29] 1.9 [N/(km/h)] [29]	0.61 [kg/km] 7.9056 [N/(m/s)^2] [29] 0.61 [N/(km/h)^2] [29]	Empty train: 156 [tonnes] Rotational equivalent mass 13.5 [tonnes] (8.6%) Passengers: 60 [tonnes] Total translational mass: 229.5 [tonnes]	Acceleration: 1.2 [m/s^2] Train has 16 motors with 17.4 kN (not power) for a total of 278 kN force.
London Underground subway in small tunnel[29] [114]	2900 [N]	8.7 [kg/h] 31.32 [N/(m/s)] [29] 8.7 [N/(km/h)] [29]	2.3 [kg/km] 29.808 [N/(m/s)^2] [29] 2.3 [N/(km/h)^2] [29]	Same as above	Same as above
"Tramway" [142]	1,552 [N]	40.320 [N/(m/s)] 11.2 [N/(km/h)] [29]	8.025 [N/(m/s)^2] 0.619 [N/(km/h)^2] [29]	52,480 [kg]	
"Suburban train" [142]	3,182 [N]	118.940 [N/(m/s)] 33 [N/(km/h)] [29]	11.700 [N/(m/s)^2] 0.9028 [N/(km/h)^2] [29]	293,700 [kg]	
"High-Speed train" [142]	2,500 [N]	118.800 [N/(m/s)] 33 [N/(km/h)] [29]	6.610 [N/(m/s)^2] 0.5100 [N/(km/h)^2] [29]	416,000 [kg]	
2017 Chevrolet Bolt EV[30] [104]	28.4 lbf 126.33 [N] [29]	0.2018 lbf/mph 2.01 [N/(m/s)] [29] 0.558 [N/(km/h)] [29]	0.01948 lbf/mph^2 0.43 [N/(m/s)^2] [29] 0.0332 [N/(km/h)] [29]	1616 [kg] – does not include rotational inertia equivalent translational mass	

Table 16: Collection of Davis equation coefficients from literature used to represent the vehicle's resistance to motion.

[28] 45% of London Underground system is in tunnels [143]
[29] Alternative units from original publication
[30] Provided for comparison with a passenger electric vehicle

7.3. Station-to-Station Drive Cycle Power Demands and Parameter Sensitivity

The railway vehicle and drive cycle studied in the remainder of this chapter make use of the modelling parameters in Table 17. These parameters are primarily based on the values for the London Underground train operating above ground from [114], which are repeated in Table 16.

Parameter	Value	Notes
Distance	1000 [m]	
Travel time	100 [s]	
Time step	0.1 [s]	
Davis equation coefficient A	2900 [N]	Surface travelling, no tunnel
Davis equation coefficient B	6.84 [N/(m/s)]	Surface travelling, no tunnel
Davis equation coefficient C	7.9056 [N/(m/s)^2]	Surface travelling, no tunnel
Translational mass	229.5 [tonnes]	156 [tonnes] -> Vehicle 13.5 [tonnes] -> Rot. Equiv. 60 [tonnes] -> Passengers
Grade	0%	
Auxiliary power load	50 kW	
Wind velocity	0 m/s	
Mechanical <-> electrical efficiency	80%	Included mechanical drive system, electric motors, motor drives and ESS DC/DC converter

Table 17: Modelling values used for a station-to-station catenary free ESS sizing exercise

Figure 69 shows the driving resistance power for a 2017 Chevrolet Bolt EV and London Underground subway (operating above ground) calculated using Equation 27 and A, B, C coefficients from Table 16. Figure 69 shows that the train requires considerably more power than the passenger electric vehicle to overcome driving resistance, especially as speed increases.

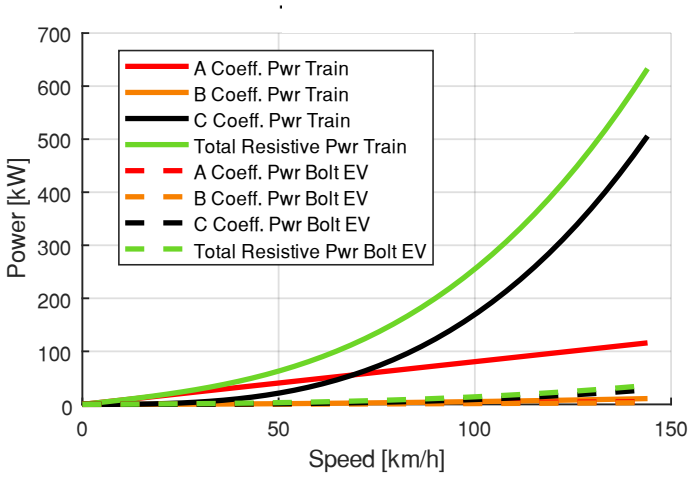

Figure 69: Driving resistance power for 2017 Chevrolet Bolt EV and London Underground subway (operating above ground) calculated using Equation 27 and A, B, C coefficients from Table 16

The railway vehicle is quite heavy compared to conventional electric cars and therefore requires additional power, especially during acceleration. For comparison, the 229.5 tonne railway vehicle (including rotational equivalent mass) is approximately 142 times the mass of a 2017 Chevrolet Bolt EV (1616 kg – excludes rotating components, 60 kWh, peak power 150 kW) [144]. To accelerate at 0.4 m/s^2 at 20 km/h (≈ 5.55 m/s), the Bolt EV would require approximately 3.57 kW while the train would require approximately 510 kW (approx. 142x). The auxiliary loads for a railway and passenger vehicle are considerably different as well. For example, the Chevy Bolt EV auxiliary power draw is approximately 0.5 to 1 kW (climate control off) while the train auxiliary power may be >100 kW (based on Table 15)

The total electrical energy required to power the railway vehicle from one station to another is dependant on the driving profile and other modelling parameters. The electrical power requirements are determined using an efficiency number that represents all losses from the wheel power to the electrical power (see Equation 36). This includes mechanical losses within gear boxes, losses within the electric motors, losses within the motor drives and losses within the power electronics that interface between the onboard energy storage system and the DC link.

$$P_{Elec} = \frac{P_{mech}}{\eta_{vehicle}}$$

Equation 36: Relating mechanical power to electrical power

Recall from Section 6.3.1 and Figure 55 that the railway vehicle drive cycle is modelled using a trapezoidal shape. Table 17 defines a travel distance of 1000 m and travel time of 100 s. These requirements can be met using multiple drive cycles that vary in the acceleration rates and travel speed. For this exercise it is assumed that the railway vehicle accelerates and brakes at the same rate without any power or rail adhesion concerns. It is also assumed that the traction

motors can provide the propulsion and braking power required without the use of mechanical brakes. A parameter sensitivity analysis was performed to see how the vehicle mass, efficiency, travel time and acceleration rate impacts both the maximum electrical power demand (occurs at transition from accelerating to travel speed) and maximum electrical energy consumption (occurs at transition from travel speed to braking). Figure 70 shows the parameter sensitivity analysis results. These values provide key benchmarks for the peak power and energy required from the onboard energy storage system.

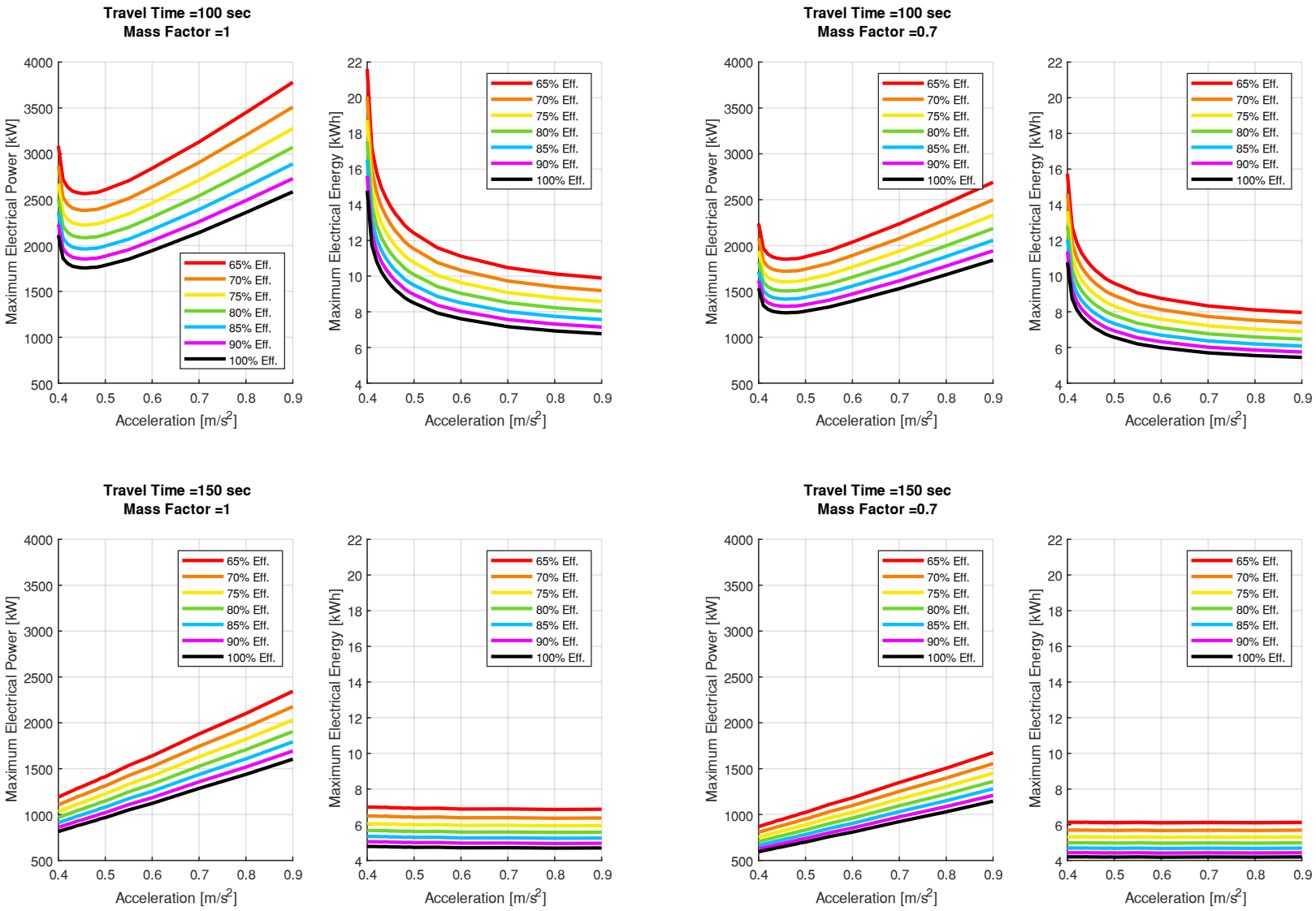

Figure 70: Maximum electrical power and electrical energy required to complete a 1 km drive using railway vehicle parameters from Table 17. Parameter sensitivity performed by changing the travel time (100, 150 seconds), the vehicle mass (100%, 70%), acceleration rate (0.4 to 0.9 m/s2) and vehicle efficiency (65 to 100%)

The following conclusions are made from the parameter sensitivity analysis in Figure 70:

- Increasing the travel time and decreasing the vehicle mass decreases both the maximum power and energy requirements – this is expected
- For the drive cycles with a travel time of 150 seconds, the maximum power required increases nearly linearly with acceleration. Although the maximum electrical energy decreases nearly linearly with acceleration, the acceleration has a relatively small impact on the max energy required (ie. small slope). For drive cycles with a 150 second travel time it may be favourable to use a small acceleration rate to take advantage of the smaller peak power requirement while only requiring a small increase in total energy consumption. For example, with a 150 second travel time, mass factor of 0.7 (70% the full train mass) and efficiency of 80 % (green lines), a +/-0.4 m/s^2 drive cycle requires a peak of approx. 705.4 kW and approx. 4.985 kWh. However, for the same conditions, accelerating at +/- 0.9 m/s^2 requires approx. 1361 kW and 4.984 kWh. Considering that the energy requirements are nearly the same (this does not consider losses within the ESS), it is beneficial to accelerate slowly to decrease the peak electrical power and ESS losses.
- The peak electrical power and energy requirements change non-linearly with acceleration for the drive cycles with a 100 second travel time. For both the 100% and 70% vehicle mass plots in Figure 70, the minimum peak power required occurs with an acceleration of approximately 0.45 m/s^2. However, the minimum energy required occurs at the maximum acceleration of 0.9 m/s^2. This presents a trade off between minimizing the peak power requirement and minimizing the energy storage requirement.

The non-linear results presented in Figure 70 with a drive time of 100 seconds and full vehicle mass are presented below. A series of drive cycle profiles, energy storage requirements and

power requirements at 80% vehicle efficiency for a variety of acceleration rates are shown in Figure 71.

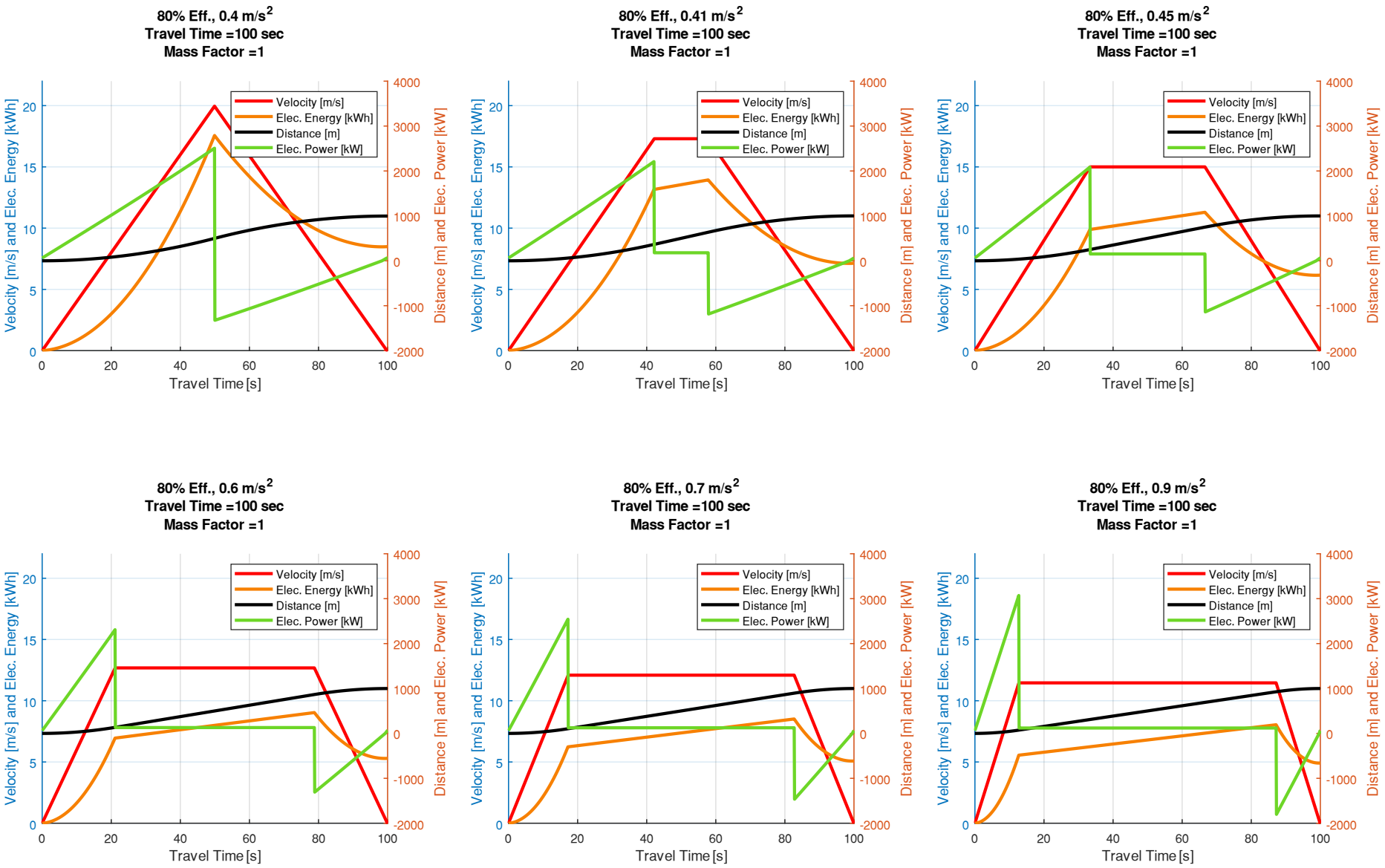

Figure 71: Multiple drive cycles showing how the acceleration rate changes the velocity, power and electrical energy consumption profile

Figure 71 shows that as the acceleration rate increases the amount of time at the travel speed increases. For example, at 0.4 m/s^2 the vehicle does not reach a travel speed and transitions from accelerating to braking. However, at 0.9 m/s^2, the vehicle spends most of the time at the travelling speed.

7.4. Power Based Cell and Pack Modelling with Operating Limits

The cell model from Section 5.8.3 is insufficient for an ESS sizing exercise and needs to be improved to accept a power command instead of a current command. The improved modelling method makes use of Equation 2 (quadratic equation) to solve for the discharge current needed to achieve the desired power level. The current value is then passed into the model from Section 5.8.3 to determine the cell terminal voltage. The capacitor cell models are scaled to represent capacitor packs with cells in series and parallel. It is assumed that the cells within a pack have the same performance and remain balanced.

It is assumed that a high-power bi-directional DC/DC converter is available to connect the on-board energy storage system to the railway vehicle DC bus. A simplified vehicle power delivery configuration is shown in Figure 72 and is similar to Figure 3 of [145] and Figure 2 of [146]. The DC/DC converter serves as a method to charge the on-board energy storage system as well as boost the ESS output voltage to match the requirements of the traction inverter. Further literature review is necessary to validate whether a DC/DC converter of the power magnitude needed in this chapter (approx. 2 MW) is commercially available and financially viable. Additionally, further investigation is required to determine a reasonable and practical voltage boost ratio that will primarily influence the minimum allowed pack voltage for an EDLC based on-board ESS. The use of an ESS with a higher minimum terminal voltage than EDLC cells may be useful for a direct connection to the traction inverter, provided a connection to the DC power

distribution system is eliminated. A direct parallel connection between the energy storage system and DC distribution system could result in a very large and catastrophic current flow into the ESS if the voltage between both systems do not match. The ESS could be charged from the DC power distribution system using a lower power DC/DC converter.

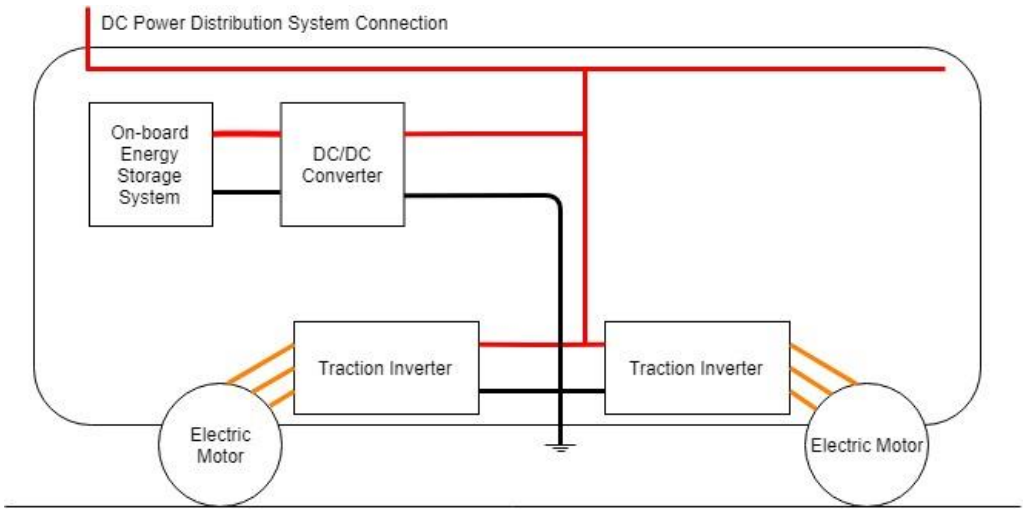

Figure 72: Vehicle power delivery architecture with an on-board energy storage system

7.5. On-board ESS Sizing for EDLC and LiC Pack

The purpose of this section is to compare the minimum number of cells, mass and volume of an energy storage system required to fulfill the drive cycle requirements of Table 17. Eight individual cases are simulated (see Table 18) with variations between the acceleration rate, operation temperature and cell type. When using the full vehicle mass (mass factor = 1) we can see that there is a trade off between the maximum power required from the ESS and the total energy required. This is shown in Figure 70. Therefore, the two accelerations studied are 0.45 m/s^2, which has the lowest peak power requirement, and 0.7 m/s^2. Recall from Section 5.7.4 that the ESR for EDLC cells was relatively unaffected by temperature while the ESR for LiC cells was significantly affected. Therefore, the eight test cases look at cells operating at 25°C and 0°C. For this analysis, it is assumed that the cell temperature remains constant. Although this is not the most reasonable assumption considering the large currents through the ESS, modelling the

temperature rise within the cell is beyond the scope of this work. Additionally, the ESR of each cell is modelled using a current direction dependant resistance but not a current magnitude dependant resistance. This introduces modelling inaccuracy at low temperature for LiC cells due to the current dependant ESR trend evaluated in Section 5.7.5. Section 5.7.5 showed that the ESR for LiC cells in cold temperatures decreased as the test current increased. Considering that the test currents per cell in the railway simulation are much larger than 50A additional work is necessary to evaluate how the current dependant ESR changes with currents greater than 50A. EDLC A and LiC Cell D were chosen for the eight test cases. These cells have the same cylindrical form factor and could replace each other inside of an ESS made for cylindrical cells. Therefore, a comparison between the volume of the cells and mass of the cells would provide a good relative comparison for an ESS that includes all pack level hardware such as bus bars, an enclosure, and energy management system. For example, if the volume of EDLC cells required was 50% more than LiC cells, then it is assumed that the EDLC ESS volume would be 50% more than the LiC ESS volume. However, this does not consider differences in equipment sizing for thermal management, which is beyond the scope of this work. The last two columns in Table 18 show the mass, in [kg], and volume, in [L], of the energy storage cells required to meet the drive cycle requirements. The modelling methods within this work provide a high-level modelling approach and are not overly detailed. The additional mass of adding an on-board ESS (approx. 2 tonnes for the cells) is considered negligible compared to the vehicle mass (approx. 230 tonnes). Although the ESS mass only includes the cells at this point, the author assumes that the power required to accelerate the additional ESS mass is negligible compared to the train. A more correct modelling method would be iterative and revaluate the train power demands with the additional ESS mass added. Additionally, the on-board ESS may occupy space that the passengers occupy (accounted

to be 60 tonnes) and therefore reduce the passenger mass. Additional analysis on the influence of the additional ESS mass is beyond the scope of this work.

The energy storage systems presented in Table 18 were designed to meet the power and energy requirements for the rail vehicle to move from one station to another. The number of cells in series was selected to have a maximum voltage equal to, or approximately equal to, the nominal DC supply voltage for the London Underground, which is 630V. From there, the number of parallel cells was modified to identify the minimum number of cells that would satisfy the drive cycle power and energy requirements without hitting a cell voltage limit nor current limit. Although the minimum number of parallel cells was often a non-integer value, the next largest integer value was used. For cases 1, 3, 5 and 7 in Table 18, which use EDLC cell A, the minimum number of parallel cells was determined by the presence of a complex valued (not a real number) current. Recall that the current value is determined from a quadratic equation that used the cell ESR, OCV and desired power level. The complex current value consistently occurred as the EDLC ESS was reaching the minimum cell voltage. At this point, it is unclear if the complex current solution is a result of the modelling methods or if an ESS with less cells in parallel than presented in Table 18 is feasible.

Recall from the footnotes of Table 5 that some, but not all, manufacturers of the LiCs studied in this work suggest using a minimal charging current below 0^{o}C. Therefore, it is assumed that Cell D can charge at the rated maximum current of 280A. It is unknown how charging at this current will impact the life of the cell. An alternative approach would be to assume the LiC cell cannot be charged at or below 0^{o}C, therefore making the LiC based ESS for cases 4 and 8 in Table 18 infeasible.

Case Num	Accel. [m/s^2]	Peak Elec Pwr. [kW]	Max Elec Energy [kWh]	Cell	Temp. [^{o}C]	Num Series	Num Parallel	Num Cells	Current limits, assuming thermal and voltage limits respected (cell, pack) [A]	Volt Limits (cell, pack) [V]	Avg Discharge ESR [33] (cell, pack) [mΩ]	Discharging Energy (2A) (cell [Wh], pack [kWh])	Num Parallel Cell Reason	Cell Mass (cell, Pack) [kg]	Cell Volume (cell, pack) [L]
1	0.45	2086.46	11.29	A EDLC	25	210	15	3150	(+/- 2,200) (+/- 33,000)	(0,3) (0, 630)	0.33, 4.62	3.64 Wh, 11.466 kWh	Complex current	0.520, 1638	0.391 1232
2				A EDLC	0		16	3360	(+/- 2,200) (+/- 35,200)		0.35, 4.59	3.63 Wh, 12.197 kWh	Complex current	0.520, 1747	0.391 1314
3				D LiC	25	156	14	2184	(+/- 280) (+/- 3,920)	(2.8 4.05) (436.8, 631.8)	1.04, 11.59	37.12 Wh, 81.070 kWh	Current limit	0.830, 1813	0.394 860.5
4				D LiC	0		33	5148	(+/- 280) [31] (+/- 9240) [31]		7.33, 34.65	35.40 Wh, 182.24 kWh	Min volt limit	0.830, 4273	0.394 2028
5	0.7	2542.41	8.51	A EDLC	25	210	12	2520	(+/- 2,200) (+/- 26,400)	(0,3) (0, 630)	0.33 5.76	3.64 Wh, 9.173 kWh	Complex current	0.520, 1310	0.391 985
6				A EDLC	0		12	2520	(+/- 2,200) (+/- 26,400)		0.35, 6.13	3.63 Wh, 9.147 kWh	Complex current	0.520, 1310	0.391 985
7				D LiC	25	156	16 [32]	2496	(+/- 280) (+/- 4480)	(2.8 4.05) (436.8, 631.8)	1.04, 10.14	37.12 Wh, 92.651 kWh	Current limit	0.830, 2072	0.394 983.4
8				D LiC	0		40 [32]	6240	(+/- 280) [31] (+/- 11,200) [31]		7.33 28.59	35.40 Wh, 220.90 kWh	Min volt limit	0.830, 5179	0.394 2459

Table 18: Eight catenary free station-to station drive cycles simulated with an EDLC or LiC based on-board ESS in 25^{0}C and 0^{0}C conditions

[31] Unknown impact on life time when charging with high current in cold temperatures.

[32] Cannot start at 100% SOC due to hitting upper voltage limit during braking phase. Larger charging resistance than discharging resistance

[33] Determined using 25 A current pulses

Figure 73 shows the ESS current, terminal voltage, power and energy throughput for case 1 (EDLC A) and case 3 (LiC D). These cases are shown graphically as they are one of two comparisons that show a desirable characteristic (minimize mass or volume) for the LiC pack. The LiC cells in case 3 are about 111% the weight and about 70% the volume of the EDLC cells in case 1. The other favourable LiC comparison exists between case 5 and 7. The cells for case 5 and 7 have a very similar volume but the LiC ESS weights approximately 158% the EDLC ESS mass.

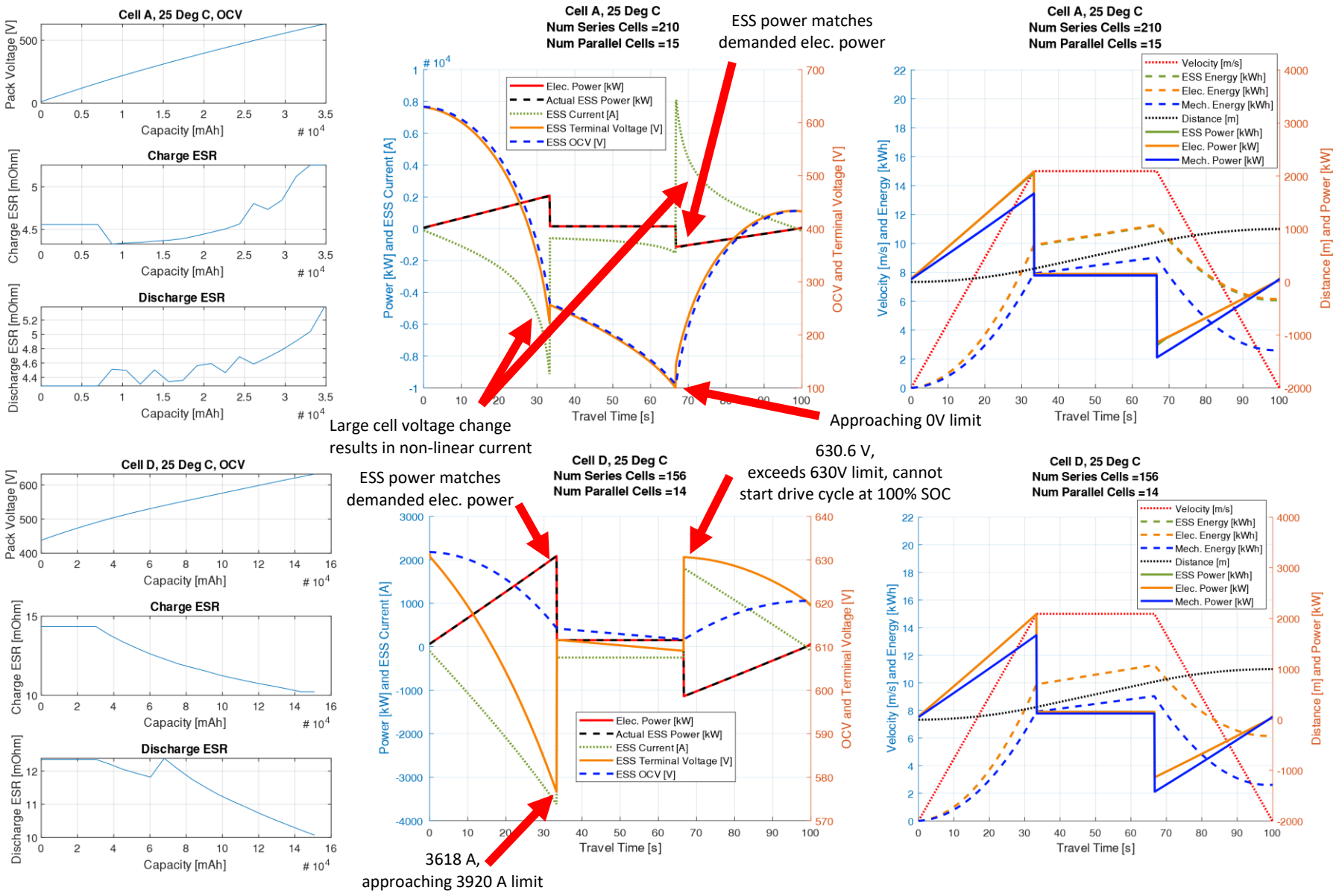

Figure 73: ESS characteristics and performance for case 1 (top row, EDLC cell A) and case 3 (bottom row, LiC cell D) from Table 18. Left - ESS pack specifications. Middle - ESS voltage, current and power. Right - drive cycle mechanical, electrical and ESS power and energy

Although a comparison of case 1 and case 3 show a favourable LiC ESS due to a cell volume reduction, the increased mass and other considerations may make the EDLC pack more favourable. For example, the relatively small variation in cell performance for EDLCs in cold temperatures is favourable considering that rail vehicles are operated year around. However, recall that the modelling for cases 4 and 8, which are at 0^{o}C, does not consider the current dependant ESR or self heating of the LiC cells and therefore the results in Table 18 may not be representative of a real-world scenario.

Additionally, as noted by the arrows in Figure 73, the LiC cells are operating near the maximum discharge current while the ELDC cells operate at a max pack current of 9135A, which is far from the 33,000A pack limit (based on cell limits only, does not consider park hardware limitations). Although not discussed in this work, the author predicts that operating near the maximum LiC cell current may further reduce the relatively limited cycle life of the LiC cells.

The LiC ESS in case 3 requires 2184 cells while the EDLC ESS in case 1 requires 3150 cells. The authors expense to acquire one LiC Cell D was approximately 316% the cost of one EDLC Cell A. Although this price difference may not be accurate when purchased in large quantities, a simple comparison with this pricing shows that the LiC cells for case 3 would cost about 219% the cost of EDLC cells for case 1.

The drive cycle in cases 1 and 3 requires approximately 11.29 kWh of electrical energy. The EDLC ESS provides approximately 11.47 kWh (102% the needed amount) while the LiC ESS provides approximately 81.07 kWh (718% the needed amount). The number of EDLC cells in parallel is

primarily defined by energy storage content while the number of LiC cells in parallel is primarily defined by the cell current limits.

As shown in Figure 73, the terminal voltage of the EDLC pack decreases significantly. The large voltage change in the EDLC pack results in large currents that may be impractical for a DC/DC converter. The LiC ESS may be favourable from a power electronics perspective due to the lower current and boost ratio required. However, if the drive cycle were modified to reduce the peak power and increasing the driving range, a LiC based on-board ESS may be favourable compared to an EDLC on-board ESS. A detailed analysis of each drive cycle is necessary to make a comparison between the favourable use of each energy storage technology studied in this work.

8. Conclusions

8.1. Summary and Conclusions

This work looked at two key topics:

a) Experimental performance characterization of two EDLC and five LiC cells using five time domain testing methods.

b) Modelling an EDLC and LiC based ESS used to power a metro railway vehicle from one station to another in catenary free operation

Discussion on the development of a custom cell cycling device and related energy storage lab safety systems was presented. The workflow and testing methods used to characterize the cells was discussed in detail. Select experimental results were presented and the following conclusions were made. Generally speaking, LiC cells offer a superior energy density compared to EDLC cells, but at the expense of a reduced cycle life, reduced operating current and increased equivalent series resistance. The EDLC performance was nearly unaffected by temperature change in the -10^{o}C to 35^{o}C range. However, the performance of LiC cells changed significantly, for the worse, in cold operating conditions. The need for a current dependant equivalent series resistance for LiC cells was identified.

The modelling methods and a collection of reasonable modelling parameters were presented for the development of a railway vehicle velocity and power profile development tool. The tool was used to analyze how drive cycle parameters, such as vehicle acceleration, impact the peak power demand and energy requirements. These values were used for an on-board energy storage system sizing exercise that compares the mass and volume of a LiC (using Cell D) and EDLC (using Cell A) based ESS for a given drive cycle. Of the eight test cases modelled, the LiC ESS was only beneficial on one application due to a reduced cell volume but the cell mass remained larger

than the EDLC ESS. Additional discussion regarding the influence of temperature, cycle life, cost, and operating conditions suggest that the EDLC energy storage system is a better solution for all test cases presented, assuming that a suitable DC/DC converter is available, and the converter cost is neglected. However, the use of LiC technology may be beneficial for catenary free operating conditions where the peak power is reduced, and the desired vehicle range is increased. Additionally, the use of an LiC ESS that maintains a higher terminal voltage during discharge compared to an EDLC ESS may be beneficial due to the reduced current and reduced boost ratio needed when developing/selecting a DC/DC converter. The author cannot provide a specific conclusion on whether LiC or EDLC cells are a better technology for on-board railway energy storage systems for catenary free operation. Both cells offer benefits and drawbacks and it is suggested that each specific application be studied before selecting a cell technology.

Additional railway vehicle modelling methods were presented for future development of a multi-vehicle railway simulation tool that can be used to analyze the impact of on-board and wayside energy storage systems when interacting with a DC power supply. The full implementation of the simulation tool remains a task for future work.

8.2. Future Work

The authors suggest the following topics of study for future work. Some of these topics build upon the experimental LiC and EDLC testing results to further develop an understanding of cell performance under conditions not explored in this work. As noted throughout Chapter 6, several modelling methods were proposed to further develop the railway simulation tool to model multiple vehicles and their interaction with the DC supply system. There is extensive work that can be studied with a more complex simulation tool. Suggested future work includes:

- Additional experimental testing to determine the maximum current that the LiCs can be charged at and still exhibit endothermic characteristics (cooling while charging). It is assumed that the endothermic charging characteristics will eventually be overcome by I^2R losses that result in cell heating. This is of interest as the LiCs may be a good candidate for fast charging applications that require minimal thermal management.
- Additional experimental testing with HPPC pulses in cold conditions with current pulse amplitudes greater than 50A to evaluate if the ESR for LiCs continues to decrease as the current increases beyond 50A. This modelling improvement may show that a smaller LiC ESS is necessary for the catenary free operation cases in Chapter 7 because the pack would be less limited by the voltage change due to a large internal resistance.
- As discussed in Chapter 7, the LiC pack in certain modelling cases must operate near the maximum rated discharge current. It is unknown how the high currents will impact the already limited cycle life of LiCs. Therefore, experimental work that quantifies the impact of high current charging and discharging on LiC cycle life is of interest.
- Additional modifications to a station-to-station drive cycle may result in situations where a LiC ESS is beneficial compared to an EDLC ESS. Additional exploration into modifying the drive cycle to identify opportunities for LiC technology is of interest.
- Further development of the railway simulation tool to model multiple vehicles and their interactions with the DC power supply. A tool of this capability can be used to identify how the headway, vehicle acceleration and other drive cycle characteristics impact the vehicle power requirements. A multi-vehicle tool will show how power is transferred from a braking vehicle to other vehicles. Situations that result in the use of resistive braking can be identified as opportunities for energy storage system use.

- Using a multi-vehicle railway simulation tool to evaluate the optimal location(s) and size of a wayside energy storage system, or multiple ESSs, for the purpose of reducing voltage droop in the DC supply and/or recovering regenerative braking energy. There is a wide variety of control strategies that can be explored to determine how the wayside ESS interacts with the DC supply. For example, a 3rd rail voltage-based control strategy or vehicle speed controller are some methods to explore. Although a large majority of the discussion in this work focuses on capturing braking energy, the ESS is also useful for peak power shaving to reduce the power required from the DC supply system during acceleration.
- Using a multi-vehicle railway simulation tool to evaluate the impact of on-board ESS size and control strategies on net energy savings. For example, future work could assess the use of small ESSs on multiple trains or larger ESSs on fewer trains. Additional work can be done to evaluate how the DC/DC converter connecting the on-board ESS should be controlled. For example, there is minimal benefit to maintain a high ESS SOC before braking so that the braking resistors must be used. Therefore, it is suggested to find an optimal operating condition to use the on-board ESS for peak shaving while discharging the ESS enough to fully capture excess regenerative braking energy.
- Using a multi-vehicle railway simulation tool to evaluate the energy savings and performance gains when using on-board ESSs or wayside ESS with the same financial limits. A detailed cost analysis would be necessary to determine the expense for retrofitting existing rollingstock and adding wayside energy storage stations.
- Using a multi-vehicle railway simulation tool to evaluate the use of reversible substations and energy storage systems to compare the capital cost, revenue

generation, total operating costs and return on investment to determine what energy saving technology is more financially viable.

The future work possible in studying energy storage systems for railway applications is vast. However, the majority of research work is primarily done with simulation tools. If possible, the author highly suggests experimental work in partnership with a passenger rail system operator and rollingstock engineering corporation to evaluate simulated work and make the results public. The author assumes that experimental work of this scale is not only expensive but also difficult to complete due to the desire for minimal service interruptions on busy public transit systems.

References

[1] International Railway Association (UIC), Community of European Railway and Infrastructure Companies, "Rail transport and environment: facts and figures," September 2015. [Online]. Available: http://www.cer.be/sites/default/files/publication/Facts%20and%20figures%202014.pdf. [Accessed 8 December 2017].

[2] The European Rail Research Advisory Council, "Rail 2050 vision, rail - the backbone of Europe's mobility," 15 December 2017. [Online]. Available: http://www.cer.be/sites/default/files/publication/122017_ERRAC%20RAIL%202050.pdf. [Accessed 14 August 2018].

[3] Community of European Railway and Infrastructure Companies (CER), "Who we are," 21 February 2018. [Online]. Available: http://www.cer.be/sites/default/files/publication/CER_WhoWeAre_2018.pdf. [Accessed 14 August 2018].

[4] International Energy Agency, International Union of Railways, "Railway handbook 2016, energy consumption and CO2 emissions," 2015. [Online]. Available: https://uic.org/IMG/pdf/iea-uic_railway_handbook_2016.pdf. [Accessed 12 August 2018].

[5] Union Internationale des Transports Publics, "Energy efficiency contribution of urban rail systems," [Online]. Available: http://www.uitp.org/sites/default/files/cck-focus-papers-files/Energy%20Efficiency%20-%20Contribution%20of%20Urban%20Rail%20Systems.pdf. [Accessed 12 August 2018].

[6] Toronto Transit Commission, "Section one system quick facts," [Online]. Available: https://ttc.ca/About_the_TTC/Operating_Statistics/2016/section_one.jsp. [Accessed 8 12 2017].

[7] S. R. Tanaka, "TTC environmental Plan - initatives and implementation," 4 July 2008. [Online]. Available: https://www.toronto.ca/legdocs/mmis/2008/pe/bgrd/backgroundfile-14566.pdf. [Accessed 8 December 2017].

[8] Toronto Transit Commission, "Staff response to commission inquiry - energy efficiency and cost savings," 27 February 2007. [Online]. Available: https://www.ttc.ca/About_the_TTC/Commission_reports_and_information/Commission_meetings/2007/Feb_27_2007/Other/Energy_Efficiency_an.jsp. [Accessed 8 December 2017].

[9] Toronto Transit Commission, "TTC environmental plan - initiatives and implementation," 6 December 2007. [Online]. Available: http://www.ttc.ca/About_the_TTC/Commission_reports_and_information/Commission_meetings/2007/Dec_6_2007/Other/TTC_Environmental_Pl.pdf. [Accessed 8 December 2017].

[10] Toronto Transit Comission, "Produrement authorization - electrical power purchase agreement," 21 January 2002. [Online]. Available: https://www.ttc.ca/About_the_TTC/Commission_reports_and_information/Commission_meetings/2002/Jan_21_2002/Other/Electrical_Power_Pur.jsp. [Accessed 8 December 2017].

[11] Toronto Hydro-Electric System Limited, "Electricity distirbution license ED-2002-0497," 2003. [Online]. Available: http://www.torontohydro.com/sites/electricsystem/Documents/2012EDR/B1.pdf.

[12] SEPTA, "SEPTA operating facts fiscal year 2016," [Online]. Available: https://septa.org/strategic-plan/reports/2016-opfacts.pdf. [Accessed 11 December 2017].

[13] Railway Technology, "Union pearson express air rail link," [Online]. Available: https://www.railway-technology.com/projects/air-rail-link/. [Accessed 11 August 2018].

[14] M. Siu, "How Toronto got a 'world-class', gold plated, half-billion-dollar empty train," The Globe and Mail, February 2016. [Online]. Available: https://www.theglobeandmail.com/opinion/editorials/how-toronto-got-a-world-class-gold-plated-half-billion-dollar-empty-train/article28708468/. [Accessed 11 August 2018].

[15] Toronto Transit Commission, "Line 1 extension now open!," 18 December 2017. [Online]. Available: https://www.ttc.ca/Spadina/Project_News/News_Events/News_by_Date/2017/December/SubwayOpens.jsp. [Accessed 11 August 2018].

[16] C. Mulligan, "Exclusive: TTC, contractors behind the scenes fighting over York-Spadina subway costs," CityNews, 14 December 2017. [Online]. Available: https://toronto.citynews.ca/2017/12/14/exclusive-real-cost-york-spadina-extension-still-unknown/. [Accessed 11 August 2018].

[17] Southeastern Pennsylvania Transportation Authority, "SEPTA energy action plan: a strategy to achieve performance targets for energy and GHG emission," November 2012. [Online]. Available: http://www.septa.org/sustain/pdf/energyaction12.pdf. [Accessed 8 December 2017].

[18] A. Gonzalez-Gil, R. Palacin, P. Batty and P. J.P, "A systems approach to reduce urban rail energy consumption," *Energy Conversion and Management,* no. 80, pp. 509-524, 2014.

[19] F. Kiessling, R. Puschmann and A. Schmieder, Contact lines for electric railways: planning, design, implementation, Publicis, 2001.

[20] "Part 2 DC railway electrification supply system," in *IET Professional Development Course on Electric Traction Systems*, London, 2010.

[21] S. S. Fazel, S. Firouxian and B. K. Shandiz, "Energy-efficient emplacement of reversible DC traction power substations in urban rail transport through regenerative energy recovery," *International Journal Of Railway Research,* pp. 1-11, 2015.

[22] Railtrack PLC, "Classic 750V d.c. 3rd rail electrification system and T&RS paramaters to ensure interworking," June 1995. [Online]. Available: https://www.rssb.co.uk/rgs/standards/GMRT1001%20Iss%201.pdf. [Accessed 10 August 2018].

[23] A. Gonzalez-Gil, P. Roberto and P. Batty, "Sustainable urban rail systems: strategies and technologies for optimal management of regenerative braking energy," *Energy Conversion and Management,* vol. 75, pp. 374-388, 2013.

[24] P. Radcliffe, J. Wallace and L. Shu, "Stationary applications of energy storage technologies for transit systems," in *IEEE Electrical Power and Energy Conference*, 201.

[25] X. Dong and S. Zhuang, "Performance study of combined test rig for metro train traction," *Journal of Modern Transportation,* vol. 19, no. 3, pp. 163-167, 2011.

[26] Kawasaki, "First test of BPS for international railways a success," 27 July 2010. [Online]. Available: http://global.kawasaki.com/en/corp/newsroom/news/detail/20100727_1.html. [Accessed 11 December 2017].

[27] M. Ogasa and Y. Taguchi, "Power electronics technology for a lithium ion battery tram," in *Fourth Power Conversion Conference-NAGOYA, PCC-NAGOYA 2007*, Nagoya, 2007.

[28] S. Akiyama, K. Tsutsumi and S. Matsuki, "The development of low floor battery-driven LRV "SWIMO"," [Online]. Available: https://uic.org/cdrom/2008/11_wcrr2008/pdf/R.2.2.3.2.pdf. [Accessed 11 December 2017].

[29] T. Konishi, S.-i. Hase and Y. Nakamicki, "Verification tests of energy storage system for DC electrified railways using EDLC," *Quarterly Report of RTRI,* vol. 48, no. 2, pp. 71-77, 2007.

[30] L. Hanmin, K. Gildong, L. Changmu and J. Euijin, "Field tests of DC 1500V stationary energy storage system," *International Journal of Railway,* vol. 5, no. 3, pp. 124-128, 202.

[31] G. Morita, T. Konishi, S. Hase, Y. Nakamichi, N. H. and T. Uemura, "Verification tests of electrical double layer capacitors for static energy storage system in DC electrified railway," in *SPEEDAM 2008 - International Symposium on Power Electronics, Electrical Drives, Automation and Motion*, 2008.

[32] H. M. Lee, "A study on development of ESS installed in DC railway systems," in *International Conference on Control, Automation and Systems 2019*, Gyeonggi-do, 2010.

[33] M. Steiner and J. Scholten, "Energy storage on board of DC fed railway vehicles," in *2004 35th Annual IEEE Power Electronics Specialists Conference*, Aachen, 2004.

[34] Siemens, "Siemens' energy storage system reduces emission by up to 80 metric tons of CO2 per year and enables trams to operate without an overhead contact line," 30 March 2009. [Online]. Available: https://www.siemens.com/press/pool/de/pressemitteilungen/2009/mobility/IMO200903024e.pdf. [Accessed 11 December 2017].

[35] V. Gelman, "Energy storage that may be too good to be true," *IEEE Vehicular Technology Magazine,* pp. 70-80, December 2013.

[36] M. Ogasa, "Application of energy storage technologies for electric railway vehicles - examples with hybrid electric railway vehicles," *IEEJ Transactions on Electrical and Electronic Engineering,* vol. 5, no. 3, pp. 304-311, 2010.

[37] T. Ratniyomchai and S. T. P. Hillmansen, "Recent developments and applications of energy storage devices in electrified railways," *IET Electrical Systems in Transportation,* vol. 4, no. 1, pp. 9-20, 2014.

[38] Siemens, "Quatar Education City people mover system," [Online]. Available: https://www.siemens.com/press/pool/de/events/2015/mobility/2015-06-uitp/presentation-qatar-e.pdf. [Accessed 11 December 2017].

[39] M. Meinert, "Hybrid energy storage systems at Siemens mobility division," [Online]. Available: http://www.cii-resource.com/cet/FBC-05-04/Presentations/ECAP/Meinert_Michael.pdf. [Accessed 11 December 2017].

[40] Bombarier Transport, "EnerGstor wayside energy storage," [Online]. Available: http://www.bombardier.com/content/dam/Websites/bombardiercom/supporting-documents/BT/Bombardier-Transportation-ECO4-EnerGstor-EN.pdf. [Accessed 11 December 2017].

[41] ABB, "Enviline ESS energy storage system for DC rail transportation," [Online]. Available: https://library.e.abb.com/public/ec0423115ec94942a4960192c3f0c6d0/ENVILINE%20ESS%20EN.pdf. [Accessed 11 August 2018].

[42] Toshiba, "Traction energy storage system with SCiB For DC railway power supply systems," [Online]. Available: http://www.toshiba.co.jp/sis/railwaysystem/en/products/catalog/pdf/c10TESS.pdf. [Accessed 11 December 2017].

[43] M. Frohlich, M. Klohr and S. Pagiela, "Energy storage system with ultracaps on board of railway vehicles," [Online]. Available: https://uic.org/cdrom/2008/11_wcrr2008/pdf/R.3.4.3.2.pdf. [Accessed 11 August 2018].

[44] H. Roussel, "Power supply for the atlantic TGV high speed line," in *1989 International Conference on Main Line Railway Electrification*, York, 1989.

[45] Toronto Transit Commission, "Schedules and maps," [Online]. Available: http://www.ttc.ca/Routes/index.jsp. [Accessed 11 December 2017].

[46] Railway Technology, "Toronto transit subway system," [Online]. Available: http://www.railway-technology.com/projects/toronto-transit/. [Accessed 11 December 2017].

[47] T. Suzuki, H. Hayashiya, T. Yamanoi and K. Kawahara, "Application examples of energy saving measures in japanese DC feeding system," in *International Power Electronics Conference*, Hiroshima, 2014.

[48] A. Okui, S. Hase, H. Shigeeda, T. Konishi and T. Yoshi, "Application of energy storage system for railway transportation in Japan," in *International Power Electronics Conference*, Sapporo, 2010.

[49] A. Steimel, Electric traction: motive power and energy supply 2nd ed., Stylus Publishing, 2014.

[50] Kawasaki, "Battery power system (BPS) for railways," [Online]. Available: http://global.kawasaki.com/en/energy/solutions/battery_energy/applications/bps.html. [Accessed 11 August 2018].

[51] "Bombardier battery-powered tram makes record test run," Charged Electric Vehicle Magazine, 12 November 2015. [Online]. Available: https://chargedevs.com/newswire/bombardier-battery-powered-tram-makes-record-test-run/. [Accessed 11 August 2018].

[52] Bombardier, "Bombardier's battery powered tram sets range record," 3 November 2015. [Online]. Available: https://www.bombardier.com/en/media/newsList/details.BT-20151103-Bombardiers-Battery-Powered-Tram-Sets-Range-Record-01.bombardiercom.html. [Accessed 11 August 2018].

[53] R. Deshpande, Ultracapacitors, New Delhi: McGraw-Hill Education (India) Private Limited, 2015.

[54] B. Conway and W. Pell, "Double-layer and pseudocapactitance types of electrochemical capacitors and their applications to the development of hybrid devices," *Journal of Solid State Electrochemistry,* vol. 7, pp. 637-644, 2003.

[55] H. Abruna, Y. Kiya and J. Henderson, "Batteries and electrochemical capacitors," *Physics Today,* vol. 61, no. 12, pp. 43-47, 2008.

[56] B. Conway, "Transition from "Supercapacitor" to "Battery" Behaviour in Electrochemical Energy Storage," *Journal of the Electrocehmical Society,* vol. 138, no. 6, pp. 1539-1548, 1991.

[57] P. Malysz, L. Gauchia and H. Yang, "Fundamentals of electric energy storage systems," in *Advanced Electric Drive Vehicles*, Boca Raton, CRC Press Taylor & Francis Group, 2015, pp. 237-282.

[58] T. Kazda and P. vanysek, "The chalkboard: lithium batteries as electrochemical sources of energy," *The Electrochemical Society Interface,* vol. 25, no. 3, pp. 47-49, Fall 2016.

[59] S.-C. S. Wang, "Advanced secondary batteries and their applications for hybrid and electric vehicles," 5 December 2011. [Online]. Available: http://sites.ieee.org/clas-sysc/files/2012/05/Wang-Battery-and-EV.pdf. [Accessed 18 August 2018].

[60] P. Voelker, "Trace degredation analysis of lithium-Ion battery components," April 2014. [Online]. Available: https://www.thermofisher.com/content/dam/tfs/ATG/CMD/cmd-documents/sci-res/pub/comm/env/AR-Lithium-Ion-Battery-Degradation-RandD-Mag-042214.pdf. [Accessed 18 August 2018].

[61] Q. Liu, C. Du, B. Shen, P. Zuo, X. Cheng, Y. Ma, G. Yin and Y. Gao, "Understanding undesirable anode lithium plating issues in lithium-ion batteries," *RSC Advances,* vol. 6, pp. 88683-88700, 2016.

[62] H. Borhan and A. Vahidi, "Model predictive control of a power-split hybrid electric vehicle with combined battery and ultracapacitor energy storage," in *2010 American Control Conference (ACC 2010)*, Baltimore, 2013.

[63] R. Gu, P. Malysz and A. Emadi, "A novel battery/ultracapacitor hybrid energy storage system analysis based on physics-based lithium-Ion battery modeling," in *Transportation Electrification Conference and Expo (ITEC)*, Hamilton, 2015.

[64] J. Cao, C. Binggang, B. Zhifend and W. Chen, "Energy-regenerative fuzzy sliding mode controller design for ultracapacitor-battery hybrid power of electric vehicle," in *International Conference on Mechatronics and Automation*, Xi'an, 2007.

[65] E. Chemali, L. McCurlie, B. Howey, T. Stiene, M. M. P. M. Rahman, R. Ahmed and A. Emadi, "Minimizing battery wear in a hybrid energy storage system using a linear quadratic regulator," in *IECON*, 2015.

[66] P. Kollmeyer, "Development and implementation of a battery-electric light-duty class 2a truck including hybrid energy storage," University of Wisconsin - Madison, Madison, 2015.

[67] P. Kollmeyer, M. Wootton, J. Riemers, T. Stiene, E. Chemali, M. Wood and A. Emadi, "Optimal performance of a full scale li-ion battery and li-ion capacitor hybrid energy storage system for a plug-in hybrid vehicle," in *IEEE Energy Conversion Congress and Exposition (ECCE)*, Cincinnati, 2017.

[68] O. Onar and A. Khaligh, "Hybrid energy storage systems," in *Advanced Electric Drive Vehicles*, Boca Raton, CRC Press Taylor & Francis Group, 2015, pp. 283-316.

[69] Green Car Congress, "JM Energy Introduces Lithium-ion Capacitor," 28 July 2008. [Online]. Available: http://www.greencarcongress.com/2008/07/jm-energy-intro.html. [Accessed 28 march 2018].

[70] S. Sivakkumar and A. Pandlolfo, "Evaluation of lithium-ion cpaacitors assembled with pre-lithiated graphite anode and activated carbon cathode," *Electrochimica Acta,* vol. 65, pp. 280-287, 2012.

[71] X. Sun, X. Zhang, K. Wang, N. Xu and Y. Ma, "Temperature effect on electrochemical performances of Li-ion hybrid capacitors," *Journal of Solid State Electrochemistry,* vol. 19, no. 8, pp. 2501-2506, 2015.

[72] JSR Micro, "The concept of lithium ion capacitor," [Online]. Available: https://www.jsrmicro.be/emerging-technologies/lithium-ion-capacitor/concept-lithium-ion-capacitor. [Accessed 18 August 2018].

[73] S. Barcellona, S. Grillo and L. Piegari, "A novel current dependent lithium ion capacitor model: analysis and experimental drive cycle test validation," in *6th International Conference on Clean Electrical Power*, Santa Margherita Ligure, 2017.

[74] S. Barcellona, F. Ciccarelli, D. Iannuzzi and L. Piegari, "Modeling and paramater identification of lithium-ion capacitor modules," *IEEE Transactions on Sustainable Energy,* vol. 5, no. 3, pp. 785-794, 2014.

[75] S. Barcellona and L. Piegari, "A lithium-ion capacitor model working on a wide temperature range," *Journal of Power Sources,* vol. 342, no. 241-251, 2017.

[76] Y. Firouz, N. Omar, J. Timmermans, P. Van den Bossche and J. Van Mierlo, "Lithium-ion capacitor - characterization and development of new electrical model," *Energy,* vol. 83, pp. 597-613, 2015.

[77] E. Manla, G. Mandic and A. Nasiri, "Development of an electrical model for lithium-ion ultracapacitors," *IEEE Journal of Emerging and Selected Topics in Power Electronics,* vol. 3, no. 2, pp. 395-404, 2015.

[78] S. Lambert, V. Pickert, J. Holden, X. He and W. Li, "Comparison of supercapacitor and lithium-ion capacitor technologies for power electornics applications," in *5th IET International Conference on Power Electronics, Machines and Drives*, Brighton, 2010.

[79] P. Arboleya, *On-board energy storage and another technological solutions for catenary free light trains and trams,* University of Oviedo, 2018.

[80] C. Goodman and M. Chymera, "Overview of electric railway systems and the calculation of train performance," in *the 9th Institution of Engineering and Technology Professional Development Course on Electric Traction Systems*, Manchester, 2006.

[81] D. Iannuzzi, E. Pagano and P. Tricoli, "The use of energy storage systems for supporting the voltage needs of urban and suburban railway contact lines," *Energies,* vol. 6, pp. 1802-1820, 2013.

[82] R. Barrero, X. Tackoen and J. v. Mierlo, "Stationary or onboard energy storage systems for energy consumption reduction in a metro network," *Proceedings of the Insitution of Mechanical Engineers, Part F: Journal of Rail and Rapid Transit,* vol. 244, pp. 207-225, 2010.

[83] M. Steiner and J. Scholten, "Energy storage on board of railway vehicles," in *European Conference on Power Electronics and Applications*, Dresden, 2005.

[84] J. Poulin, "An energy storage system which reduces costs and generates revenue for the transit authority," November 2014. [Online]. Available: https://www.polisnetwork.eu/uploads/Modules/PublicDocuments/2b-poulin_energy_system_system_which_reduces_costs2.pdf. [Accessed 18 August 2018].

[85] D. Roch-Dupre, A. Lopez-Lopez, R. Pecharroman, A. Cucala and A. Fernandex-Cardador, "Analysis of the demand charge in DC railway systems and reduction of its economic impact with energy storage systems," *Electrical Power and Energy Systems,* vol. 93, pp. 459-467, 2017.

[86] Alstom, "APS: Service-proven catenary-free tramway operations," [Online]. Available: https://www.alstom.com/aps-service-proven-catenary-free-tramway-operations. [Accessed 16 August 2018].

[87] CBC, "TTC reviews safety protocols after rail left live during subway evacuation," 14 November 2014. [Online]. Available: https://www.cbc.ca/news/canada/toronto/ttc-reviews-safety-protocols-after-rail-left-live-during-subway-evacuation-1.2836116. [Accessed 21 August 2018].

[88] F. Ciccarelli, A. Del Pizzo and D. Iannuzzi, "Improvement of energy efficiency in light railway vehicles based on power management control of wayside lithium-ion capacitor storage," *IEEE Transactions on Power Electronics,* vol. 29, no. 1, pp. 275-286, 2014.

[89] F. Ciccarelli, D. Iannuzzi, D. Lauria and P. Natale, "Optimal control of stationary lithium-ion capacitor-based storage device for light electrical transportation network," *IEEE Transactions on Transportation Electrification,* vol. 3, no. 3, pp. 618-631, 2017.

[90] F. Ciccarelli and D. Iannuzzi, "A novel energy management control of wayside Li-ion capacitors-based storage for urban mass transit systems," in *International Symposium on Power Electronics, Electrical Drives, Automation and Motion*, Sorrento, 2012.

[91] P. Smith, T. Tran and T. C. J. Jiang, "Li-ion capacitors: electrochemical performance and thermal behavior," *Journal Of Power Sources,* vol. 243, pp. 982-992, 2003.

[92] M. Yassine and D. Fabris, "Performance of commercially available supercapacitors," *Energies,* vol. 10, no. 9, 2017.

[93] A. Chu and P. Braatz, "Comparison of commercial supercapacitors and high-power lithium ion batteries for power-assist applications in hybrid electric vehicles I. initial characterization," *Journal of Power Sources,* vol. 112, no. 1, pp. 236-246, 2002.

[94] A. Burke and M. Z. H. Miller, "Ultracapacitors in hybrid vehicle applications: testing of new high power devices and prospects for increased energy density," in *EVS26 International Battery, Hybrid and Fuel Cell Electric Vehicle Symposium*, Los Angeles, 2012.

[95] A123 Systems, "Nanophosphate(R) lithium ion prismatic pouch cell AMP20M1HD-A," [Online]. Available: http://liionbms.com/pdf/a123/AMP20M1HD-A.pdf. [Accessed 23 August 2018].

[96] Skeleton Technologies, "Data sheet SkelCap ultracapacitor," [Online]. Available: https://www.skeletontech.com/hubfs/170525-1C-DataSheet-SCA.pdf?hsCtaTracking=9dad2c8b-c8b1-4a0e-acba-913103f71ac2%7C1b0ce536-e940-43b8-b00a-9d371a854c27. [Accessed 7 August 2018].

[97] FreedomCAR Program Electrochemical Energy Storage Team, "FreedomCAR battery test manaual for power-assist hybrid electric vehicles," October 2003. [Online]. Available: https://avt.inl.gov/sites/default/files/pdf/battery/freedomcar_manual_04_15_03.pdf. [Accessed Sept 2018].

[98] H. Gualous, H. Louahlia and R. Gallay, "Supercapacitor characterization and thermal modelling with reversible and irreversible heat effect," *IEEE Transactions on Power Electronics,* vol. 26, no. 11, pp. 3402-3409, 2011.

[99] National Renewable Energy Laboratory, "Battery thermal modeling and testing," May 2011. [Online]. Available: https://www.nrel.gov/transportation/assets/pdfs/50916.pdf. [Accessed 6 June 2018].

[100] P. Kollmeyer, A. Shridar and T. Jahns, "Modeling of low-temperature operation of a hybrid energy storage system with a butler-volmer equation based battery model," in *IEEE Energy Conversion Congress and Exposition (ECCE)*, Milwaukee, 2016.

[101] P. Keil and A. Jossen, "Improving the low-temperature performance of electric vehicles by hybrid energy storage systems," in *IEEE Vehicle Power and Propulsion Conference*, Coimbra, 2014.

[102] L. Juang, P. Kollmeyer, T. Jahns and R. Lorenz, "Improved modeling of lithium-based batteries using temperature-dependent resistance and overpotential," in *IEEE Transportation Electrification Conference and Expo*, Dearborn, 2014.

[103] S. Liu, J. Jiang, W. Shi, Z. Ma, L. Y. Wang and H. Guo, "Butler-volmer-equation-based electrical model for high-power lithium titanate batteries used in electric vehicles," *IEEE Transactions on Inductrial Electronics,* vol. 62, no. 12, pp. 7557-7568, 2015.

[104] "Annual certification data for vehicles, engines, and equipment," Enivronmental Protection Agency, [Online]. Available: https://www.epa.gov/compliance-and-fuel-economy-data/annual-certification-data-vehicles-engines-and-equipment.

[105] G. Mohan, F. Assadian and S. Longo, "Comparative analysis of forward-facing models vs backward-facing models in powertrain component sizing," in *EIT 4th Hybrid and Electric Vehicle Conference*, London, 2013.

[106] K. Wipke, M. Cuddy and S. Burch, "ADVISOR 2.1: A user-friendly advanced powertrain simulation using a combined backward/forward approach," *IEEE Transactions on Vehicular Technology,* vol. 48, no. 6, pp. 1751-1761, 1999.

[107] D. Choi, L. Seong, B.-H. Cho and Y. Yoon, "Development of design tool for hybrid power systems of hybrid electric military combat vehicles," in *IEEE Vehicle Power and Propulsion Conference*, Lille, 2010.

[108] B. Rochard and F. Schmid, "A review of methods to measure and calculate train resistances," *Proceedings of the Institution of Mechanical Engineers, Part F: Journal of Rail and Rapid Transit,* no. 214, pp. 158-199, 2000.

[109] Kollmeyer and Phillip, "Electromechanical modeling and analysis of a corbin sparrow electric vehicle using on the road data," University of Wisconsin - Madison, Madison, 2011.

[110] W. W. Hay, Raiload engineering, John Wiley & Sons, Inc., 1982.

[111] M. Spiryagin, C. Cole, Y. Q. Sun, M. McClanachan, V. Spiryagin and T. McSweeney, Design and simulation of rail vehicles, CRC Press, 2014.

[112] M. U. Nawaz, "Estimation of running resistance in train tunnels," Norwegian University of Science and Technology, 2015.

[113] D. Seimbille, "Design of power supply system in DC electrified transit railways - influence of the high voltage network," KTH Royal Institute of Technology, Stockholm, 2014.

[114] T. Nicholson, "DC & AC traction motors," in *IET Professional Development Course on Electric Traction Systems*, Manchester, 2008.

[115] V. Garg and R. Dukkipati, Dynamics of railway vehicle systems, Don Mills: Academic Press Canada, 1984.

[116] A. Jaschinski, H. Chollet, S. Iwnicki, A. Wickens and J. Wurzen, "The application of roller rigs to railway vehicle dynamics," *Vehicle System Dynamics,* vol. 31, pp. 345-395, 1999.

[117] Anonymous, "Would electrically-driven trains benefit from batteries to handle regenerative braking," [Online]. Available: https://anonw.com/tag/mark-4-coach/. [Accessed 10 August 2018].

[118] F. Bennell, "Rectifiers for railway-traction substations," *Electrical Power Applications,* vol. 2, no. 1, pp. 22-26, 1979.

[119] B. Wu, High-power converters and AC drives, Hoboken: John Wiley & Sons, 2006.

[120] M. Fracchia, M. Galaverna, P. Pozzobon and L. Puglisi, "Voltage regulation in electrical supply substations for DC traction systems," *WIT Transactions on the Built Environment,* vol. 7, pp. 387-394, 1994.

[121] Z. Tian, S. Hillmansen, C. Roberts, P. Weston, L. Chen, N. Xhao, S. Su and T. Xin, "Modeling and simulation of DC rail traction systems for energy saving," in *IEEE International Conference on Intelligent Transportation Systems*, Qingdao, 2014.

[122] R. Barrero, O. Hegazy, T. Lataire, T. Coosemans and J. Van Mierlo, "An accurate multi-train simulation tool for energy recovery evaulation in DC rail networks," *International Review on Modelling and Simulations,* vol. 4, no. 6, pp. 2985-3003, 2011.

[123] T. Kulworawanichpong, "Multi-train modeling and simulation integrated with traction power supply solver using simplified Newton-Raphson method," *Journal of Modern Transportation,* vol. 23, no. 4, pp. 241-251, 2015.

[124] Conductix, "Welded cap conductor rail," [Online]. Available: https://www.conductix.us/sites/default/files/downloads/Brochure_-_Welded_Cap_Conductor_for_Third_Rail.pdf. [Accessed 11 August 2018].

[125] K. Forman, "Aluminium/stainless steel conductor technology: A case for its adoption in the US," in *Proceedings of the 2013 Joint Rail Conference*, Knoxville, 2013.

[126] E. Cheever, "Modified node analysis," [Online]. Available: https://www.swarthmore.edu/NatSci/echeeve1/Ref/mna/MNA2.html#Introduction. [Accessed 10 August 2018].

[127] C.-W. Ho, A. Ruehli and P. Brennan, "The modified nodal approach to network analysis," *IEEE Transactions on Circuits and Systems,* vol. 22, no. 6, pp. 504-509, 1975.

[128] F. Al-Naima and B. Al-Jewad, Element stamp algorithm for matrix formulation of symbolic circuits, New York: Nova Science Publishers Inc, 2010.

[129] A. Yildiz, "A MNA-based unified ideal switch model for analysis of switching circuitrs," *Journal of Circuits, Systems, and Computers,* vol. 22, no. 6, 2013.

[130] C, Circuit oriented electromagnetic modeling using the PEEC techniques, first edition, John Wiley & Sons, 2017.

[131] L. Pillage, R. Rohrer and C. Visweswariah, Electronic circuit and system simulation methods, McGraw-Hill, 1995.

[132] V. Litovski and M. Zwonlinski, VLSI circuit simulation and optimization, Springer, 1996.

[133] R. Barrero, X. Tackoen and J. V. Mierlo, "Supercapacitors on-board light rail vehicles: enhanced energy storage systems for improved efficiency," in *IEEE/ASME Joint Rail Conference*, Wilmington, 2008.

[134] R. Barrero, *Energy savings in public transportation,* IEEE Vehicular Technology Magazine, 2008.

[135] D. Iannuzzi, P. Pighetti and P. Tricoli, "A study on stationary supercapacitor sets for voltage droops compensation of streetcar feeder lines," in *Electrical Systems for Aircraft, Railway and Ship Propulsion*, Bologna, 2010.

[136] D. Iannuzzi, F. Ciccarelli and D. Lauria, "Stationary ultracapacitors storage device for improving energy savings and voltage profile of light transportation networks," *Transportation Research Part C: Emerging Technologies,* vol. 21, no. 1, pp. 321-337, 2012.

[137] F. Ciccarelli, D. Iannuzzi and P. Tricoli, "Control of metro-trains equipped with onboard supercapacitors for energy saving and reduction of power peak demand," *Transportation Research Part C: Emerging Technologies,* vol. 24, pp. 36-49, 2012.

[138] G. Graber, V. Calderaro, V. Galdi, A. Piccolo, R. Lamedica and A. Ruvio, "Techno-economic sizing of auxilary-battery-based substation in DC railway systems," *IEEE Transaction on Transportation Electrification,* vol. 4, no. 2, pp. 616-625, 2018.

[139] H. Ohsaki, N. Matsushita, T. Koseki and M. Tomita, "Characteristic analysis of DC electric railway systems with superconducting power cables connecting power substations," in *European Conference on Applied Superconductivity*, 2014.

[140] R. Barrero, X. Tackoen and J. V. Mierlo, "Improving energy efficiency in public transport: stationary supercapacitor based energy storage systems for a metro network," in *IEEE Vehicle Power and Propulsion conference*, Harbin, 2008.

[141] D. Iannuzzi and P. Tricoli, "Speed-based state-of-charge tracking control for metro trains with onboard supercapacitors," *IEEE Transactions on Power Electronics,* vol. 24, no. 4, pp. 2129-2140, 2012.

[142] B. Robyns, C. Saudemont, D. Hissel, R. Xavier, B. Sareni and J. Pouget, Electrical energy storage in transportation systems, Wiley, 2016.

[143] J. Attwooll, "150 London Underground facts," The Telegraph, 9 January 2017. [Online]. Available: https://www.telegraph.co.uk/travel/destinations/europe/united-kingdom/england/london/articles/London-Underground-150-fascinating-Tube-facts/. [Accessed 23 August 2018].

[144] General Motors Chevrolet, "Bolt EV 2017," [Online]. Available: https://www.chevrolet.ca/content/dam/Chevrolet/northamerica/ca/nscwebsite/en/home/vehicles/cars/2017_bolt_ev/pdfs/CH-CAT-BOL-10674238_MY17_CDN_Bolt_EV_Catalog_FINAL_EN.pdf. [Accessed 24 August 2017].

[145] H. M. T. S. Al-Ezee, I. Taylor, S. D. and S. J., "An on-board energy storage system for catenary free operation of a tram," in *International Conference on Renewable Energies and Power Quality*, Malaga, 2017.

[146] H. Al-Ezee, S. Tennakoon, I. Taylor and D. Scheidecker, "Aspects of catenary free operation of DC traction systems," in *International Universities Power Engineering Conference*, Stoke on Trent, 2015.